INTERNATIONAL DOCTORAL
SCHOOL OF THE USC

Ana
Iglesias-Mejuto

PhD Thesis

Development of aerogel-based formulations for regenerative medicine

Santiago de Compostela, 2024

Doctoral Programme in Drug Research and Development

ESCOLA DE DOUTORAMENTO
INTERNACIONAL DA USC

DOCTORAL THESIS

DEVELOPMENT OF AEROGEL-BASED FORMULATIONS FOR REGENERATIVE MEDICINE

Ana Iglesias-Mejuto

Directors: Carlos Alberto García González, Inés Ardao Palacios

Tutor: Carlos Alberto García González

DOCTORAL PROGRAM IN DRUG RESEARCH AND DEVELOPMENT

SANTIAGO DE COMPOSTELA

USC
UNIVERSIDADE
DE SANTIAGO
DE COMPOSTELA

AGRADECIMIENTOS

A mis directores Carlos García-González e Inés Ardao-Palacios por su paciencia y apoyo constante durante toda la tesis. Por haberme escuchado y comprendido siempre.

Al grupo I+D Farma por ser mi familia durante toda esta etapa. A Clara y a María Vivero, por estar presentes desde el principio hasta el final de mi tesis aun estando a veces en la distancia. También a Iago, por todas esas hemólisis en las que no hicieron falta controles positivos. A mis compañeros de laboratorio, por todos los buenos momentos vividos.

Al grupo Paraquasil por ser los mejores compañeros de enfrente. Muy en especial a Victoria, Selene y a Vini por su inestimable apoyo emocional y su siensia loca. Valoro mucho todos los cafeses y vuestra amistad.

Al grupo de la Prof. Luisa Durães por haberme acogido en plena pandemia y por seguirme ayudando en la actualidad.

Al grupo de la Prof. Catarina Pinto-Reis por haberme hecho sentir como en casa durante los tres meses que pasé en Lisboa. A Tânia, Joana y Mariana por ser mis compañeras de aventuras durante esos meses y aún a día de hoy. Especialmente a Tânia, por acogerme en casa ya en varias ocasiones y por todos los viajes juntas. Amenazo seriamente con volver.

A mis amigos Ary, John y Ana por mantener la amistad a lo largo del tiempo. En especial a Ana y a su hermano César por las veces que vinisteis a visitarme por el mundo. Grandes viajeros, mejores personas.

A mis padres y a mi hermano por apoyarme siempre de manera incondicional en todo lo que ha estado de su mano. Sin vosotros nunca habría sido posible llegar hasta aquí.

USC
UNIVERSIDADE DE SANTIAGO DE COMPOSTELA

USC
UNIVERSIDADE
DE SANTIAGO
DE COMPOSTELA

INDEX

RESUMO..... ix
EXTENDED ABSTRACT xix
ABBREVIATION LIST..... xxix

Chapter 1. INTRODUCTION 1
1.1. Background 2
1.2. Natural polymer gels for drug delivery applications 4
1.3. Natural polymer gels for tissue engineering 9
1.3.1. Cell culture 10
1.3.2. Scaffolds 12
1.4. Natural polymer gels for the treatment of wounds 15
1.4.1. Protein-based gels for wound treatment 18
1.4.2. Polysaccharide-based gels for wound treatment 19
1.5. Natural polymer gels for biomedical imaging and sensing 21
1.6. Future perspectives and conclusions 27
1.7. References 29

Chapter 2. OBJECTIVES AND ORGANIZATION 41

SECTION I. DEVELOPMENT OF A DUAL PROCESSING STRATEGY TO OBTAIN 3D-PRINTED AEROGELS
Chapter 3. 3D-PRINTED ALGINATE-HYDROXYAPATITE AEROGEL SCAFFOLDS FOR BONE TISSUE ENGINEERING 47
3.1. Introduction 48
3.2. Materials and Methods 51
3.2.1. Materials 51
3.2.2. 3D-printing of hydrogels 51
3.2.3. $scCO_2$ drying of 3D-printed alcogels 52
3.2.4. Physicochemical characterization of 3D-printed alginate aerogels 53
3.2.5. Printing fidelity tests 54
3.2.6. Cellular studies 54
3.2.6.1. Cell viability tests 54
3.2.6.2. Cell attachment tests 55
3.2.6.3. Cell migration tests 56
3.2.7. Statistical analysis 56
3.3. Results and Discussion 56
3.3.1. Effect of alginate and $CaCl_2$ content on scaffold morphology 56
3.3.2. Effect of HA content on scaffold morphology 59
3.3.3. Printing fidelity tests 62
3.3.4. Cellular studies 63
3.3.4.1. Cell viability tests 63
3.3.4.2. Cell attachment tests 64
3.3.4.3. Cell migration tests 65
3.4. Conclusions 66
3.5. References 67

Chapter 4. 3D-PRINTED, DUAL CROSSLINKED AND STERILE AEROGEL SCAFFOLDS FOR BONE TISSUE ENGINEERING 71
4.1. Introduction 72
4.2. Materials and Methods 75

USC UNIVERSIDADE DE SANTIAGO DE COMPOSTELA

4.2.1. Materials 75
4.2.2. 3D-printing of hydrogels 76
4.2.3. Rheological evaluation of alginate-HA inks 76
4.2.4. $scCO_2$ drying of 3D-printed alcogels 77
4.2.5. Post-crosslinking of aerogels with GA vapor 77
4.2.6. Physicochemical characterization of dual crosslinked aerogels 78
4.2.7. Bioactivity tests 79
4.2.8. Cell viability tests 79
4.2.9. Hemolytic activity test 80
4.2.10. $scCO_2$ sterilization of 3D-printed aerogels 80
4.2.11. Statistical analysis 81
4.3. Results and Discussion 81
4.3.1. Rheological properties of alginate-HA inks 81
4.3.2. Effect of ageing of aerogels 82
4.3.3. Effect of GA chemical post-crosslinking of aerogels 85
4.3.4. Chemical analysis of dual crosslinked aerogels 87
4.3.5. Bioactivity tests of dual crosslinked aerogels 89
4.3.6. Cell compatibility of dual crosslinked aerogels 90
4.3.7. Hemolytic activity of dual crosslinked aerogels 92
4.3.8. Sterilization of dual crosslinked aerogels 92
4.4. Conclusions 94
4.5. References 95

SECTION II. ENGINEERING OF A STRATEGY TO *IN VIVO* MONITOR AEROGELS BY BIOIMAGING
Chapter 5. SYNTHESIS OF HIGHLY LUMINESCENT SILICA-COATED UPCONVERSION NANOPARTICLES FROM LANTHANIDE OXIDES OR NITRATES USING CO-PRECIPITATION AND SOL-GEL METHODS 99
5.1. Introduction 100
5.2. Materials and Methods 104
5.2.1. Materials 104
5.2.2. Synthesis of UCNPs by co-precipitation and sol-gel methods 104
5.2.3. Physicochemical evaluation of UCNPs 106
5.2.4. Cell viability tests 107
5.2.5. Hemolytic activity test 108
5.2.6. Statistical analysis 108
5.3. Results and Discussion 109
5.3.1. Physicochemical evaluation of UCNPs 109
5.3.2. Cell compatibility and hemolytic activity evaluation 119
5.4. Conclusions 120
5.5. References 121

Chapter 6. 3D-PRINTED AEROGELS AS THERANOSTIC IMPLANTS MONITORED BY FLUORESCENCE BIOIMAGING 125
6.1. Introduction 126
6.2. Materials and Methods 128
6.2.1. Materials 128
6.2.2. Synthesis of UCNPs by co-precipitation and sol-gel methods 129
6.2.3. 3D-printing of UCNPs-labeled hydrogels 129
6.2.4. Rheological evaluation of inks 130
6.2.5. $scCO_2$ drying of UCNPs-labeled 3D-printed alcogels 130
6.2.6. Physicochemical characterization of UCNPs-labeled aerogels 131
6.2.7. Cellular studies 132

USC UNIVERSIDADE DE SANTIAGO DE COMPOSTELA

6.2.7.1. Cell viability tests 132
6.2.7.2. Cell attachment tests 132
6.2.7.3. Cell migration tests 133
6.2.8. Hemocompatibility studies 133
6.2.8.1. Hemolytic activity test 133
6.2.8.2. HET-CAM assay 134
6.2.9. Animals care and subcutaneous implantation of scaffolds 134
6.2.9.1. Safety studies 134
6.2.9.1.1. Circulating Cytokine Quantification 136
6.2.9.1.2. Histological evaluation of major organs 136
6.2.9.2. Bioimaging studies 136
6.2.10. Statistical analysis 137
6.3. Results and Discussion 138
6.3.1. Rheological assessment of inks 138
6.3.2. Physicochemical evaluation of UCNPs-decorated aerogels 139
6.3.3. Cell studies 145
6.3.4. Hemocompatibility studies 147
6.3.5. Safety studies 148
6.3.5.1. Determination of plasmatic cytokines 148
6.3.5.2. Histological evaluation of major organs 150
6.3.6. Bioimaging studies 152
6.4. Conclusions 155
6.5. References 155

SECTION III. IMPLEMENTATION OF ADVANCED 3D-PRINTED AEROGELS LOADED WITH BIOACTIVE AGENTS AND NANOCELLULOSE

Chapter 7. VANCOMYCIN-LOADED METHYLCELLULOSE AEROGEL SCAFFOLDS FOR ADVANCED BONE TISSUE ENGINEERING 159

7.1. Introduction 160
7.2. Materials and Methods 162
7.2.1. Materials 162
7.2.2. 3D-printing of hydrogels 162
7.2.3. Rheological evaluation of inks 163
7.2.4. $scCO_2$ drying of 3D-printed alcogels 163
7.2.5. Physicochemical characterization of 3D-printed aerogels 164
7.2.6. Printing fidelity tests 165
7.2.7. Mechanical evaluation by DMA 165
7.2.8. Bioactivity tests 166
7.2.9. VAN loading and entrapment yield on aerogels 166
7.2.10. VAN release tests from aerogels 166
7.2.11. Cell viability and mineralization tests 167
7.2.12. Safety tests using *A. salina* model 169
7.2.13. HET-CAM test 169
7.2.14. Antimicrobial tests of 3D-printed aerogels 169
7.2.15. $scCO_2$ sterilization of 3D-printed aerogels 170
7.2.16. Statistical analysis 170
7.3. Results and Discussion 170
7.3.1. Rheological evaluation of inks 170
7.3.2. Physicochemical characterization of 3D-printed aerogels 172
7.3.3. Printing fidelity evaluation 178
7.3.4. Mechanical analysis 179
7.3.5. Bioactivity assessment 179

USC UNIVERSIDADE DE SANTIAGO DE COMPOSTELA

7.3.6. VAN loading, entrapment yield, and release from aerogels 181
7.3.7. Cytocompatibility tests 183
7.3.8. Safety tests using *A. salina* model 184
7.3.9. HET-CAM test 185
7.3.10. Antimicrobial assessment of 3D-printed aerogels 185
7.3.11. Mineralization assay 185
7.3.12. Sterility procedure evaluation 186
7.4. Conclusions 187
7.5. References 188

Chapter 8. CELLULOSE-IN-CELLULOSE 3D-PRINTED BIOAEROGELS FOR BONE TISSUE ENGINEERING 193
8.1. Introduction 194
8.2. Materials and Methods 196
8.2.1. Materials 196
8.2.2. Preparation of BC-NF and SPIONs doped BC-NF 197
8.2.3. 3D-printing of cellulose-in-cellulose hydrogels 198
8.2.4. Rheological evaluation of aqueous cellulose-in-cellulose inks 198
8.2.5. $scCO_2$ drying of cellulose-in-cellulose alcogels 198
8.2.6. Physicochemical characterization of cellulose-in-cellulose aerogels 199
8.2.7. Printing fidelity tests 200
8.2.8. Cytocompatibility tests 201
8.2.9. Hemolytic activity test 201
8.2.10. HET-CAM test 202
8.2.11. Preliminary safety test 202
8.2.12. $scCO_2$ sterilization of aerogels 203
8.2.13. Statistical analysis 203
8.3. Results and discussion 203
8.3.1. Aerogel processing and printing fidelity assessment 203
8.3.2. Physicochemical characterization of cellulose-in-cellulose aerogels 208
8.3.3. Magnetic properties of SPIONs decorated aerogels 214
8.3.4. Biocompatibility and preliminary safety tests 215
8.3.5. Sterility procedure evaluation 217
8.4. Conclusions 218
8.5. References 219

Chapter 9. GENERAL DISCUSSION 223

Chapter 10. CONCLUSIONS 229

ANNEX 1: AUTHOR DECLARATION 233

ANNEX 2: PERMISSIONS 235

ANNEX 3: ETHICAL APPROVALS 247

USC UNIVERSIDADE DE SANTIAGO DE COMPOSTELA

RESUMO

Os enxertos biolóxicos e sintéticos son na actualidade estratexias empregadas no manexo clínico das fracturas óseas. Os autoenxertos, aloenxertos e xenoenxertos son as opcións principais para a recuperación de áreas danadas pero, debido á súa escaseza, os implantes sintéticos están en auxe. Sen embargo, estas solucións adoitan carecer de certas propiedades esenciais para a reparación ósea como a bioactividade, a liberación controlada de antibióticos que mitiguen a infección ósea trala implantación ou unha estratexia para o seguimento en tempo real dos enxertos e dos seus produtos de degradación. Todas estas propiedades en conxunto non están presentes nas solucións comerciais para as fracturas óseas malia que mellorarían o rendemento destes implantes na rexeneración ósea.

A enxeñaría de tecidos ósea é unha disciplina que busca a recuperación anatómica e funcional do tecido que rodea os defectos óseos. Estúdanse diferentes aproximacións para a fabricación de implantes adaptados ó paciente con capacidade de rexeneración de tecido. Entre elas, a impresión en tres dimensións (3D) é unha técnica novidosa baseada no uso mínimo de recursos materiais e empregada para fabricar construcións personalizadas en termos de composición e morfoloxía externa. Diferentes materiais son empregados para a impresión 3D de andamiaxes para a reparación ósea, pero salientan os polímeros naturais por seren similares á estrutura nativa da matriz extracelular (ECM) ósea. A impresión 3D por extrusión é o método mais empregado para obter andamiaxes biopoliméricas dirixidas á enxeñaría de tecidos ósea. Entre outras vantaxes, permite a xeración de macroporos entre as capas das andamiaxes, inducindo unha nova poboación de tamaños de poro.

A tecnoloxía dos fluídos supercríticos (SCF) é outra alternativa verde empregada para dotar ás andamiaxes de propiedades atractivas para a reparación ósea como alta porosidade e baixa densidade. Esta tecnoloxía baséase no uso do dióxido de carbono supercrítico ($scCO_2$) en condicións suaves para manter a porosidade do xel húmido no estado seco, para así fabricar

USC UNIVERSIDADE DE SANTIAGO DE COMPOSTELA

aeroxeles cunha nanoestrutura porosa avanzada. Especificamente, a macroporosidade entre 100-300 μm é necesaria para a formación ósea, mentres que o transporte efectivo de nutrientes e eliminación de residuos dos implantes son levados a cabo polos mesoporos. En definitiva, requírense poros de diferentes tamaños para a correcta rexeneración do tecido e reparación ósea a longo prazo.

A esterilidade dunha andamiaxe debe garantirse antes da súa implantación. As técnicas convencionaiss son capaces de alcanzar o nivel de esterilización requirido pero poderían causar un efecto prexudicial no rendemento fisicoquímico dos materiais biopoliméricos. O procedemento de esterilización baseado no uso do $scCO_2$ é considerados unha alternativa segura e capaz de esterilizar de forma efectiva mantendo as propiedades texturais e biolóxicas destes materiais. Utilízanse aditivos como o peróxido de hidróxeno (H_2O_2) para potenciar o efecto bactericida do $scCO_2$ e alcanzar o nivel de esterilización requirido. A estabilidade a longo prazo é outro parámetro chave dos biomateriais xa que os seus rendementos fisicoquímico e biolóxico deben ser asegurados desde a súa fabricación ata a súa implantación. A escasez de estudos de estabilidade dos aeroxeles biopoliméricos motiva o estudo deste parámetro tralo seu almacenamento.

A impresión 3D de xeles personalizados e o seu secado e esterilización mediante o uso de SCF podería dar lugar a aeroxeles estériles con porosidade dual e cun rendemento avanzado e estable. A carga de fármacos e de sondas fluorescentes nas estruturas altamente porosas conduciría á fabricación de implantes rastexables cunha cesión controlada de axentes bioactivos. Neste contexto e no marco desta Tese de Doutoramento, fabricáronse andamiaxes óseas estables, estériles e adaptadas ó paciente mediante a novidosa combinación tecnolóxica da impresión 3D e dos SCF. Estas andamiaxes dotáronse de bioactividade, dunha liberación sostida de antibiótico e de trazabilidade *in vivo* mediante bioimaxe, abordando así as desvantaxes importantes dos implantes óseos comerciais actuais.

USC DE COMPOSTELA

No Capítulo 3 desta Tese de doutoramento, fabricáronse aeroxeles con porosidade dual mediante unha novidosa combinación metodolóxica. Desenvolveuse unha estratexia de procesamento dual con dúas etapas consistentes na impresión 3D de xeles e no seu secado mediante $scCO_2$ para fabricar aeroxeles altamente porosos por impresión 3D. Axustáronse os parámetros da impresión 3D para obter xeles de alxinato-hidroxiapatita (HA) cunha alta fidelidade de impresión con respecto ó arquivo de impresión orixinal. O alxinato foi seleccionado polas súas propiedades beneficiosas para a enxeñaría de tecidos ósea como biocompatibilidade, non toxicidade e estrutura porosa similar á observada na ECM ósea. A HA foi escollida debido á súa similaridade co óso humano e ás súas propiedades bioactivas. Diferentes concentracións de alxinato, cloruro cálcico ($CaCl_2$) e HA foron examinadas para seleccionar as que dan lugar a estruturas co maior rendemento fisicoquímico. Realizouse o secado dos xeles impresos de alxinato usando a tecnoloxía dos SCF para asegurar o mantemento da estrutura porosa nos aeroxeles. Observáronse mesoporos e macroporos cunha alta interconectividade nos aeroxeles impresos, confirmando así as súas propiedades texturais avanzadas. Obtivéronse un menor encollemento volumétrico e unha maior fidelidade de impresión cando se incrementaron os contidos de HA nos aeroxeles. Observouse tamén un marcado descenso nos parámetros texturais, é dicir, na área superficial, no volume dos poros e na porosidade xeral co contido máis alto de HA. Estudáronse as propiedades biolóxicas dos aeroxeles con valores de citocompatibilidade superiores ó 80% tras 24 e 48 h en contacto con fibroblastos murinos. Ademais, realizáronse ensaios de migración celular con fibroblastos con resultados similares para as diferentes formulacións, pero con valores superiores para os aeroxeles con respecto á capacidade de migración natural desta liña celular. Os ensaios de adhesión leváronse a cabo en células nai mesenquimais (MSCs) derivadas da médula ósea humana, cunha tendencia proliferativa para as diferentes formulacións. Todos estes resultados reforzan a idoneidade dos aeroxeles impresos de alxinato-HA como plataformas para a rexeneración do tecido óseo.

USC UNIVERSIDADE DE SANTIAGO DE COMPOSTELA

No Capítulo 4 desta Tese de doutoramento, avaliáronse estratexias de procesamento para a produción de andamiaxes impresas cunha estabilidade estrutural mellorada e cunha esterilidade de grado médico, fabricando así aeroxeles listos para a súa implantación. A estratexia de procesamento dual mellorouse con dúas etapas de post-procesado: o entrecruzamento con glutaraldehido (GA) e a esterilización. Empregouse un baño de $CaCl_2$ nos hidroxeles seguido por unha atmósfera de GA nos aeroxeles, realizando así un entrecruzamento dual (iónico e covalente) para incrementar a integridade das andamiaxes. Estudouse o efecto deste tratamento no rendemento fisicoquímico dos aeroxeles sen observar diferenzas relevantes tras diferentes períodos de envellecemento en $CaCl_2$, pero cun lixeiro descenso nos parámetros texturais cando se aplicou o entrecruzamento dual. Cabe destacar que a porosidade dual e o encollemento volumétrico das estruturas non exhibiron diferenzas relevantes co entrecruzamento dual ou sen el. Observouse unha integridade estrutural superior para tódalas formulacións cando se aplicou o post-procesamento, coas capas impresas unidas nunha estrutura compacta case sen exfoliación. Ademais, o rendemento biolóxico dos aeroxeles non se veu afectado polo entrecruzamento con GA, cunha citocompatibilidade superior ó 80 % en fibroblastos murinos, tras 24 e 48 h de contacto. A hemólise foi tamén desprezable tralo contacto dos aeroxeles co sangue humano, suxerindo así a non toxicidade da atmosfera de GA como método de entrecruzamento. A bioactividade dos aeroxeles de alxinato-HA estudouse mediante inmersión en fluído biolóxico simulado (SBF) por diferentes períodos de tempo (3, 7, 15 e 28 días). Observouse unha elevada bioactividade nas formulacións que contiñan HA, cunha maior cantidade de depósitos de apatita, así como un incremento no seu tamaño, detectado nos aeroxeles co maior contido en HA. Este resultado suxire que a bioactividade a longo prazo das andamiaxes depende da súa composición, especificamente, do seu contido en HA. As propiedades reolóxicas das tintas mostraron un claro adelgazamento por cizalla que foi máis salientable cando se acrecentou o contido en HA.

USC UNIVERSIDADE DE SANTIAGO DE COMPOSTELA

Nesta Tese de Doutoramento explorouse outra etapa de post-procesado, neste caso, para a esterilización de aeroxeles poliméricos obtidos por impresión 3D. A esterilización realizouse mediante o uso de $scCO_2$ e de H_2O_2 como aditivo, en condicións suaves (100 bar, 40 °C, 30 min, 1200 ppm H_2O_2). Realizáronse ensaios microbiolóxicos e a avaliación do rendemento textural trala esterilización dos aeroxeles para demostrar a eficacia do procedemento e o mantemento das propiedades fisicoquímicas, respectivamente. As andamiaxes estériles incubáronse durante 24 h en placas de agar tríptico de soia (TSA) e en tubos de caldo de soia tripticaseína (TSB) sen detectar ningunha unidade formadora de colonias (CFU) ou turbidez no medio, asegurando así o alcance das condicións de esterilidade. Ademais, avaliouse a estabilidade estrutural dos aeroxeles en termos de propiedades texturais, sen observar diferenzas relevantes con respecto ás mesmas formulacións analizadas antes da esterilización. Estes resultados reforzan o uso dos SCF en condicións suaves como método de esterilización de andamiaxes biopoliméricas.

No Capítulo 5 desta Tese de Doutoramento, sintetizáronse nanopartículas sobreconversoras (UCNPs) como parte dunha estratexia para permitir a trazabilidade dos implantes e dos seus produtos de degradación *in vitro* e *in vivo*. Desenvolveuse unha aproximación sintética novidosa, combinando a coprecipitación dun núcleo de lantánidos coa formación dun recubrimento de sílice por método sol-xel. Obtivéronse diferentes formulacións das UCNPs combinando diferentes precursores dos lantánidos (óxidos e nitratos) e métodos de secado (SCF e estufa). O espectro de sobreconversión de luz e a estabilidade seleccionáronse como criterios principais para escoller a formulación das UCNPs a incorporar nos aeroxeles previamente deseñados para fabricar un nanodispositivo teranóstico. O espectro de sobreconversión de luz sinalou os nitratos dos lantánidos e o secado en estufa como as condicións máis adecuadas para sintetizar UCNPs altamente fluorescentes. Realizouse un estudo de estabilidade mediante o almacenamento durante 2 anos da formulación seleccionada das UCNPs e avaliouse despois as súas propiedades fisicoquímicas. Preservouse a fluorescencia das UCNPs e as súas características morfolóxicas, suxerindo así a súa estabilidade a longo prazo de almacenamento. A biocompatibilidade dos

USC UNIVERSIDADE DE SANTIAGO DE COMPOSTELA

nanocomplexos seleccionados avaliouse medindo da viabilidade de fibroblastos murinos tras 24 e 48 h cas UCNPs e determinando a hemólise tralo contacto co sangue humano. A viabilidade celular foi superior ó 90 % e non se detectou hemólise, indicando así que as UCNPs non son tóxicas incluso ás altas concentracións estudadas (5 and 10 mg/ mL). Este é un fito importante para ser cargadas nas andamiaxes e convertilas así en dispositivos monitorizables *in vivo*.

No Capítulo 6 desta Tese de Doutoramento, fabricáronse aeroxeles marcados con UCNPs por vez primeira mediante a incorporación das UCNPs previamente sintetizadas a concentracións baixas (0,4 e 0,8 wt.%) nas tintas de impresión 3D. As propiedades reolóxicas das tintas apenas se viron alteradas trala incorporación das UCNPs, mostrando adelgazamento por cizalla en tódolos casos. O rendemento de fluorescencia dos aeroxeles cargados coas UCNPs confirmou a efectiva fabricación de aeroxeles fluorescentes. As propiedades fisicoquímicas dos aeroxeles dopados con UCNPs foron similares ás das mesmas formulacións sen dopaxe. Preserváronse a estrutura porosa interconectada, parámetros texturais, encollemento volumétrico e fidelidade de impresión dos aeroxeles trala incorporación das UCNPs. O rendemento biolóxico foi estudado *in vitro* mediante avaliación da viabilidade e da migración celulares en fibroblastos murinos e mediante ensaios de adhesión en MSCs. Non apareceron diferenzas relevantes trala comparación das propiedades biolóxicas das andamiaxes dopadas ou non con UCNPs, suxerindo a ausencia dun impacto negativo dos nanocomplexos incorporados a contidos baixos. Tamén se estudou a hemocompatibilidade dos aeroxeles cargados con UCNPs mediante medición da actividade hemolítica e mediante o ensaio na membrana corioalantoidea de ovo fertilizado (HET-CAM). Non se detectou coagulación ou sangrado dos vasos tralo contacto coa CAM, establecéndose potencialmente unha boa interacción entre o sangue e a andamiaxe unha vez implantada.

A estabilidade dos aeroxeles foi estudada por primeira vez tras 3 anos de almacenamento. Mantivéronse as propiedades de fluorescencia, os parámetros texturais e a estrutura porosa

USC DE COMPOSTELA

interconectada sen observar diferenzas relevantes con respecto ás mesmas formulacións analizadas xusto trala súa fabricación. Estes resultados resaltan a estabilidade fisicoquímica e da fluorescencia dos aeroxeles dopados con UCNPs e reforzan a súa idoneidade como nanodispositivos teranósticos. A versatilidade da estratexia de procesamento dual desenvolta no marco desta Tese de Doutoramento demostrouse mediante a fabricación de aeroxeles impresos altamente estables e biocompatibles coa posibilidade de seren dopados con nanocomplexos, ampliando así as súas aplicacións potenciais.

A seguridade *in vivo* dos aeroxeles cargados con UCNPs foi avaliada mediante implantación subcutánea en ratos e ratas. Non se obtiveron diferenzas significativas entre o perfil de citocinas, a histoloxía dos órganos principais e o índice tisular dos animais controis e dos animais cunha implantación subcutánea de aeroxeles dopados con UCNPs. Cabe destacar que se detectou unha reacción de corpo estraño en tódolos animais que se podería vencellar co material de sutura. Realizáronse estudos *in vivo* de bioimaxe en ratos e foi posible a monitorización das andamiaxes marcadas con UCNPs ata 3 semanas trala implantación. Non se observou unha fluorescencia destacada nunha análise de bioimaxe *post-mortem* do órganos principais, suxerindo así que o metabolismo das UCNPs podería ter lugar mediante o sistema urinario. Tódolos resultados sinalan a seguridade do nanodispositivo deseñado así como as súas capacidades de monitorización e enxeñaría de tecidos a longo prazo.

No Capítulo 7 desta Tese de Doutoramento, incorporouse vancomicina (VAN) en formulacións de aeroxeles impresos a base de metilcelulosa mediante a estratexia de procesamento dual, demostrando así a súa versatilidade en canto a biopolímeros e a súa capacidade para carga de fármaco. A selección da metilcelulosa debeuse á súa ampla aplicación na enxeñaría de tecidos e na impresión 3D así como ás súas propiedades texturais e biolóxicas. Ademais, incorporouse a nanohidroxiapatita (nHA) ós aeroxeles para obter implantes bioactivos adecuados para aplicacións en enxeñaría de tecidos ósea. Analizouse o rendemento fisicoquímico dos aeroxeles

USC DE COMPOSTELA

de metilcelulosa-nHA cos mellores resultados en termos de fidelidade de impresión e encollemento volumétrico observados para as andamiaxes co maior contido en nHA. Obtivéronse valores elevados dos parámetros texturais para as diferentes formulacións cargadas con VAN, cunha porosidade elevada, dual e interconectada. Cabe destacar que o descenso nos parámetros texturais trala incorporación de nHA foi menos marcado nos aeroxeles impresos de metilcelulosa que nos de alxinato, representando así unha importante vantaxe das formulacións de metilcelulosa respecto ás de alxinato. O rendemento mecánico así como a elevada bioactividade observada para os aeroxeles de metilcelulosa cargados con nHA trala inmersión en SBF reforza a súa selección como mellores candidatos para rexeneración ósea a longo prazo.

A biocompatibilidade dos aeroxeles cargados con VAN confirmouse mediante varios ensaios. Avaliouse a compatibilidade celular tras 24 e 72 h en fibroblastos murinos e obtivéronse valores próximos ó 80 % para as diferentes formulacións. A seguridade preliminar analizouse medindo a mortalidade da *Artemia salina* tras 24 h en contacto cas formulacións. A viabilidade da *A. Salina* foi próxima ó 100 % para tódolos aeroxeles estudados. A hemocompatibilidade avaliouse en sangue humano e detectáronse valores desprezables de hemólise. O ensaio HET-CAM realizouse para os aeroxeles cargados con nHA e VAN sen observar coagulación ou sangrado dos vasos, confirmando así a bio- e hemocompatibilidade dos aeroxeles impresos de metilcelulosa. Os ensaios microbiolóxicos con *Staphylococcus aureus* revelaron unha zona de inhibición e foron coherentes co perfil de cesión da VAN observado *in vitro*.

A estabilidade dos aeroxeles cargados con VAN estudouse tras 7 meses de almacenamento. Non se observaron diferenzas na estrutura porosa e nos parámetros texturais dos aeroxeles antes e despois do almacenamento, suxerindo así a súa estabilidade fisicoquímica por este período de tempo. A esterilización post-procesado realizouse tamén para os aeroxeles de metilcelulosa sen observar ningún efecto prexudicial no seu rendemento textural cando se compara cas mesmas formulacións non esterilizadas. Este resultado reforza a idoneidade da esterilización mediante o

USC DE COMPOSTELA

$scCO_2$ en condicións suaves e o H_2O_2 como aditivo para a fabricación de aeroxeles listos para implantar.

No Capítulo 8 desta Tese de Doutoramento, cargáronse os aeroxeles impresos de metilcelulosa con nanofibras de celulosa bacteriana (BC-NF) para fabricar aeroxeles de celulosa-en-celulosa. A razón para a selección das BC-NF baseouse no estreito ordenamento da nanocelulosa, que pode mellorar o rendemento mecánico do nanomaterial resultante. As tintas de impresión 3D con diferentes concentracións das BC-NF mostraron un comportamento reolóxicode adelgazamento por cizalla, máis salientable coa concentración máis alta de BC-NF, suxerindo así un efecto de reforzo debido á incorporación de BC-NF. O rendemento textural dos aeroxeles de celulosa-en-celulosa mostrou melloras na fidelidade de impresión, no encollemento volumétrico e na integridade estrutural dos aeroxeles impresos cando se incorporaron as BC-NF. Tamén se observou un ordenamento da estrutura porosa dual cando a nanocelulosa se incluíu nos aeroxeles sen un efecto perxudicial nos parámetros texturais. As BC-NF dopáronse con nanopartículas superparamagnéticas de óxido de ferro (SPIONs) para permitir a detección das BC-NF cargadas nos aeroxeles e para fabricar aeroxeles de celulosa-en-celulosa con propiedades magnéticas. A magnetización dos aeroxeles confirmouse trala aplicación dun campo magnético externo, pero este comportamento debe ser potenciado para inducir unha resposta magnética biorelevante.

A esterilización dos aeroxeles de celulosa-en-celulosa levouse a cabo mediante o método de SCF previamente desenvolto nesta Tese de Doutoramento sen observar diferencias relevantes debido á etapa de post-procesado en termos de parámetros texturais, distribución de tamaños de poro e interconectividade entre poros. Confirmouse a estabilidade tras 4 meses xa que o rendemento fisicoquímico dos aeroxeles e a integridade e distribución das BC-NF mantívose tralo almacenamento por este período de tempo. Tódolos resultados suxiren a fabricación de aeroxeles impresos de celulosa-en-celulosa estables e listos para implantar.

USC DE COMPOSTELA

A biocompatibilidade dos aeroxeles de celulosa-en-celulosa foi estudada mediante ensaios de compatibilidade celular en fibroblastos murinos tras 24 e 48 h, con valores superiores ó 90 %. Confirmouse a seguridade preliminar *in vivo* cunha mortalidade da *A. salina* próxima ó 0 % para as diferentes formulacións estudadas, incluíndo as dopadas con SPIONs. A hemocompatibilidade tamén foi comprobada mediante medición da actividade hemolítica en sangue humano, con valores próximos ó 0 % que confirmaron a ausencia de hemólise debido ós aeroxeles de celulosa-en-celulosa. Tamén se levaron a cabo ensaios HET-CAM sen observar sangrado dos vasos ou coagulación polo contacto cos aeroxeles.

En xeral, a estratexia de procesamento dual para obter aeroxeles impresos cunha alta fidelidade de impresión desenvolveuse por vez primeira no marco desta Tese de Doutoramento. A impresión 3D de xeles de alxinato e metilcelulosa seguiuse do seu secado mediante SCF para fabricar aeroxeles personalizados. A versatilidade desta estratexia confirmouse mediante o uso de diferentes biopolímeros e mediante a incorporación de VAN, un fármaco empregado no manexo das infeccións óseas. Os aeroxeles impresos foron esterilizados tamén mediante SCF sen un efecto prexudicial no seu rendemento fisicoquímico. Tamén se estudou a monitorización dos aeroxeles e dos seus produtos de degradación *in vivo* mediante o desenvolvemento doutra estratexia consistente en dopar os aeroxeles con UCNPs para o seu seguimento trala implantación mediante bioimaxe.

USC
UNIVERSIDADE DE SANTIAGO DE COMPOSTELA

EXTENDED ABSTRACT

Biological and synthetic grafts are current common strategies employed in the clinical management of bone fractures. Autografts, allografts, and xenografts are the preferred options for the recovery of the damaged area but, due to their scarcity, the synthetic implants are also extensively employed. Nevertheless, these solutions lack certain properties essential for an advanced bone repair such as the long-term bioactivity, the controlled delivery of antibiotics that mitigates the bone infection after implantation, or a strategy for the real-time monitoring of the grafts and their degradation products. All these features are not present in commercial solutions for bone fractures and their incorporation could ameliorate their performances by enabling bone regeneration.

Bone tissue engineering is a discipline that seeks the anatomical and functional recovery of the damaged tissue surrounding bone defects. Different methodological approaches are being studied for the manufacturing of adapted-to-patient implants with long-term tissue regeneration capabilities. Among them, three-dimensional (3D) printing is a novel technique based on the minimal use of resources and usually employed to fabricate customized constructs in terms of inner composition and external morphology. Different materials have been used for the 3D-printing of scaffolds for bone tissue repair, but the natural polymers are especially able to resemble the native structure of the bone extracellular (ECM) matrix. Extrusion-based 3D-printing is the most employed method to obtain biopolymeric scaffolds aimed at bone tissue engineering through a layer-by-layer deposition of inks. It is also hypothesized that macropores would appear between subsequent layers of 3D-printed scaffolds, thus inducing a new pore size population.

Supercritical fluid (SCF) technology is another green alternative commonly employed to endow scaffolds with attractive properties for bone tissue repair, such as high porosity and low density. This technology is based on the use of supercritical carbon dioxide ($scCO_2$) under mild conditions

USC UNIVERSIDADE DE SANTIAGO DE COMPOSTELA

to maintain the porous architecture of the wet gel in the dry state, thereby manufacturing aerogels with an advanced porous structure. Specifically, macroporosity in the range of 100-300 μm is necessary for the new bone tissue formation, whereas the effective transport of the nutrients and waste elimination from implants are usually carried out through mesopores. Overall, pores of different sizes are required for the correct tissue regeneration and long-term bone repair.

The sterilization at a medical grade must be ensured before implantation for all biomedical devices. The common sterilization techniques achieve the required sterilization level but may cause a detrimental effect in the physicochemical performance of the biopolymeric materials. Sterilization procedures based on the use of $scCO_2$ are regarded as safe alternatives capable of effectively sterilizing polymeric biomaterials while maintaining their textural and biological properties. Additives like hydrogen peroxide (H_2O_2) need to be used to enhance the bactericidal effect of $scCO_2$ to thus achieve the sterilization level required before implantation. Long-term stability is other key parameter for biomaterials as their physicochemical and biological performances must be ensured from their fabrication until their implantation. The lack of stability studies of biopolymeric aerogels motivates the study of this parameter in terms of textural features after storage of different aerogel formulations for mid-to-long periods.

The 3D-printing of personalized gels and their subsequent drying and sterilization by using SCF could render sterile and dual porous aerogels with an advanced and stable physicochemical performance. The loading of drugs and fluorescent probes into the highly porous structures could lead to the fabrication of traceable implants with a controlled drug release. Under this context and in the frame of this PhD Thesis, stable, sterile, and adapted-to-patient bone scaffolds were manufactured by the novel technological combination of 3D-printing and SCF. These scaffolds are endowed with long-term bioactivity, with a sustained antibiotic release able to

USC UNIVERSIDADE DE SANTIAGO DE COMPOSTELA

prevent bacterial infections after implantation and also with *in vivo* traceability properties by a bioimaging technique, thus addressing important disadvantages in commercial bone implants.

In Chapter 3 of this PhD Thesis, dual porous and 3D-printed aerogels aimed at bone tissue engineering were manufactured by a novel technological combination. A dual processing strategy with two steps consisting on the 3D-printing of gels and their drying by using $scCO_2$ was developed to manufacture highly porous 3D-printed aerogels. The parameters of the 3D-printing process were adjusted to obtain alginate-hydroxyapatite (HA) gels with a high printing fidelity with respect to the original printing file. Alginate was selected due to their beneficial properties for bone tissue engineering, such as biocompatibility, non-toxicity, and porous structure close to the one observed in the bone ECM. HA was chosen due to their similarity with the native human bone as well as its bioactive properties required for scaffolds aimed at long-term bone regeneration. Different alginate, calcium chloride ($CaCl_2$) and HA concentrations were screened to select the ones that yield structures with the best physicochemical performance. The drying of the 3D-printed alginate gels was performed by using SCF technology to ensure the maintenance of the advanced porous structure in the aerogels. The alginate concentration was set at 6 wt.% to enable the incorporation of HA concentrations as high as 24 wt.% while the $CaCl_2$ concentration was fixed at 1 M to provide a higher chemical crosslinking and structural integrity to aerogel scaffolds. Mesopores and macropores with a high interconnectivity were observed in the 3D-printed aerogels thereby confirming their advanced textural properties. A lower volume shrinkage and a higher printing fidelity appeared when higher HA contents were incorporated into the aerogels. Nevertheless, it was also noted a marked decrease in the textural parameters, namely, surface area, volume of pores and overall porosity with the highest HA content. The biological properties of the 3D-printed aerogels were studied with cytocompatibility values always higher than 80 % after 24 and 48 h in contact with murine fibroblasts. Furthermore, migration tests were performed with similar results of wound closure for the different 3D-printed formulations, but with higher values for alginate aerogels with respect to the natural migration

USC UNIVERSIDADE DE SANTIAGO DE COMPOSTELA

capability of the fibroblasts. Adhesion assays were carried out on human bone marrow mesenchymal stem cells (MSCs), with a proliferation tendency observed after 13 days for the different aerogel formulations. All these results endorse the suitability of the 3D-printed alginate-HA aerogels as platforms for bone tissue regeneration.

In Chapter 4, processing strategies for the production of 3D-printed scaffolds with an improved structural integrity and sterilized at a medical grade, thereby manufacturing ready-to-implant aerogels, were evaluated. The dual processing strategy was upgraded with two different post-processing steps: the glutaraldehyde (GA) crosslinking and the sterilization of the 3D-printed aerogels. A $CaCl_2$ bath was used in the hydrogels and was followed by a contact with GA atmosphere in the aerogels thus performing a dual crosslinking (ionic and covalent) to increase the integrity of the aerogel scaffolds. The effect of this treatment on the physicochemical performance of aerogels was studied without observing relevant differences after different ageing periods in $CaCl_2$, but with a slight decrease in the textural parameters when the dual crosslinking was applied. It should be noted that the dual porosity and the volume shrinkage of structures did not exhibit relevant differences with the dual crosslinking or without it. A higher structural integrity was visually observed for all formulations studied when the post-processing treatment was applied, with the 3D-printed layers bonded in one compact structure almost without exfoliation. Furthermore, the biological performance of aerogels was not affected by the GA crosslinking, with a cytocompatibility higher than 80 % in murine fibroblasts, after 24 and 48 h. Hemolysis was also neglectable after contact of the aerogels with human blood, thus suggesting the non-toxicity of the GA atmosphere as crosslinking method. Bioactivity of alginate-HA aerogels was studied by immersion in simulated body fluid (SBF) for different time periods (3, 7, 15 and 28 days). A high bioactivity was observed for the formulations containing HA, with a higher number of apatite depositions as well as an increase in their size detected for aerogels with the highest HA content. This result suggests that the long-term bioactivity of the scaffolds depends on their composition, specifically, on their HA content. Rheological properties of the

USC UNIVERSIDADE DE SANTIAGO DE COMPOSTELA

inks displayed a shear thinning behavior that was even more remarkable when the HA concentration increased.

Another post-processing step was explored in this PhD Thesis, in this case, for the sterilization of the polymeric 3D-printed aerogels. Sterilization was performed by using $scCO_2$ and H_2O_2 as additive at mild conditions (100 bar, 40 °C, 30 min, 1200 ppm H_2O_2). Microbiological tests and textural performance evaluation was performed after the sterilization treatment of different aerogel formulations to demonstrate the efficacy of the procedure and the maintenance of the physicochemical properties, respectively. Sterile scaffolds were incubated for 24 h in tryptic soy agar (TSA) plates and in trypto-casein soy broth (TSB) vials without detecting any colony forming unit (CFU) or turbidity in the medium, thus ensuring the achievement of the sterile conditions. Moreover, the structural stability of 3D-printed aerogels was evaluated in terms of textural properties without observing relevant differences with respect to the same formulations analyzed before the sterilization. These results endorse the use of SCF at mild conditions as sterilization method for biopolymeric scaffolds.

In Chapter 5, upconversion nanoparticles (UCNPs) were synthesized as part of a strategy to enable the traceability of implants and their degradation products *in vitro* and *in vivo*. A novel synthetic approach combining the co-precipitation of a lanthanide core with the formation of a silica coating by a sol-gel method was developed. Different UCNPs formulations were obtained by combining different lanthanide precursors (oxides and nitrates) and drying methods (SCF and oven drying). The upconversion spectra and the stability were chosen as the main criteria to select the formulation of UCNPs to be incorporated into the previously developed 3D-printed aerogels to manufacture a theranostic nanodevice. The upconversion spectra clearly pointed the nitrates of the lanthanides and the oven drying as the more suitable conditions to synthesize highly fluorescent UCNPs. Consistently, a stability study was performed by storing for 2 years the selected formulation of the UCNPs and evaluating after that their physicochemical properties.

USC DE COMPOSTELA

The high fluorescence of the UCNPs as well as their morphological characteristics were preserved, thereby suggesting their stability after long-term storage. Cytocompatibility of the selected nanocomplexes was evaluated by measuring the viability of murine fibroblasts after 24 and 48 h of culture with UCNPs and by determining the hemolysis after contact with human blood. Cell viability was always higher than 90 % and no remarkable hemolysis was detected thus indicating that UCNPs were non-toxic even at the very high concentrations studied (5 and 10 mg/ mL). This is an important milestone to be loaded into scaffolds and thereby turn them into *in vivo* monitorable devices.

In Chapter 6, UCNPs-labeled aerogels were manufactured for the first time by incorporation of the previously synthesized UCNPs at low concentrations (0.4 and 0.8 wt.%) into 3D-printing inks. The rheological properties of the inks were almost unaltered after the incorporation of the UCNPs, with a clear shear thinning behavior exhibited in all cases. The fluorescence performance of the UCNPs-loaded aerogels was studied by confocal microscopy and the manufacturing of highly fluorescent aerogels was thus confirmed. The physicochemical properties of UCNPs-doped aerogels were similar to the same formulations without the fluorescent probes. The interconnected pore structure, textural parameters, volume shrinkage and printing fidelity of aerogels were preserved after UCNPs incorporation. The biological performance was *in vitro* studied by evaluation of the cell viability and migration on murine fibroblasts and by adhesion tests on human bone marrow MSCs. No relevant differences appeared after comparing the biological properties of the aerogel scaffolds doped or not with UCNPs, thereby suggesting the absence of a negative impact of the nanocomplexes incorporated into aerogels at low contents. Hemocompatibility of UCNPs-loaded aerogels was also studied by hemolytic activity measurements and Hen's egg test on the chorioallantoic membrane (HET-CAM). No hemolysis, clotting, or vessel bleeding was detected after contact with the CAM, so a potential good interaction between the blood and the scaffold once implanted was stablished.

USC UNIVERSIDADE DE SANTIAGO DE COMPOSTELA

Stability of the 3D-printed aerogels was first-time studied after 3 years of storage. Fluorescence properties, textural parameters and an interconnected and highly porous structure were maintained without observing relevant differences with respect to the same formulations analyzed just after being manufactured. These results highlight the physicochemical and fluorescence stability of the 3D-printed UCNPs-doped aerogels and endorse their suitability as theranostic nanodevices. The versatility of the dual processing strategy developed in the frame of this PhD Thesis was demonstrated by the manufacturing of highly stable and biocompatible 3D-printed aerogels with the possibility of being doped with nanocomplexes thereby broadening their potential applications.

In vivo safety was assessed by 1-week subcutaneous implantation of UCNPs-loaded aerogels in mice and rats. No statistically significant differences were obtained between the cytokines profile, the histology of the main organs and the tissue index of control animals (without scaffold implantation) and the animals with a subcutaneous implantation of UCNPs-doped aerogels. It should be noted that a foreign body reaction was detected in all animals of the *in vivo* study that could be linked with the suture material. *In vivo* bioimaging studies were performed in mice and the monitoring of the UCNP-labeled scaffolds was possible until 3 weeks post-implantation. No remarkable fluorescence was observed in a *post-mortem* bioimaging analysis of the main organs, thus suggesting that the metabolism of the UCNPs could take place through the urinary system. All results pointed out the safety of the designed nanodevice as well as its long-term monitoring and tissue engineering capabilities.

In Chapter 7, vancomycin (VAN) was incorporated into 3D-printed methylcellulose aerogels through the dual processing strategy, thus demonstrating its biopolymer versatility and drug loading capability. The choice of the methylcellulose was due to its broad application in the tissue engineering and 3D-printing fields as well as its beneficial textural and biological properties. Also, nanohydroxyapatite (nHA) was incorporated into aerogels to render bioactive implants adequate

USC DE COMPOSTELA

for bone tissue engineering applications. The physicochemical performance of 3D-printed methylcellulose-nHA aerogels was analyzed with the best results in terms of printing fidelity and volume shrinkage observed for scaffolds with the highest nHA content. High values of textural parameters were obtained for the different VAN-loaded aerogel formulations with a high, dual, and interconnected porosity. It should be noted that the decrease in textural parameters after nHA incorporation was less noticeable in methylcellulose 3D-printed aerogels than in their alginate counterparts, thereby representing an important advantage of the methylcellulose formulations with respect to the alginate ones. The mechanical performance as well as the high bioactivity observed for the nHA-loaded methylcellulose aerogels after immersion in SBF medium for 13 and 26 days further endorses their selection as the best candidates for long-term bone regeneration.

The biocompatibility of VAN-loaded aerogels was confirmed throughout several tests. Cell compatibility after 24 and 72 h was evaluated on murine fibroblasts and values close to 80 % were obtained for the different formulations tested. Preliminary safety was analyzed by measuring the mortality of *Artemia salina* after contact with the formulations for 24 h. Viability of *A. salina* was close to 100 % for the aerogels studied. Hemocompatibility was evaluated on human blood and neglectable values of hemolysis were detected. HET-CAM test was performed for aerogels loaded with nHA and VAN without observing coagulation or vessel bleeding thus confirming the bio- and hemocompatibility of the 3D-printed methylcellulose aerogels. Microbiological tests with *Staphylococcus aureus* unveiled an inhibition zone and were coherent with the sustained VAN release profile observed *in vitro*.

The stability of VAN-loaded aerogels was studied after 7 months of storage. No relevant differences were observed in the porous structure and textural parameters of 3D-printed aerogels before and after the storage, thus suggesting the physicochemical stability of the scaffolds for this time period. The post-processing sterilization step was also performed for the

USC DE COMPOSTELA

methylcellulose aerogels without observing any detrimental effect on their textural performance when compared with the same formulations non-sterilized. This result endorses the suitability of the sterilization by using $scCO_2$ at mild conditions and H_2O_2 as additive for the manufacturing of stable and ready-to-implant 3D-printed aerogels.

In Chapter 8, 3D-printed methylcellulose aerogels were loaded with bacterial cellulose nanofibers (BC-NF) to manufacture cellulose-in-cellulose aerogels. The rationale for the selection of BC-NF was based on the described tight arrangement of the nanocellulose that can improve the mechanical performance of the resulting nanomaterial. The 3D-printing inks with different concentrations of BC-NF exhibited rheological properties characterized by a clear shear thinning behavior, being even more remarkable with the highest concentration of BC-NF, thus suggesting a reinforcement effect due to the BC-NF incorporation. Textural performance of the cellulose-in-cellulose aerogels showed an improved printing fidelity, volume shrinkage and structural integrity of the 3D-printed aerogels when BC-NF were incorporated. A tighter arrangement of the dual porous structure was also observed when the nanocellulose was included into the aerogels without a detrimental effect on the studied textural parameters. BC-NF were doped with superparamagnetic iron oxide nanoparticles (SPIONs) to enable the detection of the BC-NF loaded into aerogels by confocal microscopy and to manufacture cellulose-in-cellulose aerogels with magnetic properties. The magnetization of the aerogels was confirmed after the application of an external magnetic field, but this behavior should be enhanced to induce a biorelevant magnetic response.

Sterilization of cellulose-in-cellulose aerogels was carried out by the SCF method previously developed in this PhD Thesis without observing relevant differences due to the post-processing step in terms of textural parameters, pore size distribution and interconnectivity between pores. Stability after 4 months was confirmed as the physicochemical performance of aerogels and the integrity and distribution of BC-NF was maintained after the storage for this period. All results

USC DE COMPOSTELA

suggested the manufacture of stable and ready-to-implant 3D-printed cellulose-in-cellulose aerogels.

The biocompatibility of cellulose-in-cellulose aerogels was studied by cell compatibility tests on murine fibroblasts after 24 and 48 h, with values higher than 90 % for all the formulations. *In vivo* preliminary safety was confirmed by *A. salina* mortality close to 0 % for the different formulations studied, including the ones doped with SPIONs. The hemocompatibility was also checked by measuring the hemolytic activity on human blood, with values close to 0 % that confirmed the absence of hemolysis due to the cellulose-in-cellulose aerogels. HET-CAM tests were also carried out without observing vessel bleeding or coagulation due to the contact of the aerogels.

Overall, a dual processing strategy to obtain 3D-printed aerogels with high printing fidelity was developed for the first time in the frame of this PhD Thesis. The 3D-printing of alginate and methylcellulose gels was followed by their drying by using SCF to thus manufacture customized aerogels. Also, the versatility of this strategy was confirmed by the use of different biopolymers and by the incorporation of VAN, a drug employed in the management of bone infections. 3D-printed aerogels were sterilized also by SCF to achieve the sterilization level required for implantable medical devices without a detrimental effect on their physicochemical performance. The monitoring of aerogels and their degradation products *in vivo* was also studied by developing other strategy consisting on the doping of 3D-printed aerogels with UCNPs for their follow-up after implantation by bioimaging.

USC
UNIVERSIDADE DE SANTIAGO DE COMPOSTELA

ABBREVIATION LIST

Apparent density (ρ_{app})

Attenuated Total Reflectance/Fourier-Transform Infrared Spectroscopy (ATR/FT-IR)

Bacterial cellulose (BC)

Bacterial cellulose nanofibers (BC-NF)

Barrett–Joyner–Halenda (BJH)

BJH-mean pore diameter (d_p)

BJH-specific pore volume (V_p)

Brunauer–Emmett–Teller (BET)

BET-specific surface area (A_{BET})

Calcium chloride ($CaCl_2$)

Colony forming unit (CFU)

Computer-aided design (CAD)

Computer tomography (CT)

4',6-diamidino-2-phenylindole (DAPI)

Deoxyribonucleic acid (DNA)

Doxorubicin (DOX)

Dulbecco's Modified Eagle's Medium (DMEM)

Dynamic mechanical analysis (DMA)

Energy-dispersive X-ray spectroscopy (EDX)

Envelope density (ρ_{env})

Erbium (III) (Er^{3+})

Ethanol (EtOH)

Ethylenediaminetetraacetic acid (EDTA)

Extracellular matrix (ECM)

Glutaraldehyde (GA)

Green fluorescent protein (GFP)

Hen's egg test on the chorioallantoic membrane (HET-CAM)

Hydrogen peroxide (H_2O_2)

Hydroxyapatite (HA)

Interagency Coordinating Committee on the Validation of Alternative Methods (ICCVAM)

Interleukin 6 (IL-6)

Interleukin 10 (IL-10)

Magnetic resonance imaging (MRI)

Mean pore diameter (d_p)

Methicillin-resistant *Staphylococcus aureus* (MRSA)

Nanofibers (NF)

Nanohydroxyapatite (nHA)

Nanoparticles (NPs)

Near infrared radiation (NIR)

Phosphate buffered saline (PBS)

Porosity (ε)

Printing accuracy (PA)

Room temperature (RT)

Scanning electron microscopy (SEM)

Shape fidelity factor (SFF)

Simulated body fluid (SBF)

Skeletal density (ρ_{skel})

Supercritical carbon dioxide ($scCO_2$)

Supercritical drying (SCD)

Supercritical fluids (SCF)

Superparamagnetic iron oxide nanoparticles (SPIONs)

Tetraethyl orthosilicate (TEOS)

Three-dimensional (3D)

Transmission electron microscopy (TEM)

Tumor necrosis alpha factor (TNF-α)

Tryptic soy agar (TSA)

Trypto-casein soy broth (TSB)

Upconversion (UC)

Upconversion nanoparticles (UCNPs)

Ultraviolet (UV)

Vancomycin (VAN)

Water-soluble tetrazolium salt (WST-1)

X-ray diffraction (XRD)

Ytterbium (III) (Yb^{3+})

CHAPTER 1. INTRODUCTION

The content in this chapter was published in part in C.A. García-González, **A. Iglesias-Mejuto**, C. López-Iglesias, V. Santos-Rosales, I. Ardao, C. Alvarez-Lorenzo; Chapter 6. Natural polymer hydrogels and aerogels for biomedical applications, in: Engineering of Natural Polymeric Gels and Aerogels for Multifunctional Applications (Editors: Sabu Thomas, Bastien Seantier, Blessy Joseph) Elsevier, 2024: pp. 125–157. https://doi.org/10.1016/B978-0-12-823135-7.00001-2.

USC
UNIVERSIDADE DE SANTIAGO DE COMPOSTELA

1.1. Background

Hydrogels and aerogels are nanostructured materials that share some common useful properties for biomedical applications and several specific ones of interest for selected biomedical uses [1,2]. Hydrogels are already present in several medical devices and drug products, whereas aerogel applications are still exclusively falling in the research and development stage. In this Chapter, relevant properties of natural polymer hydrogels and aerogels are identified and the exploitation of these gels for biomedical applications is discussed. Finally, future trends in biomedicine linked to the use of gels are presented.

Natural polymer hydrogels usually have high capacity for the absorption of water and high biocompatibility, thus resulting an attractive solution to mimic soft biological tissues and the ECM [2]. Hydrogels can be processed in the form of particles through different techniques resulting in formats of different sizes classified as macrogels (larger than 100 μm), microgels (0.1-1 μm) and nanogels (below 100 nm) [3]. The mechanical properties of the hydrogels are modulated through the crosslinking mechanism (physical or chemical) and its extent. The 3D-polymeric network of hydrogels has a high content of wet pores susceptible of being loaded with bioactive compounds such as drugs or deoxyribonucleic acid (DNA). Specific interactions with the polymer chains may be exploited to tune the loading yield and the release pattern. Moreover, the capacity of certain gels to reversibly change their volume triggered by external stimuli (e.g., temperature, pH, solute concentration, light and ultraviolet -UV- radiations) and with a response proportional to the intensity of the stimuli render the so-called intelligent gels with a myriad of biomedical uses [4,5].

Aerogels are highly porous materials obtained from the removal of the liquid phase of a gel without significant damage to the 3D-structure [6,7]. Natural polymer aerogels have a nanostructure in the dry form with a large surface area, open porosity in the mesoporous range and biocompatibility [6]. Moreover, they can be endowed with a high water absorption capacity and a shape adapted to the application site, which is very interesting for regenerative medicine

USC UNIVERSIDADE DE SANTIAGO

[8]. The lightweight character of aerogels coupled to the free-flowing and excellent aerodynamic properties are very promising for pulmonary and nasal delivery of drugs [6]. Finally, the amorphization of low water-soluble drugs has been reported when loaded in aerogels resulting in enhanced drug bioavailability [9].

Regarding natural polymers, collagen, silk fibroin and keratins are among the most common protein-based gel sources for biomedical applications, whereas cellulose, chitosan, alginate, and hyaluronic acid are the most common polysaccharides. Collagen is the most abundant animal protein on earth and particularly interesting from a biomimetic perspective since it is the main component of the ECM and responsible for maintaining connective tissue structural integrity. There are 29 types of collagen with similar triple-helical tertiary structure and different quaternary structures [10], being type I collagen the most abundant and frequently used as biomaterial. Silk fibroin is the structural protein of silk fibers obtained from silkworms (*Bombyx mori*). It is mainly composed by glycine, alanine and serine residues and presents two main conformational states (random coils/α-helix and β-sheets). Silk fibroin chains can be physically crosslinked into hydrogels with crystalline β-sheet structure in aqueous solution, forming intra- and intermolecular hydrophobic interactions and hydrogen bonds. Silk fibroin presents excellent mechanical properties, such as tensile strength, breaking elongation and elasticity [11,12]. Keratins are structural components of important skin structures, such as nails, hair wool and feathers in different animals. Particularly, keratin extracted from human hair has received attention as biomaterial due to its capability for autologous transplantation and abundant availability [13]. Keratin is composed of alpha keratins types I and II that interact with each other forming a left-handed heterodimer helix.

Regarding the polysaccharide sources, cellulose is a polysaccharide obtained from a variety of sources (plants, seaweed, bacteria) and made of repeating units of β-D-glucopyranose rings connected through β-1-4 glycosidic bonds [14]. Namely, bacterial cellulose presents a higher

USC DE COMPOSTELA

degree of crystallinity and is obtained without impurities. Nanocellulose refers to cellulose materials in the nanoscale (1–100 nm), including nanocrystals and nanofibers, and endowed with high mechanical strength, degree of polymerization, purity, and crystallinity. Cellulose ethers, a kind of water-dispersable derivatives, are widely used in the preparation of pharmaceutical gels [15]. Chitosan is the deacetylated derivative of chitin, a natural linear aminopolysaccharide from the exoskeletons of crustaceans, the cell wall of some fungi and yeast, and the endoskeleton of some cephalopods [16]. Chitosan has enhanced hydrosolubility in acidic medium due to protonation of the free amino groups and has good cytocompatibility and biodegradability. Alginate is a linear copolymer formed by units of β-D-mannuronic acid and α-L-guluronic acid and obtained from brown algae and some bacteria. The anionic nature of alginate allows for its ionic crosslinking with divalent cations (typically calcium) [17]. It is also highly hydrophilic, which provides it with high fluid sorption capacity. Finally, hyaluronic acid is a glycosaminoglycan consisting of glucuronic acid and N-acetyl-D-glucosamine units and with high presence in the connective tissue of mammals [18].

Finally, the abovementioned natural polymers can be combined between them in or with other components of organic and inorganic origin to obtain hybrid or composite hydrogel and aerogel designs with specific physicochemical and/or biological properties. In other approach, gels can be surface modified with functional chemical groups to promote the bioconjugation of the natural polymer-based structure with target cells, and to generate different gel morphologies (core-shell, hollow, multi-membrane onion-like) for target therapies or enhanced stability [5,19].

1.2. Natural polymer gels for drug delivery applications

Hydrogel performance is strongly influenced by the mechanical (deformation capacity and flexibility) and physicochemical (permeability, chemical functionalities) properties of its 3D-structure, but also to the gel size (macro-, micro- or nanogels). Macrogels are mainly used for

USC UNIVERSIDADE DE SANTIAGO DE COMPOSTELA

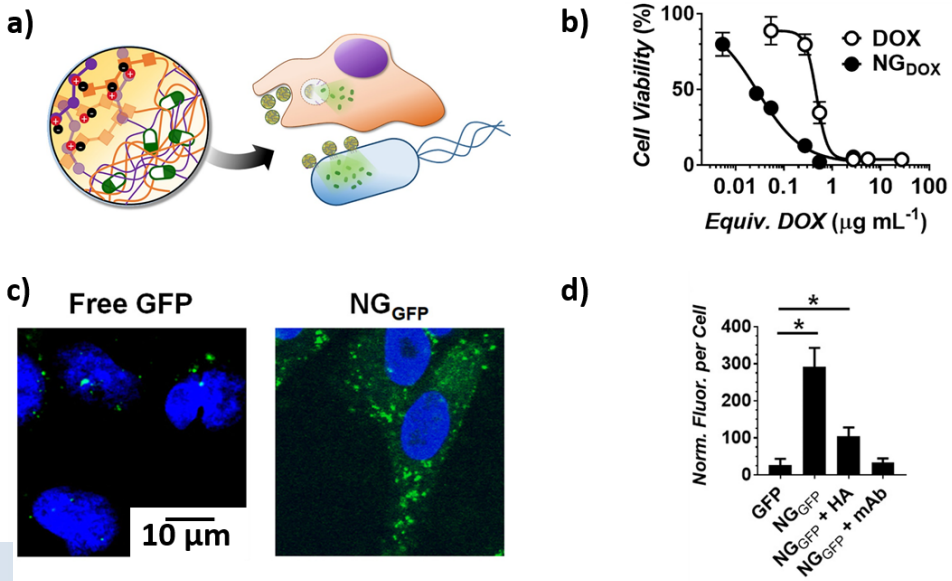
the intelligent delivery of drugs (e.g., proteins), local drug delivery (e.g., injectable gels in chemotherapy or in hyperthermia treatment) as well as protection (longer half-lives of drugs) and enhancement of the bioavailability of drugs (e.g., hydrophobic drugs) [20]. As an example, a hyaluronic acid-alginate composite macrogel was prepared for the local sustained delivery of cyclosporine A for 14 days, a hydrophobic immunosuppressive drug [21]. The hydrogel system can be injected *in vivo* and drug release was confirmed by murine T cells activity tests during the release time period. In other example, injectable alginate hydrogels containing AG/MoS_2/Bi_2S_3-poly(ethylene glycol) and doxorubicin (DOX) were processed where AG/MoS_2/Bi_2S_3-poly(ethylene glycol) had excellent photothermal conversion efficiency that favored the on-demand local release of DOX [22].

Microgels are soft and deformable matter that can interact with the cells environment by exchanging solvent and bioactive molecules [2]. Microgels can be also endowed with functional chemical groups that favors their bioconjugation with the target cells. The volume change of the microgel due to the microgel-cell interaction as well as the drug release pattern can be responsive and reversible in function of an external stimuli. Microgels can act not only as drug transporters to target cells but also protect and stabilize the conformation and prevent the agglomeration of bioactive compounds like enzymes, growth factors and cytokines [23,24]. Microgels of a carboxymethyl starch derivative and 2-isobutyl-acrylic acid were successful enteric carriers for the oral delivery of insulin [25]. Cell studies confirmed the intestinal absorption capacity of the microgels, and *in vitro* tests showed that the insulin release was triggered by a change of the pH of the medium coupled to the addition of amylase. Finally, *in vivo* tests in diabetic rats confirmed the reduction in the blood glucose levels upon oral administration of the insulin-loaded microgels.

The size of nanogels allows their administration by injection and can transport and deliver the bioactive compound inside the cells by active or passive transport [26]. The nanometric size of

USC DE COMPOSTELA

nanogels also results in longer residence times in the blood circulation that favors the intracellular accumulation of the drugs for chemotherapy and reduces the size effects by stabilization of the drug against degradation (e.g., with enzymes). Polysaccharides are commonly used as nanogel source alone or in hybrid gels [27]. As an example, an anti-biofilm peptide (DJK-5) was incorporated in hyaluronic acid nanogels [28]. The nanogel was administered subcutaneously to an *in vivo* murine model showing that the DJK-5 dose that induced toxicity was more than four times higher after encapsulation in the gels with respect to the non-encapsulated peptide and that maintained the antimicrobial activity. In other study, hybrid nanogels composed of hyaluronic acid and a cationic peptide (poly-L-lysine) and obtained by electrospray ionization resulted in a polyvalent carrier able to deliver drugs in mammalian cells as well as in bacterial cells [29]. This nanogel combination of an anionic polysaccharide and a cationic peptide had a biorresponsive behavior that resulted successful for the delivery of chemotherapeutic drugs (DOX) and membrane-impermeable proteins (green fluorescent protein, GFP) in the cytoplasm of carcinoma cells as well as for the permeabilization of microbial membranes (Gram-positive and Gram-negative) to deliver an antibiotic (VAN), with enhanced drug potency in both cases (Fig. 1.1).



USC UNIVERSIDADE DE SANTIAGO DE COMPOSTELA

Figure 1.1. Hybrid hyaluronic acid-poly-L-lysine nanogels endowed with bioresponsive behavior to enhance the potency of drugs in mammalian and bacterial cells. **a)** Sketch of the nanogel 3D-network

leading to complementary drug delivery mechanisms compatible with the intracellular delivery of drugs in eukaryotic and prokaryotic cells. **b)** Toxicity of free DOX and DOX incorporated in nanogels (NG_{DOX}) against A549 lung carcinoma cells. **c)** Merged confocal images of 4',6-diamidino-2-phenylindole (DAPI) (bluish cell nuclei staining) and GFP (green) after 72 h incubation of A549 cells with free GFP and GFP-loaded nanogels (NG_{GFP}) showing the enhanced cell internalization of GFP in the case of NG_{GFP} formulation as confirmed **d)** by the average GFP fluorescence per cell quantification. Fluorescence values were compared with those of NG_{GFP} in the presence of an excess of free hyaluronic acid (NG_{GFP}+HA) and in the presence of monoclonal anti-CD44 blocking antibody (NG_{GFP}+mAb) to elucidate the nanogel internalization mechanism. Reprinted from reference [29] with permission from Elsevier.

On the other hand, the aerogel structure with high surface area and interconnected pores allows for a fast and high drug loading if the drug has a high affinity for the aerogel matrix. This affinity is mainly dependent on the aerogel source [9,30]. The incorporation of drugs in the aerogels is carried out either during the aerogel processing (i.e. during gelation or during the solvent exchange) or once aerogels are produced (i.e. post-processing) [31]. In the latter case, the $scCO_2$ drug impregnation of aerogels is the most common strategy as it is endowed of attractive advantages for drug products manufacturing, such as the easy scalability or the oxygen-free environment [30,32]. Drugs loaded in aerogels by $scCO_2$ impregnation are usually in the amorphous form, which is of special interest to aid the solubilization of Class II or Class IV drugs according to the Biopharmaceutics Classification System [33,34] and that can also lead to increased bioavailability [35]. The release in the aqueous media of the drug contained in the aerogel matrix can be either uncontrolled or sustained depending on different parameters (crosslinking extent, drug partition coefficient, crystalline or amorphous form of the drug, and presence of coatings), being both options attractive depending on the intended drug administration route. The high water sorption capacity of aerogel carriers and the noticeable adaptability to the defect shape are of special interest for local treatments in exudative wounds. Finally, the light weight of aerogel powder also results in outstanding aerodynamic properties as carriers for pulmonary administration of drugs.

Natural polymer aerogels have different behavior when put in contact in water (swelling or without significant volume changes) depending on the source and the gelation conditions [9]. This feature has a direct impact on the drug release mechanism and on the drug release rate.

USC DE COMPOSTELA

Accordingly, drug release governed by Fickian diffusion was obtained for aerogels remaining almost intact when immersed in water, as observed with starch, cellulose and silk fibroin aerogels loaded with ketoprofen, dexpanthenol and ibuprofen, respectively [9,36,37]. On the other hand, natural polymer aerogels that may swell in the presence of water (e.g., alginate and whey protein aerogels) resulted in drug release patterns fitting to Korsmeyer-Peppas model, which is governed by diffusion assisted by swelling coupled to degradation [9,38,39]. In general, protein aerogels obtained by thermal gelation usually have an enhanced stability against erosion in the gastroinstestinal medium with respect to polysaccharide aerogels [40]. Finally, the structure collapse of aerogels with a sudden release of the drug payload typical for silica aerogels is not observed for natural polymers aerogels [41,42]. The rigidity of the biopolymer chains may prevent the collapse of the structure and this is exploited in drug-loaded natural polymer-silica hybrid aerogels to retard the drug release pattern [43,44].

Aerogels may also have a pH-sensitive behavior that can be used to target the drug release to a specific body region, typically a certain organ in the gastrointestinal tract in the case of oral administration. Alginate and pectin aerogels showed a reverse pH-response towards pH 1.2 and 6.8, showing favorable drug release patterns for stomach and intestine deliveries, respectively [9,45,46]. The divalent cation used as crosslinker for the ionic gelation of alginate had a noticeable effect on the drug release pattern and more prolonged release of diclofenac are reported for $Ca^{2+}<Sr^{2+}<Zn^{2+}$ in this order [46].

Technologies for the coating of aerogels and for the production of core-shell aerogel particles have been developed in an attempt to regulate drug release patterns (Fig. 1.2). Dipping, emulsion-based and spouted bed methods are reported as facilitating technologies for the coating of natural polymer aerogel particles or cylinders [47–49]. The choice of the coating materials had a clear effect on the obtained drug release profile for the case of ketoprofen loaded in emulsion-based coated silica-alginate aerogel beads [48]. The coating thickness had a

USC UNIVERSIDADE DE SANTIAGO DE COMPOSTELA

significant influence on the nicotinic acid release profile from multi-membrane alginate and pectin aerogels [49–51].

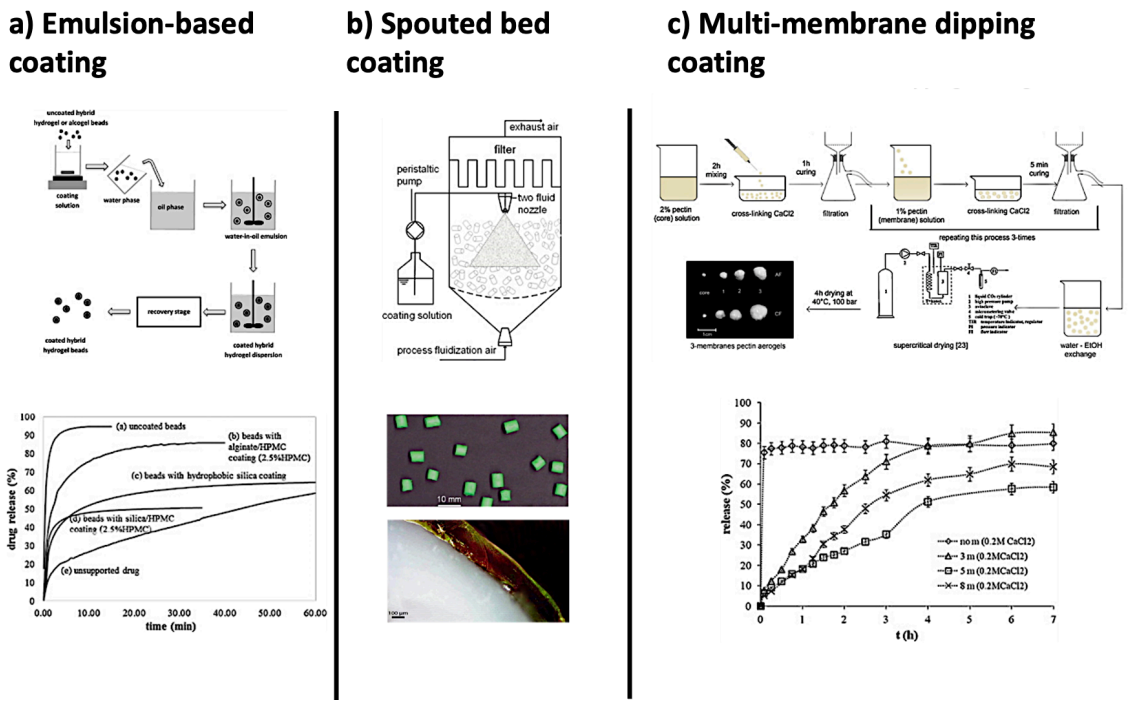


Figure 1.2. Aerogel coating technologies. **a)** Emulsion-based coating of silica-alginate aerogel beads with different coatings (alginate- hydroxypropylmethylcellulose (HPMC), silica-HPMC and silica) displaying a different ketoprofen *in vitro* release profile (pH 1.2, 37ºC, 50 rpm). **b)** Spouted bed coating of starch-alginate aerogel cylinders with Eudragit® L 30 D-55 showing an homogeneous coating layer. **c)** Multi-membrane polysaccharide aerogels with several (up to 8) membranes around the core showing a more retarded nicotinic acid release (pH 6.5, 37ºC, 50 rpm) with an increasing number of membranes (0, 3, 5 and 8). Reprinted from references [47], [48], [49] and [51] with permission from Elsevier.

1.3. Natural polymer gels for tissue engineering

Tissue engineering is a multidisciplinary field with the main goal of restoring or replacing damaged biological tissues or entire organs. Implants are designed by a synergistic combination of biocompatible matrices (scaffolds), living cells and bioactive agents that ultimately stimulate the self-regenerative capacity of the human body. Scaffolds should mimic the native ECM and its physiological functions to provide integrity and mechanical support to the tissue , to modulate the cell differentiation and to preserve the cellular communication [52]. These 3D-constructs are produced from biocompatible materials with biodegradation rates matching the growth rate of the target tissue. In this context, the use of gels from different natural sources is exploited for

tissue regeneration as well as to simulate the 3D-environment for cell culture and for *in vitro* evaluation.

1.3.1. Cell culture

The monolayer culture has been by far the most common method used in the 20th century to analyze adherent cell lines. Its simplicity, low cost of maintenance and long-standing use are the main advantages that led to universal and straightforward protocols to reduce contamination and to facilitate the *in vitro* testing. 2D-culture is useful to directly check the cell viability and morphology, but it does not simulate the *in vivo* 3D-environment [53] (Fig. 1.3).

Hydrogels mimic the ECM with high water contents and facile transport of nutrients, oxygen and wastes. The physical properties of the matrix material (porosity, stiffness) strongly influences the cell behavior [54]. Collagen, fibrin and hyaluronic acid are natural constituents of ECM intensively used for the development of hydrogels for cell culture.

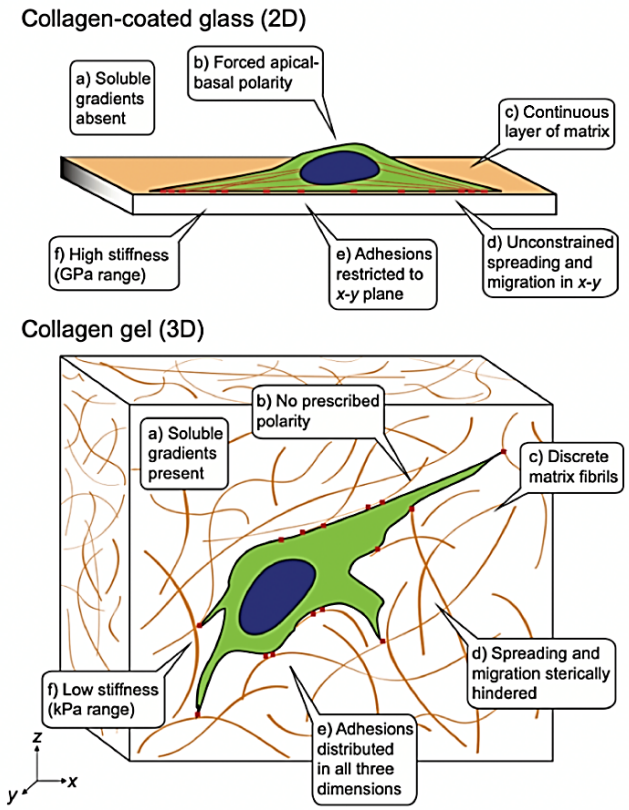


Figure 1.3. Different cues (topographical, mechanical, soluble) encountered by cells in 2D- (glass surface) and 3D-culture (collagen gel mimicking ECM). Adapted with permission from reference [53].

A wide variety of cell lines has been cultured in 3D-collagen hydrogels due to its ECM-biomimetic properties [55–60]. Matrigel is a commercial cell culture matrix composed of ECM proteins, mainly laminin, collagen IV and enactin extracted from Engelbreth-Holm-Swarm tumors in mice. This environment was shown to be optimal for culture stem cells and mimic the ECM in cancer. Matrigel stands out as the most common collagen-containing hydrogels for cell culture studies. Nevertheless, Matrigel is not a well-defined matrix, leading to inter-batch variability in mechanical and biochemical terms, directly inducing a source of variability in experimental results [61,62]. Other hydrogels for cell culture purposes, with more reproducible, well defined and tunable properties are herein presented.

The natural fiber alignment of collagen prompted the use of hydrogels in nerve tissue regeneration, where the relevance of the biochemical signalization for cell development and survival was established [63–66]. The major drawback of collagen hydrogels relies on their poor mechanical properties [67]. Moreover, the cell-matrix interaction was reported to result in loss of shape and integrity of type I collagen hydrogels for certain cell lineages [68]. For *in vitro* biomineralization, the use of dense collagen 3D-hydrogels was validated as cell culture model to evaluate the behavior of stem cells from human exfoliated deciduous teeth [69].

Fibrin hydrogels represent an interesting tool to study the coagulation process and angiogenesis, [70,71]. The flexibility and inherent presence of cell binding sites enhance cell adhesion, displaying high seeding efficiency and uniform cell distribution [72,73]. Fibrin hydrogels were reported to induce endometrial stem cells growth, migration and differentiation to pancreatic B cells able to produce insulin due to the similar natural properties of fibrin and the pancreatic tissue [74]. A higher stem cells differentiation of human endometrial to Schwann cells of fibrin hydrogels compared to tissue culture plates was reported [75]. 3D-fibrin hydrogels can also be used to evaluate neuronal stem cell viability, neuronal differentiation and ECM deposition [76].

USC UNIVERSIDADE DE SANTIAGO DE COMPOSTELA

However, the susceptibility of fibrin to protease action restricts their use for long-term cell culture [62].

Hyaluronic acid presents cell binding sites that favors its use as hydrogel component for stem cell culture and differentiation [77,78]. As an example, neural precursor cells seeded in hyaluronic acid hydrogels were able to differentiate into neurons and glial cells depending on the physical or chemical modifications of the hydrogels [79]. The mechanical properties and degradation rates of hyaluronic acid-based hydrogels can be modulated by chemical modifications, covalent crosslinking or the use of gelation agents [80].

1.3.2. Scaffolds

In tissue engineering, scaffolds can act as cell carriers or cell hosts by providing an appropriate environment to promote cell growth and differentiation (Fig. 1.4). Based on the advances in the 3D-culture using scaffolds, the incorporation of bioactive agents and further grafting in the human body is logical. Although hydrogels as scaffolds played a central role [81,82], the use of aerogels for tissue regeneration have experienced a huge development is recent years [83,84].

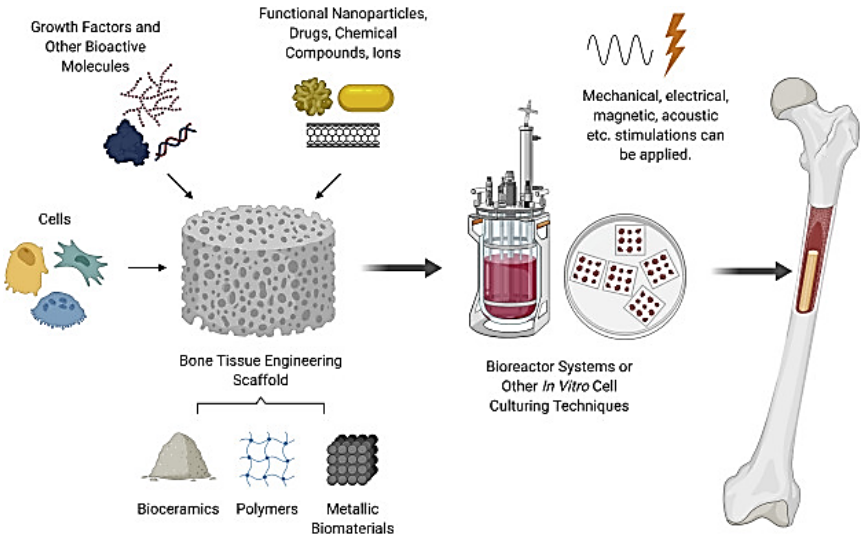


Figure 1.4. Development of scaffolds for bone tissue engineering. Scaffolds can act as cells carriers, including a huge portfolio of bioactive compounds. However, if appropriate designed, the cell colonization of the scaffold can occur once implanted in the patient, avoiding immune rejection phenomena. Reprinted from reference [85] with permission from Elsevier.

USC UNIVERSIDADE DE SANTIAGO DE COMPOSTELA

The paracrine effect between adipose-derived MSCs and osteoblasts seeded in collagen hydrogel scaffolds was recently reported [86]. This co-culture system enhanced *in vivo* bone formation in a rat calvarial defect model. The incorporation of fibroblast growth factor-2 into type I collagen scaffolds significantly increased the *in vivo* alveolar bone healing and periodontal attachment in furcation defects in a dog model [87]. Regarding the weak mechanical properties of pure collagen hydrogels, the combination with synthetic polymers, ceramics, or bioactive glass has been reported to obtain suitable scaffolds for load-bearing tissues regeneration, such as bone [88,89]. As an example, collagen/ poly(ethylene glycol) fumarate hydrogels enhance the mechanical strength of the gel when compared to their unmodified counterparts, while the biocompatibility and the fibroblast growth and proliferation was preserved [90]. An innovative approach using highly porous aerogels made of type I collagen and graphene oxide enhanced the *in vivo* bone regeneration in rat cranial critical-sized defects [91].

Hyaluronic acid plays an important role in lubrication, cell differentiation and cell growth in the connective tissue due to its hydrophilic character and high molecular weight. hyaluronic acid hydrogels are used in absence of doping agents since hyaluronic acid presents cell surface receptors (including CD44) that strongly interacts with many stem cell surface receptors, influencing cell proliferation, survival and differentiation [92,93]. Hyaluronic acid-based scaffolds combined with MSCs are frequently used for articular cartilage regeneration [94–98], although the use of hyaluronic acid hydrogels for other cartilage lesions were reported too [99,100]. On the other hand, osteogenic differentiation was reported for MSCs seeded in hyaluronic acid hydrogels [101]. The intrinsic hyaluronic acid differentiation properties can be modulated by chemical derivatization. As an example, the biofunctionalization of hyaluronic acid hydrogels with N-cadherin peptide enhanced the expression of osteogenic markers in human MSCs, the promotion of alkaline phosphatase activity and matrix mineralization both *in vitro* and *in vivo* [102]. In another example, hyaluronic acid/ polylysine hydrogels showed *in vitro* cytocompatibility to neural stem cells and favored the cell ingrowth and angiogenesis once

USC UNIVERSIDADE DE SANTIAGO DE COMPOSTELA

implanted in rats [103]. Nevertheless, hyaluronic acid has a fast *in vivo* degradation and a combination with other polymers is required for an appropriate scaffold performance.

For chondroitin sulfate hydrogels, cells can be introduced either during or after gel polymerization depending on the cell line [104]. The combination with other natural polymers (gelatin, hyaluronic acid) results in hybrid hydrogel scaffolds for cartilage/fibrocartilage repair with satisfactory *in vivo* results in a pig model [105,106]. An enhanced preservation of cell viability, proliferation and matrix synthesis of human nucleus pulposus cells were reported when seeded in tri-copolymeric scaffolds containing chondroitin sulfate, highlighting its application for intervertebral disc regeneration [107].

Cellulose presents tunable physicochemical and mechanical properties representing an ideal scaffolding material. The functionalization of cellulose with biomolecules (e.g. growth factors) or through chemical modifications ensures the viability and growth of different cell types in cellulose-based matrices [108–110]. The tunable morphological and mechanical properties of cellulose hydrogels were compatible with the growth and proliferation of chondrocytes [111,112]. The incorporation of biocompatible polymers, such as polylactic acid or poly(methyl methacrylate), in bacterial cellulose aerogels reinforced their mechanical performance towards compressive stress [113]. The poly(methyl methacrylate) interpenetration was further investigated in terms of fibroblast viability, distribution and spreading with positive outcomes [114]. In a recent study, chemically modified cellulose nanocrystal aerogels showed robust bone formation after 3 weeks post-implantation in a rat model [115].

Starch consists of a mixture of amylose and amylopectin, whose relative ratio strongly varies depending on the starch source [116]. Starch-based materials incorporating HA were proposed as promising candidates as temporary bone replacements [117]. A series of starch/N-vinylpyrrolidone hydrogels showed *in vitro* biocompatibility and apatite formation in SBF, supporting their application as bone scaffolds [118]. In another study, citrate starch scaffolds

USC UNIVERSIDADE DE SANTIAGO

immersed in SBF presented calcification up to 28 days, with significant MG63 osteoblast-like cells attachment and biocompatibility [119]. Aerogels commonly lack of pores in the macroscale, which are required for suitable cell-scaffold-environment interaction. To overcome this pitfall, starch-based aerogels scaffolds endowed with larger pores were prepared by the incorporation of zein and further leaching during the hydrogel-alcogel transition [120]. The *in vitro* biocompatibility of the scaffolds was evaluated with human bone marrow-derived MSCs, showing outstanding results for the modified starch aerogels. Finally, the incorporation of starch aerogel microspheres in polycaprolactone scaffolds significantly improved their water permeability and MSCs infiltration capacity, supporting their use for bone regeneration [121].

Silk fibroin has been tested as component of scaffolds for cartilage and bone regeneration [122–124]. Sonication-induced silk fibroin hydrogels were reported to encapsulate and support the proliferation and growth of MSCs [125]. In other study, silk fibroin/ poly-L-lysine hydrogels were reported to support cell viability and the differentiation of MSCs towards an osteogenic lineage in the absence of osteogenic stimulants in the medium [126]. In a recent study, 3D-printed silk fibroin-based hydrogels incorporating growth factors were manufactured, displaying good biomechanical properties and degradation rates matching those of cartilage tissue [127]. The clinical application of 3D-printed glycidyl methacrylated/ silk fibroin hydrogels laden with chondrocytes was reported *in vivo* for cartilage reconstruction [128]. The formation of new cartilage-like tissue was found surrounding the grafted hydrogels in trachea defects in a rabbit model. Regarding aerogels, the *in vivo* bone regeneration enhancement in rat calvarial model using silk fibroin-aerogel/ polycaprolactone scaffolds doped with dexamethasone was reported [129].

1.4. Natural polymer gels for the treatment of wounds

Skin is the largest organ in the human body [130]. It is the main barrier against microorganisms, mechanical injuries, substances and radiation, and also has the purpose to regulate temperature

USC UNIVERSIDADE DE SANTIAGO

and balance water content [131,132]. When skin injury occurs, several cellular and extracellular pathways are activated to restore tissue integrity and to reactivate skin biological functions [133]. Wound healing comprises four main stages (hemostasis, inflammation, proliferation and remodeling) until complete tissue regeneration. In acute wounds, the first stages elapse several days, while the remodeling phase may last up to several months depending on the severity of the injury [134]. However, in chronic wounds this sequence is altered, remaining in chronic inflammation and delaying the first stages of healing for several months [135]. Chronic wounds represent the main cause of non-traumatic amputation, and are a cause for morbidity [136]. Hypoxia, metabolic changes related to age or disease, unhealthy habits, pharmacological treatments and infection are the main factors that can cause chronic wounds.

The high prevalence of chronic wounds has led to intensive research to unveil the biological processes behind the wound healing process as well as to develop strategies for the regulation of the varied mechanisms implicated in the regeneration of the tissue [137,138]. Traditionally, the standard clinical practice involves the use of wound dressings that protect the wound from the environment and remove excessive exudate, maintaining an adequate moist environment for the healing process [139]. Several aspects of the wound, such as injured area, moisture or presence of infection, are evaluated to select an adequate dressing that meets the specific requirements.

Hydrogels present high water content, good biocompatibility, and good mechanical properties, such as softness and flexibility, to be applied as wound dressings [140]. They are usually easy to replace and comfortable to the patient, alleviating pain due to their cooling effect [141]. Hydrogels are able to absorb wound exudate (up to 10 times or more their weight [142]), and also their high content in water is able to provide a moist environment in the case of dry wounds, so they are ideal to maintain wound moisture balance [140]. They are permeable to metabolites and air, as well as non-reactive and non-irritant. Furthermore, they can be loaded with bioactive

USC DE COMPOSTELA

substances that can enhance the healing process, such as growth factors, or can deal with wound complications, such as antibiotics or antiseptics to treat and prevent infections [143–146]. Hydrogels are usually prepared as films and sometimes they are difficult to adapt to the wound surface, requiring cutting by the healthcare personnel. *In situ* forming injectable hydrogels have been developed to avoid this manual procedure, being minimally invasive and capable for molding into the injection cavity, and reducing procedure costs and patient discomfort (Fig. 1.5) [147].

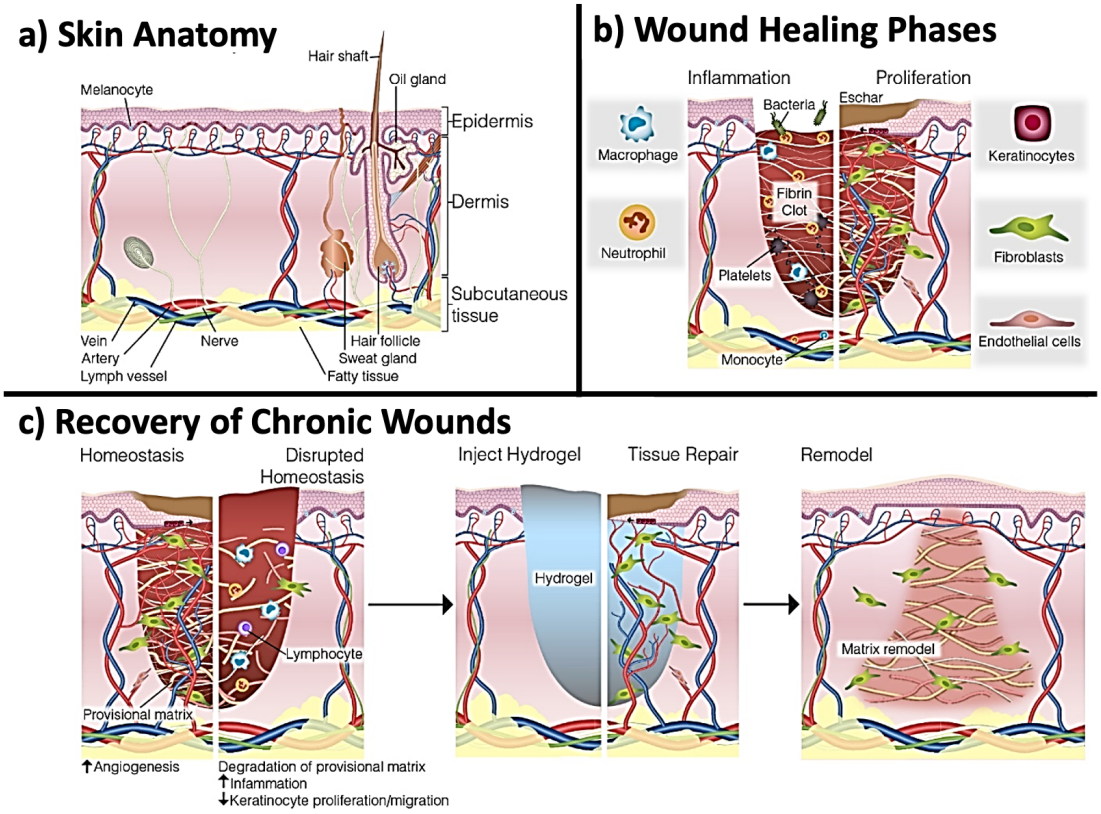


Figure 1.5. a) Skin anatomy, **b)** main wound healing stages, and **c)** healing process after the injection of an *in situ* forming hydrogel. Reprinted from reference [147] with permission from Elsevier.

During the last decades aerogels are being studied for biomedical applications, including wound healing. Their highly porous structure is similar to the ECM and provides aerogels with large surface area that leads to high loading capacity of bioactive agents [148–150]. As dry porous materials, they are able to absorb high amounts of fluids and adapt to the shape of the wound upon hydration [151–153]. Their open porosity also favors transpiration-evaporation balance

USC UNIVERSIDADE DE SANTIAGO DE COMPOSTELA

and gas permeability, preventing from tissue hypoxia and the growth of anaerobic microorganisms.

Natural polymer-based gels and aerogels are especially attractive for wound healing since they are easily obtained from abundant natural sources, present good biocompatibility and are non-toxic to skin [154]. Properties such as mechanical stability, degradability, release of bioactive agent from the gels, and water sorption capacity are highly dependent on the type of polymer and crosslinking interactions [155]. Physical crosslinking of gels does not involve the use of chemical agents that could cause *in vivo* toxicity, but the mechanical stability of the resultant gels may be limited. Chemical crosslinking of gels usually leads to higher stability, improved mechanical properties and enhanced resistance to *in vivo* degradation due to covalent bonding of the polymer chains, which could reduce the frequency of dressing changes [140,156].

1.4.1. Protein-based gels for wound treatment

A number of type I collagen-based wound hydrogel dressings are in the market in different forms, such as powder (CellerateRX®, Medifil®) or films (Wun'Dres®, Collasorb®, Fibracol®). They present high liquid absorbance capacity and mechanical strength, and are able to enhance vascularization, granulation tissue formation and native collagen deposition. Type I collagen can be hydrolyzed by matrix metalloproteinases, leading to fragments that can be degraded by other proteases [157]. While biodegradability is desirable in wound dressings, rapid enzymatic degradation can be a cause for instability. To reduce this and also to increase the mechanical properties of the dressing, collagen can be crosslinked by physical, chemical and biological methods. Frequent chemical crosslinking agents (e.g. GA) could lead to toxic residues upon degradation, and therefore the crosslinking with biocompatible molecules has been proposed. For instance, curcumin crosslinked collagen aerogels showed enhanced mechanical properties combined with antiproteolytic, antimicrobial and proangiogenic activities [158]. Wheat grass has also been used to reinforce the mechanical properties of collagen, as well as carrier for the

USC UNIVERSIDADE DE SANTIAGO

release the intrinsic bioactive molecules of wheat grass that provide proangiogenic and antibacterial activities, enhancing tissue regeneration [159].

Silk fibroin dressings present slow degradation, low immunogenicity, high water absorbance and good air permeability, and can be prepared in a number of structures including sponges, films and hydrogels. Silk fibroin hydrogels may improve burn wound healing by creating a moist environment, enhancing cell adhesion and migration through the talin-1 pathway [160]. It was also recently demonstrated that silk fibroin hydrogels are able to reduce scar thickness in hypertrophic scars [161].

Finally, keratin from different sources accelerates re-epithelialization in animal wound models, improving wound healing [162]. Kim et al. developed *in situ* forming human hair keratin hydrogels and studied their interaction with skin keratinocytes [163].

1.4.2. Polysaccharide-based gels for wound treatment

Cellulose aerogels can be prepared by $scCO_2$ drying or freeze-drying of nanofibrilated cellulose or bacterial cellulose [164]. Cellulose nanofiber aerogels provide oxygen permeability due to high porosity and surface area, preventing anaerobic bacteria growth. Cellulose aerogels can be loaded with antibacterial substances such as copper to extend its antimicrobial activity to aerobic bacteria [165]. Cellulose has been combined with other biopolymers, such as chitosan, for the development of injectable composite aerogels with rapid shape recovery for rapid hemostasis of non-compressible hemorrhage [166].

Chitosan has intrinsic antimicrobial, haemostatic and mucoadhesive properties of interest for wound healing applications [167–169]. The antimicrobial activity of chitosan may rely on the crosslinking between the anions of the bacteria surface and the polycations of the chitosan, which results in the alteration of membrane permeability [170]. Chitosan hydrogels loaded with a number of substances, such as growth factors, nanoparticles and drugs for wound healing, have been developed [171,172]. Chitosan aerogels have also been loaded with bioactive

USC DE SANTIAGO DE COMPOSTELA

substances such as antibiotics to treat infected wounds [172], and studied as haemostatic agents [151,173].

Alginate has a high exudate sorption capacity [174]. Thus, alginate-based wound dressings are able to maintain a moist environment and with reduced bacterial infection [175]. Alginate also has a haemostatic effect, and can support the healing process by increasing angiogenesis and production of type I collagen, enhancing cell migration, and reducing inflammatory cytokines [176]. Several alginate-based wound dressings are already in the market (Algicell™, Tegagen™, SeaSorb®, Kaltostat™), but their capabilities of processing strategies and combination with other polymeric materials are still under research. Examples of alginate aerogels for wound treatments include core-shell particles for sustained antibiotic delivery (Fig. 1.6a) [152], and aerogels loaded with metal cations for antiseptic and anti-inflammatory activities with high liquid uptake capacity (Fig. 1.6b) [177].

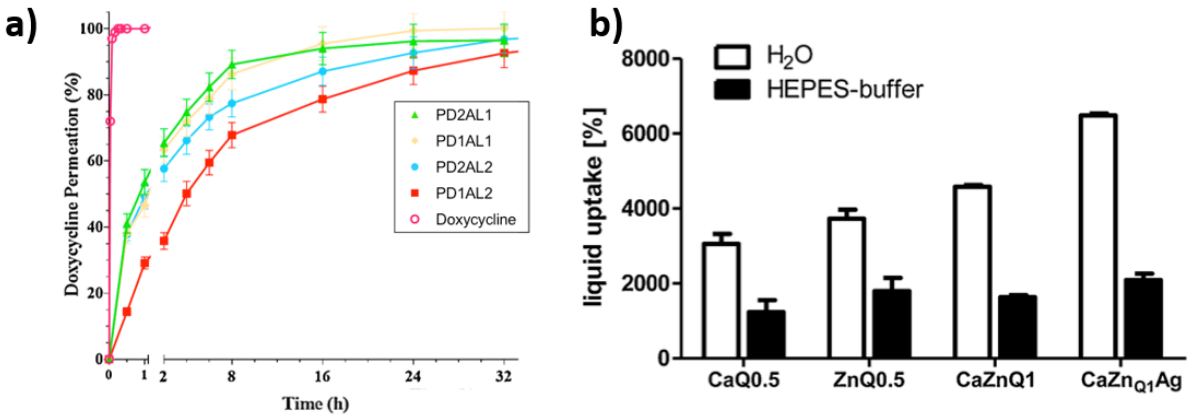


Figure 1.6. a) Controlled release of doxycycline from core-shell alginate particles produced by prilling and $scCO_2$ drying. PD1 and PD2 indicate a doxycycline-pectin ratio in the core of 0.2 and 0.1, respectively, and AL1 and AL2 indicate alginate concentrations of 1.5 and 1.75% in the outer layer, respectively. **b)** Water and HEPES buffer uptakes of alginate aerogels containing different calcium, zinc and silver molar ratios and alginate crosslinking degrees. Q0.5 and Q1 indicate a crosslinking degree of 0.9 and 1.8 mmol of metal/g of alginate. Reprinted from reference [152] and [177] with permission from Elsevier.

Finally, the hygroscopicity of hyaluronic acid makes its hydrogels ideal materials for exudate removal. Hyaluronic acid hydrogels also help keratinocyte migration and angiogenesis, leading

USC UNIVERSIDADE DE SANTIAGO DE COMPOSTELA

to better reconstruction of the damaged area and reduced scarring [178]. This effect is highly dependent on the molecular weight of the hyaluronic acid.

1.5. Natural polymer gels for biomedical imaging and sensing

Techniques to obtain medical images are focused on the imaging of selected biological entities and remains a crucial aspect of regenerative medicine nowadays [179]. The tracking of the development of abnormal processes like cancer or necrosis through diagnostic imaging techniques allows the understanding and monitoring of multiple processes in living cells, in tissues and in the whole body. The delivery of the correct dose of imaging agent at a precise location is critical for a successful diagnosis through medical imaging [180]. The feasibility of using hydrogel-based systems in diagnostic imaging was demonstrated with the design of a novel carrier for quantum dots based on nanogels and tested for intracellular imaging [181]. This hybrid hydrogel system composed of quantum dots and nanogels of cholesterol modified with amino groups was employed as a fluorescent probe in biological and imaging applications. Furthermore, hydrogels have been applied as carriers for radiochemotherapy administration and as coatings to encapsulate radioisotopes for radiation delivery devices [182,183].

An ideal imaging agent must give response to disease biomarkers with high sensitivity, specificity and efficiency with the aim of assisting in the diagnosis and/or treatment of diseases. These effective contrast agents must fulfill biological requirements (biodegradability, biocompatibility, and appropriate transport mechanism to the targeted tissue) and require fast and sensitive detection tools [179]. There are different imaging modes like optical imaging, magnetic resonance imaging (MRI), computer tomography (CT), positron emission tomography (PET) or ultrasounds, being MRI the most commonly employed imaging diagnostic method due to its high resolution and soft tissue contrast [184].

USC UNIVERSIDADE DE SANTIAGO DE COMPOSTELA

Optical imaging presents high spatial resolution in terms of imaging contrast. Confocal microscopy is an optical imaging tool used to monitor cells and tissues *in vivo* and *in vitro* with

fluorescence markers. Fluorescence imaging is the most promising imaging modality since it provides a non-invasive way for locating, monitoring and tracking implants *in situ*. It also has high sensitivity, fast imaging capture speed, easy operation and low cost. For all these reasons, biocompatible fluorescent polymeric materials with integrated fluorescent properties are under research [184]. In this context, the properties of protoporphyrin-incorporated alginate hydrogels were studied by fluorescence spectrophotometry. These alginate-based hydrogels were monitored and tracked *in vivo* using a multispectral fluorescence imaging system with nude mice as models and they exhibited fluorescence with good biocompatibility [185]. Furthermore, different methods have been tested to confer special optical properties including fluorescence, long-life luminescence, and polarized light to nanocellulose-based hydrogels and aerogels [186]. In general, nanocellulose itself exhibits low toxicity, good biocompatibility, biodegradability and can be derivatized into excellent fluorescent nanoprobes for *in vivo* imaging and tracking.

MRI is a radiation-free imaging modality that generates an anatomical and physiological image of the body by applying high magnetic fields, radio frequencies and electrical fields combined with exogenous or endogenous contrast agents. Magnetic resonance technique is a non-ionizing, non-invasive and relatively safe analysis widely used *in vivo* [184]. Injectable hyaluronic acid-based hydrogels labeled with ^{19}F were designed to be monitored by MRI [187]. The ^{19}F labeling of hyaluronic acid polymer did not affect hydrogel mechanical properties and the hydrogel presents potential clinical applications because it is injectable, biocompatible, and can be tracked in a non-invasive way. In another example, chitosan and poly(ethylen glycol)-based hydrogels were synthesized by conjugating chitosan with diethylene triamine pentaacetic acid and using a macromolecular chelator of Gd(III) as a contrast agent to label hydrogels and monitor implants in real time by MRI [188]. MRI-visible, injectable, and self-healing hydrogels were obtained. The MRI of contrast agent binding hydrogels was performed *in vitro* and *in vivo* in rats. Hydrogels were always detected before complete biodegradation and they exhibited strong signals on MRI

USC UNIVERSIDADE DE SANTIAGO DE COMPOSTELA

images, so these *in situ* hydrogels present potential application for the tracking of long-term implants by MRI (Fig. 1.7).

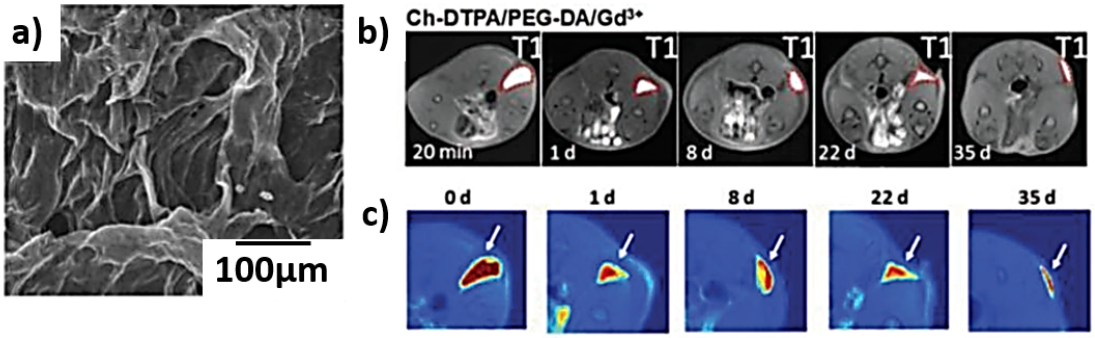


Figure 1.7. a) SEM image of chitosan and poly(ethylen glycol)-based hydrogel. **b)** MRI of subcutaneously injected hydrogels into a rat after different periods of time. **c)** Transverse cross-sections of *in vivo* MRI images after different periods of time with arrows indicating the contrast agent-labeled hydrogels. Reproduced from reference [188] with permission from the Royal Society of Chemistry.

The CT technique employs low-energy X-ray sources and a rotating charged detector that responds to incident X-rays. The differences of X-ray absorbance among fat, air, bone and water provide the CT contrast, which is low in tumors and surrounding tissues [189]. However, the contrast can be increased with the help of contrast agents, like barium sulfate or iodine, and the current state of organs and tumors can be analyzed [190]. In case of bone repairing hydrogel scaffolds, the structure is implanted deeply under tissues, where light could hardly penetrate. Optical imaging is not applicable while CT and MRI offer possibilities due to their penetrating capacity throughout the whole body, enabling the imaging of materials in any location. As an example, injectable shear-thinning poly(lactide-co-glycolide)-chitin hydrogels exhibit certain characteristics like easy handling, ability to be injected into deeper tissue defects and margin adaptability that make them potential candidates for large bone defect regeneration and for longitudinal CT-imaging of live animals without using a contrast agent [191]. In the case of aerogels, mechanical properties of hybrid aerogels of type I collagen reinforced with graphene oxide are suitable for large bone repair because the good biocompatibility and *in vivo* osteogenic ability as confirmed by micro-CT imaging analysis of aerogels implanted into rat cranial bone defects without the employment of any contrast agent [192].

PET is a diagnostic imaging tool with a high sensitivity and minimally invasive capacity of relevance in clinical imaging. PET is used in biological imaging studies concerning bone metabolism and metastasis, a common phenomenon for most cancer types. Radioactive tracers are incorporated into metabolically active molecules to perform 3D images. Gelatin-based hydrogels were subcutaneously implanted in mice to investigate the clinical relevance of this biopolymer and the interaction between hydrogel and tissue and the degradation were explored *in vivo* by PET. The degradation time was dependent on the number of implants but it was demonstrated a complete restoration of the original healthy tissue without observing local or systemic adverse tissue responses [184].

Ultrasounds are an imaging technique employed to generate 3D images of newly formed tissue. It is a low cost and rapid method clinically employed that presents low wave energy and high imaging speed and penetration depth, but it lacks sensitivity. This method has been employed for visualizing injected chitosan and chitosan-HA hydrogels and also for monitoring and assessing the *in vivo* characteristics of injected hydrogel-based bone scaffolds [184].

All these bioimaging techniques can be combined with biosensing to be used both *in vivo* and *in vitro* assays in order to evaluate the biological and pathological processes in living systems at the molecular level for the early diagnosis of diseases. Namely, molecular probes and sensors are crucial in the transduction of molecular or cellular events (targets) into detectable signals [193]. In general, a biosensor is an integrated device that employs the molecular recognition between the analyte to be detected and a biomolecule (called bioreceptor) to trigger a biological response converted into electrical signal by a transducer. Antibodies, DNA, enzymes, organelles, whole cells and microorganisms are used as bioreceptors. The transducer is a device that transforms the biological interaction into a measurable signal by a transduction mechanism (optical, electrical, electrochemical, piezoelectric or calorimetric). Finally, the signal is processed and displayed as an image, number or graph on a digital display unit [194]. A biosensor must present

USC DE COMPOSTELA

high sensitivity, stability, selectivity, reproducibility, portability, cost effectiveness, detection velocity as well as ease of use and manufacture. Biosensors have important advantages like miniaturization, portability, minimum sample preparation and versatile applications. Most biosensors allow quantitative analysis, like the blood glucose test for diabetes, while others allow a semi-quantitative evaluation like the pregnancy test. Some biosensors are disposable of single-use (pregnancy test), while others are designed as long-term monitoring sensors (glucose monitoring sensors) [194,195].

Some hydrogel characteristics are attractive for their use in biosensing like the 3D-nature of the polymer gel networks, the capture capability of the target and its transport inside the gel network, as well as the swelling behavior, the solutes diffusion on the bulk structure and the solute-solvent interaction. In general, the control of the hydrogel structure is essential for the target transport because it determines how a molecule diffuses inside the matrix and the target capture and detection mechanism. The optimization of the composition, porosity, particle rigidity and hydrogel swelling behavior is needed [196]. Furthermore, hydrogels designed for biosensing incorporate a molecular recognition element that initiates the responsive behavior. These recognitive biomolecules can be conjugated or encapsulated in hydrogel networks either during or after gelation. Biomolecules are incorporated during polymerization, provided that they are soluble and stable in the reaction medium. Alternatively, different post-synthetic reactions can also incorporate biomolecules to hydrogels in function of the biomolecule and application [197].

Hydrogels are used as immobilizing scaffolds for biomolecules to measure biospecific interactions [198]. Alginate hydrogels are the first choice in biosensors development because of their extraordinary ability to entrap stable biomolecules in biocompatible membranes. However, alginate membranes are poorly repetitive and limits their application in biosensing. Cell electrotrapping in conductive alginate hydrogels is under research to overcome this drawback

USC DE COMPOSTELA

[199]. Bacterial electrotrapping in conductive alginate matrices resulted in a highly sensitive and repetitive biosensor without compromising bacterial activity and with an increasing response of four times with respect to non-conductive alginate membranes, while toxicity values were comparable.

Biomolecules can be also covalently attached to hydrogel films on a resonance sensor chip to provide a solution that mimics biological environment in a two dimensional rigid substrate [198]. The resulting biosensor is able to measure biomolecular concentration and interaction kinetics of biomolecules with the advantage of the use in multiples cycles and the lack of requirement of other biomolecular labeling. Nucleic acids can also be immobilized on biosensor solid supports to be employed in the detection of DNA and other biomolecules. A chitosan hydrogel-based platform was designed for enzyme detection and implemented in wound dressings for infection sensing [200]. Wound dressing films were functionalized with a fluorogenic substrate covalently conjugated to chitosan. This molecule was released after enzymatic degradation, resulting in an increment in fluorescence emission intensity. This approach can be exploited to target the detection of specific pathogens in different diseases by choosing appropriate fluorogenic or chromogenic substrates.

Hydrogels can also contain or respond to enzymes for sensing applications. These enzyme-containing or enzyme-responsive hydrogels are based on an enzyme-substrate interaction detected by enzyme-linked immunosorbent assays through the generation of a colored product. The entrapment of the enzymes within the small volume of the hydrogel enables high local concentrations of the enzyme and sensitive detection [197]. In this context, a novel and simple optical biosensor formed by a pectin hydrogel as pH indicator and a chromoionophore with lipase as catalyst was developed to detect triglycerides. The enzymatic system releases protons in the presence of triglycerides changing the absorbance color of chromoionophore and the triglycerides biosensor worked correctly [201].

USC DE COMPOSTELA

Several features of aerogels are relevant for biosensor applications. Firstly, aerogels present unique physicochemical properties (low density, high specific surface area) and are formed by an open, highly porous and interconnected network [202]. In this sense, aerogels with specific biosensors incorporated can be employed, for example, to report the presence of certain biomolecules like H_2O_2 [203]. Cellulose aerogels as biosensors are under research due to the abundance, accessibility, high hydrophilicity, purity and biocompatibility of its source [204]. Nanocellulose aerogels were designed with a peptide substrate immobilized in the surface of the aerogel to detect protease activity in wounds [202]. Bioactivity tests showed acceptable detection sensitivity for human neutrophil elastase, a diagnostic biomarker in inflammatory diseases. The physical properties (specific surface area, density, thickness, porosity and pore and fiber diameter) were also appropriate for wound dressing applications (Fig. 1.8).

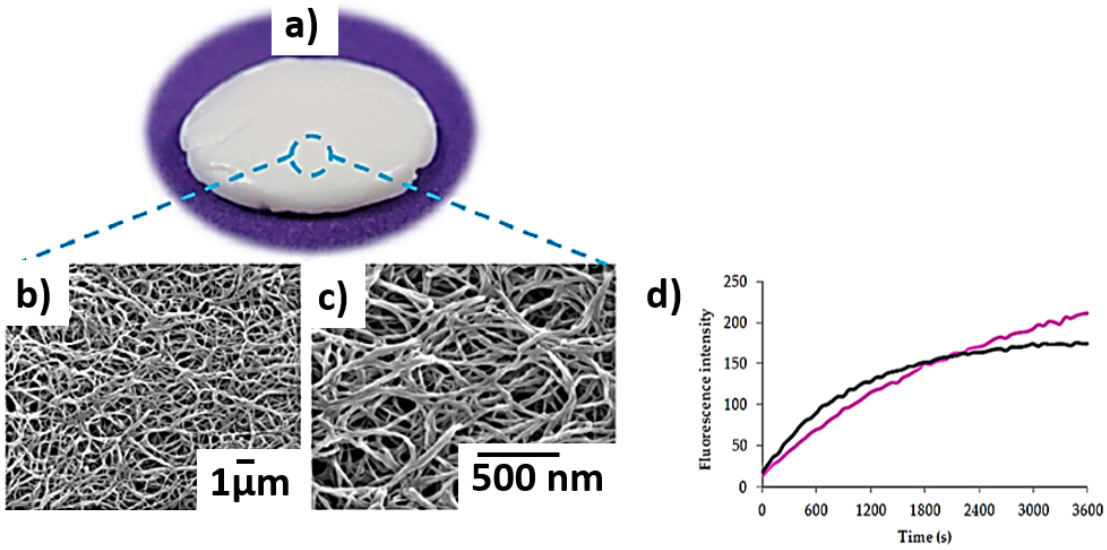


Figure 1.8. Structure of nanocellulosic aerogels by **a)** optical, **b)** SEM and **c)** FE-SEM imaging. **d)** Progress curve of unbound peptide substrate (0.06 M -black-) and 2 mg of the biosensor (pink) in a wound-like fluid. Adapted from reference [202] under the terms and conditions of the Creative Commons Atribbution (CC-BY) license.

1.6. Future perspectives and conclusions

USC DE SANTIAGO DE COMPOSTELA

In this Chapter, the most relevant properties on hydrogels and aerogels from natural polymers and recent developments for biomedical applications, ranging from drug delivery, tissue

engineering and treatment of wounds to biomedical imaging and sensing, are described. The versatility of design of hydrogels and aerogels confers them a huge variety of biomedical possibilities and enables them to solve currently unmet demands. Namely, the preparation of intelligent materials based on hydrogels already found a significant progress in the biomedical research, whereas current work on aerogels is still incipient. Such gel designs will increase the complexity of their preparation, although the advantages of these multi-stimuli responsive aerogels are of relevance for drug delivery and tissue engineering to trigger specific biological responses [205,206].

Mechanical strength, biocompatibility and sterile conditions are common issues for hydrogels and aerogels under development. Coatings, changes in gel composition and use of chemical crosslinkers are among the strategies currently tested to reinforce the mechanical properties of gels to counteract the biodegradation and swelling phenomena taking place when inserted in a biological environment [4,7]. Natural polymer gels usually have an excellent biocompatibility, but cytotoxic events may appear when combined with other admixtures in hybrid and composite gels. It should be noted that conventional sterilization methods may be incompatible with advanced gel designs as they can result in their degradation of physicochemical properties and loss of functionality. Moreover, the intricate structure of gels with high porosity and tortuosity may turn inefficient the common sterilization methods, and alternative sterilization methods ($scCO_2$ and plasma sterilization) for gels are currently under evaluation [32].

Finally, the vast knowledge generated on the tuning of the size and textural properties of hydrogels and aerogels as well the variety of polymeric sources, opens up plenty of possibilities for these materials in biomedical application and related fields (e.g., food industry) [207]. The advent of gel and aerogel preparation by additive manufacturing widens the design possibilities for customized biomedical applications. The incorporation of biolabels to hydrogels and aerogels for non-invasive biomedical imaging will represent a prominent field for the *in vivo* tracking of

USC DE COMPOSTELA

grafts and injectables, which is so far limited by the low penetration depth of visible and UV-lights. Overall, new administration routes (aerogels for chemotherapy) or drug delivery approaches (e.g., remote controlled release, long-term release, theranostics) are still to be explored with gels by technological combinations.

1.7. References

1. García-González, C.A.; Alnaief, M.; Smirnova, I. Polysaccharide-Based Aerogels - Promising Biodegradable Carriers for Drug Delivery Systems. Carbohydr. Polym. 2011, 86, 1425–1438, doi:10.1016/j.carbpol.2011.06.066.
2. Lima, C.S.A. de; Balogh, T.S.; Varca, J.P.R.O.; Varca, G.H.C.; Lugão, A.B.; A Camacho-Cruz, L.; Bucio, E.; Kadlubowski, S.S. An Updated Review of Macro, Micro, and Nanostructured Hydrogels for Biomedical and Pharmaceutical Applications. Pharmaceutics 2020, 12, 970, doi:10.3390/pharmaceutics12100970.
3. Chyzy, A.; Tomczykowa, M.; Plonska-Brzezinska, M.E. Hydrogels as Potential Nano-, Micro- and Macro-Scale Systems for Controlled Drug Delivery. Mater. Basel Switz. 2020, 13, 188, doi:10.3390/ma13010188.
4. Montero, A.; Valencia, L.; Corrales, R.; Jorcano, J.L.; Velasco, D. Chapter 9 - Smart Polymer Gels: Properties, Synthesis, and Applications. In Smart Polymers and their Applications (Second Edition); Aguilar, M.R., San Román, J., Eds.; Woodhead Publishing, 2019; pp. 279–321 ISBN 978-0-08-102416-4.
5. Vasile, C.; Pamfil, D.; Stoleru, E.; Baican, M. New Developments in Medical Applications of Hybrid Hydrogels Containing Natural Polymers. Mol. Basel Switz. 2020, 25, 1539, doi:10.3390/molecules25071539.
6. García-González, C.A.; Budtova, T.; Durães, L.; Erkey, C.; Del Gaudio, P.; Gurikov, P.; Koebel, M.; Liebner, F.; Neagu, M.; Smirnova, I. An Opinion Paper on Aerogels for Biomedical and Environmental Applications. Molecules 2019, 24, 1815, doi:10.3390/molecules24091815.
7. García-González, C.A.; López-Iglesias, C.; Concheiro, A.; Alvarez-Lorenzo, C. Chapter 16. Biomedical Applications of Polysaccharide and Protein Based Aerogels. In Green Chemistry Series; Thomas, S., Pothan, L.A., Mavelil-Sam, R., Eds.; Royal Society of Chemistry: Cambridge, 2018; pp. 295–323 ISBN 978-1-78262-765-4.
8. De Cicco, F.; Russo, P.; Reverchon, E.; García-González, C.A.; Aquino, R.P.; Del Gaudio, P. Prilling and Supercritical Drying: A Successful Duo to Produce Core-Shell Polysaccharide Aerogel Beads for Wound Healing. Carbohydr. Polym. 2016, 147, 482–489, doi:10.1016/j.carbpol.2016.04.031.
9. García-González, C.A.; Jin, M.; Gerth, J.; Alvarez-Lorenzo, C.; Smirnova, I. Polysaccharide-Based Aerogel Microspheres for Oral Drug Delivery. Carbohydr. Polym. 2015, 117, 797–806, doi:10.1016/j.carbpol.2014.10.045.
10. Chattopadhyay, S.; Raines, R.T. Collagen-Based Biomaterials for Wound Healing. 2014, 101, 821–833, doi:10.1002/bip.22486.
11. Farokhi, M.; Mottaghitalab, F.; Fatahi, Y.; Khademhosseini, A.; Kaplan, D.L. Overview of Silk Fibroin Use in Wound Dressings. Trends Biotechnol. 2018, 36, 907–922, doi:10.1016/j.tibtech.2018.04.004.
12. Gholipourmalekabadi, M.; Sapru, S.; Samadikuchaksaraei, A.; Reis, R.L.; Kaplan, D.L.; Kundu, S.C. Silk Fibroin for Skin Injury Repair: Where Do Things Stand? Adv. Drug Deliv. Rev. 2020, 153, 28–53, doi:10.1016/j.addr.2019.09.003.
13. Kim, S.Y.; Park, B.J.; Lee, Y.; Park, N.J.; Park, K.M.; Hwang, Y.-S.; Park, K.D. Human Hair Keratin-Based Hydrogels as Dynamic Matrices for Facilitating Wound Healing. J. Ind. Eng. Chem. 2019, 73, 142–151, doi:10.1016/j.jiec.2019.01.017.
14. Portela, R.; Leal, C.R.; Almeida, P.L.; Sobral, R.G. Bacterial Cellulose: A Versatile Biopolymer for Wound Dressing Applications. Microb. Biotechnol. 2019, 12, 586–610, doi:10.1111/1751-7915.13392.
15. Kabir, S.M.F.; Sikdar, P.P.; Haque, B.; Bhuiyan, M.A.R.; Ali, A.; Islam, M.N. Cellulose-Based Hydrogel Materials: Chemistry, Properties and Their Prospective Applications. Prog. Biomater. 2018, 7, 153–174, doi:10.1007/s40204-018-0095-0.
16. Patrulea, V.; Ostafe, V.; Borchard, G.; Jordan, O. Chitosan as a Starting Material for Wound Healing Applications. Eur. J. Pharm. Biopharm. 2015, 97, 417–426, doi:10.1016/j.ejpb.2015.08.004.

UAH UNIVERSIDAD DE ALCALÁ

17. Gurikov, P.; Smirnova, I. Non-Conventional Methods for Gelation of Alginate. Gels Basel Switz. 2018, 4, 14, doi:10.3390/gels4010014.
18. Burdick, J.A.; Prestwich, G.D. Hyaluronic Acid Hydrogels for Biomedical Applications. Adv. Mater. Deerfield Beach Fla 2011, 23, H41–H56, doi:10.1002/adma.201003963.
19. Amgoth, C.; Phan, C.; Banavoth, M.; Rompivalasa, S.; Tang, G. Polymer Properties: Functionalization and Surface Modified Nanoparticles. In Role of Novel Drug Delivery Vehicles in Nanobiomedicine; K. Tyagi, R., Garg, N., Shukla, R., Singh Bisen, P., Eds.; IntechOpen, 2020 ISBN 978-1-78923-985-0.
20. Zhu, T.; Mao, J.; Cheng, Y.; Liu, H.; Lv, L.; Ge, M.; Li, S.; Huang, J.; Chen, Z.; Li, H.; et al. Recent Progress of Polysaccharide-Based Hydrogel Interfaces for Wound Healing and Tissue Engineering. 2019, 6, 1900761, doi:10.1002/admi.201900761.
21. Kim, H.-S.; Yang, J.; Kim, K.; Shin, U.S. Biodegradable and Injectable Hydrogels as an Immunosuppressive Drug Delivery System. Mater. Sci. Eng. C 2019, 98, 472–481, doi:10.1016/j.msec.2018.11.051.
22. Zhao, J.; Li, J.; Zhu, C.; Hu, F.; Wu, H.; Man, X.; Li, Z.; Ye, C.; Zou, D.; Wang, S. Design of Phase-Changeable and Injectable Alginate Hydrogel for Imaging-Guided Tumor Hyperthermia and Chemotherapy. ACS Appl Mater Interfaces 2018, 10, 3392–3404, doi:10.1021/acsami.7b17608.
23. Newsom, J.P.; Payne, K.A.; Krebs, M.D. Microgels: Modular, Tunable Constructs for Tissue Regeneration. Acta Biomater. 2019, 88, 32–41, doi:10.1016/j.actbio.2019.02.011.
24. Wang, K.; Liu, M.; Mo, R. Polysaccharide-Based Biomaterials for Protein Delivery. Med. Drug Discov. 2020, 7, 100031, doi:10.1016/j.medidd.2020.100031.
25. Liu, L.; Zhang, Y.; Yu, S.; Zhang, Z.; He, C.; Chen, X. pH- and Amylase-Responsive Carboxymethyl Starch/Poly(2-Isobutyl-Acrylic Acid) Hybrid Microgels as Effective Enteric Carriers for Oral Insulin Delivery. Biomacromolecules 2018, 19, 2123–2136, doi:10.1021/acs.biomac.8b00215.
26. Soni, K.S.; Desale, S.S.; Bronich, T.K. Nanogels: An Overview of Properties, Biomedical Applications and Obstacles to Clinical Translation. J. Controlled Release 2016, 240, 109–126, doi:10.1016/j.jconrel.2015.11.009.
27. Neamtu, I.; Chiriac, A.P.; Nita, L.E.; Diaconu, A.; Rusu, A.G. Chapter 11 - Nanogels Containing Polysaccharides for Bioapplications. In Polymeric Nanomaterials in Nanotherapeutics; Vasile, C., Ed.; Elsevier, 2019; pp. 387–420 ISBN 978-0-12-813932-5.
28. Kłodzińska, S.N.; Pletzer, D.; Rahanjam, N.; Rades, T.; Hancock, R.E.W.; Nielsen, H.M. Hyaluronic Acid-Based Nanogels Improve *in Vivo* Compatibility of the Anti-Biofilm Peptide DJK-5. Nanomedicine Nanotechnol. Biol. Med. 2019, 20, 102022, doi:10.1016/j.nano.2019.102022.
29. Simonson, A.W.; Lawanprasert, A.; Goralski, T.D.P.; Keiler, K.C.; Medina, S.H. Bioresponsive Peptide-Polysaccharide Nanogels - A Versatile Delivery System to Augment the Utility of Bioactive Cargo. Nanomedicine Nanotechnol. Biol. Med. 2019, 17, 391–400, doi:10.1016/j.nano.2018.10.008.
30. Gurikov, P.; Smirnova, I. Amorphization of Drugs by Adsorptive Precipitation from Supercritical Solutions: A Review. J. Supercrit. Fluids 2018, 132, 105–125, doi:10.1016/j.supflu.2017.03.005.
31. Stergar, J.; Maver, U. Review of Aerogel-Based Materials in Biomedical Applications. J. Sol-Gel Sci. Technol. 2016, 77, 738–752, doi:10.1007/s10971-016-3968-5.
32. Ribeiro, N.; Soares, G.C.; Santos-Rosales, V.; Concheiro, A.; Alvarez-Lorenzo, C.; García-González, C.A.; Oliveira, A.L. A New Era for Sterilization Based on Supercritical CO_2 Technology. J Biomed Mater Res B Appl Biomater 2020, 108, 399–428, doi:10.1002/jbm.b.34398.
33. Kalepu, S.; Nekkanti, V. Insoluble Drug Delivery Strategies: Review of Recent Advances and Business Prospects. Acta Pharm. Sin. B 2015, 5, 442–453, doi:10.1016/j.apsb.2015.07.003.
34. Obaidat, R.M.; Alnaief, M.; Mashaqbeh, H. Investigation of Carrageenan Aerogel Microparticles as a Potential Drug Carrier. AAPS PharmSciTech 2018, 19, 2226–2236, doi:10.1208/s12249-018-1021-4.
35. Pawar, J.; Ali, M.T.; Fule, R.; Moravkar, K.; Seervi, M.; Sathaye, S.; Amin, P. Biodegradable Porous Starch Spheres as a Novel Carrier for Enhancement of Dissolution Rate and Oral Bioavailability of Itraconazole. Curr Drug Deliv 2017, 14, 944–954, doi:10.2174/1567201813666160920154209.
36. Haimer, E.; Wendland, M.; Schlufter, K.; Frankenfeld, K.; Miethe, P.; Potthast, A.; Rosenau, T.; Liebner, F. Loading of Bacterial Cellulose Aerogels with Bioactive Compounds by Antisolvent Precipitation with Supercritical Carbon Dioxide. 2010, 294, 64–74, doi:10.1002/masy.201000008.
37. Marin, M.A.; Mallepally, R.R.; McHugh, M.A. Silk Fibroin Aerogels for Drug Delivery Applications. J. Supercrit. Fluids 2014, 91, 84–89, doi:10.1016/j.supflu.2014.04.014.
38. Betz, M.; García-González, C.A.; Subrahmanyam, R.P.; Smirnova, I.; Kulozik, U. Preparation of Novel Whey Protein-Based Aerogels as Drug Carriers for Life Science Applications. J. Supercrit. Fluids 2012, 72, 111–119, doi:10.1016/j.supflu.2012.08.019.

39. Mustapa, A.N.; Martin, A.; Sanz-Moral, L.M.; Rueda, M.; Cocero, M.J. Impregnation of Medicinal Plant Phytochemical Compounds into Silica and Alginate Aerogels. J. Supercrit. Fluids 2016, 116, 251–263, doi:10.1016/j.supflu.2016.06.002.
40. Kleemann, C.; Schuster, R.; Rosenecker, E.; Selmer, I.; Smirnova, I.; Kulozik, U. In-Vitro-Digestion and Swelling Kinetics of Whey Protein, Egg White Protein and Sodium Caseinate Aerogels. Food Hydrocoll. 2020, 101, 105534, doi:10.1016/j.foodhyd.2019.105534.
41. Mohammadian, M.; Jafarzadeh Kashi, T.S.; Erfan, M.; Pashaei Soorbaghi, F. In-Vitro Study of Ketoprofen Release from Synthesized Silica Aerogels (as Drug Carriers) and Evaluation of Mathematical Kinetic Release Models. Iran. J. Pharm. Res. IJPR 2018, 17, 818–829.
42. Smirnova, I.; Suttiruengwong, S.; Arlt, W. Feasibility Study of Hydrophilic and Hydrophobic Silica Aerogels as Drug Delivery Systems. J. Non-Cryst. Solids 2004, 350, 54–60, doi:10.1016/j.jnoncrysol.2004.06.031.
43. Kéri, M.; Forgács, A.; Papp, V.; Bányai, I.; Veres, P.; Len, A.; Dudás, Z.; Fábián, I.; Kalmár, J. Gelatin Content Governs Hydration Induced Structural Changes in Silica-Gelatin Hybrid Aerogels – Implications in Drug Delivery. Acta Biomater. 2020, 105, 131–145, doi:10.1016/j.actbio.2020.01.016.
44. Nita, L.E.; Ghilan, A.; Rusu, A.G.; Neamtu, I.; Chiriac, A.P. New Trends in Bio-Based Aerogels. Pharmaceutics 2020, 12, 449, doi:10.3390/pharmaceutics12050449.
45. Del Gaudio, P.; Auriemma, G.; Mencherini, T.; Porta, G.D.; Reverchon, E.; Aquino, R.P. Design of Alginate-Based Aerogel for Nonsteroidal Anti-Inflammatory Drugs Controlled Delivery Systems Using Prilling and Supercritical-Assisted Drying. J. Pharm. Sci. 2013, 102, 185–194, doi:10.1002/jps.23361.
46. Tkalec, G.; Knez, Ž.; Novak, Z. PH Sensitive Mesoporous Materials for Immediate or Controlled Release of NSAID. Microporous Mesoporous Mater. 2016, 224, 190–200, doi:10.1016/j.micromeso.2015.11.048.
47. Antonyuk, S.; Heinrich, S.; Gurikov, P.; Raman, S.; Smirnova, I. Influence of Coating and Wetting on the Mechanical Behaviour of Highly Porous Cylindrical Aerogel Particles. Powder Technol. 2015, 285, 34–43, doi:10.1016/j.powtec.2015.05.004.
48. Bugnone, C.A.; Ronchetti, S.; Manna, L.; Banchero, M. An Emulsification/Internal Setting Technique for the Preparation of Coated and Uncoated Hybrid Silica/Alginate Aerogel Beads for Controlled Drug Delivery. J. Supercrit. Fluids 2018, 142, 1–9, doi:10.1016/j.supflu.2018.07.007.
49. Veronovski, A.; Knez, Ž.; Novak, Z. Comparison of Ionic and Non-Ionic Drug Release from Multi-Membrane Spherical Aerogels. Int. J. Pharm. 2013, 454, 58–66, doi:10.1016/j.ijpharm.2013.06.074.
50. Veronovski, A.; Knez, Ž.; Novak, Z. Preparation of Multi-Membrane Alginate Aerogels Used for Drug Delivery. J. Supercrit. Fluids 2013, 79, 209–215, doi:10.1016/j.supflu.2013.01.025.
51. Veronovski, A.; Tkalec, G.; Knez, Ž.; Novak, Z. Characterisation of Biodegradable Pectin Aerogels and Their Potential Use as Drug Carriers. Carbohydr. Polym. 2014, 113, 272–278, doi:10.1016/j.carbpol.2014.06.054.
52. Zhao, P.; Gu, H.; Mi, H.; Rao, C.; Fu, J.; Turng, L. Fabrication of Scaffolds in Tissue Engineering: A Review. Front. Mech. Eng. 2018, 13, 107–119, doi:10.1007/s11465-018-0496-8.
53. Baker, B.M.; Chen, C.S. Deconstructing the Third Dimension – How 3D Culture Microenvironments Alter Cellular Cues. J. Cell Sci. 2012, 125, 3015–3024, doi:10.1242/jcs.079509.
54. Chaudhuri, O. Viscoelastic Hydrogels for 3D Cell Culture. Biomater. Sci. 2017, 5, 1480–1490, doi:10.1039/C7BM00261K.
55. Lam, N.T.; Lam, H.; Sturdivant, N.M.; Balachandran, K. Fabrication of a Matrigel–Collagen Semi-Interpenetrating Scaffold for Use in Dynamic Valve Interstitial Cell Culture. Biomed. Mater. 2017, 12, 045013, doi:10.1088/1748-605X/aa71be.
56. Joo, S.; Oh, S.-H.; Sittadjody, S.; Opara, E.C.; Jackson, J.D.; Lee, S.J.; Yoo, J.J.; Atala, A. The Effect of Collagen Hydrogel on 3D Culture of Ovarian Follicles. Biomed. Mater. 2016, 11, 065009, doi:10.1088/1748-6041/11/6/065009.
57. Liu, J.; Yu, C.; Chen, Y.; Cai, H.; Lin, H.; Sun, Y.; Liang, J.; Wang, Q.; Fan, Y.; Zhang, X. Fast Fabrication of Stable Cartilage-like Tissue Using Collagen Hydrogel Microsphere Culture. J. Mater. Chem. B 2017, 5, 9130–9140, doi:10.1039/C7TB02535A.
58. Nguyen, B.-N.B.; Moriarty, R.A.; Kamalitdinov, T.; Etheridge, J.M.; Fisher, J.P. Collagen Hydrogel Scaffold Promotes Mesenchymal Stem Cell and Endothelial Cell Coculture for Bone Tissue Engineering. J. Biomed. Mater. Res. A 2017, 105, 1123–1131, doi:10.1002/jbm.a.36008.
59. James-Bhasin, M.; Siegel, P.; Nazhat, S. A Three-Dimensional Dense Collagen Hydrogel to Model Cancer Cell/Osteoblast Interactions. J. Funct. Biomater. 2018, 9, 72, doi:10.3390/jfb9040072.

USC UNIVERSIDAD DE SANTIAGO

60. Sokol, E.S.; Miller, D.H.; Breggia, A.; Spencer, K.C.; Arendt, L.M.; Gupta, P.B. Growth of Human Breast Tissues from Patient Cells in 3D Hydrogel Scaffolds. Breast Cancer Res. 2016, 18, doi:10.1186/s13058-016-0677-5.
61. Hughes, C.S.; Postovit, L.M.; Lajoie, G.A. Matrigel: A Complex Protein Mixture Required for Optimal Growth of Cell Culture. PROTEOMICS 2010, 10, 1886–1890, doi:10.1002/pmic.200900758.
62. Caliari, S.R.; Burdick, J.A. A Practical Guide to Hydrogels for Cell Culture. Nat. Methods 2016, 13, 405–414, doi:10.1038/nmeth.3839.
63. O'Connor, S.M.; Stenger, D.A.; Shaffer, K.M.; Ma, W. Survival and Neurite Outgrowth of Rat Cortical Neurons in Three-Dimensional Agarose and Collagen Gel Matrices. Neurosci. Lett. 2001, 304, 189–193, doi:10.1016/S0304-3940(01)01769-4.
64. Ma, W.; Fitzgerald, W.; Liu, Q.-Y.; O'Shaughnessy, T.J.; Maric, D.; Lin, H.J.; Alkon, D.L.; Barker, J.L. CNS Stem and Progenitor Cell Differentiation into Functional Neuronal Circuits in Three-Dimensional Collagen Gels. Exp. Neurol. 2004, 190, 276–288, doi:10.1016/j.expneurol.2003.10.016.
65. Li, G.N.; Livi, L.L.; Gourd, C.M.; Deweerd, E.S.; Hoffman-Kim, D. Genomic and Morphological Changes of Neuroblastoma Cells in Response to Three-Dimensional Matrices. Tissue Eng. 2007, 13, 1035–1047, doi:10.1089/ten.2006.0251.
66. Martens, W.; Sanen, K.; Georgiou, M.; Struys, T.; Bronckaers, A.; Ameloot, M.; Phillips, J.; Lambrichts, I. Human Dental Pulp Stem Cells Can Differentiate into Schwann Cells and Promote and Guide Neurite Outgrowth in an Aligned Tissue-engineered Collagen Construct *in Vitro*. FASEB J. 2014, 28, 1634–1643, doi:10.1096/fj.13-243980.
67. Knapp, D.M.; Barocas, V.H.; Moon, A.G.; Yoo, K.; Petzold, L.R.; Tranquillo, R.T. Rheology of Reconstituted Type I Collagen Gel in Confined Compression. J. Rheol. 1997, 41, 971–993, doi:10.1122/1.550817.
68. Vernon, R.B.; Sage, E.H. Contraction of Fibrillar Type I Collagen by Endothelial Cells: A Study *in Vitro*. J. Cell. Biochem. 1996, 60, 185–197, doi:10.1002/(SICI)1097-4644(19960201)60:2<185::AID-JCB3>3.0.CO;2-T.
69. Coyac, B.R.; Chicatun, F.; Hoac, B.; Nelea, V.; Chaussain, C.; Nazhat, S.N.; McKee, M.D. Mineralization of Dense Collagen Hydrogel Scaffolds by Human Pulp Cells. J. Dent. Res. 2013, 92, 648–654, doi:10.1177/0022034513488599.
70. Mosesson, M.W.; Siebenlist, K.R.; Meh, D.A. The Structure and Biological Features of Fibrinogen and Fibrin. Ann. N. Y. Acad. Sci. 2006, 936, 11–30, doi:10.1111/j.1749-6632.2001.tb03491.x.
71. Rohringer, S.; Hofbauer, P.; Schneider, K.H.; Husa, A.-M.; Feichtinger, G.; Peterbauer-Scherb, A.; Redl, H.; Holnthoner, W. Mechanisms of Vasculogenesis in 3D Fibrin Matrices Mediated by the Interaction of Adipose-Derived Stem Cells and Endothelial Cells. Angiogenesis 2014, 17, 921–933, doi:10.1007/s10456-014-9439-0.
72. des Rieux, A.; Shikanov, A.; Shea, L.D. Fibrin Hydrogels for Non-Viral Vector Delivery *in Vitro*. J. Controlled Release 2009, 136, 148–154, doi:10.1016/j.jconrel.2009.02.004.
73. Yasuda, H.; Kuroda, S.; Shichinohe, H.; Kamei, S.; Kawamura, R.; Iwasaki, Y. Effect of Biodegradable Fibrin Scaffold on Survival, Migration, and Differentiation of Transplanted Bone Marrow Stromal Cells after Cortical Injury in Rats: Laboratory Investigation. J. Neurosurg. 2010, 112, 336–344, doi:10.3171/2009.2.JNS08495.
74. Niknamasl, A.; Ostad, S.N.; Soleimani, M.; Azami, M.; Salmani, M.K.; Lotfibakhshaiesh, N.; Ebrahimi-Barough, S.; Karimi, R.; Roozafzoon, R.; Ai, J. A New Approach for Pancreatic Tissue Engineering: Human Endometrial Stem Cells Encapsulated in Fibrin Gel Can Differentiate to Pancreatic Islet Beta-Cell: A New Approach for Pancreatic Tissue Engineering. Cell Biol. Int. 2014, 38, 1174–1182, doi:10.1002/cbin.10314.
75. Bayat, N.; Ebrahimi-Barough, S.; Ardakan, M.M.M.; Ai, A.; Kamyab, A.; Babaloo, N.; Ai, J. Differentiation of Human Endometrial Stem Cells into Schwann Cells in Fibrin Hydrogel as 3D Culture. Mol. Neurobiol. 2016, 53, 7170–7176, doi:10.1007/s12035-015-9574-7.
76. Bento, A.R.; Quelhas, P.; Oliveira, M.J.; Pêgo, A.P.; Amaral, I.F. Three-Dimensional Culture of Single Embryonic Stem-Derived Neural/Stem Progenitor Cells in Fibrin Hydrogels: Neuronal Network Formation and Matrix Remodelling: Three-Dimensional Culture of Single Embryonic Stem-Derived Neural/Stem Progenitor Cells. J. Tissue Eng. Regen. Med. 2017, 11, 3494–3507, doi:10.1002/term.2262.
77. Gerecht, S.; Burdick, J.A.; Ferreira, L.S.; Townsend, S.A.; Langer, R.; Vunjak-Novakovic, G. Hyaluronic Acid Hydrogel for Controlled Self-Renewal and Differentiation of Human Embryonic Stem Cells. Proc. Natl. Acad. Sci. 2007, 104, 11298–11303, doi:10.1073/pnas.0703723104.

USC DE SANTIAGO DE COMPOSTELA

78. Chen, P.-Y.; Huang, L.L.H.; Hsieh, H.-J. Hyaluronan Preserves the Proliferation and Differentiation Potentials of Long-Term Cultured Murine Adipose-Derived Stromal Cells. Biochem. Biophys. Res. Commun. 2007, 360, 1–6, doi:10.1016/j.bbrc.2007.04.211.
79. Pan, L.; Ren, Y.; Cui, F.; Xu, Q. Viability and Differentiation of Neural Precursors on Hyaluronic Acid Hydrogel Scaffold. J. Neurosci. Res. 2009, 87, 3207–3220, doi:10.1002/jnr.22142.
80. Lou, J.; Stowers, R.; Nam, S.; Xia, Y.; Chaudhuri, O. Stress Relaxing Hyaluronic Acid-Collagen Hydrogels Promote Cell Spreading, Fiber Remodeling, and Focal Adhesion Formation in 3D Cell Culture. Biomaterials 2018, 154, 213–222, doi:10.1016/j.biomaterials.2017.11.004.
81. Naahidi, S.; Jafari, M.; Logan, M.; Wang, Y.; Yuan, Y.; Bae, H.; Dixon, B.; Chen, P. Biocompatibility of Hydrogel-Based Scaffolds for Tissue Engineering Applications. Biotechnol. Adv. 2017, 35, 530–544, doi:10.1016/j.biotechadv.2017.05.006.
82. Nezhad-Mokhtari, P.; Ghorbani, M.; Roshangar, L.; Soleimani Rad, J. A Review on the Construction of Hydrogel Scaffolds by Various Chemically Techniques for Tissue Engineering. Eur. Polym. J. 2019, 117, 64–76, doi:10.1016/j.eurpolymj.2019.05.004.
83. García-González, C.A.; Budtova, T.; Durães, L.; Erkey, C.; Del Gaudio, P.; Gurikov, P.; Koebel, M.; Liebner, F.; Neagu, M.; Smirnova, I. An Opinion Paper on Aerogels for Biomedical and Environmental Applications. Molecules 2019, 24, 1815, doi:10.3390/molecules24091815.
84. Zheng, L.; Zhang, S.; Ying, Z.; Liu, J.; Zhou, Y.; Chen, F. Engineering of Aerogel-Based Biomaterials for Biomedical Applications. Int. J. Nanomedicine 2020, Volume 15, 2363–2378, doi:10.2147/IJN.S238005.
85. Jodati, H.; Yılmaz, B.; Evis, Z. A Review of Bioceramic Porous Scaffolds for Hard Tissue Applications: Effects of Structural Features. Ceram. Int. 2020, 46, 15725–15739, doi:10.1016/j.ceramint.2020.03.192.
86. Kim, H.; Han, S.H.; Kook, Y.-M.; Lee, K.-M.; Jin, Y.-Z.; Koh, W.-G.; Lee, J.H.; Lee, K. A Novel 3D Indirect Co-Culture System Based on a Collagen Hydrogel Scaffold for Enhancing the Osteogenesis of Stem Cells. J. Mater. Chem. B 2020, doi:10.1039/D0TB01770A.
87. Momose, T.; Miyaji, H.; Kato, A.; Ogawa, K.; Yoshida, T.; Nishida, E.; Murakami, S.; Kosen, Y.; Sugaya, T.; Kawanami, M. Collagen Hydrogel Scaffold and Fibroblast Growth Factor-2 Accelerate Periodontal Healing of Class II Furcation Defects in Dog. Open Dent. J. 2016, 10, 347–359, doi:10.2174/1874210601610010347.
88. Ferreira, A.M.; Gentile, P.; Chiono, V.; Ciardelli, G. Collagen for Bone Tissue Regeneration. Acta Biomater. 2012, 8, 3191–3200, doi:10.1016/j.actbio.2012.06.014.
89. Liu, Y.; Gu, J.; Fan, D. Fabrication of High-Strength and Porous Hybrid Scaffolds Based on Nano-Hydroxyapatite and Human-Like Collagen for Bone Tissue Regeneration. Polymers 2020, 12, 61, doi:10.3390/polym12010061.
90. Ji, Q.; Zhang, H.; Zhang, X.; Ma, Q.; Teng, L.; Qiu, L. Hydrosoluble Collagen Based Biodegradable Hybrid Hydrogel for Biomedical Scaffold. J. Biomater. Sci. Polym. Ed. 2020, 1–21, doi:10.1080/09205063.2020.1796229.
91. Liu, S.; Zhou, C.; Mou, S.; Li, J.; Zhou, M.; Zeng, Y.; Luo, C.; Sun, J.; Wang, Z.; Xu, W. Biocompatible Graphene Oxide–Collagen Composite Aerogel for Enhanced Stiffness and in Situ Bone Regeneration. Mater. Sci. Eng. C 2019, 105, 110137, doi:10.1016/j.msec.2019.110137.
92. Bellail, A.C.; Hunter, S.B.; Brat, D.J.; Tan, C.; Van Meir, E.G. Microregional Extracellular Matrix Heterogeneity in Brain Modulates Glioma Cell Invasion. Int. J. Biochem. Cell Biol. 2004, 36, 1046–1069, doi:10.1016/j.biocel.2004.01.013.
93. Prè, E.D.; Conti, G.; Sbarbati, A. Hyaluronic Acid (HA) Scaffolds and Multipotent Stromal Cells (MSCs) in Regenerative Medicine. Stem Cell Rev. Rep. 2016, 12, 664–681, doi:10.1007/s12015-016-9684-2.
94. Chung, C.; Burdick, J.A. Influence of Three-Dimensional Hyaluronic Acid Microenvironments on Mesenchymal Stem Cell Chondrogenesis. Tissue Eng. Part A 2009, 15, 243–254, doi:10.1089/ten.tea.2008.0067.
95. Yeh, H.-Y.; Lin, T.-Y.; Lin, C.-H.; Yen, B.L.; Tsai, C.-L.; Hsu, S. Neocartilage Formation from Mesenchymal Stem Cells Grown in Type II Collagen–Hyaluronan Composite Scaffolds. Differentiation 2013, 86, 171–183, doi:10.1016/j.diff.2013.11.001.
96. Snyder, T.N.; Madhavan, K.; Intrator, M.; Dregalla, R.C.; Park, D. A Fibrin/Hyaluronic Acid Hydrogel for the Delivery of Mesenchymal Stem Cells and Potential for Articular Cartilage Repair. J. Biol. Eng. 2014, 8, 10, doi:10.1186/1754-1611-8-10.
97. Erickson, I.E.; Kestle, S.R.; Zellars, K.H.; Farrell, M.J.; Kim, M.; Burdick, J.A.; Mauck, R.L. High Mesenchymal Stem Cell Seeding Densities in Hyaluronic Acid Hydrogels Produce Engineered Cartilage with Native Tissue Properties. Acta Biomater. 2012, 8, 3027–3034, doi:10.1016/j.actbio.2012.04.033.

USC DE SANTIAGO

98. Meng, F.; He, A.; Zhang, Z.; Zhang, Z.; Lin, Z.; Yang, Z.; Long, Y.; Wu, G.; Kang, Y.; Liao, W. Chondrogenic Differentiation of ATDC5 and hMSCs Could Be Induced by a Novel Scaffold-Tricalcium Phosphate-Collagen-Hyaluronan without Any Exogenous Growth Factors *in Vitro*: Chondrogenesis-Inducing Capacity of Tcp-Col-Ha Scaffold. J. Biomed. Mater. Res. A 2014, 102, 2725–2735, doi:10.1002/jbm.a.34948.
99. Kim, Y.-M.; Oh, S.H.; Choi, J.-S.; Lee, S.; Ra, J.C.; Lee, J.H.; Lim, J.-Y. Adipose-Derived Stem Cell-Containing Hyaluronic Acid/Alginate Hydrogel Improves Vocal Fold Wound Healing: AdMSC Hydrogel for Vocal Fold Wound Healing. The Laryngoscope 2014, 124, E64–E72, doi:10.1002/lary.24405.
100. Frith, J.E.; Menzies, D.J.; Cameron, A.R.; Ghosh, P.; Whitehead, D.L.; Gronthos, S.; Zannettino, A.C.W.; Cooper-White, J.J. Effects of Bound versus Soluble Pentosan Polysulphate in PEG/HA-Based Hydrogels Tailored for Intervertebral Disc Regeneration. Biomaterials 2014, 35, 1150–1162, doi:10.1016/j.biomaterials.2013.10.056.
101. Zou, L.; Zou, X.; Chen, L.; Li, H.; Mygind, T.; Kassem, M.; Bünger, C. Effect of Hyaluronan on Osteogenic Differentiation of Porcine Bone Marrow Stromal Cells *in Vitro*. J. Orthop. Res. 2008, 26, 713–720, doi:10.1002/jor.20539.
102. Zhu, M.; Lin, S.; Sun, Y.; Feng, Q.; Li, G.; Bian, L. Hydrogels Functionalized with N-Cadherin Mimetic Peptide Enhance Osteogenesis of hMSCs by Emulating the Osteogenic Niche. Biomaterials 2016, 77, 44–52, doi:10.1016/j.biomaterials.2015.10.072.
103. Zhang, T.; Yan, Y.; Wang, X.; Xiong, Z.; Lin, F.; Wu, R.; Zhang, R. Three-Dimensional Gelatin and Gelatin/Hyaluronan Hydrogel Structures for Traumatic Brain Injury. J. Bioact. Compat. Polym. 2007, 22, 19–29, doi:10.1177/0883911506074025.
104. Castiaux, A.D.; Spence, D.M.; Martin, R.S. Review of 3D Cell Culture with Analysis in Microfluidic Systems. Anal. Methods 2019, 11, 4220–4232, doi:10.1039/C9AY01328H.
105. Chang, C. Gelatin–Chondroitin–Hyaluronan Tri-Copolymer Scaffold for Cartilage Tissue Engineering. Biomaterials 2003, 24, 4853–4858, doi:10.1016/S0142-9612(03)00383-1.
106. Chang, C.-H.; Kuo, T.-F.; Lin, C.-C.; Chou, C.-H.; Chen, K.-H.; Lin, F.-H.; Liu, H.-C. Tissue Engineering-Based Cartilage Repair with Allogenous Chondrocytes and Gelatin–Chondroitin–Hyaluronan Tri-Copolymer Scaffold: A Porcine Model Assessed at 18, 24, and 36 Weeks. Biomaterials 2006, 27, 1876–1888, doi:10.1016/j.biomaterials.2005.10.014.
107. Yang, S.-H.; Chen, P.-Q.; Chen, Y.-F.; Lin, F.-H. An In-Vitro Study on Regeneration of Human Nucleus Pulposus by Using Gelatin/Chondroitin-6-Sulfate/Hyaluronan Tri-Copolymer Scaffold. Artif. Organs 2005, 29, 806–814, doi:10.1111/j.1525-1594.2005.00133.x.
108. Pértile, R.; Moreira, S.; Andrade, F.; Domingues, L.; Gama, M. Bacterial Cellulose Modified Using Recombinant Proteins to Improve Neuronal and Mesenchymal Cell Adhesion. Biotechnol. Prog. 2012, 28, 526–532, doi:10.1002/btpr.1501.
109. Taokaew, S.; Phisalaphong, M.; Newby, B.Z. Modification of Bacterial Cellulose with Organosilanes to Improve Attachment and Spreading of Human Fibroblasts. Cellulose 2015, 22, 2311–2324, doi:10.1007/s10570-015-0651-x.
110. Birkheur, S.; Faria-Tischer, P.C. de S.; Tischer, C.A.; Pimentel, E.F.; Fronza, M.; Endringer, D.C.; Butera, A.P.; Ribeiro-Viana, R.M. Enhancement of Fibroblast Growing on the Mannosylated Surface of Cellulose Membranes. Mater. Sci. Eng. C 2017, 77, 672–679, doi:10.1016/j.msec.2017.04.006.
111. Isobe, N.; Komamiya, T.; Kimura, S.; Kim, U.-J.; Wada, M. Cellulose Hydrogel with Tunable Shape and Mechanical Properties: From Rigid Cylinder to Soft Scaffold. Int. J. Biol. Macromol. 2018, 117, 625–631, doi:10.1016/j.ijbiomac.2018.05.071.
112. Andersson, J.; Stenhamre, H.; Bäckdahl, H.; Gatenholm, P. Behavior of Human Chondrocytes in Engineered Porous Bacterial Cellulose Scaffolds. J. Biomed. Mater. Res. A 2010, 9999A, NA-NA, doi:10.1002/jbm.a.32784.
113. Pircher, N.; Veigel, S.; Aigner, N.; Nedelec, J.M.; Rosenau, T.; Liebner, F. Reinforcement of Bacterial Cellulose Aerogels with Biocompatible Polymers. Carbohydr. Polym. 2014, 111, 505–513, doi:10.1016/j.carbpol.2014.04.029.
114. Pircher, N.; Fischhuber, D.; Carbajal, L.; Strauß, C.; Nedelec, J.-M.; Kasper, C.; Rosenau, T.; Liebner, F. Preparation and Reinforcement of Dual-Porous Biocompatible Cellulose Scaffolds for Tissue Engineering. Macromol. Mater. Eng. 2015, 300, 911–924, doi:10.1002/mame.201500048.
115. Osorio, D.A.; Lee, B.E.J.; Kwiecien, J.M.; Wang, X.; Shahid, I.; Hurley, A.L.; Cranston, E.D.; Grandfield, K. Cross-Linked Cellulose Nanocrystal Aerogels as Viable Bone Tissue Scaffolds. Acta Biomater. 2019, 87, 152–165, doi:10.1016/j.actbio.2019.01.049.
116. Van Nieuwenhove, I.; Salamon, A.; Peters, K.; Graulus, G.-J.; Martins, J.C.; Frankel, D.; Kersemans, K.; De Vos, F.; Van Vlierberghe, S.; Dubruel, P. Gelatin- and Starch-Based Hydrogels. Part A: Hydrogel

Development, Characterization and Coating. Carbohydr. Polym. 2016, 152, 129–139, doi:10.1016/j.carbpol.2016.06.098.
117. Mendes, S.C.; Reis, R.L.; Bovell, Y.P.; Cunha, A.M.; van Blitterswijk, C.A.; de Bruijn, J.D. Biocompatibility Testing of Novel Starch-Based Materials with Potential Application in Orthopaedic Surgery: A Preliminary Study. Biomaterials 2001, 22, 2057–2064, doi:10.1016/S0142-9612(00)00395-1.
118. Raafat, A.I.; Saad Eldin, A.A.; Salama, A.A.; Ali, N.S. Characterization and Bioactivity Evaluation of (Starch/N-Vinylpyrrolidone)-Hydroxyapatite Nanocomposite Hydrogels for Bone Tissue Regeneration. J. Appl. Polym. Sci. 2012, n/a-n/a, doi:10.1002/app.38113.
119. Nourmohammadi, J.; Shahriarpanah, S.; Asadzadehzanjani, N.; Khaleghpanah, S.; Heidari, S. Biomimetic Apatite Layer Formation on a Novel Citrate Starch Scaffold Suitable for Bone Tissue Engineering Applications: Bioactivity Evaluation of 3D Porous Starch Scaffold. Starch - Stärke 2016, 68, 1275–1281, doi:10.1002/star.201500216.
120. Santos-Rosales, V.; Ardao, I.; Alvarez-Lorenzo, C.; Ribeiro, N.; Oliveira, A.; García-González, C. Sterile and Dual-Porous Aerogels Scaffolds Obtained through a Multistep Supercritical CO_2-Based Approach. Molecules 2019, 24, 871, doi:10.3390/molecules24050871.
121. Goimil, L.; Braga, M.E.M.; Dias, A.M.A.; Gómez-Amoza, J.L.; Concheiro, A.; Alvarez-Lorenzo, C.; de Sousa, H.C.; García-González, C.A. Supercritical Processing of Starch Aerogels and Aerogel-Loaded Poly(ε-Caprolactone) Scaffolds for Sustained Release of Ketoprofen for Bone Regeneration. J. CO_2 Util. 2017, 18, 237–249, doi:10.1016/j.jcou.2017.01.028.
122. Kasoju, N.; Bora, U. Silk Fibroin in Tissue Engineering. Adv. Healthc. Mater. 2012, 1, 393–412, doi:10.1002/adhm.201200097.
123. Melke, J.; Midha, S.; Ghosh, S.; Ito, K.; Hofmann, S. Silk Fibroin as Biomaterial for Bone Tissue Engineering. Acta Biomater. 2016, 31, 1–16, doi:10.1016/j.actbio.2015.09.005.
124. Cheng, G.; Davoudi, Z.; Xing, X.; Yu, X.; Cheng, X.; Li, Z.; Deng, H.; Wang, Q. Advanced Silk Fibroin Biomaterials for Cartilage Regeneration. ACS Biomater. Sci. Eng. 2018, 4, 2704–2715, doi:10.1021/acsbiomaterials.8b00150.
125. Wang, X.; Kluge, J.A.; Leisk, G.G.; Kaplan, D.L. Sonication-Induced Gelation of Silk Fibroin for Cell Encapsulation. Biomaterials 2008, 29, 1054–1064, doi:10.1016/j.biomaterials.2007.11.003.
126. Calabrese, R.; Kaplan, D.L. Silk Ionomers for Encapsulation and Differentiation of Human MSCs. Biomaterials 2012, 33, 7375–7385, doi:10.1016/j.biomaterials.2012.06.043.
127. Li, Z.; Zhang, X.; Yuan, T.; Zhang, Y.; Luo, C.; Zhang, J.; Liu, Y.; Fan, W. Addition of Platelet-Rich Plasma to Silk Fibroin Hydrogel Bioprinting for Cartilage Regeneration. Tissue Eng. Part A 2020, 26, 886–895, doi:10.1089/ten.tea.2019.0304.
128. Hong, H.; Seo, Y.B.; Kim, D.Y.; Lee, J.S.; Lee, Y.J.; Lee, H.; Ajiteru, O.; Sultan, M.T.; Lee, O.J.; Kim, S.H.; et al. Digital Light Processing 3D Printed Silk Fibroin Hydrogel for Cartilage Tissue Engineering. Biomaterials 2020, 232, 119679, doi:10.1016/j.biomaterials.2019.119679.
129. Goimil, L.; Santos-Rosales, V.; Delgado, A.; Évora, C.; Reyes, R.; Lozano-Pérez, A.A.; Aznar-Cervantes, S.D.; Cenis, J.L.; Gómez-Amoza, J.L.; Concheiro, A.; et al. scCO_2-Foamed Silk Fibroin Aerogel/Poly(ε-Caprolactone) Scaffolds Containing Dexamethasone for Bone Regeneration. J. CO_2 Util. 2019, 31, 51–64, doi:10.1016/j.jcou.2019.02.016.
130. Rauma, M.; Boman, A.; Johanson, G. Predicting the Absorption of Chemical Vapours. Adv. Drug Deliv. Rev. 2013, 65, 306–314, doi:10.1016/j.addr.2012.03.012.
131. Dąbrowska, A.K.; Rotaru, G.-M.; Derler, S.; Spano, F.; Camenzind, M.; Annaheim, S.; Stämpfli, R.; Schmid, M.; Rossi, R.M. Materials Used to Simulate Physical Properties of Human Skin. Skin Res. Technol. 2016, 22, 3–14, doi:10.1111/srt.12235.
132. Baroli, B. Penetration of Nanoparticles and Nanomaterials in the Skin: Fiction or Reality? J. Pharm. Sci. 2010, 99, 21–50, doi:10.1002/jps.21817.
133. Harper, D.; Young, A.; McNaught, C.-E. The Physiology of Wound Healing. Wound Manag. 2014, 32, 445–450.
134. Reinke, J.M.; Sorg, H. Wound Repair and Regeneration. Eur. Surg. Res. 2012, 49, 35–43, doi:10.1159/000339613.
135. Morton, L.M.; Phillips, T.J. Wound Healing and Treating Wounds: Differential Diagnosis and Evaluation of Chronic Wounds. J. Am. Acad. Dermatol. 2016, 74, 589–605.
136. Werdin, F.; Tennenhaus, M.; Schaller, H.-E.; Rennekampff, H.-O. Evidence-Based Management Strategies for Treatment of Chronic Wounds. Eplasty 2009, 9, e19.
137. Ganapathy, N.; Venkataraman, S.S.; Daniel, R.; Aravind, R.J.; Kumarakrishnan, V.B. Molecular Biology of Wound Healing. J. Pharm. Bioallied Sci. 2012, 4, S334-337, doi:10.4103/0975-7406.100294.

138. Kasuya, A.; Tokura, Y. Attempts to Accelerate Wound Healing. J. Dermatol. Sci. 2014, 76, 169–172.
139. Dhivya, S.; Padma, V.V.; Santhini, E. Wound Dressings – a Review. BioMedicine 2015, 5, 22.
140. Francesko, A.; Petkova, P.; Tzanov, T. Hydrogel Dressings for Advanced Wound Management. Curr. Med. Chem. 2019, 25, 5782–5797, doi:10.2174/0929867324666170920161246.
141. Madaghiele, M.; Sannino, A.; Ambrosio, L.; Demitri, C. Polymeric Hydrogels for Burn Wound Care: Advanced Skin Wound Dressings and Regenerative Templates. Burns Trauma 2014, 2, 153, doi:10.4103/2321-3868.143616.
142. Chen, Y.; Zhang, Y.; Wang, F.; Meng, W.; Yang, X.; Li, P.; Jiang, J.; Tan, H.; Zheng, Y. Preparation of Porous Carboxymethyl Chitosan Grafted Poly (Acrylic Acid) Superabsorbent by Solvent Precipitation and Its Application as a Hemostatic Wound Dressing. Mater. Sci. Eng. C 2016, 63, 18–29, doi:10.1016/j.msec.2016.02.048.
143. Park, J.; Hwang, S.; Yoon, I.-S. Advanced Growth Factor Delivery Systems in Wound Management and Skin Regeneration. Molecules 2017, 22, 1259, doi:10.3390/molecules22081259.
144. Zhang, X.; Kang, X.; Ji, L.; Bai, J.; Liu, W.; Wang, Z. Stimulation of Wound Healing Using Bioinspired Hydrogels with Basic Fibroblast Growth Factor (bFGF). Int. J. Nanomedicine 2018, Volume 13, 3897–3906, doi:10.2147/IJN.S168998.
145. Grolman, J.M.; Singh, M.; Mooney, D.J.; Eriksson, E.; Nuutila, K. Antibiotic-Containing Agarose Hydrogel for Wound and Burn Care. J. Burn Care Res. 2019, 40, 900–906, doi:10.1093/jbcr/irz113.
146. Verma, J.; Kanoujia, J.; Parashar, P.; Tripathi, C.B.; Saraf, S.A. Wound Healing Applications of Sericin/Chitosan-Capped Silver Nanoparticles Incorporated Hydrogel. Drug Deliv. Transl. Res. 2017, 7, 77–88, doi:10.1007/s13346-016-0322-y.
147. Dimatteo, R.; Darling, N.J.; Segura, T. In Situ Forming Injectable Hydrogels for Drug Delivery and Wound Repair. Adv. Drug Deliv. Rev. 2018, 127, 167–184, doi:10.1016/j.addr.2018.03.007.
148. Ubeyitogullari, A.; Ciftci, O.N. Formation of Nanoporous Aerogels from Wheat Starch. Carbohydr. Polym. 2016, 147, 125–132, doi:10.1016/j.carbpol.2016.03.086.
149. Guo, X.; Xu, D.; Zhao, Y.; Gao, H.; Shi, X.; Cai, J.; Deng, H.; Chen, Y.; Du, Y. Electroassembly of Chitin Nanoparticles to Construct Freestanding Hydrogels and High Porous Aerogels for Wound Healing. ACS Appl. Mater. Interfaces 2019, 11, 34766–34776, doi:10.1021/acsami.9b13063.
150. García-González, C.A.; Alnaief, M.; Smirnova, I. Polysaccharide-Based Aerogels—Promising Biodegradable Carriers for Drug Delivery Systems. Carbohydr. Polym. 2011, 86, 1425–1438.
151. Duong, H.M.; Lim, Z.K.; Nguyen, T.X.; Gu, B.; Penefather, M.P.; Phan-Thien, N. Compressed Cotton Aerogels for Stopping Liquid Leakage. Colloids Surf. Physicochem. Eng. Asp. 2017.
152. De Cicco, F.; Russo, P.; Reverchon, E.; García-González, C.A.; Aquino, R.P.; Del Gaudio, P. Prilling and Supercritical Drying: A Successful Duo to Produce Core-Shell Polysaccharide Aerogel Beads for Wound Healing. Carbohydr. Polym. 2016, 147, 482–489.
153. Ganesan, K.; Dennstedt, A.; Barowski, A.; Ratke, L. Design of Aerogels, Cryogels and Xerogels of Cellulose with Hierarchical Porous Structures. Mater. Des. 2016, 92, 345–355, doi:10.1016/j.matdes.2015.12.041.
154. Mogoşanu, G.D.; Grumezescu, A.M. Natural and Synthetic Polymers for Wounds and Burns Dressing. Int. J. Pharm. 2014, 463, 127–136, doi:10.1016/j.ijpharm.2013.12.015.
155. Hu, W.; Wang, Z.; Xiao, Y.; Zhang, S.; Wang, J. Advances in Crosslinking Strategies of Biomedical Hydrogels. Biomater. Sci. 2019, 7, 843–855, doi:10.1039/C8BM01246F.
156. Lu, H.; Yuan, L.; Yu, X.; Wu, C.; He, D.; Deng, J. Recent Advances of On-Demand Dissolution of Hydrogel Dressings. Burns Trauma 2018, 6, 35–35, doi:10.1186/s41038-018-0138-8.
157. Page-McCaw, A.; Ewald, A.J.; Werb, Z. Matrix Metalloproteinases and the Regulation of Tissue Remodelling. Nat. Rev. Mol. Cell Biol. 2007, 8, 221–233, doi:10.1038/nrm2125.
158. Dharunya, G.; Duraipandy, N.; Lakra, R.; Korapatti, P.S.; Jayavel, R.; Kiran, M.S. Curcumin Cross-Linked Collagen Aerogels with Controlled Anti-Proteolytic and pro-Angiogenic Efficacy. Biomed. Mater. 2016, 11, 045011, doi:10.1088/1748-6041/11/4/045011.
159. Govindarajan, D.; Duraipandy, N.; Srivatsan, K.V.; Lakra, R.; Korapatti, P.S.; Jayavel, R.; Kiran, M.S. Fabrication of Hybrid Collagen Aerogels Reinforced with Wheat Grass Bioactives as Instructive Scaffolds for Collagen Turnover and Angiogenesis for Wound Healing Applications. ACS Appl. Mater. Interfaces 2017, 9, 16939–16950.
160. Guan, Y.; Sun, F.; Zhang, X.; Peng, Z.; jiang, B.; Liang, M.; Wang, Y. Silk Fibroin Hydrogel Promote Burn Wound Healing through Regulating TLN1 Expression and Affecting Cell Adhesion and Migration. J. Mater. Sci. Mater. Med. 2020, 31, 48, doi:10.1007/s10856-020-06384-8.

161. Li, Z.; Song, J.; Zhang, J.; Hao, K.; Liu, L.; Wu, B.; Zheng, X.; Xiao, B.; Tong, X.; Dai, F. Topical Application of Silk Fibroin-Based Hydrogel in Preventing Hypertrophic Scars. Colloids Surf. B Biointerfaces 2020, 186, 110735, doi:10.1016/j.colsurfb.2019.110735.
162. Wang, J.; Hao, S.; Luo, T.; Cheng, Z.; Li, W.; Gao, F.; Guo, T.; Gong, Y.; Wang, B. Feather Keratin Hydrogel for Wound Repair: Preparation, Healing Effect and Biocompatibility Evaluation. Colloids Surf. B Biointerfaces 2017, 149, 341–350, doi:10.1016/j.colsurfb.2016.10.038.
163. Kim, S.Y.; Park, B.J.; Lee, Y.; Park, N.J.; Park, K.M.; Hwang, Y.-S.; Park, K.D. Human Hair Keratin-Based Hydrogels as Dynamic Matrices for Facilitating Wound Healing. J. Ind. Eng. Chem. 2019, 73, 142–151, doi:10.1016/j.jiec.2019.01.017.
164. El-Naggar, M.E.; Othman, S.I.; Allam, A.A.; Morsy, O.M. Synthesis, Drying Process and Medical Application of Polysaccharide-Based Aerogels. Int. J. Biol. Macromol. 2020, 145, 1115–1128, doi:10.1016/j.ijbiomac.2019.10.037.
165. Wang, X.; Cheng, F.; Liu, J.; Smått, J.-H.; Gepperth, D.; Lastusaari, M.; Xu, C.; Hupa, L. Biocomposites of Copper-Containing Mesoporous Bioactive Glass and Nanofibrillated Cellulose: Biocompatibility and Angiogenic Promotion in Chronic Wound Healing Application. Acta Biomater. 2016, 46, 286–298, doi:10.1016/j.actbio.2016.09.021.
166. Fan, X.; Li, Y.; Li, X.; Wu, Y.; Tang, K.; Liu, J.; Zheng, X.; Wan, G. Injectable Antibacterial Cellulose Nanofiber/Chitosan Aerogel with Rapid Shape Recovery for Noncompressible Hemorrhage. Int. J. Biol. Macromol. 2020, 154, 1185–1193, doi:10.1016/j.ijbiomac.2019.10.273.
167. Kozen, B.G.; Kircher, S.J.; Henao, J.; Godinez, F.S.; Johnson, A.S. An Alternative Hemostatic Dressing: Comparison of CELOX, HemCon, and QuikClot. Acad. Emerg. Med. 2008, 15, 74–81, doi:10.1111/j.1553-2712.2007.00009.x.
168. Yilmaz Atay, H. Antibacterial Activity of Chitosan-Based Systems. In Functional Chitosan; Jana, S., Jana, S., Eds.; Springer Singapore: Singapore, 2019; pp. 457–489 ISBN 9789811502620.
169. Sogias, I.A.; Williams, A.C.; Khutoryanskiy, V.V. Why Is Chitosan Mucoadhesive? Biomacromolecules 2008, 9, 1837–1842, doi:10.1021/bm800276d.
170. Younes, I.; Sellimi, S.; Rinaudo, M.; Jellouli, K.; Nasri, M. Influence of Acetylation Degree and Molecular Weight of Homogeneous Chitosans on Antibacterial and Antifungal Activities. Int. J. Food Microbiol. 2014, 185, 57–63.
171. Hamedi, H.; Moradi, S.; Hudson, S.M.; Tonelli, A.E. Chitosan Based Hydrogels and Their Applications for Drug Delivery in Wound Dressings: A Review. Carbohydr. Polym. 2018, 199, 445–460, doi:10.1016/j.carbpol.2018.06.114.
172. López-Iglesias, C.; Barros, J.; Ardao, I.; Monteiro, F.J.; Alvarez-Lorenzo, C.; Gómez-Amoza, J.L.; García-González, C.A. Vancomycin-Loaded Chitosan Aerogel Particles for Chronic Wound Applications. Carbohydr. Polym. 2019, 204, 223–231, doi:10.1016/j.carbpol.2018.10.012.
173. Lovskaya, D.; Menshutina, N.; Mochalova, M.; Nosov, A.; Grebenyuk, A. Chitosan-Based Aerogel Particles as Highly Effective Local Hemostatic Agents. Production Process and *in Vivo* Evaluations. Polymers 2020, 12, 2055, doi:10.3390/polym12092055.
174. Koehler, J.; Brandl, F.P.; Goepferich, A.M. Hydrogel Wound Dressings for Bioactive Treatment of Acute and Chronic Wounds. Eur. Polym. J. 2018, 100, 1–11, doi:10.1016/j.eurpolymj.2017.12.046.
175. Blessing Aderibigbe; Buhle Buyana Alginate in Wound Dressings. Pharmaceutics 2018, 10, 42, doi:10.3390/pharmaceutics10020042.
176. Lee, W.-R.; Park, J.-H.; Kim, K.-H.; Kim, S.-J.; Park, D.-H.; Chae, M.-H.; Suh, S.-H.; Jeong, S.-W.; Park, K.-K. The Biological Effects of Topical Alginate Treatment in an Animal Model of Skin Wound Healing. Wound Repair Regen. Off. Publ. Wound Heal. Soc. Eur. Tissue Repair Soc. 2009, 17, 505–510, doi:10.1111/j.1524-475X.2009.00496.x.
177. Raman, S.P.; Keil, C.; Dieringer, P.; Hübner, C.; Bueno, A.; Gurikov, P.; Nissen, J.; Holtkamp, M.; Karst, U.; Haase, H.; et al. Alginate Aerogels Carrying Calcium, Zinc and Silver Cations for Wound Care: Fabrication and Metal Detection. J. Supercrit. Fluids 2019, 153, 104545, doi:10.1016/j.supflu.2019.104545.
178. Catanzano, O.; Docking, R.; Schofield, P.; Boateng, J. Advanced Multi-Targeted Composite Biomaterial Dressing for Pain and Infection Control in Chronic Leg Ulcers. Carbohydr. Polym. 2017, 172, 40–48, doi:10.1016/j.carbpol.2017.05.040.
179. Tadyszak, K.; Wychowaniec, J.; Litowczenko, J. Biomedical Applications of Graphene-Based Structures. Nanomaterials 2018, 8, 944, doi:10.3390/nano8110944.
180. Peppas, N.A.; Hilt, J.Z.; Khademhosseini, A.; Langer, R. Hydrogels in Biology and Medicine: From Molecular Principles to Bionanotechnology. Adv. Mater. 2006, 18, 1345–1360, doi:10.1002/adma.200501612.

181. Hasegawa, U.; Nomura, S.M.; Kaul, S.C.; Hirano, T.; Akiyoshi, K. Nanogel-Quantum Dot Hybrid Nanoparticles for Live Cell Imaging. Biochem. Biophys. Res. Commun. 2005, 331, 917–921, doi:10.1016/j.bbrc.2005.03.228.
182. Azhdarinia, A.; Yang, D.J.; Yu, D.-F.; Mendez, R.; Oh, C.; Kohanim, S.; Bryant, J.; Kim, E.E. Regional Radiochemotherapy Using In Situ Hydrogel. Pharm. Res. 2005, 22, 776–783, doi:10.1007/s11095-005-2594-7.
183. Qu, X.; Weinberger, J. Deposition of90YPO4 and144CePO4 Radioisotopes on Polymer Surfaces for Radiation Delivery Devices. J. Biomed. Mater. Res. 2002, 63, 98–105, doi:10.1002/jbm.10095.
184. Sontyana, A.G.; Mathew, A.P.; Cho, K.-H.; Uthaman, S.; Park, I.-K. Biopolymeric In Situ Hydrogels for Tissue Engineering and Bioimaging Applications. Tissue Eng. Regen. Med. 2018, 15, 575–590, doi:10.1007/s13770-018-0159-1.
185. Dong, X.; Wei, C.; Liu, T.; Lv, F. Protoporphyrin Incorporated Alginate Hydrogel: Preparation, Characterization and Fluorescence Imaging *in Vivo*. RSC Adv. 2015, 5, 96336–96344, doi:10.1039/C5RA19285D.
186. Zhang, Z.; Liu, G.; Li, X.; Zhang, S.; Lü, X.; Wang, Y. Design and Synthesis of Fluorescent Nanocelluloses for Sensing and Bioimaging Applications. ChemPlusChem 2020, 85, 487–502, doi:10.1002/cplu.201900746.
187. Yang, X.; Sun, Y.; Kootala, S.; Hilborn, J.; Heerschap, A.; Ossipov, D. Injectable Hyaluronic Acid Hydrogel for 19F Magnetic Resonance Imaging. Carbohydr. Polym. 2014, 110, 95–99, doi:10.1016/j.carbpol.2014.03.070.
188. Liu, J.; Wang, K.; Luan, J.; Wen, Z.; Wang, L.; Liu, Z.; Wu, G.; Zhuo, R. Visualization of in Situ Hydrogels by MRI *in Vivo*. J. Mater. Chem. B 2016, 4, 1343–1353, doi:10.1039/C5TB02459E.
189. Weissleder, R. Scaling down Imaging: Molecular Mapping of Cancer in Mice. Nat. Rev. Cancer 2002, 2, 11–18, doi:10.1038/nrc701.
190. Lei, K.; Ma, Q.; Yu, L.; Ding, J. Functional Biomedical Hydrogels for *in Vivo* Imaging. J. Mater. Chem. B 2016, 4, 7793–7812, doi:10.1039/C6TB02019D.
191. Sivashanmugam, A.; Charoenlarp, P.; Deepthi, S.; Rajendran, A.; Nair, S.V.; Iseki, S.; Jayakumar, R. Injectable Shear-Thinning $CaSO_4$ /FGF-18-Incorporated Chitin–PLGA Hydrogel Enhances Bone Regeneration in Mice Cranial Bone Defect Model. ACS Appl. Mater. Interfaces 2017, 9, 42639–42652, doi:10.1021/acsami.7b15845.
192. Liu, S.; Zhou, C.; Mou, S.; Li, J.; Zhou, M.; Zeng, Y.; Luo, C.; Sun, J.; Wang, Z.; Xu, W. Biocompatible Graphene Oxide–Collagen Composite Aerogel for Enhanced Stiffness and in Situ Bone Regeneration. Mater. Sci. Eng. C 2019, 105, 110137, doi:10.1016/j.msec.2019.110137.
193. Pu, K. Biosensors and Bioimaging. ChemBioChem 2019, 20, 420–421, doi:10.1002/cbic.201900021.
194. Zuber, A.A.; Klantsataya, E.; Bachhuka, A. Biosensing. In Comprehensive Nanoscience and Nanotechnology; Elsevier, 2019; pp. 105–126 ISBN 978-0-12-812296-9.
195. Bhalla, N.; Jolly, P.; Formisano, N.; Estrela, P. Introduction to Biosensors. Essays Biochem. 2016, 60, 1–8, doi:10.1042/EBC20150001.
196. Battista, E.; Causa, F.; Netti, P. Bioengineering Microgels and Hydrogel Microparticles for Sensing Biomolecular Targets. Gels 2017, 3, 20, doi:10.3390/gels3020020.
197. Culver, H.R.; Clegg, J.R.; Peppas, N.A. Analyte-Responsive Hydrogels: Intelligent Materials for Biosensing and Drug Delivery. Acc. Chem. Res. 2017, 50, 170–178, doi:10.1021/acs.accounts.6b00533.
198. Peppas, N.A.; Van Blarcom, D.S. Hydrogel-Based Biosensors and Sensing Devices for Drug Delivery. J. Controlled Release 2016, 240, 142–150, doi:10.1016/j.jconrel.2015.11.022.
199. Vigués, N.; Pujol-Vila, F.; Marquez-Maqueda, A.; Muñoz-Berbel, X.; Mas, J. Electro-Addressable Conductive Alginate Hydrogel for Bacterial Trapping and General Toxicity Determination. Anal. Chim. Acta 2018, 1036, 115–120, doi:10.1016/j.aca.2018.06.062.
200. Sadat Ebrahimi, M.M.; Schönherr, H. Enzyme-Sensing Chitosan Hydrogels. Langmuir 2014, 30, 7842–7850, doi:10.1021/la501482u.
201. Hasanah, U.; Sani, N.D.M.; Heng, L.Y.; Idroes, R.; Safitri, E. Construction of a Hydrogel Pectin-Based Triglyceride Optical Biosensor with Immobilized Lipase Enzymes. Biosensors 2019, 9, 135, doi:10.3390/bios9040135.
202. Edwards, J.; Fontenot, K.; Prevost, N.; Pircher, N.; Liebner, F.; Condon, B. Preparation, Characterization and Activity of a Peptide-Cellulosic Aerogel Protease Sensor from Cotton. Sensors 2016, 16, 1789, doi:10.3390/s16111789.
203. Maleki, H.; Shahbazi, M.-A.; Montes, S.; Hosseini, S.H.; Eskandari, M.R.; Zaunschirm, S.; Verwanger, T.; Mathur, S.; Milow, B.; Krammer, B.; et al. Mechanically Strong Silica-Silk Fibroin Bioaerogel: A Hybrid

Scaffold with Ordered Honeycomb Micromorphology and Multiscale Porosity for Bone Regeneration. ACS Appl. Mater. Interfaces 2019, 11, 17256–17269, doi:10.1021/acsami.9b04283.
204. Ghafari, R.; Jonoobi, M.; Amirabad, L.M.; Oksman, K.; Taheri, A.R. Fabrication and Characterization of Novel Bilayer Scaffold from Nanocellulose Based Aerogel for Skin Tissue Engineering Applications. Int. J. Biol. Macromol. 2019, 136, 796–803, doi:10.1016/j.ijbiomac.2019.06.104.
205. Alvarado-Hidalgo, F.; Ramírez-Sánchez, K.; Starbird-Perez, R. Smart Porous Multi-Stimulus Polysaccharide-Based Biomaterials for Tissue Engineering. Molecules 2020, 25, 5286, doi:10.3390/molecules25225286.
206. García-González, C.A.; Sosnik, A.; Kalmár, J.; De Marco, I.; Erkey, C.; Concheiro, A.; Alvarez-Lorenzo, C. Aerogels in Drug Delivery: From Design to Application. J. Controlled Release 2021, 332, 40–63, doi:10.1016/j.jconrel.2021.02.012.
207. Manzocco, L.; Mikkonen, K.S.; García-González, C.A. Aerogels as Porous Structures for Food Applications: Smart Ingredients and Novel Packaging Materials. Food Struct. 2021, 100188, doi:10.1016/j.foostr.2021.100188.

USC UNIVERSIDADE DE SANTIAGO DE COMPOSTELA

USC
UNIVERSIDADE
DE SANTIAGO
DE COMPOSTELA

CHAPTER 2. OBJECTIVES AND ORGANIZATION

The therapeutical applications of aerogels as part of medical devices or drug delivery systems are highlighted in the Introduction of this PhD Thesis. Specifically, natural polymer-based aerogels have excellent biological and textural properties, with mesopores integrated in their open structure. Macropores in the 100-300 μm size range are essential in the design of scaffolds for regenerative medicine to promote an effective bone regeneration. However, aerogels usually lack macropores in their structure thereby limiting their application in this field. Porogenic agents can be used to induce macroporosity, but must then be eliminated from the final structure, so the manufacturing process complexity increases and its yield decreases. According to this, the **main objective of this PhD Thesis** was to develop a strategy to fabricate drug-loaded, dual porous and sterile aerogels, with mesopores and macropores in the same structure, able to mimic the bone natural ECM in the long-term while being *in vivo* traceable.

This PhD Thesis was organized in three sections. The first section (Chapters 3 and 4) describes the production, characterization, and evaluation of sterile alginate aerogels obtained through a dual processing strategy, combining 3D-printing and SCF technologies. The population of macropores, obtained through the 3D-printing of aerogels, was essential for their application as scaffolds for bone tissue engineering. The specific objectives linked to this section were ● *to assess the feasibility of the technological combination proposed*, and ● *to check the operating window of the 3D-printing method and of the SCF process to manufacture sterile personalized aerogel scaffolds*.

In **Chapter 3**, the dual processing strategy to fabricate 3D-printed alginate aerogel scaffolds was herein reported for the first time. The conditions to perform the 3D-printing and the $scCO_2$ drying were defined and different ink formulations were explored by the proposed methodology. Different concentrations of HA were also incorporated to the most promising formulations of the previously employed alginate-based inks. 3D-printed aerogels were evaluated regarding textural

USC UNIVERSIDADE DE SANTIAGO DE COMPOSTELA

properties, printing fidelity with respect to the computer-aided design and volume shrinkage after the $scCO_2$ drying to assess their suitability and potential as personalized-to-patient structures. The biocompatibility of aerogel scaffolds was evaluated by cell viability and migration tests on murine fibroblasts, and by adhesion assays on human MSCs.

In **Chapter 4**, the 3D-printed alginate aerogel scaffolds were post-crosslinked with GA to obtain scaffolds with further structural integrity while preserving their advanced textural performance in terms of the dual porous structure. The physicochemical performance of the dual crosslinked and 3D-printed aerogels was studied and compared to the previously reported formulations. The cell toxicity and hemocompatibility of the GA-crosslinked 3D-printed aerogels were also tested by compatibility tests on murine fibroblasts and human blood, respectively. The bioactivity of the HA-loaded aerogels was tested *in vitro* by long-term SBF immersion and the subsequent analysis of the apatite depositions. Sterility at a medical grade level was also achieved by a rapid, simple, and green post-processing step performed also using SCF technology. The operating window employed to fulfill the requirement of sterility for medical devices was assessed by confirming the absence of microbial growth and of physicochemical modifications of aerogels.

The second section of this PhD Thesis (Chapters 5 and 6) includes the development and characterization of highly fluorescent and stable UCNPs as well as their effective loading into the 3D-printed aerogels previously designed to act as advanced theranostic devices with monitoring capabilities. For the first time, UCNPs decorated aerogels were manufactured by the dual processing strategy and were evaluated by *in vivo* safety and bioimaging studies. This section was carried out in collaboration with the Department of Chemical Engineering from the University of Coimbra in the frame of a 4-week research stay. The specific objectives of this section were ● *the definition of the synthetic procedure to obtain fluorescent and stable core-shell UCNPs*, ● *the loading of the resulting UCNPs into the 3D-printed aerogels with a high*

USC UNIVERSIDADE DE SANTIAGO DE COMPOSTELA

entrapment yield, and ● the in vivo validation of the suitability of these structures for in vivo bioimaging.

In **Chapter 5**, the synthesis of UCNPs was developed by a novel synthetic approach combining the co-precipitation of a lanthanide core with the formation of a silica shell via a sol-gel method. The experimental conditions suitable for the synthesis of shape- and phase-controlled UCNPs were defined. Oxide and nitrates of the lanthanides were evaluated as precursors of the UCNPs in terms of fluorescent intensity, physicochemical characteristics and simplicity of the synthetic procedure involved. The cell compatibility of UCNPs was tested with murine fibroblasts and the hemocompatibility of different UCNPs concentrations was studied in human blood. The best formulation of UCNPs regarding their fluorescent, biocompatibility and stability was selected for their loading into aerogels in Chapter 6.

In **Chapter 6**, the UCNPs synthesized in Chapter 5 were incorporated into the 3D-printed alginate aerogels manufactured according to the procedure set in Chapter 3. The morphological properties of the fluorescent scaffolds were compared with the performance previously unveiled for 3D-printed aerogels. Bio- and hemocompatibility were tested by cell compatibility, adhesion, and migration studies. The long-term stability of 3D-printed UCNPs-labeled aerogels were assessed in terms of physicochemical performance. *In vivo* safety tests were performed by subcutaneous implantation of 3D-printed scaffolds to assess the organ toxicity by plasmatic cytokines measurement and by histological evaluation. Furthermore, a bioimaging *in vivo* test was carried out to check the functionality of UCNPs-decorated aerogels by fluorescence evaluation at different timepoints. This chapter was carried out in collaboration with the Research Institute for Medicines (iMed) and with the Faculty of Pharmacy from the University of Lisbon, in the frame of a 3-month international stay.

The third section of this PhD Thesis (Chapters 7 and 8) incorporates bioactive agents into the sterile porous structure of methylcellulose aerogels and aims to induce long-term structural

USC UNIVERSIDADE DE SANTIAGO

integrity and stability of the 3D-printed aerogels while preserving their physicochemical and biological properties. This section was carried out in collaboration with iMed and with the Faculty of Pharmacy from the University of Lisbon, in the frame of the previously mentioned 3-month international stay. The specific objectives of this section were ● *the demonstration of the versatility of the dual processing strategy developed in Chapter 3 in terms of different biopolymers and drug loading capabilities*, and ● the *manufacturing of dual porous and sterile 3D-printed aerogels with an improved integrity and stability*.

In **Chapter 7**, 3D-printed VAN-loaded methylcellulose aerogels were manufactured by 3D-printing and $scCO_2$ drying and post-sterilized also with SCF technology. The physicochemical performance of the sterile 3D-printed aerogels was studied to check if the composition (biopolymer source, or the presence of the drug) modifies the dual porosity of the scaffolds. The release kinetics of the drug incorporated into the aerogels was determined, as well as the drug loading and entrapment yield. Antimicrobial tests were also performed by contact of the VAN-loaded aerogels with *S. aureus*. The biological performance of the aerogels was tested *in vitro* by cytocompatibility tests on murine fibroblasts and by mineralization tests on murine pre-osteoblasts. Hemocompatibility was evaluated *in vitro* by hemolytic activity tests, and *in ovo* by HET-CAM. Preliminary *in vivo* safety was also assessed by using an *A. salina* model.

In **Chapter 8**, sterile cellulose-in-cellulose 3D-printed aerogels were manufactured by the dual processing strategy. BC-NF were incorporated into methylcellulose aerogels and the printing fidelity, volume shrinkage and textural performance were measured and compared with the results obtained in Chapter 7. BC-NF were doped with SPIONs to localize the nanocellulose in the 3D-printed aerogel structure and to endow them with magnetic properties. The biological performance of cellulose-in-cellulose aerogels was unveiled *in vitro* by cytocompatibility tests on murine fibroblasts, and hemocompatibility tests in human blood, and *in ovo* by HET-CAM.

USC UNIVERSIDADE DE SANTIAGO DE COMPOSTELA

Preliminary safety was assessed *in vivo* by *A. salina* viability. This chapter was carried out in collaboration with the Institute of Materials Science of Barcelona (ICMAB-CSIC).

Finally, this PhD Thesis is well aligned with the Sustainable Development Goals (SDG) of the United Nations (Fig. 2.1), adopted by all Member States in 2015 as an urgent call for action in a global partnership. These global goals are part of the 2030 Agenda to promote the sustainable development for people and the planet, now and in the future. The aerogels herein obtained would be employed as adapted-to-patient implantable devices for bone repair, so they are in line with the SDG3 entitled "***Good health and well-being***", and also with the SDG17 "***Partnerships for the goals***" as are achieved in the frame of national (Barcelona) and international (Portugal, Costa Rica) collaborations. This PhD Thesis also contributes to SDG 12 "***Responsible consumption and production***" as 3D-printing is a technique that employs a minimal use of resources, thus taking advantage of all the materials employed and producing almost no waste. SCF is well-known as a green and clean technology that valorizes a residue (CO_2) by its use as drying and sterilizing agent. All these characteristics highlight the value of the dual processing strategy fully developed in this PhD Thesis, expanding its uses and applications, and broadening its impact. SDG9 "***Industry, innovation and infrastructure***" is also well integrated in this PhD Thesis with innovations of industrial interest in the production of bone implants with dual porosity, bioactivity and cell adhesion and migration capabilities, and in the manufacturing of a novel nanosystem to be incorporated into the 3D-printed aerogels to turn them into *in vivo* monitorable devices.

USC UNIVERSIDADE DE SANTIAGO DE COMPOSTELA

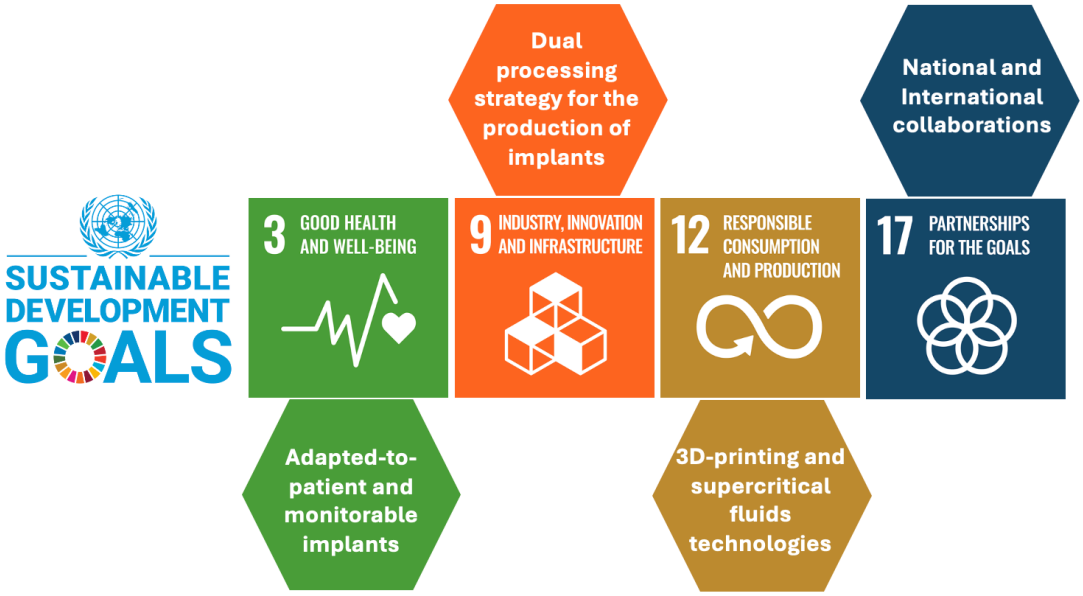
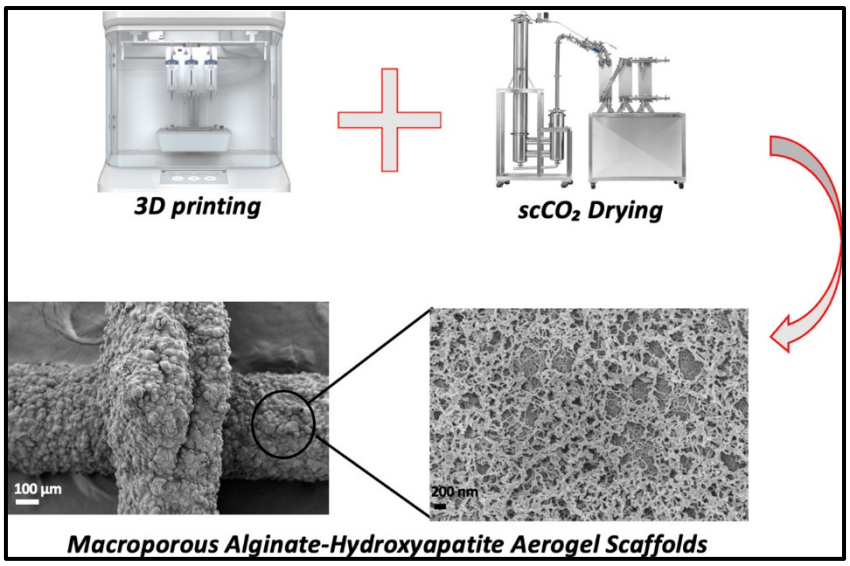


Figure 2.1. SDG involved in this PhD Thesis.

USC UNIVERSIDADE DE SANTIAGO DE COMPOSTELA

CHAPTER 3. 3D-PRINTED ALGINATE-HYDROXYAPATITE AEROGEL SCAFFOLDS FOR BONE TISSUE ENGINEERING



The content in this chapter was published in part in **A. Iglesias-Mejuto**, C.A. García-González; 3D-printed alginate-hydroxyapatite aerogel scaffolds for bone tissue engineering, in: Materials Science and Engineering: C 131 (2021) 112525. https://doi.org/10.1016/j.msec.2021.112525.

USC UNIVERSIDADE DE SANTIAGO DE COMPOSTELA

3.1. Introduction

Bone defects resulting from tumors, infections, trauma, biochemical disorders and abnormal skeletal developments generate severe health problems and represent high sociosanitary costs for the national health services [1–3]. Biological grafts (autografts, allografts) and non-degradable grafts (metallic and ceramic implants) are the most common solutions for these pathologies. However, their low availability (for biological grafts) and frequent post-surgical complications such as the lack of osseointegration or the generation of immune response (for non-degradable grafts) are among the important drawbacks that may occur [4,5]. Regenerative medicine aims to anatomically and functionally restore damaged tissues using a combination of (i) advanced biodegradable 3D-scaffolds as temporary ECM, (ii) cells, and (iii) growth factors [4,6,7]. The processing method used to obtain these bone scaffolds should provide an optimum design to promote the new tissue formation. These bone scaffolds should have a well-defined internal structure, dual interconnected porosity, and bioactivity. Given the increasing complexity in morphology and composition of these structures and the high sensitivity to processing environments (e.g., high temperature, shear stress, pH, use of organic solvents), innovative and benign strategies are sought to generate these new biomedical products [8].

3D-printing is a cutting-edge technology that allows the automated and reproducible fabrication of functional, scalable and customized artificial structures for personalized medicine [9]. In general, this technology uses a layer-by-layer deposition of biocompatible materials to achieve stable 3D-constructs. Specifically, extrusion-based bioprinting is an additive manufacturing technique commonly used to create hydrogel scaffolds [10,11]. It is a pressure-based method that employs a robotic system linked to a bioink dispensing syringe. A computer-aided design (CAD) is used to deposit the bioink in a 3D-predefined shaped structure. This technique is able to print different tissues with the generation of macroporous structures [12]. A limited (but growing) number of biomaterials are suitable for bioink formulations to generate 3D-printed scaffolds as they must be printable, biocompatible and present attractive structural and

USC UNIVERSIDADE DE SANTIAGO DE COMPOSTELA

mechanical properties [13]. Nevertheless, structures obtained by 3D-printing have the customized external morphology essential for personalized medicine, but they usually lack the high precision required to generate nanostructured scaffolds, with a control in the macro and microstructural levels. For this reason, the combination of 3D-printing with other techniques is needed to yield customized nanostructured biomaterials.

Polymeric nanostructures with advanced properties can be obtained using SCF technology based on the use $scCO_2$ [14]. Namely, $scCO_2$ drying is adequate for the extraction of the solvent of a gel while preserving the internal gel structural properties, such as high porosity and high specific surface areas, in the so-called aerogels. This technology can be used to obtain aerogel-containing grafts and implants [15], among them aerogel bone scaffolds for tissue engineering applications [16–18]. Aerogels present a high mesoporosity comparable to that of the native ECM, which favor cell growth, and can be obtained from polysaccharides and proteins [19].

Alginate is a natural biopolymer widely used for bone scaffolds and for bioink formulation because it is biocompatible, biodegradable, non-toxic and non-immunogenic, and supports cell growth [20]. Alginate generates a stable hydrogel in the presence of low concentrations of divalent cations, namely Ca^{2+} which presents the advantage of its low toxicity with respect to other divalent ions. Finally, alginate composition resembles glycosaminoglycan (GAG) structure, one of the major components of the natural ECM in human tissue. However, alginate-based structures usually lack bioactivity and should be combined with other admixtures for bone tissue engineering purposes [21].

HA is the major inorganic component in mammalian hard tissues and also an excellent bone substitute material because it is bioactive, osteoconductive, non-toxic and highly biocompatible due to its chemical and structural similarity to natural bone minerals [22,23]. This chemical similarity is essential for apatite deposition and subsequent bone regeneration. HA may also have a role as an inorganic mechanical reinforcer [24]. Moreover, HA and its composites are suitable for attachment, proliferation, and differentiation of MSCs. All these properties render

USC UNIVERSIDADE DE SANTIAGO

HA favorable for osteointegration [25–27]. The source and size of HA particles is an important factor on alginate-HA gel scaffolds because the HA grain size and specific surface area affect the gelling time and rheological properties of the hydrogels. HA has been proposed for applications requiring rapid gelation kinetics and improved mechanical properties, while nHA is appropriate to render homogeneous hydrogels under more controlled gelation kinetics [24]. Overall, alginate-HA composites are promising candidates for bone tissue engineering where HA also triggers the mineralization process and stimulates calcium phosphate and HA nanocrystals nucleation and growth [23,25].

Strategies for the generation of a complex 3D-shaped structures with different functionalities and architectures ranging from the nanoscale to the macroscale are under development to generate structures with this pore hierarchy [28]. The design and optimization of the final pore structure (pore size hierarchy and proportions) is also essential for the material performance in tissue engineering applications. The use of aerogel technology can solve some of the current 3D-printing limitations regarding the nanostructuration of 3D-scaffolds, but the production of aerogels with a customized external morphology is a remaining remarkable challenge [29]. Recently, several 3D-printed aerogels have shown an excellent printability in the wet state and the preservation of their textural properties like a high specific surface area [29–31]. Nevertheless, aerogels usually lack macroporosity and methods to confer it and to control the macropore size are under development (Salerno and Domingo, 2014, García-González et al., 2015, Martins et al., 2015, Santos-Rosales et al., 2020). In general, aerogels with various pore size ranges are highly desirable for applications like bone tissue engineering [33].

The unexplored combination of 3D-printing and aerogel technologies for bone tissue engineering is herein proposed as a win-win strategy to obtain biomaterials with improved performance and architecture. Finally, new strategies to improve the aerogels strengthening and the printing process necessary to obtain more fine and intricate structures are still a challenge nowadays. In this work, 3D-printed alginate aerogel scaffolds containing HA were

USC UNIVERSIDADE DE SANTIAGO

processed by a combination of 3D-printing of hydrogels and $scCO_2$ drying for bone regeneration purposes. The effects of alginate, HA and Ca^{2+} concentrations on the 3D-printed hydrogel scaffolds processability were assessed. Then, the 3D-printed aerogels obtained after $scCO_2$ drying were evaluated regarding their textural (specific surface area, porosity, density, shrinkage) and biological (cytocompatibility, adhesion, migration) properties. The fidelity of the different aerogel formulations with respect to the original CAD file was also evaluated.

3.2. Materials and Methods

3.2.1. Materials

Alginic acid sodium salt from brown algae with medium viscosity (guluronic acid/mannuronic acid ratio of 70/30, Mw 403 kDa, 3170 cps) and $CaCl_2$ (M_w 110.98 g/mol, 99.99% purity) were provided by Sigma Aldrich (Madrid, Spain). HA (M_w 502.31 g/mol, reagent grade purity, micropowder) was provided by Fluidinova (Moreira da Maia, Portugal). CO_2 (purity > 99.9%) was supplied by Nippon Gases (Madrid, Spain) and absolute ethanol (EtOH) by VWR (Radnor, PA, USA). Water was purified using reverse osmosis (resistivity > 18 MΩ·cm; Milli-Q, Millipore®, Madrid, Spain).

3.2.2. 3D-printing of hydrogels

Aqueous inks with three different alginate concentrations (6, 8 and 10 wt.% with respect to water) were prepared using milliQ water as a solvent. Furthermore, different HA concentrations (0, 8, 16 and 24 wt.% with respect to water) were added to the 6 wt.% alginate solutions. All alginate solutions were prepared under vigorous agitation (600 rpm) employing a homogenizer (VWR vos 60, Pennsylvania, USA) for at least 1 h at room temperature (RT). The thus obtained alginate solutions were degassed in a sonication bath (Branson 3510 Emerson, Ferguson, MO, USA) for 10 min to eliminate air bubbles. Hydrogels were obtained by printing the alginate inks with a Cellink BIOX Bioprinter (Boston, MA, USA) at RT using an extrusion printhead with a 3-mL syringe and a 410-µm nozzle at the printing pressure of 60 kPa and a printing velocity of 12

USC UNIVERSIDADE DE SANTIAGO

mm/s. 3D-printed alginate hydrogels with dimensions of 2 x 2 x 0.1 cm^3 were obtained using a grid pattern and 3 layers. After the printing process, all scaffolds were put directly in contact with $CaCl_2$ aqueous solutions (0.1, 0.5 and 1M) for gelation (Fig. 3.1).

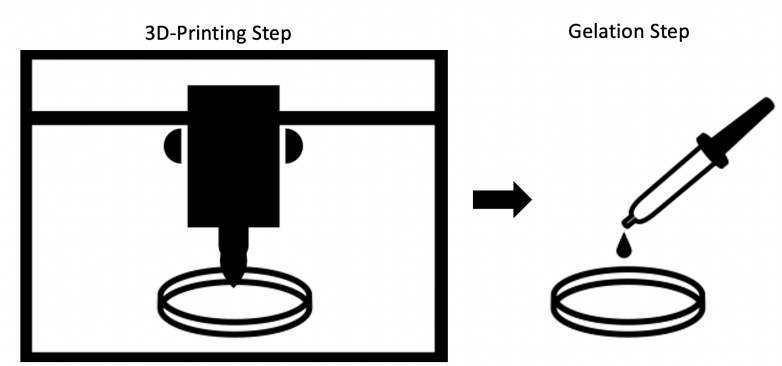


Figure 3.1. Experimental setup for the preparation of the 3D-printed hydrogel precursor of the aerogel-based scaffolds: The hydrogels were first obtained by 3D-printing of aqueous inks consisting on alginate (6-10 wt.%) and HA (0-24 wt.%) (left), and then the ionic gelation was performed by the addition of $CaCl_2$ (0.1 – 1M) (right).

3.2.3. $scCO_2$ drying of 3D-printed alcogels

Alginate hydrogels turn alcogels by immersion in EtOH. Two solvent exchanges to EtOH were carried out with an exchange frequency of 24 h. The alcogels were wrapped in filter paper and dried by $scCO_2$ drying to obtain the aerogels. Briefly, gels were placed into a 100-mL stainless steel autoclave (Thar Process, Pittsburg, PA, USA) and immersed in 25 mL of EtOH to prevent them from shrinkage before being in contact with compressed CO_2. $scCO_2$ was supplied using a dual piston pump and introduced from the top of a vessel heated at the constant temperature of 40 °C. Firstly, a continuous CO_2 flow rate (5-7 g/min) at 120 bar took place for 4 h. Aerogels were then obtained after CO_2 depressurization at a rate of 2 bar/min, collected from the autoclave and stored for characterization. The obtained scaffolds were described in Table 3.1 and denoted as Alg *x*, HA *y*, $CaCl_2$ z (*x*= 6, 8, 10 wt.%; *y*= 8, 16, 24 wt.%; *z*= 0.1, 0.5, 1 M).

USC UNIVERSIDADE DE SANTIAGO DE COMPOSTELA

Table 3.1. 3D-printed aerogel formulations studied.

Aerogel Formulations	Ink Composition		$CaCl_2$ (M)
	Alginate (wt.%)	HA (wt.%)	
Alg 6, HA 0, $CaCl_2$ 0.1M	6	0	0.1
Alg 6, HA 0, $CaCl_2$ 0.5M	6	0	0.5
Alg 6, HA 0, $CaCl_2$ 1M	6	0	1
Alg 8, HA 0, $CaCl_2$ 0.1M	8	0	0.1
Alg 8, HA 0, $CaCl_2$ 0.5M	8	0	0.5
Alg 8, HA 0, $CaCl_2$ 1M	8	0	1
Alg 10, HA 0, $CaCl_2$ 0.1M	10	0	0.1
Alg 10, HA 0, $CaCl_2$ 0.5M	10	0	0.5
Alg 10, HA 0, $CaCl_2$ 1M	10	0	1
Alg 6, HA 0, $CaCl_2$ 1M	6	0	1
Alg 6, HA 8, $CaCl_2$ 1M	6	8	1
Alg 6, HA 16, $CaCl_2$ 1M	6	16	1
Alg 6, HA 24, $CaCl_2$1M	6	24	1

3.2.4. Physicochemical characterization of 3D-printed alginate aerogels

The skeletal density of the aerogels (ρ_{skel}) was determined using a helium pycnometer (Quantachrome, Boynton Beach, FL, USA) at 25 °C and 1.01 bar. Values were obtained from five replicates. The apparent density of the aerogel scaffolds formulations (ρ_{app}) was determined following the Equation 3.1:

$$\rho_{app} = \frac{Aerogel\ mass}{Aerogel\ volume} \qquad \textit{Equation 3.1}$$

where the volume of the aerogels was obtained by measuring the three dimensions of the aerogel obtained with a digital caliper (Fowler™, Newton, MA, USA). The porosity of the structures (ε) was obtained from Equation 3.2 from the specific volume considering the external dimensions of the material (V_t) and the specific volume occupied by the voids in the full volume (V_{void}).

$$\varepsilon\ (\%) = \left[1 - \left(\frac{\rho app}{\rho skel}\right)\right] \cdot 100 = \left(\frac{Vvoid}{Vt}\right) \cdot 100 \qquad \textit{Equation 3.2}$$

The inner porosity of the aerogel fibers (ε_f) was obtained from Equation 3.3 from the specific volume occupied by the fibers (V_{fibers}) and the specific volume occupied by the voids (i.e. pores) in the fibers ($V_{void\ fibers}$) (Equation 3.4).

USC UNIVERSIDADE

$$\varepsilon_f\,(\%) = \left(\frac{Vvoid\ fibers}{Vfibers}\right) \cdot 100 \qquad \textit{Equation 3.3}$$

$$V_{void\ fibers} = V_{fibers} - \left(\frac{1}{\rho skel}\right) \qquad \textit{Equation 3.4}$$

The volumetric shrinkage (%) of the aerogel scaffolds was calculated from the external dimensions of the material before and after the $scCO_2$ drying following the Equation 3.5:

$$\textit{Volume shrinkage}\ (\%) = \left(\frac{Alcogel\ volume - Aerogel\ volume}{Alcogel\ volume}\right) \cdot 100 \qquad \textit{Equation 3.5}$$

Low-temperature N_2 adsorption/desorption analysis (ASAP 2000 Micromeritics Inc.; Norcross, GA, USA) was performed to assess aerogel textural properties. Before measurements, samples were degassed under vacuum at 40 °C for 24 h. Brunauer–Emmett–Teller (BET) method was employed to evaluate the BET-specific surface area (A_{BET}) of aerogels. Barrett–Joyner–Halenda (BJH) method was applied to determine BJH-specific pore volume (V_p), and BJH-mean pore diameter (d_p). Their morphology was evaluated by scanning electron microscopy (SEM) (EVO LS15, Zeiss, Oberkochen, Germany). Aerogels were iridium-sputtered prior to imaging to minimize charging and to improve the image quality.

3.2.5. Printing fidelity tests

Two dimensional accuracy indices (printing accuracy –PA– and shape fidelity factor –SFF–) were employed to assess the fidelity of the gel structures (for alcogels and aerogels) with respect to the original printing file processed by 3D-printing in the first step of the dual processing strategy. The PA (%) and SFF were calculated from Equations 3.6 and 3.7, respectively:

$$PA\ (\%) = \left[1 - \frac{|Ai - A|}{A}\right] \cdot\ 100 \qquad \textit{Equation 3.6}$$

$$SFF = \frac{Ai}{A} \qquad \textit{Equation 3.7}$$

where A_i is the alcogel or aerogel printed area, and A is the CAD area (printing file).

3.2.6. Cellular studies

3.2.6.1. Cell viability tests

USC UNIVERSIDADE DE SANTIAGO DE COMPOSTELA

The cytocompatibility of the different alginate-HA aerogel scaffolds was determined by assessing the viability of mouse embryo fibroblasts (BALB/c 3T3) after 24 and 48 h of culture in

the presence of the aerogel formulations, by using the water-soluble tetrazolium salt (WST-1) test. This test is based on the degradation of WST-1 into formazan and is directly correlated with the number of metabolically active cells. BALB/c 3T3 cells (6500 cells/cm^2) were seeded in 24-well plates in Dulbecco's Modified Eagle's Medium (DMEM) supplemented with 15% fetal bovine serum, penicillin 100 U/mL and streptomycin 100 g/mL. Cells were incubated at 37 °C in a humidified atmosphere enriched with 5% CO_2. Scaffolds (1 x 1 x 0.1 cm^3) were UV-sterilized for 30 min and then placed in the wells with cells containing 1500 µL of DMEM supplement. Positive controls of cells with 1000 µL of medium and blanks of 1000 µL of medium (both in triplicate) were maintained at the same conditions. After 24 and 48 h of culture, scaffolds were removed, 250 µL of medium was left in the wells and 25 µL of WST 1 reagent was added. The plate was incubated for 2 h at the same conditions and then shaken thoroughly for 1 min. Finally, 110 µL were transferred to a 96-well plate to measure the absorbance at λ=450 nm in a microplate reader (Infinite® M200, Tecan Group Ltd., Männedorf, Switzerland).

3.2.6.2. Cell attachment tests

The spreading of human bone marrow MSCs onto the scaffolds (1 x 1 x 0.1 cm^3) was evaluated by 4',6-diamidino-2-phenylindole (DAPI) staining to visualize the cellular nuclei after 6 and 13 days of culture [34]. MSC-seeded scaffolds were fixed with paraformaldehyde (4% wt/v) for 10 min and washed with phosphate buffered saline (PBS). Then, they were incubated in Triton/PBS (0.2% v/v) solution for 5 min. Finally, scaffolds were washed with PBS, placed on glass slides, and one drop of the DAPI-containing ProLong gold antifade mountant (Molecular Probes Inc., Eugene, OR, USA) was added to each scaffold before their storage at −20 °C. Finally, cell attachment in the scaffolds was evaluated using a Leica TCS-SP2 spectral confocal microscope (Leica TCS-SP2, Leica Microsystems Heidelberg GmbH, Mannheim, Germany) [35]. An open-source software (ImageJ 1.5i, US National Institutes of Health, Bethesda, MD, USA) was used to analyze the images.

USC UNIVERSIDADE DE SANTIAGO DE COMPOSTELA

3.2.6.3. Cell migration tests

Cell migration was evaluated by a scratch wound healing assay [36,37]. After the confluence, BALB/c 3T3 cells monolayer was scratched by a straight line using a sterile pipette tip and mimicking a wound *in vitro*. PBS was then employed to wash cells and remove cell debris. The different aerogel formulations (1 x 1 x 0.1 cm^3) were placed in the wells with fresh cell culture medium at 37 °C. Images of the scratch wound were obtained with an inverted microscope (Olympus, Japan) immediately (t=0 h) and at 24 h to analyze the cell migration. The migration area (%) was assessed as follows Equation 3.8:

$$Migration\ area\ (\%) = \left(\frac{A_0 - A_{24}}{A_0}\right) \cdot 100 \qquad Equation\ 3.8$$

where A_0 represents the initial wound area (t = 0 h) and A_{24} represents the residual wound area at 24 h measured by ImageJ software.

3.2.7. Statistical analysis

Results obtained from at least 3 experiments were reported as mean value ± standard deviation. Post hoc Tukey HSD multiple comparison tests were performed to assess the statistical significance of the differences among the groups and values of $p < 0.05$ were considered as statistically significant.

3.3. Results and discussion

3.3.1. Effect of alginate and $CaCl_2$ content on scaffold morphology

The feasible operating region of alginate ink formulation composition and Ca^{2+} concentration ranges for 3D-printing was firstly determined. The following criteria were followed: (i) alginate bioink must be liquid-like in the printhead to avoid the tip clogging, but (ii) it must be solid-like in the printbed to maintain the customized 3D-geometry during the deposition process and avoid the structural integrity loss.

USC UNIVERSIDADE DE SANTIAGO DE COMPOSTELA

Homogeneous 3D-structures formed by differentiated filaments arranged in layers were accordingly obtained with alginate concentrations in the 6-10 wt.% range and a $CaCl_2$

concentration of 0.5 M (Fig. 3.2). Inks below or above this alginate concentration range were discarded due to the non-homogeneous appearance obtained for the 3D-printed hydrogels. The 3D-structure and porosity, with mesopores and macropores, was clearly recognized in all aerogels produced in the feasible region. Tighter fiber interactions appear to be present at alginate concentrations of 10 wt.%. A highly interconnected structure with mesopores and macropores was observed. An improvement in the textural parameters (A_{BET} and V_p) in all aerogels was also observed (Table 3.2) with respect to other alginate aerogels previously described [38].

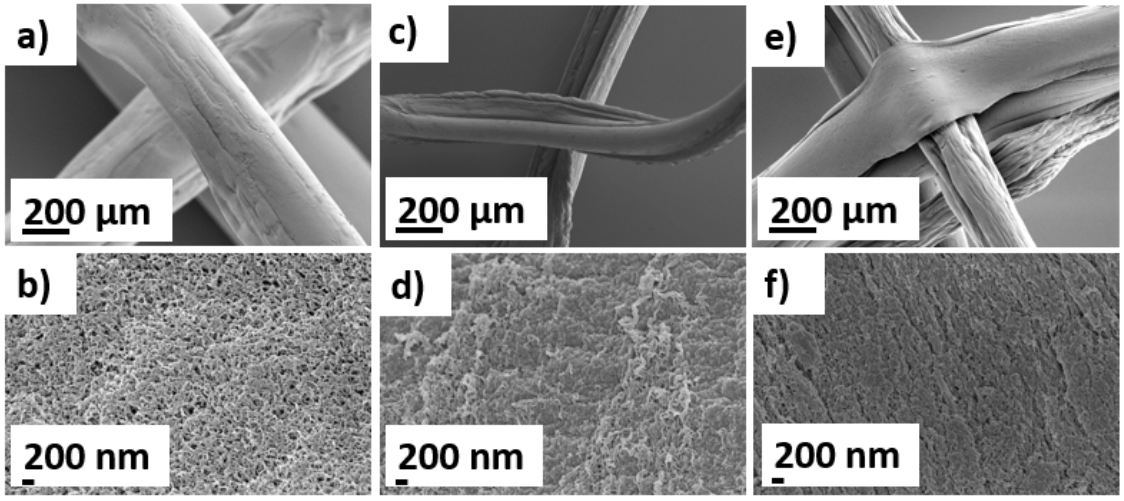


Figure 3.2. SEM pictures of 3D-printed alginate aerogels prepared at $CaCl_2$ concentration of 0.5 M and from aqueous alginate inks of different concentrations: 6 (a, b); 8 (c, d); and 10 wt.% (e, f). Aerogels are observed at two different magnifications.

Ionic crosslinking of alginate gels provided long-term stability to final structures in the 0.1-1 M $CaCl_2$ range. Alginate scaffolds crosslinked at this $CaCl_2$ concentration range had a highly porous structure throughout the scaffold with a high aerogel surface area (Fig. 3.3 and Table 3.2). Finally, alginate scaffolds crosslinked with $CaCl_2$ 1M solution had more homogeneously printed strands, which could be attributed to more Ca^{+2} ions being involved in the ionic crosslinking of the alginate [39]. In general, aerogel scaffolds obtained at alginate concentration 6 wt.% and gelified with $CaCl_2$ 1M exhibited non-woven fibers with tighter junctions if compared to the rest of formulations studied and resulting in less brittle constructs.

USC UNIVERSIDADE DE SANTIAGO DE COMPOSTELA

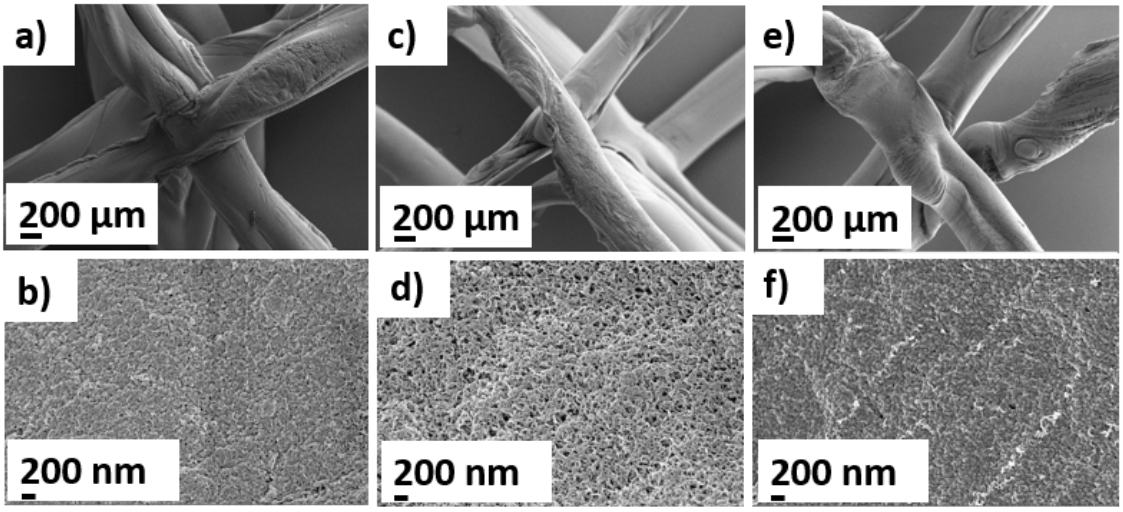


Figure 3.3. SEM pictures of 3D-printed alginate aerogels prepared from 6 wt.% aqueous alginate inks and at different $CaCl_2$ concentrations: 0.1(a, b), 0.5 (c, d) and 1 M (e, f). Aerogels are observed at two different magnifications.

High values of textural properties were obtained for all the tested aerogel formulations, although the composition and crosslinking method had an influence in the results (Table 3.2), being the highest values found in aerogels obtained from inks using an alginate concentration of 6 wt.% (Table 3.2). A similar trend in terms of textural properties was obtained in aerogels from alginate and alginate composites, like alginate-pectin microspheres generated with different alginate-to-pectin proportions [40].

Table 3.2. Textural properties of aerogel-based scaffolds from inks at different alginate concentrations (6, 8, 10 wt%) and crosslinked in gelation baths of different $CaCl_2$ concentrations (0.1, 0.5, 1 M). **Notation:** A_{BET}: BET-specific surface area, d_p: BJH-mean pore diameter, V_p: BJH-specific pore volume.

Aerogel scaffold	A_{BET} (m^2/g)	d_p (nm)	V_p (cm^3/g)
Alg 6, HA 0, $CaCl_2$ 0.1M	438 ± 22	22 ± 1	3.14 ± 0.16
Alg 6, HA 0%, $CaCl_2$ 0.5M	277 ± 14	22 ± 1	2.00 ± 0.10
Alg 6, HA 0, $CaCl_2$ 1M	183 ± 9	19 ± 1	1.16 ± 0.06
Alg 8, HA 0, $CaCl_2$ 0.1M	180 ± 9	17 ± 1	0.95 ± 0.05
Alg 8, HA 0, $CaCl_2$ 0.5M	177 ± 9	22 ± 1	1.00 ± 0.05
Alg 8%, HA 0, $CaCl_2$ 1M	147 ± 7	21 ± 1	0.97 ± 0.05
Alg 10, HA 0, $CaCl_2$ 0.1M	172 ± 9	18 ± 1	1.04 ± 0.05
Alg 10, HA 0, $CaCl_2$ 0.5M	158 ± 8	16 ± 1	0.87 ± 0.04
Alg 10, HA 0, $CaCl_2$ 1M	219 ± 11	14 ± 1	1.11 ± 0.06

USC UNIVERSIDADE DE SANTIAGO DE COMPOSTELA

3.3.2. Effect of HA content on scaffold morphology

Alginate hydrogel printing resulted in stable single filaments (Fig. 3.2), but without significant binding between layers. Moreover, alginate aerogel scaffolds started to dissolve just after their immersion in aqueous solutions losing their integrity after 24 h. The addition of HA to the alginate ink was hypothesized to preserve the strands geometry while improving structure stability and bioactivity of scaffolds yielding an improved 3D-structure for bone tissue engineering. HA is hydrophobic and the scaffolds would dissolve more gradually under physiological conditions and maintain their shape, at the expense of a reduction in the porosity of the structure [2,41]. To compensate this, alginate aerogels were herein crosslinked at high concentrations of the divalent cations solution ($CaCl_2$ 1M), so that more cations were captured inside the scaffolds and bridged the gel network. Finally, HA is involved in protein adsorption and this process causes cells transportation into the scaffold, which is positive because it may promote cell adhesion and proliferation on scaffold surfaces [42].

Homogeneous 3D-structures were obtained for the HA concentration range tested (0-24 wt.%) with fibers and layers consistently arranged. The macroporous and mesoporous structures of the scaffolds were maintained as well. At higher HA contents, more HA granules appear forming the filaments stacked together by the alginate (Fig. 3.4). The easy handling of the synthesized alginate-HA scaffolds and the SEM images showing binding between strands appear to confirm the structural integrity and stability of the aerogels after 3D-printing.

USC UNIVERSIDADE DE SANTIAGO DE COMPOSTELA

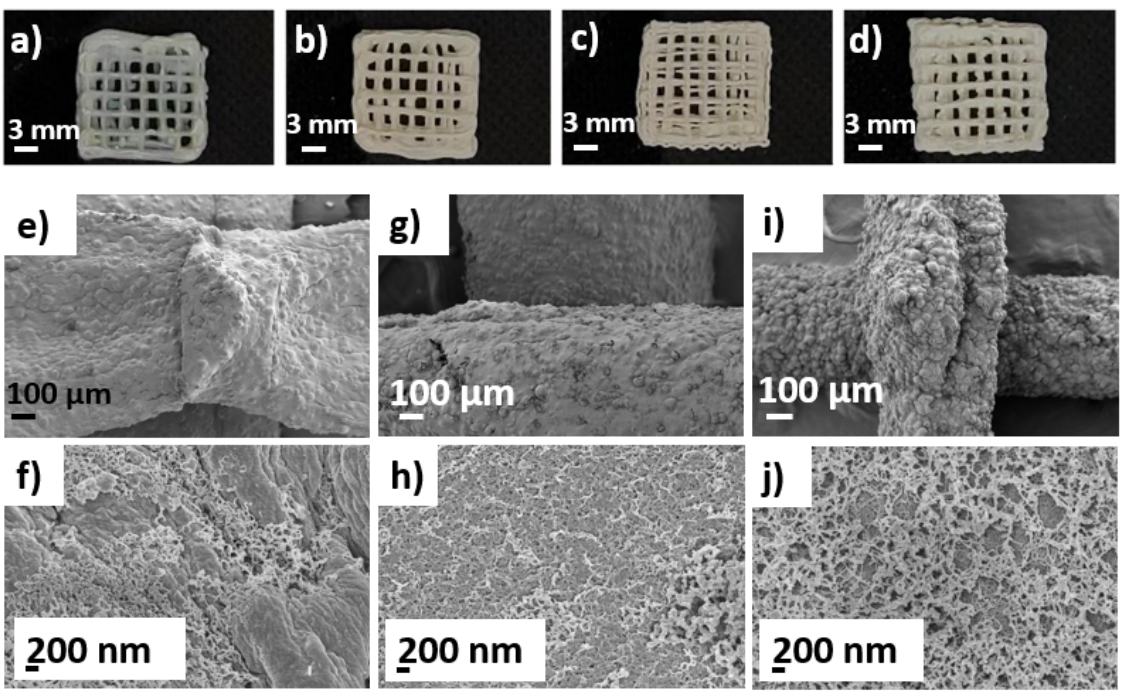


Figure 3.4. Images and SEM pictures of 3D-printed alginate-HA aerogels prepared from 6 wt.% alginate inks with different HA concentrations: 0(a), 8 (b, e, f), 16(c, g, h), and 24 wt.% (d, i, j). In all cases the gelation was performed using $CaCl_2$ 1M.

N_2 adsorption-desorption analysis of alginate-HA aerogel scaffolds show an important decrease in the specific surface area and total pore volume, while the pore diameter is almost unaltered with respect to scaffolds fabricated with alginate only (Table 3.3). The decrease in the total pore volume could be attributed to the interactions between $–NH_3^+$ groups of alginate and –OH groups and Ca^{2+} ions of HA that lead to the final deposition of HA over the scaffold creating an irregular surface structure [20]. In general, the HA addition decreased the textural properties in all alginate-HA formulations, due to the low mesoporosity of the HA powder (2 m^2/g). Despite that, the textural properties of the HA-containing alginate aerogels may still be enough to favor cell seeding and nutrient diffusion throughout the scaffold structure. The results obtained in terms of textural parameters after the addition of HA are coherent with previous studies using other polymeric scaffolds [20,43]. Apparent density values increased gradually with the addition of HA resulting in a reverse effect on porosity, although all aerogel scaffold formulations tested reached values above 80 % (Table 3.3). The porosity of the fibers also decreased with the addition of HA. The total porosity values of the scaffolds (88.56 to 80.33 %) are slightly higher

USC UNIVERSIDADE DE SANTIAGO DE COMPOSTELA

than the aerogel fibers porosity values (86.58 to 76.68 %) as the scaffolds are formed by a 3D-mesh of vertically and horizontally aligned aerogel microfibers separated by macroporous gaps. These are good results since the addition of HA have strongly affected other textural parameters (A_{BET}) but not porosity. Nevertheless, higher porosity (80 – 99 %) and lower densities (0.02 g/ cm^3 as bulk density) values were previously reported for alginate aerogel in the form of microparticles [44]. Consistently, the incorporation of HA has advantages (bioactivity, similarity to human bone mineral phase) [22,23] at the expense of a slight decrease in textural parameters.

Table 3.3. Textural properties of aerogel-based scaffolds processed from 6 wt% alginate inks with different HA concentrations (0, 8, 16, 24 wt%) and crosslinked with $CaCl_2$ 1M. **Notation:** A_{BET}: BET-specific surface area, d_p: BJH-mean pore diameter, V_p: BJH-specific pore volume, ρ_{app}*:* apparent density, ρ_{skel}: skeletal density, ε: scaffold porosity, ε_f: aerogel fibers porosity.

Aerogel scaffold	A_{BET} (m^2/g)	d_p (nm)	V_p (cm^3/g)	ρ_{app} (g/mL)	ρ_{skel} (g/cm^3)	ε (%)	ε_f (%)
Alg 6, HA 0, $CaCl_2$ 1M	183 ± 9	19 ± 1	1.16 ± 0.06	0.14 ± 0.01	1.18 ± 0.16	88.56 ± 1.29	86.58 ± 2.26
Alg 6, HA 8, $CaCl_2$ 1M	118 ± 6	24 ± 1	0.99 ± 0.05	0.24 ± 0.03	1.72 ± 0.09	85.85 ± 1.59	85.25 ± 4.02
Alg 6, HA 16, $CaCl_2$ 1M	67 ± 3	26 ± 1	0.60 ± 0.03	0.29 ± 0.04	1.93 ± 0.04	85.06 ± 2.40	79.78 ± 3.92
Alg 6, HA 24, $CaCl_2$ 1M	29 ± 2	31 ± 2	0.21 ± 0.01	0.34 ± 0.02	1.72 ± 0.14	80.33 ± 1.19	76.68 ± 3.54

The volumetric shrinkage of aerogel scaffolds after performing the $scCO_2$ drying was tested (Fig. 3.5) to unveil the influence of this process in the end aerogel scaffolds. The dual strategy allows the direct solvent exchange to EtOH without high volumetric shrinkage values and reducing the overall processing time to obtain the aerogels. Structures containing HA had a lower volume shrinkage with respect to the formulation without HA (Alg 6, HA 0, $CaCl_2$ 1M). These are good results since higher volume shrinkage values (42 - 65 %) have been reported for alginate aerogels obtained by sequential solvent exchanges [45].

USC UNIVERSIDADE DE SANTIAGO DE COMPOSTELA

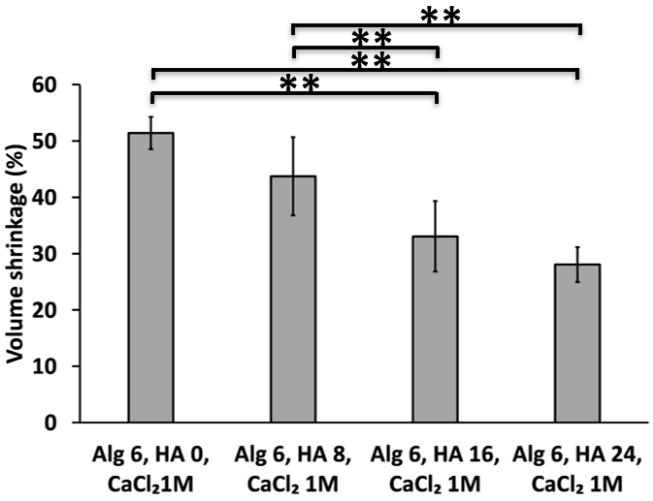


Figure 3.5. Volume shrinkage (%) of different alginate-HA formulations. Significant differences among groups were denoted as ** (post hoc Tukey HSD multiple comparison test, $p < 0.01$).

3.3.3. Printing fidelity tests

PA and SFF indices were employed to assess the reproducibility and the fidelity of the dual processing strategy herein proposed. The values obtained for both parameters are higher when assessed in the alcogels than when assessed in the aerogels (Table 4). This feature was expected since the volume shrinkage reported influences the dimensional accuracy indices. Nonetheless, the alcogel PA and SFF values obtained are close to the values previously reported for 3D-printed alginate gels and for other polysaccharide gels [41],[46].

Table 4. Printing fidelity indices of aerogels prepared from alginate-HA formulations. Aerogels were manufactured at an alginate concentration of 6 wt.%, at different HA concentrations (0, 8, 16 and 24 wt.%) and at a $CaCl_2$ concentration of 1M.

Aerogel scaffold	Alcogel PA (%)	Aerogel PA (%)	Alcogel SFF	Aerogel SFF
Alg 6, HA 0, $CaCl_2$ 1M	77.73 ± 11.03	43.56 ± 12.94	0.82 ± 0.08	0.64 ± 0.05
Alg 6, HA 8, $CaCl_2$ 1M	75.51 ± 8.54	39.06 ± 10.70	0.81 ± 0.05	0.62 ± 0.04
Alg 6, HA 16, $CaCl_2$ 1M	83.51 ± 2.29	50.18 ± 6.05	0.86 ± 0.02	0.67 ± 0.03
Alg 6, HA 24, $CaCl_2$ 1M	83.35 ± 6.21	48.14 ± 4.84	0.86 ± 0.05	0.66 ± 0.02

USC UNIVERSIDADE DE SANTIAGO DE COMPOSTELA

3.3.4. Cellular studies

3.3.4.1. Cell viability tests

BALB/c 3T3 cells were cultured in the presence of alginate-HA aerogel scaffolds for cell cytotoxicity evaluation. Fig. 3.6 represents the cell viability after culture for 24 and 48 h with values reaching *ca.* 100 % for alginate aerogels, which means that they had no negative effect on cell proliferation. Similar results on BALB/c 3T3 cells viability after 48 h were found for alginate-HA aerogels, regardless of the HA concentration.

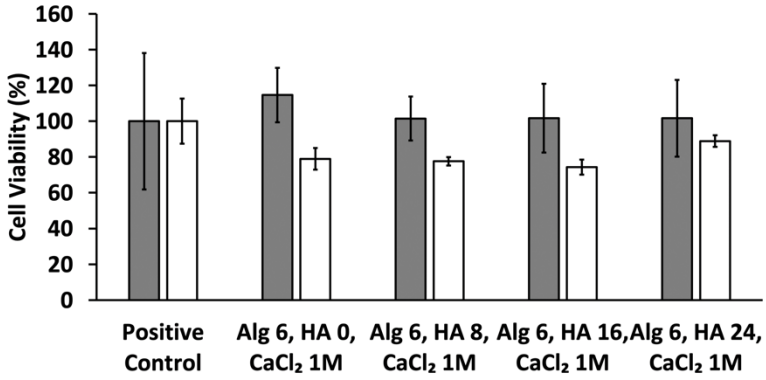


Figure 3.6. Cell viability (%) of alginate-HA aerogels after 24 (grey bars) and 48 h (white) of contact with BALB/c 3T3 cells. There were no statistically significant differences among groups ($p < 0.05$).

In general, these viability results indicate that neither the scaffold composition nor the dual processing strategy compromised the cell viability. The high cell viability observed after the tests confirmed the non-toxicity of the aerogel structures and correlates with scaffolds of similar composition (alginate and HA) [47]. Indeed, the cell compatibility of the initial components of the scaffolds (alginate and HA) was already reported [48]. Overall, these are promising results since cytocompatibility, and a suitable microstructure (pore size and porosity) govern the properties of an ideal scaffold.

USC UNIVERSIDADE DE SANTIAGO DE COMPOSTELA

3.3.4.2. Cell attachment tests

A challenge in tissue engineering is the generation of biomaterials with an adequate structure to act as a substrate for cell bonding, development and reproduction [49]. MSCs attachment and proliferation in aerogels were herein tested as this cell line is attractive for tissue engineering applications aiming at the generation of artificial bone substitutes. MSCs present self-renewal potential, they can differentiate *in vivo* and *ex vivo* into different cell types like chondrocytes or osteoblasts and their isolation is not related to donor-site morbidity [50]. In the case of osteoblasts, their attachment to scaffolds depends on the surface area and the porosity of the materials.

No differences in MSCs attachment and spreading were observed between aerogels formulations in terms of nuclei staining (Fig. 3.7). The presence of HA in the scaffolds did not influence MSCs attachment as previously observed for structures with similar composition [47,50]. Nevertheless, for higher HA concentrations (16 and 24 wt.%) the attachment decreases at 6 and 13 days probably due to the high superficial roughness and irregularity that generally favor cell attachment (HA concentration of 8 wt.%) but at such higher levels it could make it hard for MSCs to proliferate fully attached to the aerogel.

A proliferation tendency is observed for all formulations since more nuclei were stained after culturing scaffolds for 13 days than after 6 days (Fig. 3.7). This feature indicates that scaffolds were non-toxic, biocompatible, suitable for the attachment and growth of MSCs and able to promote cell adhesion and proliferation, as well as the cell colonization of the scaffold. Small pore diameters and high surface areas as obtained for the aerogels of this work are suitable for osteoblast attachment because these conditions allow cell interpenetration and full migration.

USC
UNIVERSIDADE DE SANTIAGO DE COMPOSTELA

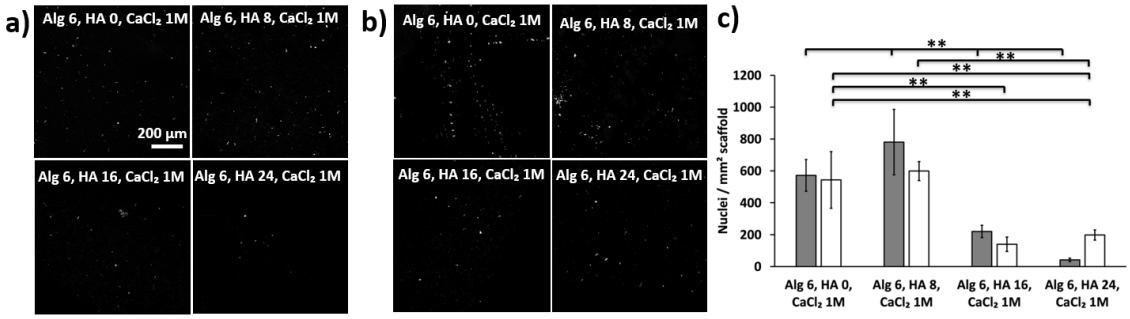


Figure 3.7. Confocal microscopy images of DAPI-stained MSCs seeded on aerogel scaffolds and cultured for (a) 6, and (b) 13 days. (c) Cell attachment and proliferation tests of alginate-HA aerogels after 6 (grey bars) and 13 (black) days of culture in MSCs. Significant differences among groups were denoted as ** (post hoc Tukey HSD multiple comparison test, $p < 0.01$).

3.3.4.3. Cell migration tests

Fig. 3.8a–f shows the evolution of the wound closure process after the scratch test with BALB/c 3T3 cells in the presence of different aerogel formulations. Fig. 3.8g shows the increase in BALB/c 3T3 cell migration in the presence of aerogel scaffolds with respect to the positive control. These are good results since the well-known bioinert properties of alginate make it hard to be degraded *in vivo* and this feature could have restricted cellular adhesion and migration as previously reported [51]. In general, structures that are stable, with satisfactory morphology and pore size allow significant human fibroblast migration in wound closure *in vitro* assays [52]. Nevertheless, finding the best microarchitecture for cell migration in tissue regeneration is still challenging. In previous studies, human dermal fibroblast migration with alginate composites showed a high closure of the scratch [52]. Furthermore, alginate composites combined with Ca^{2+} cations resulted in an enhancement on fibroblasts migration like the herein observed, probably due to changes in the regulation of genes involved in the wound healing process carried out by fibroblasts. Finally, as chemotaxis is an inherent response of cells it was hypothesized to be involved in the cell migration process since the higher concentration of biochemical factors secreted by injured tissues activate the surrounding cells and stimulate the migration of cells [53]. This biological response could also play a significant role in the increase of the migration of fibroblasts in the presence of alginate-based aerogels herein observed.

USC UNIVERSIDADE DE SANTIAGO DE COMPOSTELA

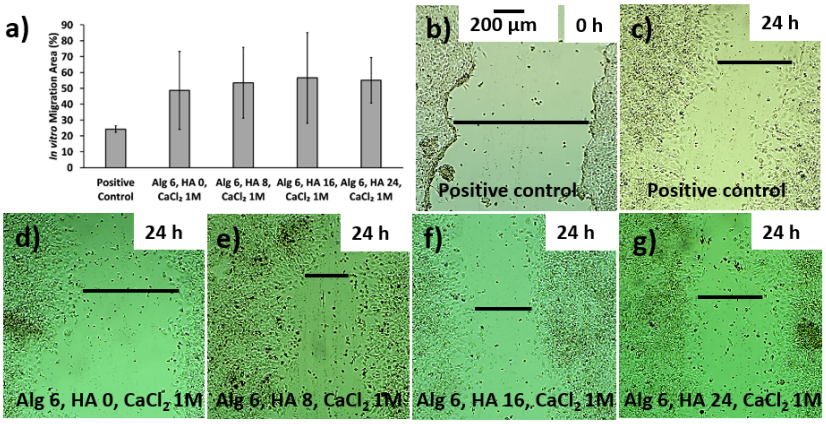


Figure 3.8. a) Quantitative analysis of the stimulation of BALB/c 3T3 cells migration by alginate-HA aerogels after 24 h in cell culture. b-g) Microscopy images of *in vitro* scratch test on BALB/c 3T3 cells treated with different aerogel formulations and cultured until 24 h. There were no statistically significant differences among groups ($p < 0.05$).

3.4. Conclusions

Alginate-HA aerogel scaffolds were successfully fabricated with a precise and customized nanostructure by the combination of 3D-printing and aerogel technologies. This technological combination resulted in nanostructured and dual porous alginate aerogels of interest for tissue engineering applications. 3D-structure is conserved after all processing steps and alginate, HA and $CaCl_2$ contents determine scaffold texture. An optimized scaffold formulation must provide a long-term stability and the required biocompatibility for tissue engineering applications. Cell viability tests revealed no toxicity effect or negative impact on BALB/c 3T3 cells on normal cell environment because of the presence of the scaffolds. Furthermore, fibroblasts also successfully accomplished the migration process when cultured with the aerogel formulations herein proposed. MSCs were able to attach and proliferate on alginate-HA aerogels upon culture for 6 and 13 days. All these features are highly desirable for scaffolds to act as temporary supports and harbor the bone regeneration process. Finally, the fidelity of the end aerogel scaffolds with respect to the original CAD is high. Consistently, the macroporous alginate-HA aerogel scaffolds obtained by this novel technological combination of 3D-printing and $scCO_2$ drying methods represent a promising alternative for bone regenerative applications opening up new possibilities to personalized medicine. Other requirements to accomplish bone tissue formation

USC UNIVERSIDADE DE SANTIAGO DE COMPOSTELA

like the degradation rate of the 3D-structures and their mechanical properties will be optimized in a future work.

3.5. References

1. Dimitriou, R.; Jones, E.; McGonagle, D.; Giannoudis, P.V. Bone Regeneration: Current Concepts and Future Directions. BMC Med. 2011, 9, 66, doi:10.1186/1741-7015-9-66.
2. Lin, H.-R.; Yeh, Y.-J. Porous Alginate/Hydroxyapatite Composite Scaffolds for Bone Tissue Engineering: Preparation, Characterization, And *in Vitro* Studies. J. Biomed. Mater. Res. 2004, 71B, 52–65, doi:10.1002/jbm.b.30065.
3. Yue, S.; He, H.; Li, B.; Hou, T. Hydrogel as a Biomaterial for Bone Tissue Engineering: A Review. Nanomaterials 2020, 10, 1511, doi:10.3390/nano10081511.
4. Amiryaghoubi, N.; Fathi, M.; Pesyan, N.N.; Samiei, M.; Barar, J.; Omidi, Y. Bioactive Polymeric Scaffolds for Osteogenic Repair and Bone Regenerative Medicine. Med. Res. Rev. 2020, 40, 1833–1870, doi:10.1002/med.21672.
5. Burg, K.J.L.; Porter, S.; Kellam, J.F. Biomaterial Developments for Bone Tissue Engineering. Biomaterials 2000, 21, 2347–2359, doi:10.1016/S0142-9612(00)00102-2.
6. Chae, T.; Yang, H.; Leung, V.; Ko, F.; Troczynski, T. Novel Biomimetic Hydroxyapatite/Alginate Nanocomposite Fibrous Scaffolds for Bone Tissue Regeneration. J. Mater. Sci. Mater. Med. 2013, 24, 1885–1894, doi:10.1007/s10856-013-4957-7.
7. Wang, Z.; Kapadia, W.; Li, C.; Lin, F.; Pereira, R.F.; Granja, P.L.; Sarmento, B.; Cui, W. Tissue-Specific Engineering: 3D Bioprinting in Regenerative Medicine. J. Controlled Release 2021, 329, 237–256, doi:10.1016/j.jconrel.2020.11.044.
8. Santos-Rosales, V.; Iglesias-Mejuto, A.; García-González, C.A. Solvent-Free Approaches for the Processing of Scaffolds in Regenerative Medicine. 2020, 20.
9. Boga, J.C.; Miguel, S.P.; de Melo-Diogo, D.; Mendonça, A.G.; Louro, R.O.; Correia, I.J. *In Vitro* Characterization of 3D Printed Scaffolds Aimed at Bone Tissue Regeneration. Colloids Surf. B Biointerfaces 2018, 165, 207–218, doi:10.1016/j.colsurfb.2018.02.038.
10. Askari, M.; Afzali Naniz, M.; Kouhi, M.; Saberi, A.; Zolfagharian, A.; Bodaghi, M. Recent Progress in Extrusion 3D Bioprinting of Hydrogel Biomaterials for Tissue Regeneration: A Comprehensive Review with Focus on Advanced Fabrication Techniques. Biomater. Sci. 2021, 9, 535–573, doi:10.1039/D0BM00973C.
11. Naghieh, S.; Sarker, M.; Sharma, N.K.; Barhoumi, Z.; Chen, X. Printability of 3D Printed Hydrogel Scaffolds: Influence of Hydrogel Composition and Printing Parameters. Appl. Sci. 2019, 10, 292, doi:10.3390/app10010292.
12. Dhawan, A.; Kennedy, P.M.; Rizk, E.B.; Ozbolat, I.T. Three-Dimensional Bioprinting for Bone and Cartilage Restoration in Orthopaedic Surgery: J. Am. Acad. Orthop. Surg. 2019, 27, e215–e226, doi:10.5435/JAAOS-D-17-00632.
13. Wang, Q.; Xia, Q.; Wu, Y.; Zhang, X.; Wen, F.; Chen, X.; Zhang, S.; Heng, B.C.; He, Y.; Ouyang, H.-W. 3D-Printed Atsttrin-Incorporated Alginate/Hydroxyapatite Scaffold Promotes Bone Defect Regeneration with TNF/TNFR Signaling Involvement. Adv. Healthc. Mater. 2015, 4, 1701–1708, doi:10.1002/adhm.201500211.
14. García-González, C.A.; Budtova, T.; Durães, L.; Erkey, C.; Del Gaudio, P.; Gurikov, P.; Koebel, M.; Liebner, F.; Neagu, M.; Smirnova, I. An Opinion Paper on Aerogels for Biomedical and Environmental Applications. Molecules 2019, 24, 1815, doi:10.3390/molecules24091815.
15. Horvat, G.; Xhanari, K.; Finšgar, M.; Gradišnik, L.; Maver, U.; Knez, Ž.; Novak, Z. Novel Ethanol-Induced Pectin–Xanthan Aerogel Coatings for Orthopedic Applications. Carbohydr. Polym. 2017, 166, 365–376, doi:10.1016/j.carbpol.2017.03.008.
16. Hegedűs, V.; Kerényi, F.; Boda, R.; Horváth, D.; Lázár, I.; Tóth-Győri, E.; Dezső, B.; Hegedus, C. β-Tricalcium Phosphate Silica Aerogel as an Alternative Bioactive Ceramic for the Potential Use in Dentistry. Adv. Appl. Ceram. 2018, 117, 476–484, doi:10.1080/17436753.2018.1498145.
17. Reyes-Peces, M.V.; Pérez-Moreno, A.; de-los-Santos, D.M.; Mesa-Díaz, M. del M.; Pinaglia-Tobaruela, G.; Vilches-Pérez, J.I.; Fernández-Montesinos, R.; Salido, M.; de la Rosa-Fox, N.; Piñero, M. Chitosan-GPTMS-Silica Hybrid Mesoporous Aerogels for Bone Tissue Engineering. Polymers 2020, 12, 2723, doi:10.3390/polym12112723.

USC DE COMPOSTELA

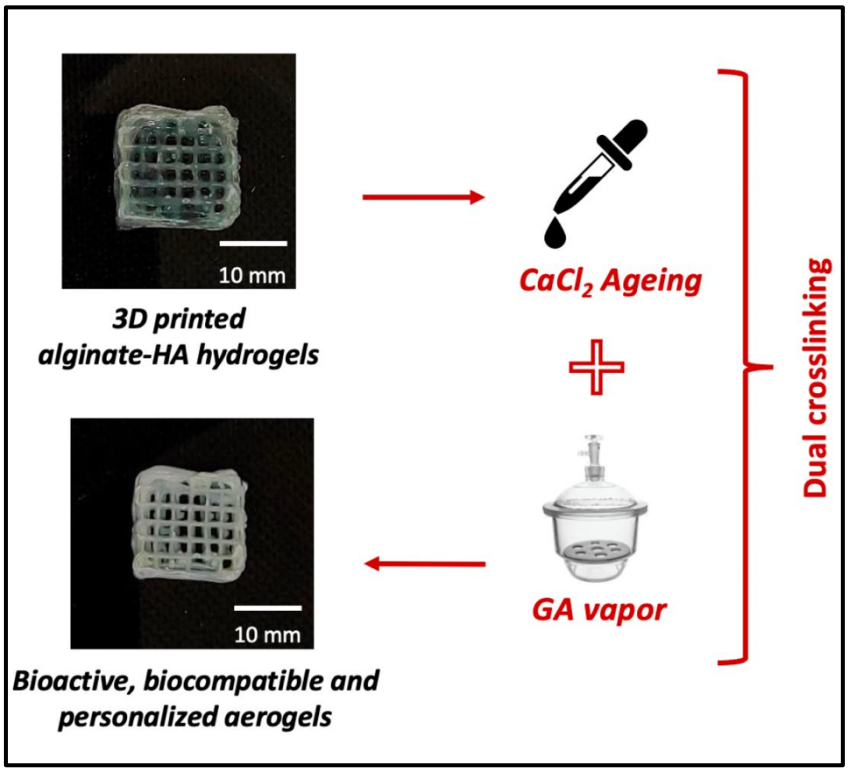
18. Santos-Rosales, V.; Ardao, I.; Alvarez-Lorenzo, C.; Ribeiro, N.; Oliveira, A.; García-González, C. Sterile and Dual-Porous Aerogels Scaffolds Obtained through a Multistep Supercritical CO_2-Based Approach. Molecules 2019, 24, 871, doi:10.3390/molecules24050871.
19. Budtova, T.; Aguilera, D.A.; Beluns, S.; Berglund, L.; Chartier, C.; Espinosa, E.; Gaidukovs, S.; Klimek-Kopyra, A.; Kmita, A.; Lachowicz, D.; et al. Biorefinery Approach for Aerogels. Polymers 2020, 12, 2779, doi:10.3390/polym12122779.
20. Sharma, C.; Dinda, A.K.; Potdar, P.D.; Chou, C.-F.; Mishra, N.C. Fabrication and Characterization of Novel Nano-Biocomposite Scaffold of Chitosan–Gelatin–Alginate–Hydroxyapatite for Bone Tissue Engineering. Mater. Sci. Eng. C 2016, 64, 416–427, doi:10.1016/j.msec.2016.03.060.
21. Turco, G.; Marsich, E.; Bellomo, F.; Semeraro, S.; Donati, I.; Brun, F.; Grandolfo, M.; Accardo, A.; Paoletti, S. Alginate/Hydroxyapatite Biocomposite For Bone Ingrowth: A Trabecular Structure With High And Isotropic Connectivity. Biomacromolecules 2009, 10, 1575–1583, doi:10.1021/bm900154b.
22. Luo, Y.; Li, Y.; Qin, X.; Wa, Q. 3D Printing of Concentrated Alginate/Gelatin Scaffolds with Homogeneous Nano Apatite Coating for Bone Tissue Engineering. Mater. Des. 2018, 146, 12–19, doi:10.1016/j.matdes.2018.03.002.
23. Wüst, S.; Godla, M.E.; Müller, R.; Hofmann, S. Tunable Hydrogel Composite with Two-Step Processing in Combination with Innovative Hardware Upgrade for Cell-Based Three-Dimensional Bioprinting. Acta Biomater. 2014, 10, 630–640, doi:10.1016/j.actbio.2013.10.016.
24. Ruixin, L.; Cheng, X.; Yingjie, L.; Hao, L.; Caihong, S.; Weihua, S.; Weining, A.; Yinghai, Y.; Xiaoli, Q.; Yunqiang, X.; et al. Degradation Behavior and Compatibility of Micro, nanoHA/Chitosan Scaffolds with Interconnected Spherical Macropores. Int. J. Biol. Macromol. 2017, 103, 385–394, doi:10.1016/j.ijbiomac.2017.03.175.
25. Barros, J.; Ferraz, M.P.; Azeredo, J.; Fernandes, M.H.; Gomes, P.S.; Monteiro, F.J. Alginate-Nanohydroxyapatite Hydrogel System: Optimizing the Formulation for Enhanced Bone Regeneration. Mater. Sci. Eng. C 2019, 105, 109985, doi:10.1016/j.msec.2019.109985.
26. Domingos, M.; Gloria, A.; Coelho, J.; Bartolo, P.; Ciurana, J. Three-Dimensional Printed Bone Scaffolds: The Role of Nano/Micro-Hydroxyapatite Particles on the Adhesion and Differentiation of Human Mesenchymal Stem Cells. Proc. Inst. Mech. Eng. [H] 2017, 231, 555–564, doi:10.1177/0954411916680236.
27. Liu, H.; Peng, H.; Wu, Y.; Zhang, C.; Cai, Y.; Xu, G.; Li, Q.; Chen, X.; Ji, J.; Zhang, Y.; et al. The Promotion of Bone Regeneration by Nanofibrous Hydroxyapatite/Chitosan Scaffolds by Effects on Integrin-BMP/Smad Signaling Pathway in BMSCs. Biomaterials 2013, 34, 4404–4417, doi:10.1016/j.biomaterials.2013.02.048.
28. Tang, X.; Zhou, H.; Cai, Z.; Cheng, D.; He, P.; Xie, P.; Zhang, D.; Fan, T. Generalized 3D Printing of Graphene-Based Mixed-Dimensional Hybrid Aerogels. ACS Nano 2018, 12, 3502–3511, doi:10.1021/acsnano.8b00304.
29. Feng, J.; Su, B.-L.; Xia, H.; Zhao, S.; Gao, C.; Wang, L.; Ogbeide, O.; Feng, J.; Hasan, T. Printed Aerogels: Chemistry, Processing, and Applications. Chem. Soc. Rev. 2021, 50, 3842–3888, doi:10.1039/C9CS00757A.
30. Maleki, H.; Fischer, T.; Bohr, C.; Auer, J.; Mathur, S.; Milow, B. Hierarchically Organized Biomimetic Architectured Silk Fibroin–Ceramic-Based Anisotropic Hybrid Aerogels for Thermal Energy Management. Biomacromolecules 2021, 22, 1739–1751, doi:10.1021/acs.biomac.1c00175.
31. Maleki, H.; Montes, S.; Hayati-Roodbari, N.; Putz, F.; Huesing, N. Compressible, Thermally Insulating, and Fire Retardant Aerogels through Self-Assembling Silk Fibroin Biopolymers Inside a Silica Structure—An Approach towards 3D Printing of Aerogels. ACS Appl. Mater. Interfaces 2018, 10, 22718–22730, doi:10.1021/acsami.8b05856.
32. Santos-Rosales, V.; Alvarez-Rivera, G.; Hillgärtner, M.; Cifuentes, A.; Itskov, M.; García-González, C.A.; Rege, A. Stability Studies of Starch Aerogel Formulations for Biomedical Applications. Biomacromolecules 2020, 21, 5336–5344, doi:10.1021/acs.biomac.0c01414.
33. Tetik, H.; Feng, D.; Oxandale, S.W.; Yang, G.; Zhao, K.; Feist, K.; Shah, N.; Liao, Y.; Leseman, Z.C.; Lin, D. Bioinspired Manufacturing of Aerogels with Precisely Manipulated Surface Microstructure through Controlled Local Temperature Gradients. ACS Appl. Mater. Interfaces 2021, 13, 924–931, doi:10.1021/acsami.0c19087.
34. Akdere, Ö.E.; Shikhaliyeva, İ.; Gümüşderelioğlu, M. Boron Mediated 2D and 3D Cultures of Adipose Derived Mesenchymal Stem Cells. Cytotechnology 2019, 71, 611–622, doi:10.1007/s10616-019-00310-9.
35. García-González, C.A.; Barros, J.; Rey-Rico, A.; Redondo, P.; Gómez-Amoza, J.L.; Concheiro, A.; Alvarez-Lorenzo, C.; Monteiro, F.J. Antimicrobial Properties and Osteogenicity of Vancomycin-Loaded Synthetic Scaffolds Obtained by Supercritical Foaming. ACS Appl. Mater. Interfaces 2018, 10, 3349–3360, doi:10.1021/acsami.7b17375.

36. Sartawi, Z.; Ryan, K.B.; Waeber, C. Bone Regenerative Potential of the Selective Sphingosine 1-Phosphate Receptor Modulator Siponimod: *In Vitro* Characterisation Using Osteoblast and Endothelial Cells. Eur. J. Pharmacol. 2020, 882, 173262, doi:10.1016/j.ejphar.2020.173262.
37. Zhang, J.; Liu, X.; Li, H.; Chen, C.; Hu, B.; Niu, X.; Li, Q.; Zhao, B.; Xie, Z.; Wang, Y. Exosomes/Tricalcium Phosphate Combination Scaffolds Can Enhance Bone Regeneration by Activating the PI3K/Akt Signaling Pathway. Stem Cell Res. Ther. 2016, 7, 136, doi:10.1186/s13287-016-0391-3.
38. Batista, M.P.; Gonçalves, V.S.S.; Gaspar, F.B.; Nogueira, I.D.; Matias, A.A.; Gurikov, P. Novel Alginate-Chitosan Aerogel Fibres for Potential Wound Healing Applications. Int. J. Biol. Macromol. 2020, 156, 773–782, doi:10.1016/j.ijbiomac.2020.04.089.
39. Naghieh, S.; Karamooz-Ravari, M.R.; Sarker, M.; Karki, E.; Chen, X. Influence of Crosslinking on the Mechanical Behavior of 3D Printed Alginate Scaffolds: Experimental and Numerical Approaches. J. Mech. Behav. Biomed. Mater. 2018, 80, 111–118, doi:10.1016/j.jmbbm.2018.01.034.
40. Chen, K.; Zhang, H. Alginate/Pectin Aerogel Microspheres for Controlled Release of Proanthocyanidins. Int. J. Biol. Macromol. 2019, 136, 936–943, doi:10.1016/j.ijbiomac.2019.06.138.
41. Giuseppe, M.D.; Law, N.; Webb, B.; A. Macrae, R.; Liew, L.J.; Sercombe, T.B.; Dilley, R.J.; Doyle, B.J. Mechanical Behaviour of Alginate-Gelatin Hydrogels for 3D Bioprinting. J. Mech. Behav. Biomed. Mater. 2018, 79, 150–157, doi:10.1016/j.jmbbm.2017.12.018.
42. Sun, J.; Tan, H. Alginate-Based Biomaterials for Regenerative Medicine Applications. Materials 2013, 6, 1285–1309, doi:10.3390/ma6041285.
43. Kim, H.-W.; Knowles, J.C.; Kim, H.-E. Hydroxyapatite and Gelatin Composite Foams Processed via Novel Freeze-Drying and Crosslinking for Use as Temporary Hard Tissue Scaffolds. J. Biomed. Mater. Res. A 2005, 72A, 136–145, doi:10.1002/jbm.a.30168.
44. Subrahmanyam, R.; Gurikov, P.; Meissner, I.; Smirnova, I. Preparation of Biopolymer Aerogels Using Green Solvents. J. Vis. Exp. 2016, 54116, doi:10.3791/54116.
45. Veronovski, A.; Novak, Z.; Knez, Ž. Synthesis and Use of Organic Biodegradable Aerogels as Drug Carriers. J. Biomater. Sci. Polym. Ed. 2012, 23, 873–886, doi:10.1163/092050611X566126.
46. Panraksa, P.; Udomsom, S.; Rachtanapun, P.; Chittasupho, C.; Ruksiriwanich, W.; Jantrawut, P. Hydroxypropyl Methylcellulose E15: A Hydrophilic Polymer for Fabrication of Orodispersible Film Using Syringe Extrusion 3D Printer. Polymers 2020, 12, 2666, doi:10.3390/polym12112666.
47. Kamalaldin, N.A.; Yahya, B.H.; Nurazreena, A. Cell Evaluation on Alginate/Hydroxyapatite Block for Biomedical Application. Procedia Chem. 2016, 19, 297–303, doi:10.1016/j.proche.2016.03.012.
48. Shaheen, Th.I.; Montaser, A.S.; Li, S. Effect of Cellulose Nanocrystals on Scaffolds Comprising Chitosan, Alginate and Hydroxyapatite for Bone Tissue Engineering. Int. J. Biol. Macromol. 2019, 121, 814–821, doi:10.1016/j.ijbiomac.2018.10.081.
49. Tohamy, K.M.; Mabrouk, M.; Soliman, I.E.; Beherei, H.H.; Aboelnasr, M.A. Novel Alginate/Hydroxyethyl Cellulose/Hydroxyapatite Composite Scaffold for Bone Regeneration: *In Vitro* Cell Viability and Proliferation of Human Mesenchymal Stem Cells. Int. J. Biol. Macromol. 2018, 112, 448–460, doi:10.1016/j.ijbiomac.2018.01.181.
50. Benning, L.; Gutzweiler, L.; Tröndle, K.; Riba, J.; Zengerle, R.; Koltay, P.; Zimmermann, S.; Stark, G.B.; Finkenzeller, G. Cytocompatibility Testing of Hydrogels toward Bioprinting of Mesenchymal Stem Cells: Cytocompatibility Testing of Hydrogels. J. Biomed. Mater. Res. A 2017, 105, 3231–3241, doi:10.1002/jbm.a.36179.
51. Yao, B.; Hu, T.; Cui, X.; Song, W.; Fu, X.; Huang, S. Enzymatically Degradable Alginate/Gelatin Bioink Promotes Cellular Behavior and Degradation *in Vitro* and *in Vivo*. Biofabrication 2019, 11, 045020, doi:10.1088/1758-5090/ab38ef.
52. Gallardo-Rivera, R.; de los Ángeles Aguilar-Santamaría, M.; Silva-Bermúdez, P.; García-López, J.; Tecante, A.; Velasquillo, C.; Román-Guerrero, A.; Pérez-Alonso, C.; Vázquez-Torres, H.; Shirai, K. Polyelectrolyte Complex of Aloe Vera, Chitosan, and Alginate Produced Fibroblast and Lymphocyte Viabilities and Migration. Carbohydr. Polym. 2018, 192, 84–94, doi:10.1016/j.carbpol.2018.03.044.
53. Lin, C.; Tao, B.; Deng, Y.; He, Y.; Shen, X.; Wang, R.; Lu, L.; Peng, Z.; Xia, Z.; Cai, K. Matrix Promote Mesenchymal Stromal Cell Migration with Improved Deformation via Nuclear Stiffness Decrease. Biomaterials 2019, 217, 119300, doi:10.1016/j.biomaterials.2019.119300.

USC UNIVERSIDADE DE SANTIAGO DE COMPOSTELA

USC
UNIVERSIDADE
DE SANTIAGO
DE COMPOSTELA

CHAPTER 4. 3D-PRINTED, DUAL CROSSLINKED AND STERILE AEROGEL SCAFFOLDS FOR BONE TISSUE ENGINEERING



The content in this chapter was published in part in **A. Iglesias-Mejuto**, C.A. García-González; 3D-Printed, Dual Crosslinked and Sterile Aerogel Scaffolds for Bone Tissue Engineering, in: Polymers 14 (2022) 1211. https://doi.org/10.3390/polym14061211.

USC
UNIVERSIDADE DE SANTIAGO DE COMPOSTELA

4.1. Introduction

Large bone defects caused due to osteosarcoma interventions or traumatic fractures can be regenerated using bone grafts to promote spontaneous biological bone healing [1]. Standard clinical practices in bone defect repair include autografts, vascularized autografting, allografts, and xenografts. Nevertheless, these alternatives have important difficulties with regard to the formation of blood vessels, short shelf lives and high costs [2]. Bone tissue engineering aims to regenerate bone tissue at the host defect site in an environment mimicking the natural bone ECM. Bone graft composition governs their biocompatibility, whereas their porous structure rules the cell penetration and nutrient diffusion. Scaffolds for bone tissue engineering must promote bone formation and eventually degrade *in situ* at a rate compatible with the pace of new tissue formation [2]. An ideal bone scaffold should also provide suitable anatomical and functional properties to the damaged area in order to preserve its physiological role [3]. Alginate scaffolds swell easily, allowing cell penetration inside the matrix scaffold [4]. Additionally, alginate is a biocompatible and hydrophilic copolymer of β-L-guluronic acid and α-D-mannuronic acid units, able to form stable gels in the presence of divalent cations, such as Ca^{2+} [5]. However, alginate scaffolds present limitations for bone defect treatment due to their poor bioactivity [6]. Accordingly, HA is used as filler in bone composite scaffolds because of its high biocompatibility, strong reabsorption ability, adequate cell adhesiveness and outstanding bioactivity [7,8].

Alginate inks are widely used to obtain 3D-scaffolds through different technologies because of their low toxicity and easy/fast crosslinking ability. 3D-printing is a disruptive and precise technology for the processing of bone scaffolds with patient-specific shapes using a CAD [9,10]. It is used to deposit living and non-living materials in a predesigned pattern using layer-by-layer deposition to fabricate bioengineered structures for regenerative medicine applications [11]. 3D-printing methods for bone tissue engineering can be classified by the technological approach in three groups: light-based, material jetting (inkjet, microvalve, laser and acoustic printing) and

USC DE COMPOSTELA

material extrusion [12,13]. Light-based printing by stereolithography, digital light processing or two-photon polymerization exploits the use of a light pulse to induce the photopolymerization of the ink in a spatially selective manner and in repeated cycles to obtain complex 3D-designs. This technology is fast and has a high resolution but uses complex equipment in terms of process control. Additionally, light-emitting diodes can induce cell damage and ink degradation. Material jetting or drop-on-demand printing is a technology able to obtain 3D scaffolds by material patterning dropwise (nano- to picolitres droplet range) and allow the incorporation of cells into personalized designs with high resolutions. However, the inks should have low viscosity for jetting, and their application is usually limited to soft tissue engineering. Extrusion-based printing is a particularly promising alternative for the fabrication of scaffolds to regenerate human tissues [14]. It is an automated manufacturing technique that allows biomaterial deposition with highly complex 3D structures to create a substrate through a pneumatic- or mechanical-driven extrusion. This method can use inks with high viscosities and is easily scalable, reproducible, and results in personalized scaffolds to allow the fabrication of patient-specific tissue-engineered constructs [15]. Precise control of the nanoscale topography of 3D-printed scaffolds is still a challenge usually carried out by post-processing approaches [16–18].

Aerogels are advanced nanostructured materials with high mesoporosity, among other extraordinary and tunable physicochemical properties of interest for regenerative medicine (high specific surface area and low density) [19–22]. Aerogels are typically obtained by the $scCO_2$ drying of gels, as this solvent extraction approach can preserve the hydrogel nanostructure in the dry form. For this reason, the aerogel technology could help to solve the lack of nanostructuration of the 3D-printed structures, one of the current 3D-printing limitations [23]. Nevertheless, the production of aerogels with customized external and internal structures is still a remarkable challenge [24,25]. In this context, the technological combination of 3D-printing technology and $scCO_2$ drying results in alginate-HA aerogel-based scaffolds with a high fidelity with respect to the original CAD design and the complex nanostructure required for bone tissue

USC UNIVERSIDADE DE SANTIAGO DE COMPOSTELA

engineering applications [7]. Nevertheless, these 3D-printed aerogels should present enhanced properties regarding their degradation behavior in biological fluids, their mechanical integrity, and their sterility conditions to be compliant with regulations for implantable medical devices.

Bone grafts should be manufactured as a structure that mimics the biomechanical behavior of the native bone [6,26] and bears the anatomical and functional efforts that suffered by the damaged area [27,28]. Different alternatives are employed to improve the performance of the scaffolds aimed at bone tissue engineering [29,30]. For instance, HA is commonly employed to yield biological and structural properties comparable to that of human bone [26,31]. Additionally, crosslinking strategies enhance the mechanical, biological and degradation properties of bone substitutes [32,33]. This process of network bonding formation is essential in scaffolding to improve the biomechanical performance of implants [34,35]. Chemical crosslinking is more effective than physical crosslinking (e.g., UV-radiation) and is extensively used to manufacture bone scaffolds due to its ability to undergo chemical modifications in the polymeric backbone that yields high crosslinking degrees [34]. GA is a commonly employed chemical crosslinker on biopolymeric scaffolds [36,37] that significantly improves the reinforcement and durability of biomaterials [33,38]. It reacts with amine or hydroxyl groups of polymers through a Schiff-base reaction that results in strongly crosslinked networks [39]. Nevertheless, aldehyde groups of unreacted GA are toxic for cells as they induce inflammation [40,41]. Thus, several detoxifying strategies are developed to increase the biocompatibility of GA-crosslinked scaffolds [42], such as washing the crosslinked structures with free amine groups solutions to remove the free aldehyde groups [33]. On the other hand, the combination of different crosslinking methods to reduce the cytotoxic effects and to improve the cost-effectiveness of the overall process is nowadays a trend in tissue engineering [33,43].

Finally, the sterilization of biomaterials prior to being implanted is crucial to avoid post-surgical complications [44]. Sterilization is defined as the absence of life and biological agents (fungi,

USC DE COMPOSTELA

bacteria, and viruses) [45]. It is commonly achieved by heat, chemicals, irradiation, or filtration by membranes. Common sterilization techniques such as steam, ethylene oxide and gamma irradiation impact negatively on scaffold structures affecting their physicochemical properties and, consequently, their biological performance [46]. The use of $scCO_2$ in combination with chemical additives is a low-temperature and radiation-free alternative to sterilize biomaterials [47].

The recently proposed combination of 3D-printing and $scCO_2$ technology yielded bone tissue engineering scaffolds with high biological and structural performance [7]. A dual crosslinking strategy ($CaCl_2$ ageing and GA vapor) is herein proposed with the aim of improving the integrity and customization of the aerogels while maintaining its superior performance and fidelity to the original CAD file. In this work, extrusion-based 3D-printing will be employed to obtain personalized 3D-scaffolds with a complex nanostructure preserved after $scCO_2$ drying, structural integrity, and customized designs. The dual crosslinking of alginate-HA scaffolds will be obtained by the $CaCl_2$ gelation and ageing of hydrogels and by GA-crosslinking of aerogels. Bioactivity, cell toxicity, hemocompatibility, and textural properties of aerogels will be evaluated regarding personalized medicine and bone tissue engineering applications. Finally, $scCO_2$ is also herein evaluated as a sterilizing technique to obtain personalized aerogel scaffolds ready for patient implantation.

4.2. Materials and Methods

4.2.1. Materials

Alginic acid sodium salt from brown algae with medium viscosity (guluronic acid/mannuronic acid ratio of 70/30, Mw 403 kDa, 3170 cps) and $CaCl_2$ (Mw 110.98 g/mol, 99.99% purity) were provided by Sigma Aldrich (Madrid, Spain) and HA (Mw 502.31 g/mol, reagent grade purity, micropowder) by Fluidinova (Moreira da Maia, Portugal). GA (50% aqueous solution) was

USC
DE SANTIAGO
DE COMPOSTELA

supplied by Scharlau (Barcelona, Spain), H_2O_2 (30% aqueous solution) by Honeywell Fluka (Madrid, Spain), CO_2 (purity > 99.9%) by Nippon Gases (Madrid, Spain) and absolute EtOH by VWR (Radnor, PA, USA). Water was purified by reverse osmosis (resistivity > 18 MΩ·cm; Milli-Q, Millipore®, Madrid, Spain).

4.2.2. 3D-printing of hydrogels

Aqueous 6 wt.% alginate solutions were prepared and different HA concentrations (0, 8, 16 and 24 wt.% with respect to water) were added. Inks were prepared under vigorous agitation (600 rpm), employing a homogenizer (VWR vos 60, Radnor, PA, USA) for at least 1 h at RT. The alginate solutions were degassed in a sonication bath (Branson 3510 Emerson, Ferguson, MO, USA) for 10 min to eliminate air bubbles. Hydrogels were obtained by 3D-printing of the alginate inks with a Cellink BIOX Bioprinter (Boston, MA, USA) at RT, using an extrusion printhead with a 3-mL syringe and a 410-µm nozzle at the printing pressure of 60 kPa, and a printing velocity of 12 mm/s. Scaffolds with dimensions of 2 x 2 x 0.1 cm^3 were obtained with a grid pattern and three layers. After the 3D-printing process, all scaffolds were put in contact with $CaCl_2$ 1M aqueous bath for gelation during 1 h (ageing step). For the comparison of the physicochemical characterization, alginate gel scaffolds were aged with $CaCl_2$ 0.5M for 1 h.

4.2.3. Rheological evaluation of alginate-HA inks

Alginate-HA inks were mechanically characterized by applying two independent tests at 20 °C. Flow behavior was recorded between 0.05 and 200 rad/s in a Rheolyst AR-1000N rheometer (TA Instruments, Newcastle, UK) equipped with a Peltier plate and a cone geometry (40 mm diameter, 2°) with a solvent trap. Viscoelastic behavior and shear-thinning properties were analyzed using a rheometer (Anton Paar MCR 302, Graz, Austria) fitted with a H PTD 200 Peltier hood and a disposable measuring aluminum plate (15 mm diameter) with 1 mm gap. Five steps in amplitude sweep mode were performed to simulate the rests and high-stress conditions of the inks before, during and after printing. The storage (G') and the loss (G") moduli were

USC UNIVERSIDADE DE SANTIAGO DE COMPOSTELA

recorded at (i) 0.5% shear strain at 1 Hz for 300 s (data points every 12 s); (ii) 100% shear strain at 1 Hz for 120 s; (iii) 0.5% shear strain at 1 Hz for 300 s; (iv) 100% shear strain at 1 Hz for 120 s; and (v) 0.5% shear strain at 1 Hz for 300 s [48,49].

4.2.4. $scCO_2$ drying of 3D-printed alcogels

Alginate hydrogels were immersed in absolute EtOH after ageing in $CaCl_2$ 1M for 1 h. Two solvent exchanges to EtOH were carried out with an exchange frequency of 24 h. The alcogels were then wrapped in filter paper and dried by $scCO_2$ drying to obtain the aerogels. Briefly, gels were placed into a 100-mL stainless steel autoclave (Thar Process, Pittsburg, PA, USA) and immersed in 25 mL of absolute EtOH. $scCO_2$ was supplied by a dual-piston pump and introduced from the top of a vessel heated at 40 °C. A continuous CO_2 flow rate (5–7 g/min) at 120 bar took place for 4 h. Aerogels were then collected from the autoclave after a CO_2 depressurization rate of 2 bar/min and stored for characterization. The obtained scaffolds were described in Table 4.1 and denoted as AlgHA x, where x denotes the HA content (0, 8, 16, 24 wt.%). $CaCl_2$ 1M1h (alternatively $CaCl_2$ 0.5M1h) denotes aged aerogels.

4.2.5. Post-crosslinking of aerogels with GA vapor

Aerogels were crosslinked in a GA-saturated atmosphere by placing them inside a desiccator containing 100 mL of 25% (v/v) GA aqueous solution at the bottom at RT [50] without direct physical contact with the formulations. The aerogels were maintained for 1 h in the GA atmosphere, and a vacuum was then applied for 20 min to remove the unreacted GA. For the comparison of the physicochemical characterization, alginate gel scaffolds non aged with $CaCl_2$ 1M for 1 h were also crosslinked with GA. The GA-crosslinked aerogels were denoted by the suffix –GA (Table 4.1).

USC UNIVERSIDADE DE SANTIAGO DE COMPOSTELA

Table 4.1. Dual crosslinked alginate-HA aerogel formulations studied.

Aerogel Formulations	Ink Composition		Crosslinking Strategy	
	Alginate (wt.%)	HA (wt.%)	Ionic Ageing	GA Vapor
AlgHA 0, $CaCl_2$ 1M1h	6	0	$CaCl_2$ 1M bath for 1h	No
AlgHA 8, $CaCl_2$ 1M1h	6	8	$CaCl_2$ 1M bath for 1h	No
AlgHA 16, $CaCl_2$ 1M1h	6	16	$CaCl_2$ 1M bath for 1h	No
AlgHA 24, $CaCl_2$ 1M1h	6	24	$CaCl_2$ 1M bath for 1h	No
AlgHA 0, $CaCl_2$ 1M1h, GA	6	0	$CaCl_2$ 1M bath for 1h	Yes, 1 h
AlgHA 8, $CaCl_2$ 1M1h, GA	6	8	$CaCl_2$ 1M bath for 1h	Yes, 1 h
AlgHA 16, $CaCl_2$ 1M1h, GA	6	16	$CaCl_2$ 1M bath for 1h	Yes, 1 h
AlgHA 24, $CaCl_2$ 1M1h, GA	6	24	$CaCl_2$ 1M bath for 1h	Yes, 1 h

4.2.6. Physicochemical characterization of dual crosslinked aerogels

The ρ_{skel} was determined using a helium pycnometer (Quantachrome, Boynton Beach, FL, USA) at 25 °C and 1.01 bar. Values were obtained from five replicates. Envelope density (ρ_{env}) was measured using the GeoPyc 1360 Envelope Density Analyzer (Micromeritics, Nor-cross, GA, USA), employing DryFlo® powder as the fluid medium. The applied force was 25 N, and each sample was measured in five cycles. The standard deviation of the values was 0.002 g/cm^3. The ε of the dual crosslinked aerogels was determined according to Equation 4.1:

$$\varepsilon\ (\%) = \left[1 - \left(\frac{\rho env}{\rho skel}\right)\right] \cdot 100 \qquad \textit{Equation 4.1}$$

The volume shrinkage (%) of aerogels was calculated from the external dimensions of the structures before $scCO_2$ drying and after performing the dual crosslinking following Equation 4.2:

$$\textit{Volume shrinkage}\ (\%) = \left(\frac{Alcogel\ volume - Aerogel\ volume}{Alcogel\ volume}\right) \cdot 100 \qquad \textit{Equation 4.2}$$

Low-temperature N_2 adsorption–desorption analysis (ASAP 2000 Micromeritics Inc.; Norcross, GA, USA) was performed to assess the textural properties of the dual crosslinked aerogels. Samples were degassed under vacuum at 40 °C for 24 h. A_{BET} of the aerogels was evaluated employing the BET method. V_p and d_p were determined applying the BJH method. Aerogels were iridium-sputtered to minimize charging and their morphology was evaluated by SEM (SEM, EVO LS15, Zeiss, Oberkochen, Germany). Attenuated Total Reflectance/Fourier-Transform Infrared Spectroscopy (ATR/FT-IR) was performed with a Gladi-ATR accessory and a diamond crystal (Pike,

USC UNIVERSIDADE DE SANTIAGO DE COMPOSTELA

Madison, WI, USA) to evaluate the chemical structure of aerogels and raw materials in the mid-IR spectrum range (400–4000 cm^{-1}) using 32 scans and at a resolution of 2 cm^{-1}.

4.2.7. Bioactivity tests

An *in vitro* test using SBF was used to assess the bioactivity of the dual crosslinked aerogels [51]. The SBF was prepared with ion concentrations nearly equal to those of human blood plasma. Aerogels of 1 × 1 × 0.1 cm^3 were immersed in 40 mL of SBF pH 7.45 in plastic conical tubes at 37°C for 3, 7, 15 and 28 days. At the end of the experiment, the wet gels were rinsed with deionized water and dried by lyophilization. Bioactivity was analyzed by SEM focusing on the surface crystals after the mineralization and by energy-dispersive X-ray spectroscopy (SEM-EDX) [52].

4.2.8. Cell viability tests

The cytocompatibility of the dual crosslinked aerogels was determined by assessing the viability of mouse embryo fibroblasts (BALB/c 3T3) after 24 and 48 h of culture in the presence of the aerogels by the WST-1 test. This assay is based on the degradation of WST-1 into formazan and is directly correlated with the number of metabolically active cells. BALB/c 3T3 cells (6500 cells/cm^2) were seeded in 24-well plates in DMEM supplemented with 15% fetal bovine serum, penicillin 100 U/mL and streptomycin 100 g/mL. Cells were incubated at 37 °C in a humidified atmosphere enriched with 5% CO_2. Aerogels of 1 × 1 × 0.1 cm^3 were UV-sterilized for 30 min and then placed in the wells with cells containing 1500 µL of DMEM supplement. Positive controls of cells with 1000 µL of medium and blanks of 1000 µL of medium (both in triplicate) were maintained at the same conditions. After 24 and 48 h of culture, scaffolds were removed, 250 µL of the medium was left in the wells and 25 µL of WST-1 was added. The plate was incubated for 2 h at the same conditions and then shaken thoroughly for 1 min. Finally, 110 µL were transferred to a 96-well plate to measure the absorbance at λ = 450 nm in a microplate reader (Infinite® M200, Tecan Group Ltd., Männedorf, Switzerland).

USC UNIVERSIDADE DE SANTIAGO DE COMPOSTELA

4.2.9. Hemolytic activity test

The hemolytic activity of the dual crosslinked aerogels was evaluated by triplicate using human blood (Galician Transfusion Center, Spain) obtained in accordance with the rules of the Declaration of Helsinki. Fresh human whole blood was diluted to 3% (v/v) in 0.9% (w/v) NaCl solution and 1 mL of the diluted blood was transferred to Eppendorf tubes containing 1 × 1 × 0.1 cm^3 aerogels, 100 µL of 4% (v/v) Triton X-100 (positive control) or 100 µL of PBS pH 7.4 (negative control). Samples were incubated for 1 h at 37°C and 100 rpm in an orbital shaker and then centrifuged at 10.000 g for 10 min (Sigma 2-16P, Sigma Laboratory Centrifuges, Osterode am Harz, Germany). 150 µL of the supernatant were transferred to a 96-well plate, and the absorbance of the hemoglobin was measured at λ = 540 nm (FLUOStar Optima, BMG Labtech, Ortenberg, Germany). The hemolysis (%) of the aerogels was determined using Equation 4.3:

$$Hemolysis\ (\%) = \left(\frac{Abss - Absn}{Absp - Absn}\right) \cdot 100 \qquad Equation\ 4.3$$

where Abss is the absorbance of the samples containing the aerogels, Absn is the absorbance of the negative control, and Absp is the absorbance of the positive control.

4.2.10. scCO$_2$ sterilization of 3D-printed aerogels

Dual crosslinked aerogels were introduced into individually and thermally sealed sterilization pouches and placed in a high-pressure 600-mL autoclave (NovaGenesis, NovaSterilis Inc., Ithaca, NY, USA) with 1200 ppm of H_2O_2, at 40 °C and pressurized with CO_2 until 100 bar. After 30 min of contact time, the system was depressurized at a constant flow rate of 5 bar/min until atmospheric pressure. Dual crosslinked formulations were then seeded in TSA plates for CFU quantification and also incubated for 24 h in TSB tubes. The structural stability of sterilized aerogels was evaluated in terms of textural properties by BET and SEM analyses.

USC UNIVERSIDADE DE SANTIAGO DE COMPOSTELA

4.2.11. Statistical analysis

Results were reported as mean value ± standard deviation and Post hoc Tukey HSD multiple comparison tests were performed to assess the statistical significance of the differences among the groups. Values of $p < 0.05$ were considered as statistically significant.

4.3. Results and Discussion

4.3.1. Rheological properties of alginate-HA inks

Inks for 3D-printed hydrogels should present good biocompatibility, adequate rheological behavior, and a quick crosslinking capacity [53]. Specifically, viscoelastic response during the extrusion-based printing process is critical. Under rest-like conditions, G" was higher than G' for all ink formulations studied (Fig. 4.1a,b), indicating a dominant viscous component. This "liquid-like" behavior is ideal for the extrusion-based 3D-printing [54]. The moduli were notably higher for inks containing HA, which evidenced the reinforcement role of this inorganic material in the mechanical properties of the inks. Under high shear strain conditions, both moduli underwent a rapid decrease, which was highly remarkable for G'. This steep decrease in G', more intense than for G", suggested that the physical entanglements among the alginate chains easily decreased and the chains oriented in the direction of the stress, which may facilitate the extrusion process. Remarkably, once the strain disappeared, the ink recovered the initial G' and G" showed at rest, which indicated a rapid recovery of the initial entanglements. This behavior is needed for the ink to maintain the desired shape after extrusion. Sequential cycles of low–high strain evidenced the reproducible mechanical performance of the alginate inks. Flow tests (Fig. 4.1c,d) confirmed the intense shear-thinning behavior of all inks (with and without HA) at low shear stress conditions, which should facilitate the extrusion process at moderate pressures [55].

USC UNIVERSIDADE DE SANTIAGO DE COMPOSTELA

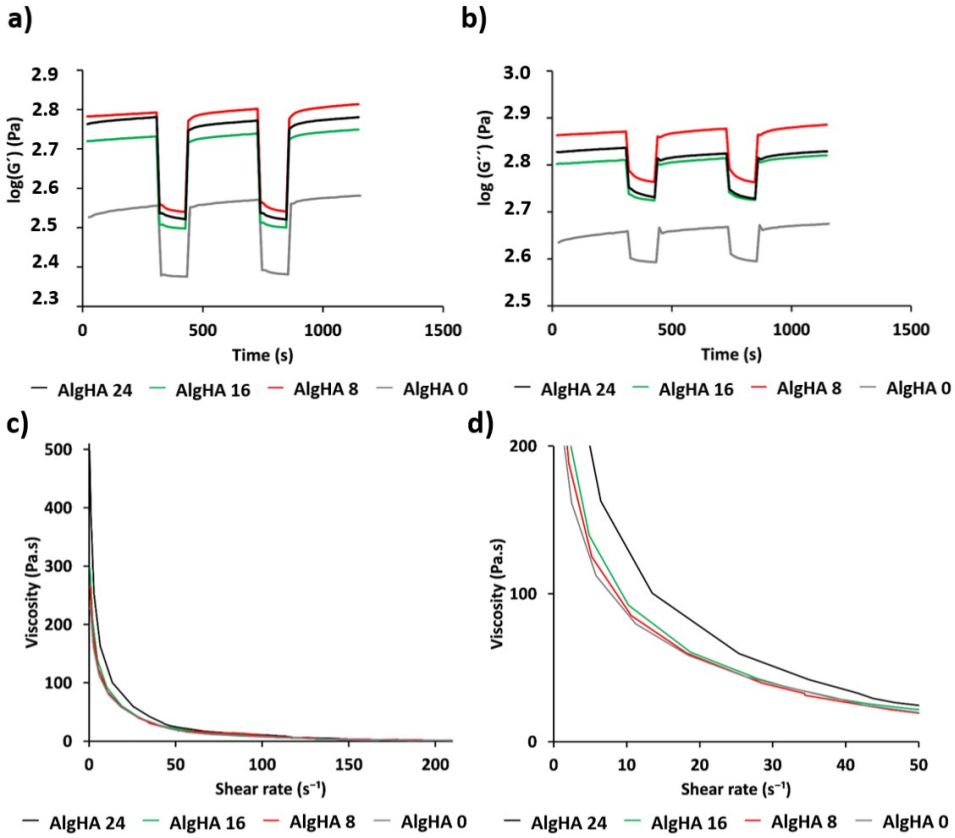


Figure 4.1. Rheological characterization of alginate-HA inks. **a,b)** Time variation of storage and loss moduli (G' and G'', respectively). **c, d)** Overall viscosity variation with respect to the shear rate.

4.3.2. Effect of ageing of aerogels

The technological combination of 3D-printing and aerogel processing previously used for the preparation of non-aged alginate-HA aerogels [7] was herein coupled with extra crosslinking steps (ageing in $CaCl_2$ 1M and exposing to GA vapor) to manufacture scaffolds with personalized and enhanced crosslinking degrees. The 3D-printing step allows the customization of the structures while the $scCO_2$ processing results in nanostructured aerogels, thus fulfilling two of the requirements for bone tissue engineering applications.

Aerogels showed, in all cases, homogeneous structures following good shape fidelity with respect to the grid pattern of the CAD and composed of fibers with similar dimensions correctly arranged in layers (Fig. 4.2 and 4.3). In the absence of HA, the hydrogel ageing in $CaCl_2$ 1M for 1

USC DE COMPOSTELA

h (AlgHA 0, $CaCl_2$ 1M1h, Table 4.2 and Fig. 4.2c,d) incremented the textural properties (A_{BET}, d_p and V_p) of the resulting aerogels with respect to the same formulations obtained without the ageing step (AlgHA 0, $CaCl_2$ 1M, Table 4.2 and Fig. 4.2a,b). This increase in textural parameters was also observed when the ageing step was alternatively performed in $CaCl_2$ 0.5M bath (AlgHA 0, $CaCl_2$ 0.5M1h, Table 4.2) with respect to the non-aged aerogel counterpart (AlgHA 0, $CaCl_2$ 0.5M, Table 4.2). The same trend in the textural properties between aged and non-aged aerogels was observed in all the formulations studied with different HA contents. The ageing step during the aerogel processing increases the crosslinking degree in the scaffolds (without layers exfoliation and with high structural integrity). This feature and the different pore sizes and morphologies observed in SEM images, are highly desirable for bone tissue engineering applications.

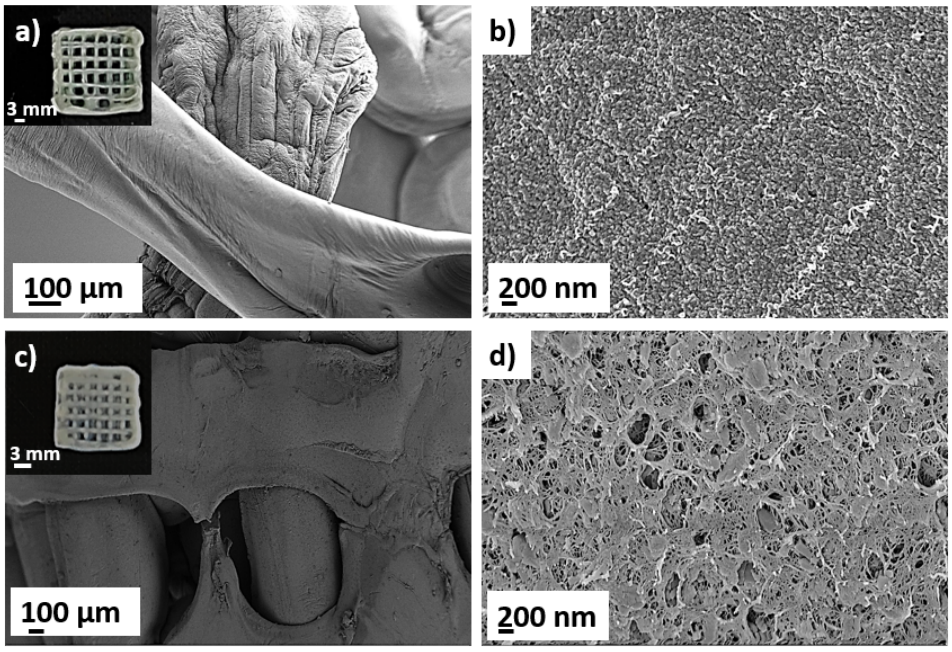


Figure 4.2. SEM images of 3D-printed aerogels. **a,b)** AlgHA 0, $CaCl_2$ 1M. **c,d)** AlgHA 0, $CaCl_2$ 1M1h. Aerogels were observed at two different magnifications. Intake in **a,c)** Visual appearance of the aerogels with a well-defined 3D-pattern.

USC UNIVERSIDADE DE SANTIAGO DE COMPOSTELA

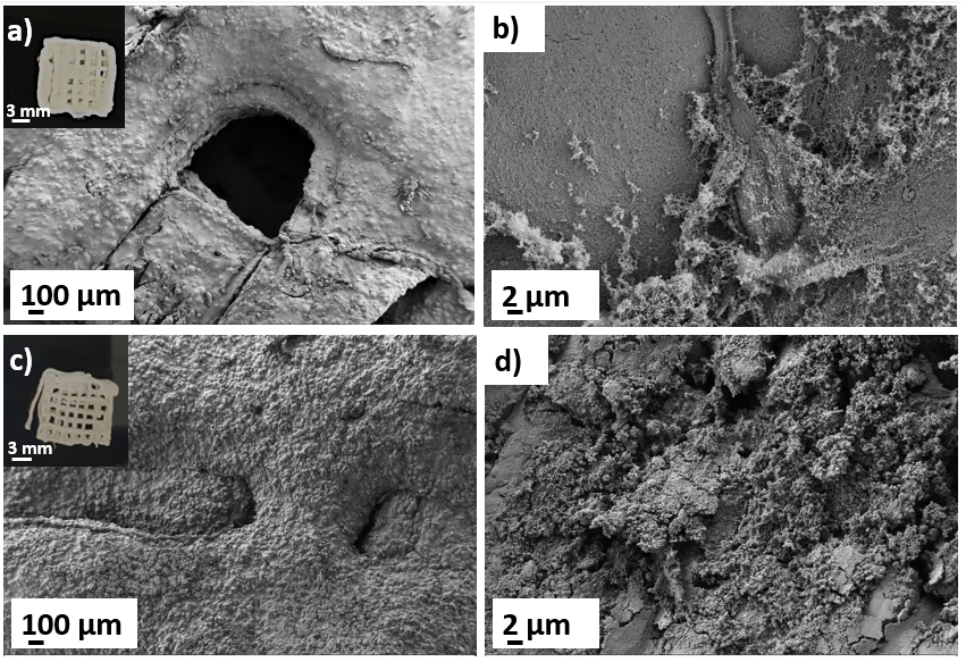


Figure 4.3. SEM images of 3D-printed and aged aerogel scaffolds. a,b) AlgHA 16 $CaCl_2$ 1M1h. c,d) AlgHA 16 $CaCl_2$ 1M1h. Intake in **a,c)** Visual appearance of the aerogels with a well-defined 3D-pattern.

Table 4.2. Textural properties of aerogels crosslinked by different strategies: $CaCl_2$ 0.5M1h/ 1M1h (aged aerogels), $CaCl_2$ 1M (non-aged aerogels) and GA (GA-crosslinked aerogels). **Notation:** A_{BET}: BET-specific surface area, d_p: BJH-mean pore diameter, V_p: BJH-specific pore volume, ρ_{env}: envelope density, ρ_{skel}: skeletal density, ε: scaffold porosity.

Aerogel Scaffold	A_{BET} (m^2/g)	d_p (nm)	V_p (cm^3/g)	ρ_{env} (g/cm^3)	ρ_{skel} (g/cm^3)	ε (%)
AlgHA 0, $CaCl_2$ 1M*	183 ± 9	19 ± 1	1.16 ± 0.06	0.14 ± 0.01‡	1.18 ± 0.16	86.58 ± 2.26
AlgHA 8, $CaCl_2$ 1M*	118 ± 6	24 ± 1	0.99 ± 0.05	0.24 ± 0.03‡	1.72 ± 0.09	85.25 ± 4.02
AlgHA 16, $CaCl_2$ 1M*	67 ± 3	26 ± 1	0.60 ± 0.03	0.29 ± 0.04‡	1.93 ± 0.04	79.78 ± 3.92
AlgHA 24, $CaCl_2$ 1M*	29 ± 2	31 ± 2	0.21 ± 0.01	0.34 ±0.02‡	1.72 ± 0.14	76.68 ± 3.54
AlgHA 0, $CaCl_2$ 0.5M1h	453 ± 23	25 ± 1	3.21 ± 0.16	0.18 ± 0.01‡	1.81 ± 0.08	90.32 ± 0.81
AlgHA 0, $CaCl_2$ 1M1h	244 ± 12	24 ± 1	1.74 ± 0.1	0.19 ± 0.003	1.44 ± 0.09	86.78 ± 0.88
AlgHA 8, $CaCl_2$ 1M1h	81 ± 4	26 ± 1	0.68 ± 0.03	0.41 ± 0.003	2.29 ± 0.03	82.27 ± 0.24
AlgHA 16, $CaCl_2$ 1M1h	49 ± 3	28 ± 1	0.39 ± 0.02	0.55 ± 0.003	2.38 ± 0.04	76.86 ± 0.35
AlgHA 24, $CaCl_2$ 1M1h	65 ± 3	28 ± 1	0.69 ± 0.03	0.63 ± 0.003	2.71 ± 0.05	76.77 ± 0.47
AlgHA0, $CaCl_2$ 1M, GA	112 ± 6	19 ± 1	0.72 ± 0.04	0.22 ± 0.07‡	1.49 ± 0.05	85.45 ± 4.60
AlgHA 8, $CaCl_2$ 1M, GA	91 ± 5	21 ± 1	0.66 ± 0.03	0.41 ± 0.09‡	1.84 ± 0.04	77.50 ± 4.80
AlgHA 0, $CaCl_2$ 1M1h, GA	26 ± 1	19 ± 1	0.15 ± 0.01	0.52 ± 0.09	1.96 ± 0.19	73.32 ± 2.62
AlgHA 8, $CaCl_2$ 1M1h, GA	28 ± 1	24 ± 1	0.21 ± 0.01	0.68 ± 0.09	2.16 ± 0.09	68.58 ± 1.41
AlgHA 16, $CaCl_2$ 1M1h, GA	21 ± 1	32 ± 2	0.24 ± 0.01	0.94 ± 0.20	2.33 ± 0.09	59.58 ± 1.47
AlgHA 24, $CaCl_2$ 1M1h, GA	21 ± 1	24 ± 1	0.19 ±0.01	0.97 ± 0.13	2.37 ± 0.05	59.14 ± 0.87

* Data obtained from the ref. [7]. ‡ Data calculated following the procedure reported in ref. [7]).

The incorporation of HA favored the printability of the ink with respect to the ones without HA. Nevertheless, the printability decreased when the HA concentration in the inks reached the threshold value of 24 wt.%, mainly due to the difficulty in the extrusion of the ink by the printer.

USC UNIVERSIDADE DE SANTIAGO

This could be due to the increase in strength of alginate hydrogels when increasing HA concentrations are used [56]. It can also be attributed to the chemical reaction between the Ca^{2+} of the HA surface and the -COO− groups of the alginate that results in an ionic bonding that increase the strength of the structures [56]. All the HA-containing aerogels were highly porous structures with mesopores and macropores homogeneously distributed (Fig. 4.3). The highest porosity values (86–87%) were obtained for aerogels without HA. The porosity of the aerogels decreases with increasing HA content (Table 4.2), which is coherent with the density values (ρ_{skel} and ρe_{nv}) and with previously reported results for non-aged aerogel formulations [7].

Finally, several macropores are clearly recognized in aged aerogels, which are homogeneously distributed following the CAD structure (Fig. 4.2). Macropores in the 100–400 µm range, as in these structures, are considered sufficient to allow bone ingrowth and regeneration [57]. Both biological processes are strongly dependent on the microporosity pattern of the structure as only pore diameters higher than 50 µm promote cell infiltration and bone mineralization [3]. Nevertheless, this pore size range may be detrimental to the scaffold textural properties increasing permeability and degradation [57]. Thus, microporosity and textural parameters (A_{BET}, d_p and V_p) must be balanced to promote an appropriate bone tissue regeneration. The enhanced dual porous structure and integrity obtained after the $CaCl_2$ ageing step could generate scaffolds that enable the balance between the natural bone healing process and the degradation of the 3D-printed construct.

4.3.3. Effect of GA chemical post-crosslinking of aerogels

Dual crosslinked aerogel scaffolds obtained after performing the GA vapor crosslinking step exhibit a compact structure with all layers well organized and bonded, resulting in entire, highly crosslinked, and personalized structures (Fig. 4.3). The customized 3D-printed pattern was successfully preserved after GA crosslinking as well as the individual fibers and the end scaffold (Fig. 4.3). SEM images show that the porous structure and architecture, as well as the HA

USC UNIVERSIDADE DE SANTIAGO

granules integrity, were preserved in the aerogels after all processing steps (Fig. 4.3c,d). These observations are coherent with previous studies where GA vapor treatment for less than 6 h caused very slight modifications on scaffold architectures, while longer periods induced important modifications on scaffold nano- and microarchitecture and toxicity [39]. Furthermore, the absence of exfoliation layers in the dual crosslinked samples with respect to the non-aged ones induces higher structural integrity in the end aerogels that improves the customization of the structures as well as the fulfillment of the bone tissue engineering requirements. An increase in ρ_{env} and a decrease in ρ_{skel} was observed after the GA treatment, suggesting higher crosslinking and a more compact end structure in the dual crosslinked aerogels than in the non-GA treated aerogels. Density reduction after GA crosslinking was previously reported in scaffolds with a similar composition for bone regeneration purposes [38]. In general, a decrease in textural properties (A_{BET}, V_p, and ε) was observed for the dual crosslinked aerogels with respect to the ones crosslinked only with Ca_{2+} ions (Table 4.2). Textural properties of the non-aged and GA-crosslinked aerogels (AlgHA0, $CaCl_2$ 1M, GA and AlgHA 8, $CaCl_2$ 1M, GA formulations, Table 4.2) were also assessed to check if each crosslinking method is contributing, by itself, to the overall decrease in these properties. A similar reduction in textural parameters was found when non-aged and GA-crosslinked aerogels were compared with the non-aged aerogels [7]. A similar trend was previously described in structures with similar composition and crosslinked with GA vapor and/or $CaCl_2$ [36,58]. According to SEM images, the decrease in textural parameters could be due to the effect of the crosslinking agent on the morphology of the fibers that leads to the fusion of alginate fibers at their junctions [58].

In general, the dual crosslinking procedure favors the ionic interactions between alginate and Ca^{2+} and the covalent bonds due to GA. These reactions result in aerogels with improved integrity, durability, and customization with respect to the structures obtained without dual crosslinking. All these features are highly desirable for personalized bone medicine and turn the dual crosslinked alginate-HA aerogels into promising candidates for this challenging application.

USC UNIVERSIDADE DE SANTIAGO DE COMPOSTELA

The volume shrinkage of the dual crosslinked aerogel scaffolds was also measured to evaluate if both crosslinking strategies, as well as the direct solvent exchange into EtOH, have a relevant effect in terms of volumetric change in the aerogels. The formulations with higher HA content have lower volumetric shrinkage than those without HA (<50%, Fig. 4.4), as previously described for same formulations without the dual crosslinking [7]. Furthermore, similar values were found for alginate-HA and dual crosslinked formulations, suggesting that the dual crosslinking strategy does not induce a higher volume shrinkage in the resulting aerogels. Other alginate aerogels showed higher shrinkage values (70–80%) with the same solvent exchange steps [59]. The obtained results suggest that the dual processing strategy improves the integrity of the material and reduces the volume shrinkage thus allowing the obtention of customized aerogels.

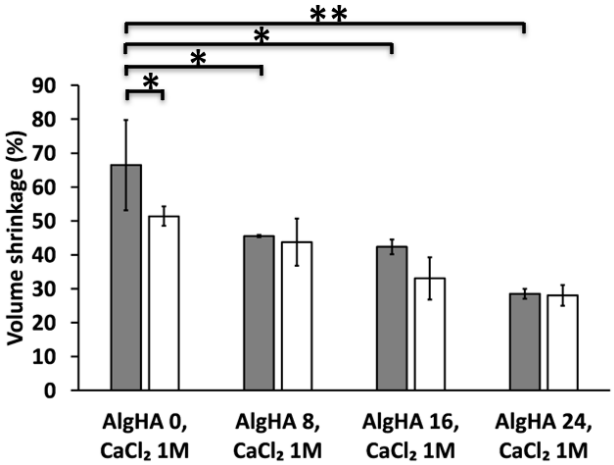


Figure 4.4. Volume shrinkage (%) of different alginate-HA aerogels without (grey bars; source: ref. [7]) and with the dual crosslinking treatment (white bars; this work).

4.3.4. Chemical analysis of dual crosslinked aerogels

ATR/FT-IR spectra of aerogels are displayed in Fig. 4.5. The main differences observed were related to a general reduction in the relative intensity of bands when aerogels are dual crosslinked with respect to the structures aged only with $CaCl_2$. This effect is probably due to a weakening in the intramolecular bonding as the bonds stretch to accommodate the coordination structure around the Ca^{2+} ion [60]. Specifically, a decrease in the intensity of the band at 1608

USC UNIVERSIDADE DE SANTIAGO DE COMPOSTELA

cm^{-1} (green asterisks in Fig. 4.5) and the appearance of the band relative to imine at 1644 cm^{-1} suggest effective GA crosslinking (purple asterisks in Fig. 4.5) [39]. Regarding the GA effect, GA reacts with hydroxyl groups of alginate through a Schiff-base reaction connecting the polymeric chains via intra- or intermolecular bonds and forming a more strongly crosslinked network [61]. Finally, the differences in the pure alginate spectrum with respect to Ca^{2+} crosslinked alginate spectra were due to ionic binding resulting from the interaction between the –COO− groups of alginate with Ca^{2+} as it is shown in all alginate aerogels with respect to alginate powder (Fig. 4.5) [60]. Specifically, the –COO− asymmetric stretching band at 1590 cm^{-1} results from the interaction between Ca^{2+} and alginate –COO− groups (red asterisks in Fig. 4.5). Additionally, the –COO− symmetric stretching band at 1414 cm^{-1} is shifted toward lower wavenumbers, thus indicating ionic binding between Ca^{2+} and alginate –COO− (grey asterisks in Fig. 4.5) [60].

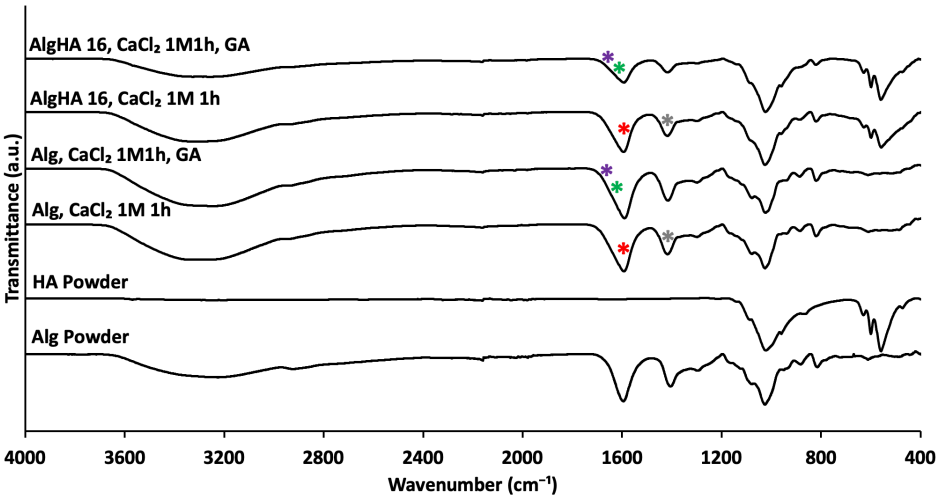


Figure 4.5. ATR/FT-IR spectra of aerogels. The spectra of the raw materials (alginate and HA powder) are also included for the sake of comparison.

4.3.5. Bioactivity tests of dual crosslinked aerogels

Scaffolds can bond to the living bone by forming bone-like apatite on its surface. This *in vivo* bone bioactivity process can be mimicked *in vitro* using an SBF medium to predict the apatite formation on the scaffold surface after its immersion in the said medium [62]. Aerogels not aged

USC UNIVERSIDADE DE SANTIAGO

in $CaCl_2$ and without GA post-crosslinking were completely disintegrated and partially dissolved after a short time in an SBF medium (less than 3 days). However, the physical stability of the aerogel scaffolds in aqueous media in the long term was significantly improved after the dual-crosslinking process (i.e., $CaCl_2$ ageing and crosslinking with GA vapor). Indeed, GA crosslinking was previously reported to significatively increase the *in vitro* half-life of collagen matrices [63].

White granules appeared on aerogel scaffold surfaces after 28 days of immersion in SBF medium (Fig. 4.6). EDX analysis of these granules confirmed to be calcium phosphate (Fig. 4.6e; spectrum 1) since there was a clear enhancement of the Ca, P and O peaks with respect to the background region (Fig. 4.6e; spectrum 2). This formation of calcium phosphate suggests good binding between organic and inorganic components of the aerogel scaffold, which is essential for the integrity and functionality of the bone [3]. Moreover, a high Ca/P ratio was found after SBF immersion for 28 days, thus suggesting the stimulation of the bone tissue deposition formation and functionality [3, 64]. The presence of HA and its uniform distribution throughout the aerogels favored higher bioactivity with increasing HA content (Fig. 4.6), as reported for scaffolds of similar composition (alginate/cellulose/HA) left in SBF for the same time [64]. Finally, HA granules grew during the immersion period in SBF medium at day 28 with respect to the predominant size at day 3 (Fig. 4.7), suggesting a progressive formation of apatite as previously described for alginate-HA and for alginate-bioactive glass composites left in SBF for the same time [65]. The enhancement of the bone mineralization process suggests the potential application of the dual crosslinked alginate-HA aerogel scaffolds for bone tissue engineering.

USC UNIVERSIDADE DE SANTIAGO DE COMPOSTELA

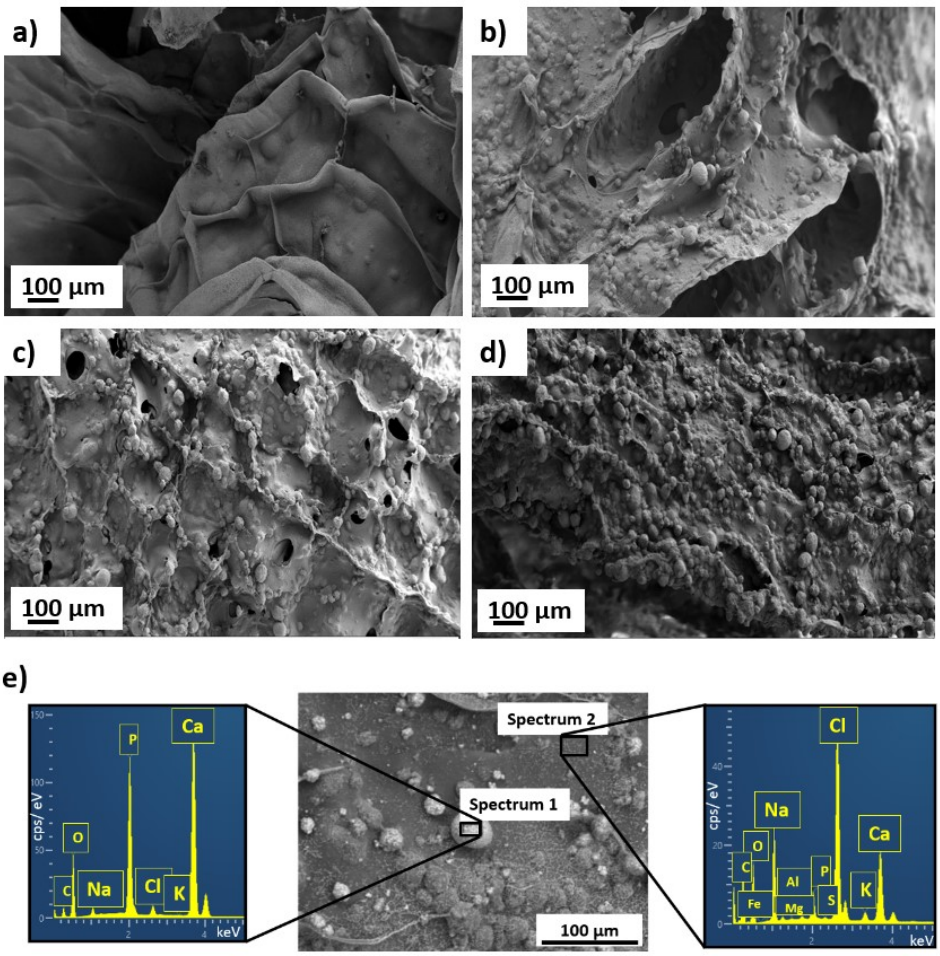


Figure 4.6. SEM pictures of different formulations of aerogels after bioactivity tests. **a)** AlgHA 0, $CaCl_2$ 1M1h, GA; **b)** AlgHA 8, $CaCl_2$ 1M1h, GA; **c)** AlgHA 16, $CaCl_2$ 1M1h, GA; **d)** AlgHA 24, $CaCl_2$ 1M1h, GA. **e)** EDX spectra of AlgHA 8, $CaCl_2$ 1M1h, GA aerogels after SBF assay in an apatite granule region (Spectrum 1, left) and in a background region (Spectrum 2, right), and representative of all the tested samples.

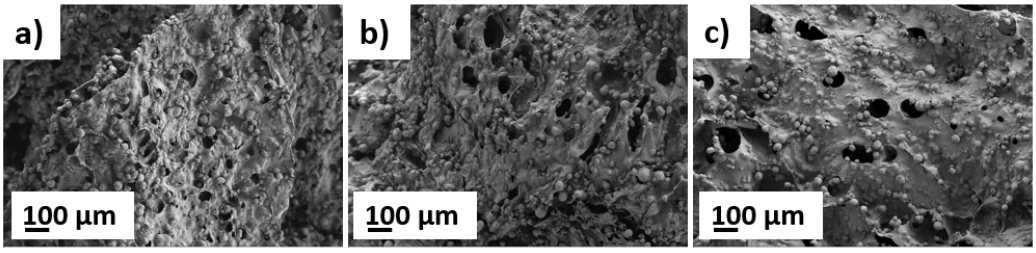


Figure 4.7. SEM pictures of AlgHA 24, $CaCl_2$ 1M1h, GA aerogels after bioactivity test. Aerogels were left in SBF medium for **a)** 3, **b)** 7 and **c)** 15 days.

4.3.6. Cell compatibility of dual crosslinked aerogels

USC UNIVERSIDADE DE SANTIAGO DE COMPOSTELA

GA was reported to increase the crosslinking density of biomaterials by creating a more rigid network due to the formation of covalent bonds (Schiff bases) [53]. Nevertheless, its application

is restricted because the chemical modification generated by GA usually results in significant cytotoxicity, as the aldehyde groups from GA incorporated into biopolymers induce inflammatory responses in soft tissues causing the failure of the regenerative process [41,53].

The BALB/c 3T3 cells viabilities present values reaching ca. 100% after 24 and 48 h of culture with different aerogel formulations crosslinked with GA vapor (Fig. 4.8). No negative effect on cell growth was thus unveiled due to the dual crosslinking strategy being regarded as a safe method.

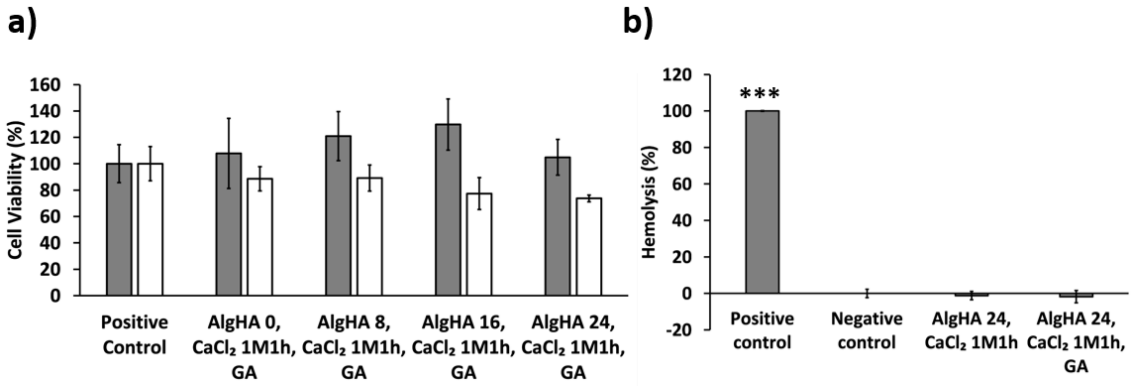


Figure 4.8. a) Viability (%) of BALB/c 3T3 cells after 24 (grey bars) and 48 h (white) of contact with dual crosslinked aerogels determined by WST-1 test. **b)** Hemolytic activity tests of dual crosslinked aerogels. Positive control: Triton solution + blood; negative control: PBS solution pH 7.4 + blood.

The high biocompatibility observed for all the aerogel formulations pointed out that neither the scaffold composition nor the processing strategy compromised the cell viability. The high cell viability observed for these aerogel structures correlates well with scaffolds of similar composition [7,66] and with the biocompatibility of the initial com-ponents of the scaffolds (alginate and HA) [67]. Furthermore, the employed strategy avoids the use of chemical agents (i.e., sodium metabisulfite and sodium borohydride) commonly needed after GA treatment to restore the material's biocompatibility [53]. However, these results contrasted with previous experiments with 3D-structures of similar composition and crosslinked with GA where low cell viability was reported [36]. The different methodology employed to perform the GA-crosslinking process (GA immersion vs. GA atmosphere) may explain these different biological behaviors.

USC UNIVERSIDADE

These results suggest that the gaseous GA-crosslinking method can shorten the overall processing time with respect to GA-immersion by avoiding the use of detoxifying strategies (e.g., washing with free amine groups solutions or amino acid solutions) commonly needed in the latter case [33] [61]. Thus, the GA vapor post-processing method could contribute to the optimization of the GA-based crosslinking to maximize the physicochemical performance of biomaterials and minimize its toxicity risk.

4.3.7. Hemolytic activity of dual crosslinked aerogels

Biomaterials for tissue engineering applications must be cytocompatible with red blood cells and do not interfere with the hemostatic activity since they are going to be placed in a damaged area in direct contact with this cell type. Furthermore, an important stage of the cell proliferation and repair process is the formation of new blood vessels (angiogenesis). Therefore, the determination of the hemocompatibility of the aerogel scaffolds is essential to exclude the possibility of blood traumas that these structures can generate [68]. According to ISO 10993-4 guidelines, materials with hemolysis values lower than 5% can be safely used.

Alginate-HA aerogels were highly compatible with the red blood cells with virtually no hemolytic activity (Fig. 4.8b) and present lower hemolytic activity than other HA scaffolds proposed for bone repair [69]. GA-crosslinking of aerogels did not alter their hemolytic behavior, so dual crosslinked alginate-HA aerogels are non-hemolytic biomaterials and meet the requirement for the biological evaluation of medical devices with respect to hemolysis.

4.3.8. Sterilization of dual crosslinked aerogels

$scCO_2$ technology was employed as a biomaterial processing method, but it is also described as a sterilizing technique convenient for grafts prior to patient implantation [44], so this possibility was herein explored. The absence of microbial growth was found on TSA plates and TSB tubes after $scCO_2$ sterilization (Fig. 4.9a). Textural and morphological properties of dual crosslinked aerogels were preserved after the sterilization procedure (Table 4.3, Fig. 4.9b–e) with respect to

USC UNIVERSIDADE DE SANTIAGO DE COMPOSTELA

the same aerogels before this post-processing step (Table 4.2, Fig. 4.3). Similar findings in terms of textural properties for other alginate composites sterilized with $scCO_2$ were previously reported [44]. Nevertheless, other polysaccharide sources for aerogels showed differing results when submitted to the same processing conditions [45]. These features highlight the importance of defining a sterilization strategy suitable for biomaterials components and structure. The mild conditions of temperature (40 °C), pressure (100 bar) and contact time (30 min) herein reported are therefore compatible with the sterilization of 3D-printed alginate-HA aerogels without compromising their structural stability. These results provide future perspectives toward the development of implants in the regenerative medicine field with clinically appropriate sterility.

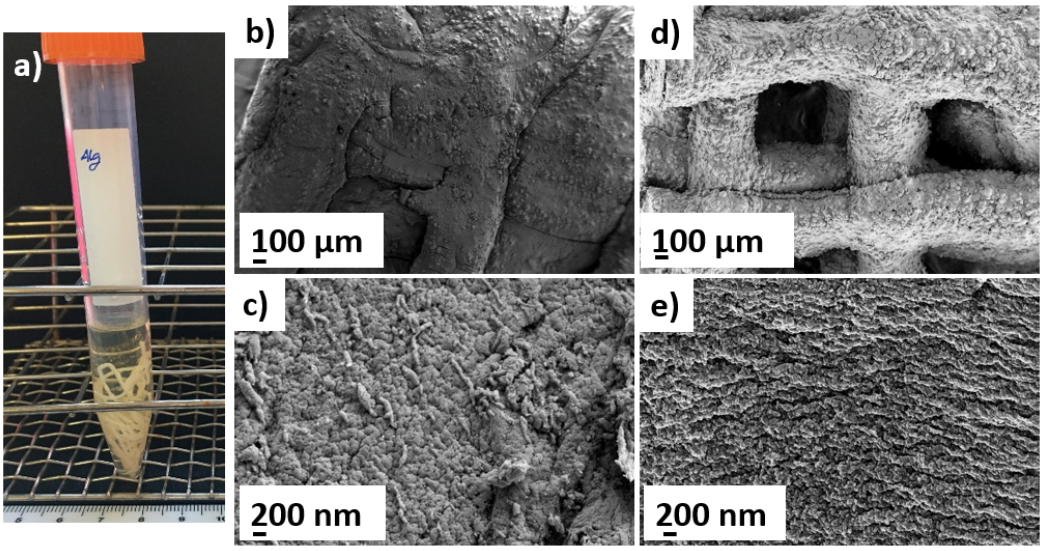


Figure 4.9. $scCO_2$ sterilization of 3D-printed aerogels. **a)** Sterile and dual crosslinked aerogels seeded on TSB tubes after 24 h of culture. b-e) SEM images of sterile aerogel scaffolds. **b,c)** AlgHA 8, $CaCl_2$ 1M1h, st and **d,e)** AlgHA 8, $CaCl_2$ 1M1h, GA, st. Aerogels were observed at two different magnifications.

Table 4.3. Textural properties of sterile aerogels. **Notation:** A_{BET}: BET-specific surface area, d_p: BJH-mean pore diameter, V_p: BJH-specific pore volume.

Sterile Aerogel Scaffold	A_{BET} (m^2/g)	d_p (nm)	V_p (cm^3/g)
AlgHA 8, $CaCl_2$ 1M1h, st	105 ± 5	28 ± 1	0.89 ± 0.04
AlgHA 16, $CaCl_2$ 1M1h, st	68 ± 3	27 ± 1	0.52 ± 0.03
AlgHA 24, $CaCl_2$ 1M1h, st	56 ± 3	26 ± 1	0.41 ± 0.02
AlgHA 8, $CaCl_2$ 1M1h, GA, st	59 ± 3	25 ± 1	0.43 ± 0.02
AlgHA 16, $CaCl_2$ 1M1h, GA, st	30 ± 2	29 ± 1	0.27 ± 0.01
AlgHA 24, $CaCl_2$ 1M1h, GA, st	32 ± 2	23 ± 1	0.17 ± 0.01

USC UNIVERSIDADE DE SANTIAGO DE COMPOSTELA

All formulations studied have acceptable textural performance and excellent biological behavior (cyto- and hemocompatibility) for bone tissue engineering applications. Nevertheless, only the dual crosslinked scaffolds present the long-term stability as well as the structural integrity and bioactivity required to act as bone scaffolds. Aerogels manufactured with the lowest HA content present slightly better textural properties than other formulations while preserving their advanced biological performance and the printability required for the obtention of customized structures suitable for personalize medicine. All these features make this formulation a promising candidate to develop aerogels for personalized bone tissue engineering.

4.4. Conclusions

Osteoinductive alginate-HA aerogels were manufactured with a precise, customized, and dual porous structure via the combination of 3D-printing and aerogel technologies. An optimized scaffold formulation obtained by dual crosslinking with $CaCl_2$ and GA provided long-term stability in an aqueous medium and the required bioactivity for promoting bone regeneration. The GA crosslinking resulted in an effective method that can be used to obtain the bioactivity properties and structural integrity required for customized bone tissue engineering applications. Additionally, GA did not have any negative impact on the cell viability of fibroblasts and showed a high hemocompatibility for all the formulations tested, thus avoiding the detoxifying strategies commonly employed after this crosslinking strategy. Finally, aerogels under sterile conditions were obtained by $scCO_2$ processing at mild conditions without compromising the structural integrity of the dual crosslinked scaffolds. The high cytocompatibility, the suitable structure (pore size and porosity), the tunable macroscopic pattern obtained by 3D-printing and the sterile condition result in dual crosslinked aerogels that represent a promising alternative for personalized bone tissue engineering.

USC UNIVERSIDADE DE SANTIAGO DE COMPOSTELA

4.5. References

1. Oryan, A. Bone Injury and Fracture Healing Biology. Biomed Environ. Sci 2015, 28, 15. https://doi.org/10.3967/bes2015.006.
2. Bharadwaz, A.; Jayasuriya, A.C. Recent trends in the application of widely used natural and synthetic polymer nanocompo-sites in bone tissue regeneration. Mater. Sci. Eng. C 2020, 110, 110698. https://doi.org/10.1016/j.msec.2020.110698.
3. Tohamy, K.M.; Soliman, I.E.; Mabrouk, M.; ElShebiney, S.; Beherei, H.H.; Aboelnasr, M.A.; Das, D.B. Novel polysaccharide hybrid scaffold loaded with hydroxyapatite: Fabrication, bioactivity, and *in vivo* study. Mater. Sci. Eng. C 2018, 93, 1–11. https://doi.org/10.1016/j.msec.2018.07.054.
4. Li, L.; Chen, Y.; Wang, Y.; Shi, F.; Nie, Y.; Liu, T.; Song, K. Effects of concentration variation on the physical properties of algi-nate-based substrates and cell behavior in culture. Int. J. Biol. Macromol. 2019, 128, 184–195. https://doi.org/10.1016/j.ijbiomac.2019.01.123.
5. Browning, K.L.; Stocker, I.N.; Gutfreund, P.; Clarke, S.M. The effect of alginate composition on adsorption to calcium car-bonate surfaces. J. Colloid Interface Sci. 2021, 581, 682–689. https://doi.org/10.1016/j.jcis.2020.07.088.
6. Sergi, R.; Bellucci, D.; Cannillo, V. A Review of Bioactive Glass/Natural Polymer Composites: State of the Art. Materials 2020, 13, 5560. https://doi.org/10.3390/ma13235560.
7. Iglesias-Mejuto, A.; García-González, C.A. 3D-printed alginate-hydroxyapatite aerogel scaffolds for bone tissue engineering. Mater. Sci. Eng. C 2021, 131, 112525. https://doi.org/10.1016/j.msec.2021.112525.
8. Park, M.; Lee, D.; Shin, S.; Hyun, J. Effect of negatively charged cellulose nanofibers on the dispersion of hydroxyapatite na-noparticles for scaffolds in bone tissue engineering. Colloids Surf. B Biointerfaces 2015, 130, 222–228. https://doi.org/10.1016/j.colsurfb.2015.04.014.
9. Latimer, J.M.; Maekawa, S.; Yao, Y.; Wu, D.T.; Chen, M.; Giannobile, W.V. Regenerative Medicine Technologies to Treat Den-tal, Oral, and Craniofacial Defects. Front. Bioeng. Biotechnol. 2021, 9, 704048. https://doi.org/10.3389/fbioe.2021.704048.
10. Lee, J.; Hong, J.; Kim, W.; Kim, G.H. Bone-derived dECM/alginate bioink for fabricating a 3D cell-laden mesh structure for bone tissue engineering. Carbohydr. Polym. 2020, 250, 116914. https://doi.org/10.1016/j.carbpol.2020.116914.
11. Ng, W.L.; Lee, J.M.; Zhou, M.; Chen, Y.-W.; Lee, K.-X.A.; Yeong, W.Y.; Shen, Y.-F. Vat polymerization-based bioprint-ing—process, materials, applications and regulatory challenges. Biofabrication 2019, 12, 022001. https://doi.org/10.1088/1758-5090/ab6034.
12. Li, X.; Liu, B.; Pei, B.; Chen, J.; Zhou, D.; Peng, J.; Zhang, X.; Jia, W.; Xu, T. Inkjet Bioprinting of Biomaterials. Chem. Rev. 2020, 120, 10793–10833. https://doi.org/10.1021/acs.chemrev.0c00008.
13. Ng, W.L.; Lee, J.M.; Yeong, W.Y.; Naing, M.W. Microvalve-based bioprinting – process, bio-inks and applications. Biomater. Sci. 2017, 5, 632–647. https://doi.org/10.1039/c6bm00861e.
14. Pati, F.; Gantelius, J.; Svahn, H.A. 3D Bioprinting of Tissue/Organ Models. Angew. Chem. Int. Ed. 2016, 55, 4650–4665. https://doi.org/10.1002/anie.201505062.
15. Ng, W.L.; Chua, C.K.; Shen, Y.-F. Print Me An Organ! Why We Are Not There Yet. Prog. Polym. Sci. 2019, 97, 101145. https://doi.org/10.1016/j.progpolymsci.2019.101145.
16. Rajasekharan, A.K.; Gyllensten, C.; Blomstrand, E.; Liebi, M.; Andersson, M. Tough Ordered Mesoporous Elastomeric Bio-materials Formed at Ambient Conditions. ACS Nano 2020, 14, 241–254. https://doi.org/10.1021/acsnano.9b01924.
17. Sayyar, S.; Gambhir, S.; Chung, J.; Officer, D.L.; Wallace, G.G. 3D printable conducting hydrogels containing chemically con-verted graphene. Nanoscale 2017, 9, 2038–2050. https://doi.org/10.1039/c6nr07516a.
18. Sultan, S.; Mathew, A.P. 3D printed scaffolds with gradient porosity based on a cellulose nanocrystal hydrogel. Nanoscale 2018, 10, 4421–4431. https://doi.org/10.1039/c7nr08966j.
19. Bernardes, B.; Del Gaudio, P.; Alves, P.; Costa, R.; García-Gonzaléz, C.; Oliveira, A. Bioaerogels: Promising Nanostructured Materials in Fluid Management, Healing and Regeneration of Wounds. Molecules 2021, 26, 3834. https://doi.org/10.3390/molecules26133834.
20. García-González, C.A.; Budtova, T.; Durães, L.; Erkey, C.; Del Gaudio, P.; Gurikov, P.; Koebel, M.; Liebner, F.; Neagu, M.; Smirnova, I. An Opinion Paper on Aerogels for Biomedical and Environmental Applications. Molecules 2019, 24, 1815. https://doi.org/10.3390/molecules24091815.
21. Yahya, E.B.; Amirul, A.A.; H.P.S., A.K.; Olaiya, N.G.; Iqbal, M.O.; Jummaat, F.; A.K., A.S.; Adnan, A.S. Insights into the Role of Biopolymer Aerogel Scaffolds in Tissue Engineering and Regenerative Medicine. Polymers 2021, 13, 1612. https://doi.org/10.3390/polym13101612.

22. El-Naggar, M.E.; Othman, S.I.; Allam, A.; Morsy, O.M. Synthesis, drying process and medical application of polysaccha-ride-based aerogels. Int. J. Biol. Macromol. 2020, 145, 1115–1128. https://doi.org/10.1016/j.ijbiomac.2019.10.037.
23. Guastaferro, M.; Reverchon, E.; Baldino, L. Agarose, Alginate and Chitosan Nanostructured Aerogels for Pharmaceutical Applications: A Short Review. Front. Bioeng. Biotechnol. 2021, 9, 688477. https://doi.org/10.3389/fbioe.2021.688477.
24. Feng, J.; Su, B.-L.; Xia, H.; Zhao, S.; Gao, C.; Wang, L.; Ogbeide, O.; Feng, J.; Hasan, T. Printed aerogels: Chemistry, processing, and applications. Chem. Soc. Rev. 2021, 50, 3842–3888. https://doi.org/10.1039/c9cs00757a.
25. Karamikamkar, S.; Naguib, H.E.; Park, C.B. Advances in precursor system for silica-based aerogel production toward im-proved mechanical properties, customized morphology, and multifunctionality: A review. Adv. Colloid Interface Sci. 2020, 276, 102101. https://doi.org/10.1016/j.cis.2020.102101.
26. Patel, P.P.; Buckley, C.; Taylor, B.L.; Sahyoun, C.C.; Patel, S.D.; Mont, A.J.; Mai, L.; Patel, S.; Freeman, J.W. Mechanical and bio-logical evaluation of a hydroxyapatite-reinforced scaffold for bone regeneration: Evaluation of Bone Scaffold. J. Biomed. Mater. Res. Part A 2019, 107, 732–741. https://doi.org/10.1002/jbm.a.36588.
27. Parai, R.; Bandyopadhyay-Ghosh, S. Engineered bio-nanocomposite magnesium scaffold for bone tissue regeneration. J. Mech. Behav. Biomed. Mater. 2019, 96, 45–52. https://doi.org/10.1016/j.jmbbm.2019.04.019.
28. Rial, R.; Soltero, J.F.A.; Verdes, P.V.; Liu, Z.; Ruso, J.M. Mechanical Properties of Composite Hydrogels for Tissue Engineering. Curr. Top. Med. Chem. 2018, 18, 1223–1232. https://doi.org/10.2174/1568026618666180810151539.
29. Dewey, M.J.; Nosatov, A.V.; Subedi, K.; Shah, R.; Jakus, A.; Harley, B.A. Inclusion of a 3D-printed Hyperelastic Bone mesh improves mechanical and osteogenic performance of a mineralized collagen scaffold. Acta Biomater. 2021, 121, 224–236. https://doi.org/10.1016/j.actbio.2020.11.028.
30. Maharjan, B.; Park, J.; Kaliannagounder, V.K.; Awasthi, G.P.; Joshi, M.K.; Park, C.H.; Kim, C.S. Regenerated cellulose nano-fiber reinforced chitosan hydrogel scaffolds for bone tissue engineering. Carbohydr. Polym. 2021, 251, 117023. https://doi.org/10.1016/j.carbpol.2020.117023.
31. Kim, H.; Hwangbo, H.; Koo, Y.; Kim, G. Fabrication of Mechanically Reinforced Gelatin/Hydroxyapatite Bio-Composite Scaffolds by Core/Shell Nozzle Printing for Bone Tissue Engineering. Int. J. Mol. Sci. 2020, 21, 3401. https://doi.org/10.3390/ijms21093401.
32. GhavamiNejad, A.; Ashammakhi, N.; Wu, X.Y.; Khademhosseini, A. Crosslinking Strategies for 3D Bioprinting of Polymeric Hydrogels. Small 2020, 16, 2002931. https://doi.org/10.1002/smll.202002931.
33. Oryan, A.; Kamali, A.; Moshiri, A.; Baharvand, H.; Daemi, H. Chemical crosslinking of biopolymeric scaffolds: Current knowledge and future directions of crosslinked engineered bone scaffolds. Int. J. Biol. Macromol. 2018, 107, 678–688. https://doi.org/10.1016/j.ijbiomac.2017.08.184.
34. Krishnakumar, G.S.; Sampath, S.; Muthusamy, S.; John, M.A. Importance of crosslinking strategies in designing smart bio-materials for bone tissue engineering: A systematic review. Mater. Sci. Eng. C 2019, 96, 941–954. https://doi.org/10.1016/j.msec.2018.11.081.
35. Yang, H.; Tan, Q.; Zhao, H. Progress in various crosslinking modification for acellular matrix. Chin. Med. J. 2014, 127, 3156–3164.
36. Erkoc, P.; Uvak, I.; Nazeer, M.A.; Batool, S.R.; Odeh, Y.N.; Akdogan, O.; Kizilel, S. 3D Printing of Cytocompatible Gelatin-Cellulose-Alginate Blend Hydrogels. Macromol. Biosci. 2020, 20, 2000106. https://doi.org/10.1002/mabi.202000106.
37. Fang, Y.; Zhang, T.; Song, Y.; Sun, W. Assessment of various crosslinking agents on collagen/chitosan scaffolds for myocardi-al tissue engineering. Biomed. Mater. 2020, 15, 045003. https://doi.org/10.1088/1748-605x/ab452d.
38. Samirah; Budiatin, A.S.; Mahyudin, F.; Khotib, J. Fabrication and characterization of bovine hydroxyapatite-gelatin-alendronate scaffold cross-linked by glutaraldehyde for bone regeneration. J. Basic Clin. Physiol. Pharmacol. 2021, 32, 555–560. https://doi.org/10.1515/jbcpp-2020-0422.
39. Soares, D.G.; Bordini, E.; Cassiano, F.; Bronze-Uhle, E.S.; Pacheco, L.E.; Zabeo, G.; Hebling, J.; Lisboa-Filho, P.N.; Bottino, M.C.; Costa, C.A.D.S. Characterization of novel calcium hydroxide-mediated highly porous chitosan-calcium scaffolds for poten-tial application in dentin tissue engineering. J. Biomed. Mater. Res. Part B Appl. Biomater. 2020, 108, 2546–2559. https://doi.org/10.1002/jbm.b.34586.
40. Delgado, L.M.; Fuller, K.; Zeugolis, D.I. Collagen Cross-Linking: Biophysical, Biochemical, and Biological Response Analysis. Tissue Eng. Part A 2017, 23, 1064–1077. https://doi.org/10.1089/ten.tea.2016.0415.

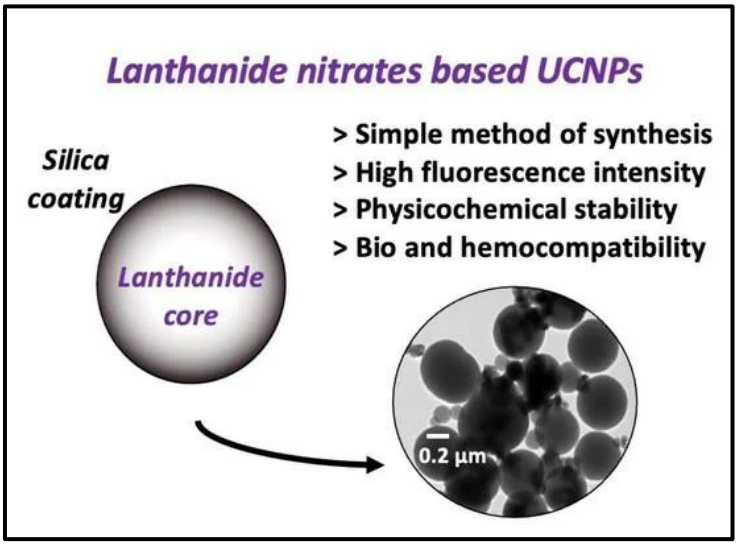
USC UNIVERSIDADE DE SANTIAGO

41. Jeong, J.E.; Park, S.Y.; Shin, J.Y.; Seok, J.M.; Byun, J.H.; Oh, S.H.; Kim, W.D.; Lee, J.H.; Park, W.H.; Park, S.A. 3D Printing of Bone-Mimetic Scaffold Composed of Gelatin/β-Tri-Calcium Phosphate for Bone Tissue Engineering. Macromol. Biosci. 2020, 20, e2000256. https://doi.org/10.1002/mabi.202000256.
42. Mathapati, S.; Bishi, D.K.; Guhathakurta, S.; Cherian, K.M.; Venugopal, J.R.; Ramakrishna, S.; Verma, R.S. Biomimetic acellu-lar detoxified glutaraldehyde cross-linked bovine pericardium for tissue engineering. Mater. Sci. Eng. C 2013, 33, 1561–1572. https://doi.org/10.1016/j.msec.2012.12.062.
43. Lei, Y.; Yang, L.; Guo, G.; Wang, Y. EGCG and enzymatic cross-linking combined treatments for improving elastin stability and reducing calcification in bioprosthetic heart valves. J. Biomed. Mater. Res. Part B Appl. Biomater. 2019, 107, 1551–1559. https://doi.org/10.1002/jbm.b.34247.
44. Hodder, E.; Duin, S.; Kilian, D.; Ahlfeld, T.; Seidel, J.; Nachtigall, C.; Bush, P.; Covill, D.; Gelinsky, M.; Lode, A. Investigating the effect of sterilisation methods on the physical properties and cytocompatibility of methyl cellulose used in combination with alginate for 3D-bioplotting of chondrocytes. J. Mater. Sci. Mater. Med. 2019, 30, 1–16. https://doi.org/10.1007/s10856-018-6211-9.
45. Santos-Rosales, V.; Ardao, I.; Alvarez-Lorenzo, C.; Ribeiro, N.; Oliveira, A.L.; García-González, C.A. Sterile and Dual-Porous Aerogels Scaffolds Obtained through a Multistep Supercritical CO_2-Based Approach. Molecules 2019, 24, 871. https://doi.org/10.3390/molecules24050871.
46. Munarin, F.; Bozzini, S.; Visai, L.; Tanzi, M.C.; Petrini, P. Sterilization treatments on polysaccharides: Effects and side effects on pectin. Food Hydrocoll. 2013, 31, 74–84. https://doi.org/10.1016/j.foodhyd.2012.09.017.
47. Ribeiro, N.; Soares, G.C.; Santos-Rosales, V.; Concheiro, A.; Alvarez-Lorenzo, C.; García-González, C.A.; Oliveira, A. A new era for sterilization based on supercritical CO 2 technology. J. Biomed. Mater. Res. Part B Appl. Biomater. 2020, 108, 399–428. https://doi.org/10.1002/jbm.b.34398.
48. Corker, A.; Ng, H.C.-H.; Poole, R.J.; García-Tuñón, E. 3D printing with 2D colloids: Designing rheology protocols to predict ‘printability’ of soft-materials. Soft Matter 2019, 15, 1444–1456. https://doi.org/10.1039/c8sm01936c.
49. Conceição, J.; Vaamonde, X.F.; Goyanes, A.; Adeoye, O.; Concheiro, A.; Cabral-Marques, H.; Lobo, J.M.S.; Alvarez-Lorenzo, C. Hydroxypropyl-β-cyclodextrin-based fast dissolving carbamazepine printlets prepared by semisolid extrusion 3D printing. Carbohydr. Polym. 2019, 221, 55–62. https://doi.org/10.1016/j.carbpol.2019.05.084.
50. Blanco-Fernandez, B.; Rial-Hermida, M.I.; Alvarez-Lorenzo, C.; Concheiro, A. Edible chitosan/acetylated monoglyceride films for prolonged release of vitamin E and antioxidant activity. J. Appl. Polym. Sci. 2012, 129, 626–635. https://doi.org/10.1002/app.38766.
51. Kokubo, T.; Takadama, H. How useful is SBF in predicting *in vivo* bone bioactivity? Biomaterials 2006, 27, 2907–2915. https://doi.org/10.1016/j.biomaterials.2006.01.017.
52. Duarte, A.R.C.; Caridade, S.G.; Mano, J.F.; Reis, R.L. Processing of novel bioactive polymeric matrixes for tissue engineering using supercritical fluid technology. Mater. Sci. Eng. C 2009, 29, 2110–2115. https://doi.org/10.1016/j.msec.2009.04.012.
53. Islam, M.M.; AbuSamra, D.B.; Chivu, A.; Argüeso, P.; Dohlman, C.H.; Patra, H.K.; Chodosh, J.; González-Andrades, M. Opti-mization of Collagen Chemical Crosslinking to Restore Biocompatibility of Tissue-Engineered Scaffolds. Pharmaceutics 2021, 13, 832. https://doi.org/10.3390/pharmaceutics13060832.
54. Gao, T.; Gillispie, G.J.; Copus, J.S.; Pr, A.K.; Seol, Y.-J.; Atala, A.; Yoo, J.J.; Lee, S.J.J. Optimization of gelatin–alginate composite bioink printability using rheological parameters: A systematic approach. Biofabrication 2018, 10, 034106. https://doi.org/10.1088/1758-5090/aacdc7.
55. Seoane-Viaño, I.; Januskaite, P.; Alvarez-Lorenzo, C.; Basit, A.W.; Goyanes, A. Semi-solid extrusion 3D printing in drug de-livery and biomedicine: Personalised solutions for healthcare challenges. J. Control. Release 2021, 332, 367–389. https://doi.org/10.1016/j.jconrel.2021.02.027.
56. D’Elía, N.L.; Silva, R.R.; Sartuqui, J.; Ercoli, D.; Ruso, J.; Messina, P.; Mestres, G. Development and characterisation of bi-layered periosteum-inspired composite membranes based on sodium alginate-hydroxyapatite nanoparticles. J. Colloid Inter-face Sci. 2020, 572, 408–420. https://doi.org/10.1016/j.jcis.2020.03.086.
57. Perez, R.A.; Mestres, G. Role of pore size and morphology in musculo-skeletal tissue regeneration. Mater. Sci. Eng. C 2016, 61, 922–939. https://doi.org/10.1016/j.msec.2015.12.087.
58. Wang, Q.; Ju, J.; Tan, Y.; Hao, L.; Ma, Y.; Wu, Y.; Zhang, H.; Xia, Y.; Sui, K. Controlled synthesis of sodium alginate electrospun nanofiber membranes for multi-occasion adsorption and separation of methylene blue. Carbohydr. Polym. 2019, 205, 125–134. https://doi.org/10.1016/j.carbpol.2018.10.023.

59. García-González, C.A.; Alnaief, M.; Smirnova, I. Polysaccharide-based aerogels—Promising biodegradable carriers for drug delivery systems. Carbohydr. Polym. 2011, 86, 1425–1438. https://doi.org/10.1016/j.carbpol.2011.06.066.
60. Saarai, A.; Kasparkova, V.; Sedlacek, T.; Saha, P. On the development and characterisation of crosslinked sodium algi-nate/gelatine hydrogels. J. Mech. Behav. Biomed. Mater. 2013, 18, 152–166. https://doi.org/10.1016/j.jmbbm.2012.11.010.
61. Ma, B.; Wang, X.; Wu, C.; Chang, J. Crosslinking strategies for preparation of extracellular matrix-derived cardiovascular scaffolds. Regen. Biomater. 2014, 1, 81–89. https://doi.org/10.1093/rb/rbu009.
62. Li, G.; Qin, S.; Liu, X.; Zhang, D.; He, M. Structure and properties of nano-hydroxyapatite/poly(butylene succinate) porous scaffold for bone tissue engineering prepared by using ethanol as porogen. J. Biomater. Appl. 2018, 33, 776–791. https://doi.org/10.1177/0885328218812486.
63. Salvatore, L.; Madaghiele, M.; Parisi, C.; Gatti, F.; Sannino, A. Crosslinking of micropatterned collagen-based nerve guides to modulate the expected half-life: Crosslinking of Micropatterned Collagen-Based Nerve Guides. J. Biomed. Mater. Res. Part A 2014, 102, 4406–4414. https://doi.org/10.1002/jbm.a.35124.
64. Tohamy, K.M.; Mabrouk, M.; Soliman, I.E.; Beherei, H.H.; Aboelnasr, M.A. Novel alginate/hydroxyethyl cellu-lose/hydroxyapatite composite scaffold for bone regeneration: *In vitro* cell viability and proliferation of human mesenchy-mal stem cells. Int. J. Biol. Macromol. 2018, 112, 448–460. https://doi.org/10.1016/j.ijbiomac.2018.01.181.
65. Valenzuela, F.; Covarrubias, C.; Martínez, C.; Smith, P.; Díaz-Dosque, M.; Yazdani-Pedram, M. Preparation and bioactive properties of novel bone-repair bionanocomposites based on hydroxyapatite and bioactive glass nanoparticles. J. Biomed. Mater. Res. Part B Appl. Biomater. 2012, 100B, 1672–1682. https://doi.org/10.1002/jbm.b.32736.
66. Kamalaldin, N.; Yahya, B.; Nurazreena, A. Cell Evaluation on Alginate/Hydroxyapatite Block for Biomedical Application. Procedia Chem. 2016, 19, 297–303. https://doi.org/10.1016/j.proche.2016.03.012.
67. Shaheen, T.; Montaser, A.; Li, S. Effect of cellulose nanocrystals on scaffolds comprising chitosan, alginate and hydroxyap-atite for bone tissue engineering. Int. J. Biol. Macromol. 2019, 121, 814–821. https://doi.org/10.1016/j.ijbiomac.2018.10.081.
68. Perera, C.J.C.; Baas, M.G.C.; Lara, G.A.A.; Borges, S.I.R.; Guzmán, A.L.R.; Cervantes, I.F.; Fuentes, N.R. Characterization and hemocompatibility assessment of porous composite scaffolds with a biomimetic human clavicle macrostructure. Health Technol. 2020, 10, 423–428. https://doi.org/10.1007/s12553-019-00374-9.
69. He, X.; Fan, X.; Feng, W.; Chen, Y.; Guo, T.; Wang, F.; Liu, J.; Tang, K. Incorporation of microfibrillated cellulose into colla-gen-hydroxyapatite scaffold for bone tissue engineering. Int. J. Biol. Macromol. 2018, 115, 385–392. https://doi.org/10.1016/j.ijbiomac.2018.04.085.

USC UNIVERSIDADE DE SANTIAGO DE COMPOSTELA

CHAPTER 5. SYNTHESIS OF HIGHLY LUMINESCENT SILICA-COATED UPCONVERSION NANOPARTICLES FROM LANTHANIDE OXIDES OR NITRATES USING CO-PRECIPITATION AND SOL–GEL METHODS



The content in this chapter was published in part in **A. Iglesias-Mejuto,** A. Lamy-Mendes, J. Pina, B.F.O. Costa, C.A. García-González, L. Durães; Synthesis of Highly Luminescent Silica-Coated Upconversion Nanoparticles from Lanthanide Oxides or Nitrates Using Co-Precipitation and Sol–Gel Methods, in: Gels 10 (2023) 13. https://doi.org/10.3390/gels10010013.

The work described in this chapter was carried out in collaboration with the University of Coimbra.

USC
DE SANTIAGO
DE COMPOSTELA

5.1. Introduction

Bioimaging enables the tracking of biological functions in real time by using technologies such as X-ray, magnetic resonance, or fluorescence for detecting biological probes employed for the monitoring and examination of anatomy and physiology [1]. Namely, optical sensing is one of the most commonly used technologies for biodetection due to its sensitivity and simplicity, but efficient labeling molecules are needed for these purposes [2]. Among them, fluorescent dyes and semiconductor quantum dots are being used as bioimaging tools, but the photobleaching of organic dyes, toxicity, poor photostability and broad emission of quantum dots limit their performance [3]. Moreover, fluorescent probes are generally excited by UV light, which induces DNA damage and cell death [4]. Thus, the development of materials with improved and highly efficient photochemical performance using biologically tolerable exciting radiation sources is required for *in vivo* bioimaging applications.

UCNPs are considered as the new generation of fluorophores due to their unique optical properties such as sharp emission bands, large anti-Stokes shifts and low photobleaching and blinking [5]. These nanocomplexes also present good signal-to-noise ratio and sensitivity due to the low scattering, autofluorescence and absorption from living tissues (background) in the red/near infrared (NIR) region (therapeutic window or NIR window) while presenting high tissue penetration depth (up to 2 mm) [2,5–7]. Upconversion (UC) luminescence is an “anti-Stokes emission”, where the emitted fluorescence (visible light from 400 to 700 nm) has shorter wavelengths and higher energy than the incident light, NIR (from 808 to 980 nm), which is a radiation usually regarded as not biologically harmful [8,9] at short exposure levels and with good transmittance through tissues [10–12]. The absorption of low-energy photons leads to the emission of high-energy photons by a non-linear UC process that enables the photomediated biosensing and bioimaging in a non-invasive process [13]. Based on this principle, UCNPs present long photoluminescence lifetimes, as well as low toxicity and photodamage for living organisms [3,14]. Indeed, UCNPs allowed the transformation of fluorescence imaging from microscopic to

USC
UNIVERSIDADE DE SANTIAGO DE COMPOSTELA

macroscopic levels with potential applications in bioimaging, biodetection, and cell and tissue labeling [4,10]. Moreover, UCNPs are one of the most promising luminescent probes for monitoring whole-body small animals, but *in vivo* UC luminescence still has some limitations [15]. Among them, sensitivity and resolution are affected by the absorption and scattering effects of organs with a rapid decrease in the signals detected from *in vivo* experiments involving UCNPs [16]. New luminescence imaging tools based on UCNPs must be developed to address all these concerns.

UCNPs are composed of a host matrix doped with a sensitizer (light absorber) and an activator (light-emitter) as guest molecules [17]. $NaYF_4$ nanocrystals are the most efficient UC host materials to date, being detected by confocal microscopy with a size of 27 nm [18] due to the low phonon energy and good absorption [19,20]. The $NaYF_4$ lattice forms two crystalline phases, the cubic (α phase) and the hexagonal (β phase) ones [8]. Thermodynamically stable hexagonal phase yields bright luminescence, but the polymorphic change from the cubic to the hexagonal phase requires high energy, e.g., hydrothermal or solvothermal treatment [21]. A decrease in particle size may also cause a decrease in emitter numbers and a high surface quenching [18]. Therefore, the process parameter control in the UCNPs synthetic methods should allow the tuning of the particle size and shape, nanocrystal phase, and doping concentration to ensure effective properties for bioimaging [19]. Regarding the ideal sensitizers, they should have the same NIR excited energy state as activators. Specifically, rare-earth doped UCNPs are photostable and have low photoblinking and photobleaching [12,22]. Namely, ytterbium (Yb^{3+}) is used as a sensitizer due to its high absorption and broad excitation spectrum. Its single excited state matches with activators like erbium (Er^{3+}), so Yb^{3+} is commonly employed as a sensitizer of Er^{3+}. These types of UCNPs contain thousands of emission center ions and can be of interest for bioimaging as they can be excited with NIR, thus enabling the deep penetration in tissues with non-invasive treatments and a low interference with the weak autofluorescence from the biological background [12,23]. It is important to highlight that luminescence intensity and

USC UNIVERSIDADE DE SANTIAGO DE COMPOSTELA

efficiency are strongly dependent on the crystal phase and morphology of the UCNPs, so an environmentally friendly synthetic approach able to yield non-toxic nanosystems with a controlled shape and phase is required [24,25].

Lanthanide-doped UCNPs are usually obtained by a thermal decomposition, hydrothermal or solvothermal method, sol-gel processing, or a co-precipitation approach [17]. Thermal decomposition consists of pyrolyzing the organometallic precursors with an organic solvent in an oxygen-free environment [26]. Hydrothermal synthesis is carried out with lanthanide nitrates or chlorides as precursors and under a high pressure and temperature environment, often above the critical point of the solvent [19,21,26]. The sol–gel method starts with a solution of precursors that forms a gel by hydrolysis and polycondensation [4]. After calcination at high temperatures, highly crystalline UCNPs are synthesized, but this strategy is not used for biomedical applications because of the lack of control of particle size [19]. In contrast, the co-precipitation method consists of the simultaneous and rapid precipitation of multiple species under supersaturation conditions in a short time [27]. This UCNPs processing method is regarded as advantageous since, in contrast to the previously mentioned techniques, it does not require complex procedures or harsh conditions (such as high temperatures or the use of solvents), while the obtained UCNPs are chemically homogeneous, and easily obtained with high yields after short reaction times [16,21].

UCNPs with biocompatible surface properties and uniform morphologies are prone to be employed as bio-labels, so ligands like polyethylene glycol, oleic acid or silica are used to functionalize UCNPs, to increase water solubilization and stability and to modulate cellular interactions [4,14,17,28]. Silica modification is a well-established and commonly employed technique, easy to obtain, effective and able to improve the biocompatibility and stability of the resulting structures [7]. By the sol–gel Stöber method [29], proposed in 1968 by Werner Stöber and coworkers, the alkoxide precursor tetraethyl orthosilicate (TEOS) is hydrolyzed to produce

USC DE COMPOSTELA

silicic acid, which undergoes a condensation reaction in mild basic conditions to form an amorphous silica coating around the previously synthesized lanthanide core, in the presence of ammonia as a catalyst [30,31]. This eco-friendly alternative sol–gel method avoids the use of potentially cytotoxic surfactants and organic solvents that would require several washing steps prior to be employed as biological labels. Moreover, the ultrathin silica shell synthesized is non-toxic, chemically inert, and optically transparent, which are important advantages to render photoluminescent UCNPs for bioimaging applications [32].

In this work, core-shell $NaYF_4$:Yb^{3+},Er^{3+}-SiO_2 UCNPs obtained from lanthanide nitrates and, alternatively, from lanthanide oxides, were synthesized. A novel and simple co-precipitation method was applied, followed by a silica coating step based on TEOS hydrolysis by the sol–gel Stöber process. The obtained UCNPs formulations were characterized regarding their crystalline structure and photophysical properties by XRD, SEM-EDX and UC fluorescence spectroscopy. TEM and confocal microscopy were performed to unveil the morphological and luminescent properties of UCNPs just after synthesis and, comparatively, after a 2-year mid-term storage. Cell viability tests with murine fibroblasts and hemolytic activity tests with human blood were also performed for biocompatibility evaluation. Lanthanide-derived core-shell $NaYF_4$:Yb^{3+},Er^{3+}-SiO_2 UCNPs yielded biocompatible nanocomplexes with high crystallinity, a controllable transition from cubic α-$NaYF_4$ to hexagonal β-$NaYF_4$ and long-term UC fluorescence emission and physicochemical stability. To the best of our knowledge, it is the first time that silica gel-coated UCNPs were synthesized using a procedure involving lanthanide nitrates or oxides as precursors, in a RT, facile, versatile, and non-hazardous co-precipitation method. Also, precursors were dissolved in aqueous solutions, thus avoiding the use of solvents or surfactants that could render toxic by-products. Overall, the novel technological combination of co-precipitation and sol–gel methods herein studied is regarded as environmentally benign and very convenient for obtaining highly photoluminescent UCNPs in a shape- and phase-controlling approach.

USC UNIVERSIDADE DE SANTIAGO DE COMPOSTELA

5.2. Materials and Methods

5.2.1. Materials

Ytterbium (III) oxide (Yb_2O_3, 99.9% purity), erbium (III) oxide (Er_2O_3, 99.9%), ytterbium (III) nitrate pentahydrate ($Yb(NO_3)_3{\cdot}5H_2O$, 99.9%), yttrium(III) nitrate hexahydrate ($Y(NO_3)_3{\cdot}6H_2O$, 99.8%), sodium fluoride (NaF, >99%) and ethylenediaminetetraacetic acid (EDTA) were provided by Sigma Aldrich (Merck Group, Darmstadt, Germany). Yttrium (III) oxide (Y_2O_3, 99.99%), erbium (III) nitrate pentahydrate ($Er(NO_3)_3{\cdot}5H_2O$, 99.9%), and TEOS ($Si(OC_2H_5)_4$, 98%), were obtained from Acros Organics (Thermo-Fisher Scientific, Geel, Belgium). Hydrochloric acid (HCl, 37%) was supplied by Fisher (Madrid, Spain) and ammonium hydroxide (25% NH_3 in H_2O) by Fluka Analytical (Honeywell International, Charlotte, NC, USA). CO_2 (purity >99.9%) was obtained from Nippon Gases (Madrid, Spain) and absolute EtOH from VWR (Radnor, PA, USA). All reagents were used as purchased and deionized water was employed in all the procedures.

5.2.2. Synthesis of UCNPs by co-precipitation and sol-gel methods

0.2 M stock solutions of Y_2O_3, Yb_2O_3, and Er_2O_3 solutions were prepared and adjusted at pH 2 by using hydrochloric acid to dissolve the oxide precursors and liberate the metal ions to the solution [52]. A total of 16 mL of 0.2 M Y_2O_3, 3.4 mL of 0.2 M Yb_2O_3 and 0.6 mL of 0.2 M Er_2O_3 was mixed with 20 mL of 0.2 M EDTA. Alternatively, another solution was prepared by mixing 16 mL of 0.2 M $Y(NO_3)_3$, 3.4 mL of 0.2 M $Yb(NO_3)_3$, 0.6 mL of 0.2 M $Er(NO_3)_3$ and 20 mL of 0.2 M EDTA. EDTA was firstly employed in the synthesis of UCNPs by Yi and coworkers [52]. It is employed as a stabilizing and chelating agent able to minimize UCNPs aggregation [53]. EDTA has been described as an efficient complexing agent for trivalent lanthanide ions because it improves the dispersibility of crystals. Complexes formed are adsorbed on the surface of UCNPs, limiting the growth in size of the resulting UCNPs. In fact, smaller UCNPs size is generally achieved by increasing the concentration of different chelators [54]. Moreover, EDTA is used to prevent precipitation before proceeding with the synthesis procedure [55].

USC UNIVERSIDADE DE SANTIAGO DE COMPOSTELA

5. SYNTHESIS OF HIGHLY LUMINESCENT SILICA-COATED UPCONVERSION NANOPARTICLES FROM LANTHANIDE OXIDES OR NITRATES USING CO-PRECIPITATION AND SOL–GEL METHODS

Rare earth solution was injected into 0.05 mol of NaF dissolved in 60 mL of water and the mixture was stirred for 1 h at RT. Obtained dispersions were centrifuged and washed three times with water and once with EtOH. UCNPs were dried in an oven at 60 °C or, alternatively, under supercritical drying (SCD) with EtOH. For the SCD, UCNPs dispersed in EtOH were placed inside an autoclave filled with EtOH, sealed, and flushed with gaseous N_2. Pressure was maintained at 80 bar until reaching 260 °C with a heating rate of 80 °C/h. The reactor valve outlet was opened for EtOH release under supercritical conditions, thus dropping the pressure gradually. The system was cooled down to RT before opening the autoclave. UCNPs annealing was carried out under a N_2 atmosphere, for 5 h and 400 °C with a heating rate of 20 °C/min. UCNPs were cooled down until RT under the same atmosphere.

To obtain the silica shell, 30 mL of UCNPs dispersed in EtOH (3 mg/mL) were placed in a bath at 0 °C under stirring [47]. TEOS (0.2 mL) was firstly added and, 5 min later, ammonium hydroxide (3 mL) was then incorporated. The reaction took place for 2 h, under stirring and at 0 °C. The thus obtained UCNPs were washed three times with EtOH. Synthesis of the lanthanide core-shell UCNPs was thus performed according to the scheme depicted in Fig. 5.1a,b.

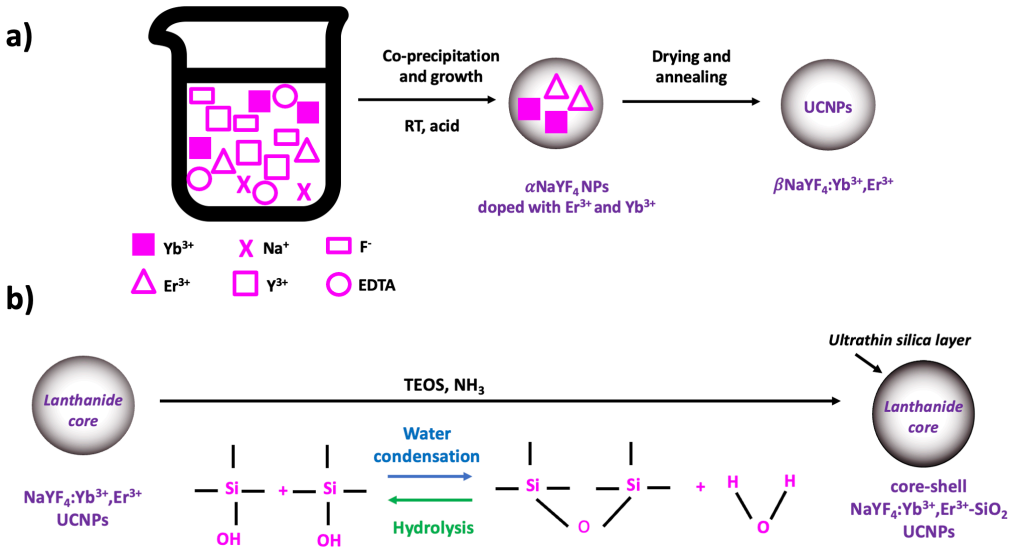


Figure 5.1. Experimental procedure used to obtain silica gel-coated UCNPs. **a)** Synthesis of UCNPs by co-precipitation. **b)** Production of core–shell $NaYF_4$:Yb^{3+},Er^{3+}-SiO_2 UCNPs by sol–gel Stöber method. The simplified chemical reactions of the sol–gel method, hydrolysis, and condensation of TEOS, are also included. Silica gel coating method was performed either before or after the drying step.

Different formulations of UCNPs were obtained (Table 5.1) and denoted differently depending on the lanthanide precursors (lanthanide nitrates–N or lanthanides oxides–O), drying procedure (SCD, or oven drying–OD) and when the drying was performed (before or after the silica coating–BC or AC, respectively). A formulation without coating (O, OD) was also obtained for the sake of particle size and morphology comparison.

Table 5.1. Different UCNPs formulations studied.

Formulation	Lanthanide Precursors	Drying Method	Drying Moment
O, OD-AC	Lanthanide oxides	Oven drying	After silica coating
O, OD-BC	Lanthanide oxides	Oven drying	Before silica coating
O, OD	Lanthanide oxides	Oven drying	-
N, OD-AC	Lanthanide nitrates	Oven drying	After silica coating
N, OD-BC	Lanthanide nitrates	Oven drying	Before silica coating
N, SCD-AC	Lanthanide nitrates	SCD	After silica coating
N, SCD-BC	Lanthanide nitrates	SCD	Before silica coating

5.2.3. Physicochemical evaluation of UCNPs

ζ-potential measurements of UCNPs were performed with a ζ-potential analyzer (Malvern Panalytical, Malvern, United Kingdom). The morphology of UCNPs was evaluated by transmission electron microscopy (TEM, JEOL JEM-2010, Tokyo, Japan) operating at 200 kV. Confocal microscopy (Leica TCS-SP2 spectral confocal microscope, Leica Microsystems Heidelberg GmbH, Mannheim, Germany) was also used to qualitatively evaluate the fluorescence emission of the UCNPs powder. A 2-year physicochemical stability of UCNPs was evaluated for the most promising formulations in terms of luminescent properties by comparative TEM and confocal microscopy analysis, performed just after synthesis and after a 2-year mid-term storage of the UCNPs at RT, protected from light and stored in closed glass vials during this time.

To obtain the luminescence measurements and verify the UC process, the UC emission spectra of the UCNPs were collected in a sample holder with a ~45° angle with respect to the excitation. The excitation source consisted of a Spectra Physics Solstice-Ace laser coupled to a TOPAS Prime Amplifier, with an excitation wavelength of 980 nm (λ_{exc} = 980 nm) while the emission was

USC DE COMPOSTELA

recorded using an AvaSpec-ULS-TEC Avantes Senseline Fiber Optic Spectrometer System. A Newport 10SWF-800-B (BG059) short-bandpass filter was used in the emission optical path to cut the laser-scattered light. The UC spectra were collected in the 450–725 nm emission range.

Crystalline phases of the nanocomplexes were identified by X-ray diffraction (XRD) using a Bruker 8D advance diffractometer (Billerica, MA, USA). Diffractograms were obtained using Cu Kα radiation (λ =0.154184 nm) in the 5–120° (2θ) range. The step was set at 0.03°, the recording time at 7 s per step, and the applied voltage and current at 40 kV and 40 mA, respectively. EDX was performed with a TESCAN VEGA3 SBH (Brno, Czech Republic) microscope with an EDX detector Burker XFlagh 410 M (Billerica, MA, USA) operating at 20 kV. ATR/FT-IR was obtained with a Gladi-ATR accessory. A diamond crystal (Pike, Madison, WI, USA) was employed to analyze the chemical structure of the nanocomplexes in the mid-IR spectrum (400–4000 cm^{-1}) with 32 scans and a resolution of 2 cm^{-1}.

5.2.4. Cell viability tests

Cytocompatibility of the most promising UCNPs formulation (N, OD-BC) was evaluated by assessing the degradation of WST-1 into formazan, which directly correlates with the number of cells that are metabolically active. BALB/c3T3 cells (6500 cells/cm^2) were seeded in 24-well plates with 1000 µL of DMEM supplemented with 15% fetal bovine serum, penicillin 100 U/mL and streptomycin 100 g/mL. After incubation at 37 °C in a humidified atmosphere enriched with 5% CO_2 for 24 h, UCNPs (N, OD-BC) in powder form (5 mg) were UV-sterilized for 30 min and placed in a culture insert in contact with cells by triplicate. The previous literature does not evaluate concentrations above 5 mg/mL for bioimaging applications, including *in vivo* experiments, since lower amounts must provide a detectable fluorescence signal without compromising biocompatibility [21,28,32]. Cells alone were also tested under the same conditions as the positive controls. After 24 and 48 h of culture, inserts were removed, 25 µL of WST-1 was pipetted

USC UNIVERSIDADE DE SANTIAGO DE COMPOSTELA

and plates were incubated for 2 h. Then, 110 µL were pipetted to a 96-well plate and absorbance was measured at λ = 450 nm (Infinite® M200, Tecan Group Ltd., Männedorf, Switzerland).

5.2.5. Hemolytic activity test

The hemolytic activity of 5 and 10 mg of the most promising formulation of UCNPs (N, OD-BC) was tested by contact with human blood. Fresh human whole blood was obtained from the Galician Transfusion Center (Spain) in accordance with the Declaration of Helsinki. Firstly, blood was diluted to 3% (v/v) in 0.9% (w/v) NaCl. Then, 1000 µL of the diluted blood was poured into conical tubes containing different amounts of UCNPs (5 or 10 mg). Furthermore, 900 µL of the diluted blood was mixed with 100 µL of 4% (v/v) Triton X-100 (positive control) or 100 µL of PBS pH 7.4 (negative control). Samples were tested by triplicate and incubated at 37 °C and 100 rpm in an orbital shaker for 60 min. After centrifugation at 10.000g for 10 min (Sigma 2-16P, Sigma Laboratory Centrifuges, Osterode am Harz, Germany), 150 µL of the supernatant were pipetted into a 96-well plate to measure the hemoglobin absorbance at λ = 540 nm (FLUOStar Optima, BMG Labtech, Ortenberg, Germany). Hemolysis was determined by Equation 5.1:

$$Hemolysis\ (\%) = \left(\frac{Abss - Absn}{Absp - Absn}\right) \cdot 100 \qquad Equation\ 5.1$$

where Abss is the absorbance of the samples containing the UCNPs, Absn is the absorbance of the negative control, and Absp is the absorbance of the positive control.

5.2.6. Statistical analysis

Results of *in vitro* assays (n = 3) were reported as the mean value ± standard deviation and post hoc Tukey HSD multiple comparison tests were performed to assess the statistical significance of the differences between groups and regarding controls. Values of $p < 0.05$ were considered statistically significant.

USC UNIVERSIDADE DE SANTIAGO DE COMPOSTELA

5.3. Results and Discussion

5.3.1. Physicochemical evaluation of UCNPs

All the tested synthetic procedures led to the production of UCNPs formulations in the form of a whitish and fine powder. Similar yields were observed for all the studied methods, with a slightly lower amount of UCNPs obtained after procedures involving SCD due to some mass losses during the drying step. Synthesis was simpler in the case of the use of nitrates of the lanthanides than in the case of oxides of the lanthanides due to the pH adjustment needed in the latter case. Near-zero and negative zeta potential (ζ-potential) values were obtained for all the formulations studied (Table 5.2). These values are good since highly negative charged UCNPs could be passively delivered to certain tissues [33] while highly positive charged UCNPs induce cell electrostatic interactions that increase endocytic uptake and are thus more toxic [4,34].

Table 5.2. ζ-potential measurements of different UCNPs formulations. For notation of the formulations, please refer to Table 5.1.

UCNPs Formulation	ζ-Potential (mV)
O, OD-AC	−7.28 ± 1.99
O, OD-BC	−17.72 ± 0.12
O, OD	−6.39 ± 2.03
N, OD-AC	−9.64 ± 1.03
N, OD-BC	−7.07 ± 1.32
N, SCD-AC	−9.04 ± 1.09
N, SCD-BC	−8.78 ± 0.52

The formation of UCNPs with uniformity in shape was observed by TEM imaging (Fig. 5.2) in all cases, regardless of the gel drying method used (SCD or oven drying) or the silica coating (presence or absence). This is a very good result since all the formulations are highly spherical (Fig. 5.2), thus demonstrating the shape-controlling ability of the co-precipitation approach herein employed. The two formulations dried by SCD (N, SCD-AC; N, SCD-BC) had an aspect and size close to that of the oven-dried UCNPs (N, OD-AC; O, OD-AC; O, OD; O, OD-BC; N, OD-BC), suggesting the absence of an impact of the drying procedure employed during synthesis in the morphology of UCNPs. It should also be noted that the formulation without a silica coating (O,

USC UNIVERSIDADE DE SANTIAGO

OD) had a similar aspect and size to the same formulation with the coating (O, OD-AC; O, OD-BC), suggesting the very low thickness of the silica coating (2.75 ± 0.49 nm). This ultrathin silica coating is beneficial to the energy transfer between UCNPs [35]. The mid-term storage (2 years) of UCNPs under controlled conditions had no effect on particle morphology (O, OD-BC just after synthesis vs. 2 years after synthesis, and N, OD-BC just after synthesis vs. 2 years after synthesis). Regarding UCNPs sizes, the major population of the O, OD-BC formulation obtained just after synthesis was lost after 2-years of mid-term storage, in contrast to the N, OD-BC formulation, where the UCNPs size was preserved after mid-term storage. Therefore, results suggest that the UCNPs obtained from the lanthanide nitrates are more stable in terms of size than the ones obtained from the lanthanide oxides. This morphological stability is adequate and esessential to satisfy the requirements of biological applications [35].

Aggregates were detected for some UCNPs formulations (N, OD-AC; O, OD-AC; O, OD and N, SCD-AC) with a decrease in their formation after mid-term storage (O, OD-BC just after synthesis vs. O, OD-BC 2 years after synthesis and N, OD-BC just after synthesis vs. N, OD-BC 2 years after synthesis). UCNPs tended to aggregate after annealing at higher temperatures and also due to the carbonization of the capping reagent EDTA after annealing, thus reducing UCNPs hydrophilicity, in agreement with observations by Wang and coworkers [21]. The aggregation may also be a consequence of the interparticle chemical bonding between the silica shells of the UCNPs [31]. It was previously described that there is an optimal size for efficient uptake of each type of nanomaterials into cells [36]. UCNPs of a very low size (<45 nm) were reported with the same sensitizers (Yb^{3+} and Er^{3+}) [20,37,38], which could be easily internalized by cells and induce high toxicity afterwards. In contrast, this particle size range just represents a very minor population in all UCNPs formulations (Fig. 5.2) and adequate sizes for biomedical applications were obtained with this novel co-precipitation approach herein developed. Furthermore, an increase in the size of the nanocrystals obtained with the same trivalent lanthanide ions was reported to increase the luminescence emission [39].

USC UNIVERSIDADE DE SANTIAGO DE COMPOSTELA

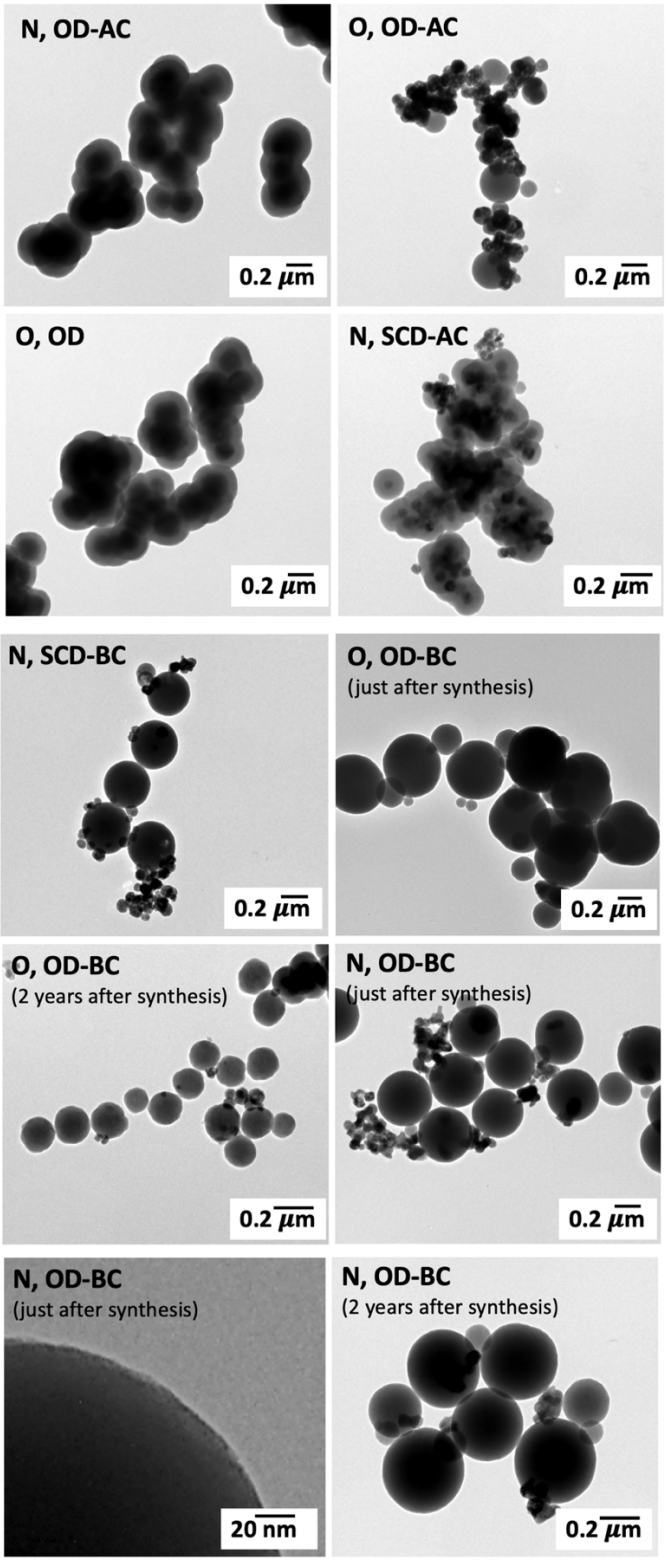


Figure 5.2. TEM images of different UCNPs formulations. For notation of the formulations, please refer to Table 5.1.

All the synthesized UCNPs emitted visible radiation when excited at 980 nm, showing three different bands at 520, 540 and 657 nm in the UC luminescence spectra (Fig. 5.3a,b), except for

the oxide-derivative O, OD-AC formulation where no meaningful UC emission was detected (Fig. 5.3b). The lower efficiency of the UC process for the O, OD-AC formulation can be attributed to the type of host matrix phase (cubic α-$NaYF_4$ or hexagonal β-$NaYF_4$) [18,19,21], which will be discussed later. The peaks at 520, 540 and 657 nm correspond to $^2H_{11/2}\rightarrow{}^4I_{15/2}$, $^4S_{3/2}\rightarrow{}^4I_{15/2}$, $^4F_{9/2}\rightarrow{}^4I_{15/2}$ optical radiative transitions of Er^{3+} ions, respectively, as previously reported for UCNPs composed of the same trivalent lanthanide ions [39,40] and in a study of Er^{3+} and Yb^{3+} UC photoluminescence on films [41]. It must be noted that an enhancement of the photoluminescence was observed when structures where co-doped with both ions, with a photoluminescence intensity more than one order-of-magnitude higher with respect to materials doped only with Er^{3+}[41].

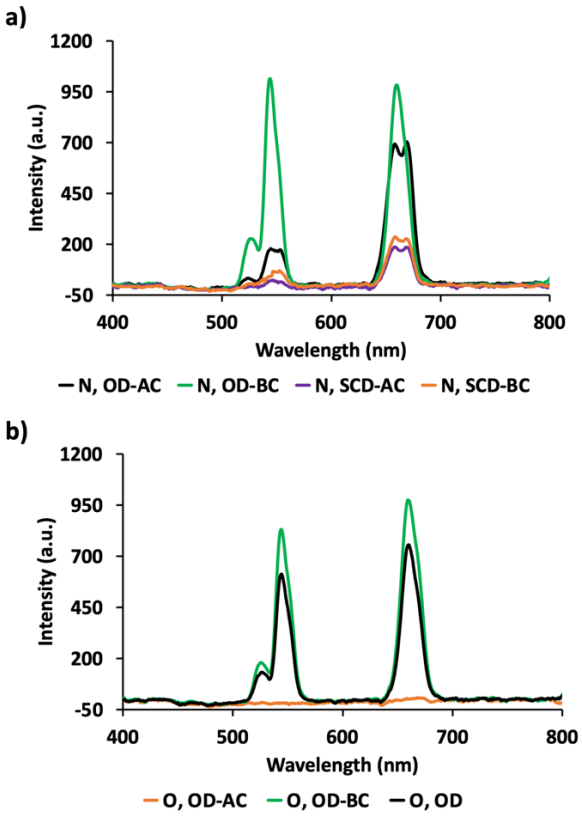


Figure 5.3. UC spectra for the **a)** lanthanide-nitrates-based UCNPs and for the **b)** lanthanide-oxides-based UCNPs in the solid state, collected with λexc = 980 nm. For notation of the formulations, please refer to Table 5.1.

USC
UNIVERSIDADE DE SANTIAGO DE COMPOSTELA

Some formulations (N, OD-AC; N, SCD-AC and N, SCD-BC) exhibited structured green and red bands maybe due to the saturation of the detector and not to the emission from different excited states [42]. Similar structured bands were also reported for different $NaYF_4$:Yb^{3+},Er^{3+} formulations [38,39,43]. In the comparative UC spectra performed under constant experimental conditions (laser intensity), the N, OD-BC and O, OD-BC formulations exhibited a higher fluorescence intensity in each peak, achieving the highest values for N, OD-BC. It has been recently published that with a very low Er^{3+} concentration (close to 1%) UC photoluminescence was not detected, so the conversion of NIR into visible light comes from the interaction between neighboring Er^{3+} ions [44]. This reaction was associated with the energy transfer from one excited Er^{3+} to another Er^{3+} and with the upgrade of the latter Er^{3+} into a higher-energy level. In this cooperative UC, Er^{3+} luminescence comes from two centers, one related to the Er^{3+} UC luminescence (520 and 540 nm peaks) and the other one related to the Er^{3+}- Yb^{3+}ion-ion interaction and its UC luminescence (657 nm peak). It is also important to note that the green band/red band UC emission intensity ratio could be related to different “excitation environments” in terms of ion size, ionic dependence of site distortions and ion concentration due to a concentration-quenching effect between Er^{3+} and Yb^{3+} ions [40,44].

The crystalline nature of UCNPs was confirmed by the corresponding XRD pattern (Fig. 5.4a,b), with similar diffractograms to those previously reported for UCNPs with the same sensitizer–activator system (Yb^{3+}-Er^{3+}) [45]. The UC process is improved with a highly crystalline host lattice holding a low-energy environment that enables the energy transfer from the sensitizer to the activator. The essential requirements for an efficient energy transfer are the distance between the sensitizer and the activator, the spectral overlap and the achievement of a high absorbance by the activator at the emission wavelength of the sensitizer [46]. Both types of crystalloid phases, cubic and hexagonal, exist at the ambient pressure being the cubic phase the dominant one, i.e., the thermodynamically metastable. However, the green emission of the crystalline hexagonal phase is 10 times stronger than that of the crystalline cubic phase and the overall

USC UNIVERSIDADE DE SANTIAGO DE COMPOSTELA

emission is ca. 5-fold higher in the thermodynamically stable β-$NaYF_4$:Yb^{3+},Er^{3+}. Nevertheless, there is a high-energy barrier between α- and β-phases, so the phase transition needs temperatures higher than 280 °C [37]. It has also been reported that both phases coexist from 290 to 300 °C and that very long reaction times are needed for the complete α→β transition at 300 °C, so 400 °C was herein selected as the reaction temperature. Consistently, the formation of β-phased UCNPs did not involve a direct phase transformation process but a dissolution/recrystallization process. As expected, the fluorescence intensity increased according to the UCNP conversion from the host matrix cubic to the hexagonal phase after annealing at 400 °C. Nevertheless, for N, SCD-AC, N, OD-AC and O, OD-AC formulations, no peaks related to the hexagonal phase were observed (Fig. 5.4a,b). The hexagonal phase peaks were detected for N, OD-BC, O, OD-BC and O, OD formulations, thus suggesting that the oven drying is a more appropriate method for the synthesis of UCNPs with respect to the SCD. Finally, the highest fluorescence intensity appeared when drying and annealing steps were performed before the silica coating step, so the best formulations in terms of fluorescence intensity (O, OD; O, OD-BC; N, OD-BC) were selected for further EDX characterization. The full accomplishment of the crystalline hexagonal phase under certain experimental conditions unveils the phase-controlling ability of the co-precipitation method herein employed.

USC UNIVERSIDADE DE SANTIAGO DE COMPOSTELA

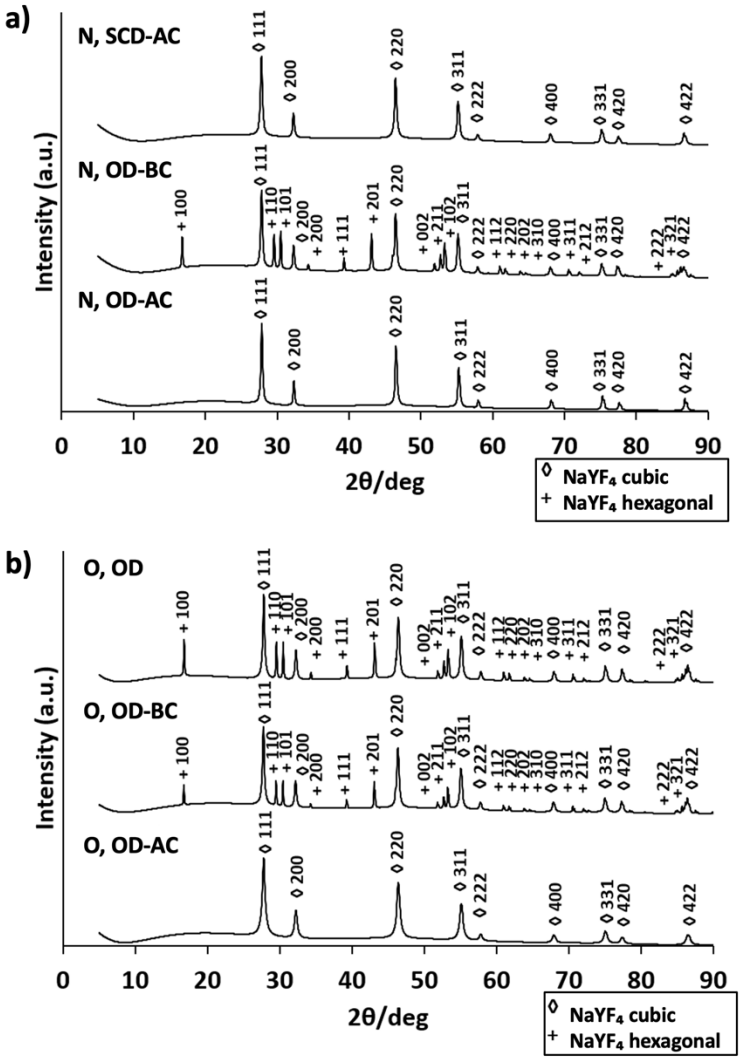


Figure 5.4. XRD diffractograms of **a)** lanthanide nitrates-based UCNPs and of **b)** lanthanide oxides-based UCNPs. For notation of the formulations, please refer to Table 5.1.

ATR/FT-IR spectroscopy was used to trace the coating step with silica of the different UCNPs formulations. The presence of the silica was confirmed in all formulations where the coating step was performed by the detection of two broad bands at 1080 cm^{-1} (Fig. 5.5, red circles) and 1175 cm^{-1} (green circles) corresponding to vSi-O-Si vibrations. Moreover, bands at 970 cm^{-1} (blue circles) and 800 cm^{-1} (purple circles), corresponding to a vSi-O vibration of the ≡Si-O-Si≡ bond, were detected and associated with the silica functionalization [47,48]. ATR/FT-IR spectra of all samples are almost completely smooth in the 1400–4000 cm^{-1} region, without exhibiting characteristic peaks that could indicate the presence of functional groups not related to silica.

USC UNIVERSIDADE DE SANTIAGO DE COMPOSTELA

Results confirmed that the functionalization of UCNPs with silica was successfully achieved regardless of the drying procedure used (SCD or oven drying) or the moment when the coating was performed (before or after the drying step).

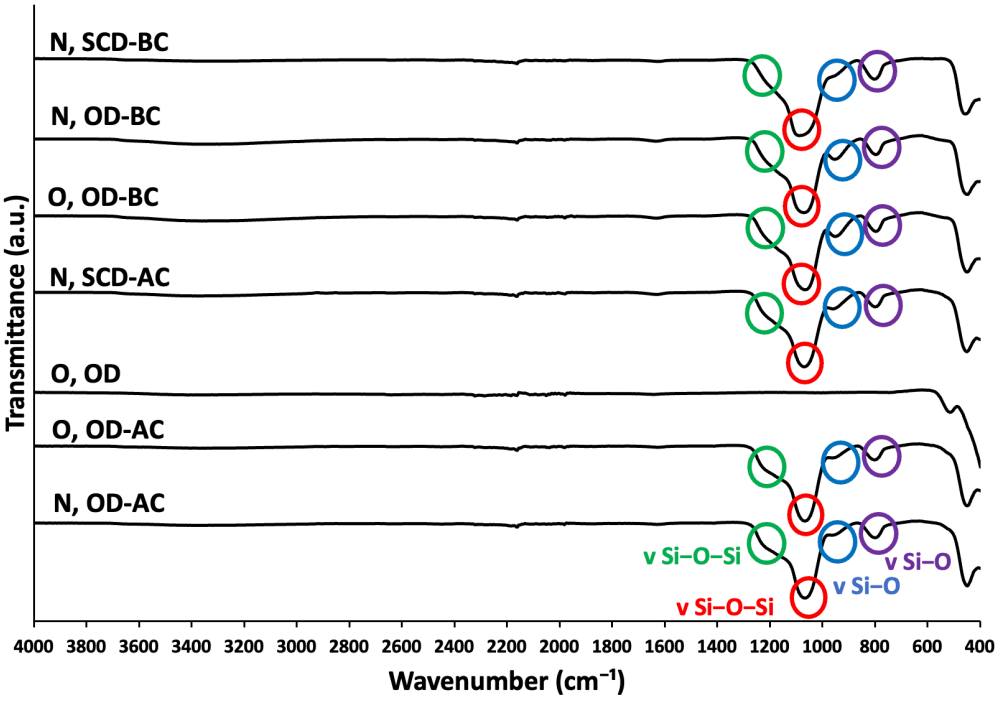


Figure 5.5. ATR/FT-IR spectra of different formulations of UCNPs. For notation of the formulations, please refer to Table 5.1.

The elemental mapping obtained by the EDX technique (Fig. 5.6a) confirmed the presence of all the employed chemical elements, including the peaks related to ions present at low concentrations (Na and F). UCNPs showed the peaks related to the host material constituents and lanthanides homogeneously distributed throughout the analyzed sample, thus confirming their expected composition and that they were congruent with the obtained UC fluorescence results. EDX results also unveiled the decoration of UCNPs with similar intensity for the elements from the host matrix (Na, F) and for the rare-earth elements (Y, Yb, Er). This elemental mapping suggests their simultaneous and homogeneous distribution throughout the sample, which is attributed to the successful connection between the rare-earth elements and the host matrix. Similar elemental mapping was previously found for UCNPs doped with the same rare-earth

USC DE SANTIAGO DE COMPOSTELA

elements [35]. The background material with lower fluorescence is mainly silica. The more homogeneous formulations in terms of fluorescence are the lanthanide nitrates-based UCNPs. This is a very beneficial result since the nitrate-derived UCNPs are much easier to synthesize than their oxide-derived counterparts and only involve non-hazardous steps. Since high crystallinity and the presence of chemical elements were confirmed for all formulations studied, the best formulation in terms of fluorescence intensity (i.e., the formulation with the highest intensity in each peak, N, OD-BC) was selected for biological characterization. This formulation also exhibited physicochemical stability in terms of particle shape and fluorescence properties after a 2-year mid-term storage.

Confocal microscopy is the main approach used for localizing UCNPs by *in vitro* cell-based tests and by *in vivo* bioimaging experiments. For this reason, the best formulations of UCNPs were also analyzed by this technique (Fig. 5.6b), with a good fluorescence signal obtained just after synthesis (for both formulations studied) and after 2-year storage, thus endorsing the possibility of their mid-to-long-term storage without detrimental in fluorescence properties. Long-term photostability was previously studied for UCNPs [32] with good results in terms of UC spectra but after shorter time periods (5 months) than those herein evaluated.

USC UNIVERSIDADE DE SANTIAGO DE COMPOSTELA

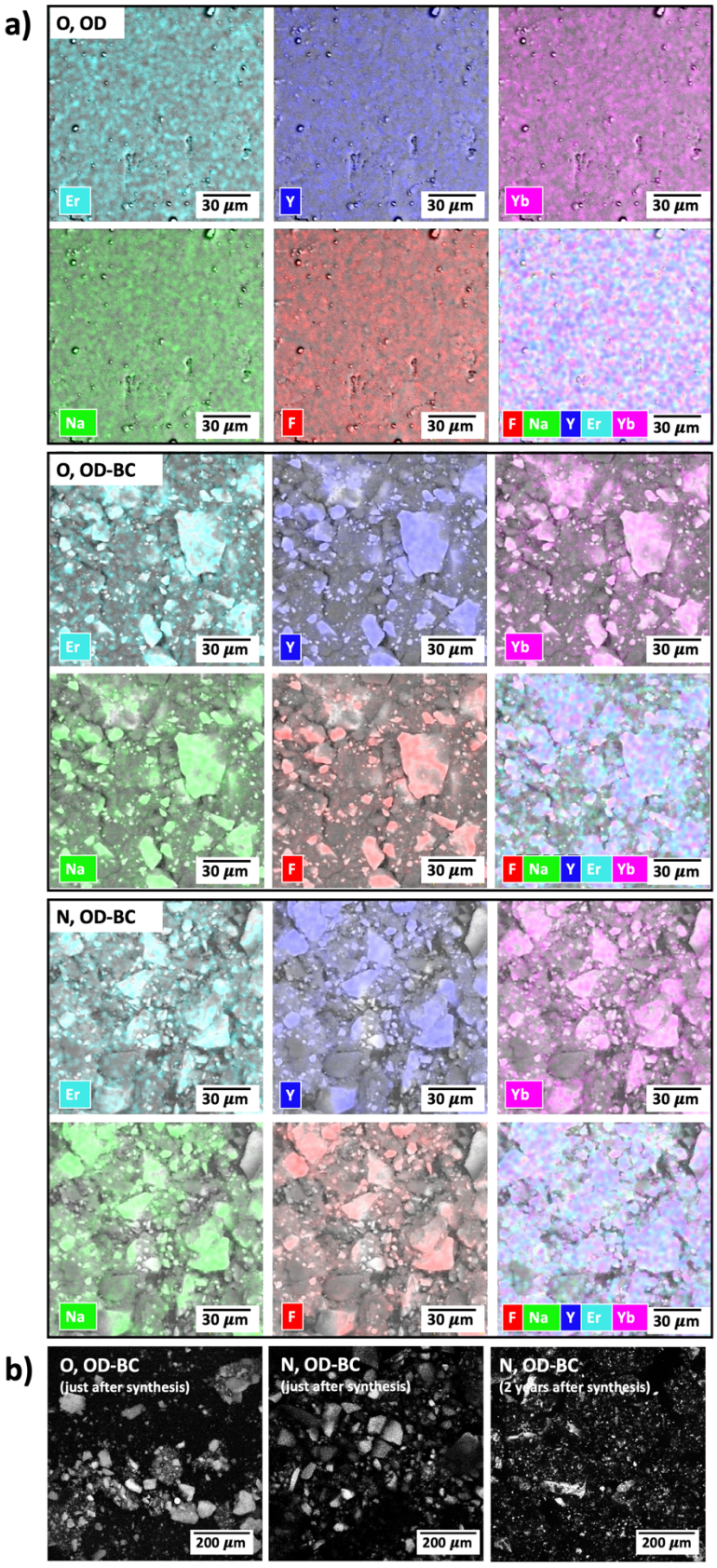


Figure 5.6. a) EDX mapping and **b)** confocal microscopy images of different UCNPs formulations. For notation of the formulations, please refer to Table 5.1.

USC UNIVERSIDADE DE SANTIAGO DE COMPOSTELA

5.3.2. Cell compatibility and hemolytic activity evaluation

The biocompatibility of UCNPs was confirmed by the high viability of mouse embryo fibroblasts in the presence of the N, OD-BC UCNP formulation for 24 and 48 h, without significant differences with respect to the positive controls (Fig. 5.7a). These results are better than those previously reported for silica-coated $NaYF_4$:Yb^{3+},Er^{3+} UCNPs with a low size (21 ± 5 nm) after contact with bone marrow-derived stem cells (79.5% after 24 h and 66.8% after 48 h) or skeletal myoblasts (87.8% after 24 h and 68.2% after 48 h) at 100 μg/mL [49]. Concentrations (0–5 mg/mL) close to those herein reported (5 mg/mL) were previously tested for $KGdF_4$:Yb^{3+},Er^{3+} UCNPs with cell viabilities higher than 60% after 20 h [50]. Moreover, lower concentrations of UCNPs (100 μg/mL) showed lower levels of biocompatibility than those herein reported (close to 75% of cell viability) and were reported as safe to be used in subcellular imaging applications [51]. A reduction in the viability after 72 h of rat glioma cells and of rat mesenchymal stem cells was observed for lower concentrations than those herein studied (1000 μg/mL) of polymer-coated UCNPs composed of the same trivalent lanthanide ions [39]. Furthermore, the relevance of the protective coating to the safety of UCNPs was assessed by evaluating the cell viability in $NaYF_4$:Yb^{3+},Er^{3+} UCNPs with different polymeric coatings [38]. Very low cell viabilities were obtained with neat UCNPs while the different polymer coatings studied increased rat mesenchymal stem cell viabilities, evaluated in the concentration range 0–1000 μg/ mL. It is important to note that much lower concentrations than those herein tested (100 μg/mL) showed a bright fluorescence signal on HeLa cells, with a high cell viability (90%) after 24 h [32]. These findings emphasized the safety of use of the herein synthesized N, OD-BC UCNPs.

No hemolysis was observed on human red blood cells after contact with N, OD-BC UCNPs (Fig. 5.7b), with no significant differences with respect to the negative controls for the two studied concentrations (5 and 10 mg/mL). No influence of UCNPs on rat red blood cells was previously reported for $NaYF_4$:Yb^{3+},Er^{3+},Gd^{3+} UCNPs at lower UCNPs concentrations (25–500 μg/mL) [35].

USC DE COMPOSTELA

Excellent human blood compatibility was also found for $NaGdF_4:Yb^{3+},Er^{3+}$ UCNPs at a Gd content of 500 ppm [45]. These results suggest the absence of a negative impact of the N, OD-BC UCNPs, even at very high concentrations (10 mg/mL), on human red blood cells. Therefore, silica coating by sol-gel Stöber process seems to create a structurally stable nanocomplex in biological fluids that effectively protect the lanthanide core from inducing any cytotoxic event.

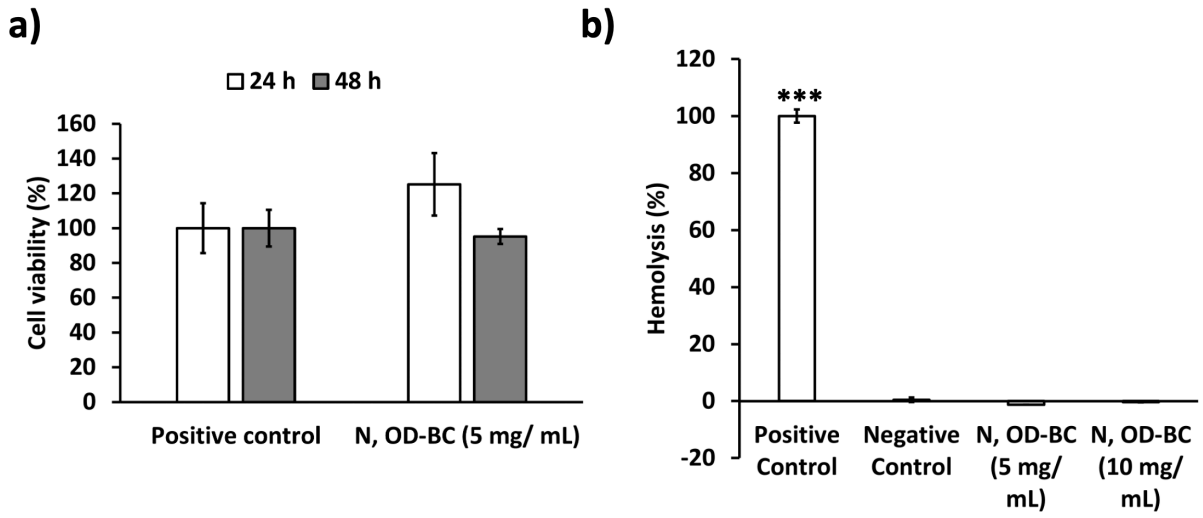


Figure 5.7. a) Cell viability of BALB/c3T3 cells in contact with N, OD-BC UCNPs at 5 mg/mL determined by WST-1 test. Positive control: BALB/c3T3 cells. No statistically significant differences among groups were detected (post hoc Tukey HSD multiple comparison-test; $p < 0.05$). **b)** Hemolytic activity (expressed in %) for N, OD-BC UCNPs (5 and 10 mg/mL). Positive and negative controls were 4% (v/v) Triton X-100 solution and PBS pH 7.4 solution, respectively. Statistically significant differences among groups were represented as *** (post hoc Tukey HSD multiple comparison test; $p < 0.001$). For notation of the formulation, please refer to Table 5.1.

5.4. Conclusions

$NaYF_4:Yb^{3+},Er^{3+}$ core-shell nanocomplexes with a highly photostable luminescent core and a non-porous silica gel shell were successfully fabricated by a facile and environmentally friendly combination of co-precipitation (core) and sol-gel (shell) approaches. The synthetic strategy was able to control the morphology and crystalline phase of the UCNPs as well as their biocompatibility. The size and ζ-potential values achieved suggest the absence of induction of negative cell interactions. Similar morphology and luminescence of silica gel-coated UCNPs were observed after 2-year mid-term storage, thus indicating their preliminary physicochemical

USC DE SANTIAGO DE COMPOSTELA

stability. An optimum formulation with the highest values of fluorescence intensity and coherent presence of all elements in the UCNPs was selected. Excellent bio- and hemocompatibility were obtained for these UCNPs, after assays with murine fibroblast and human blood, respectively. The protective silica coating synthesized by the sol-gel Stöber process seems to preserve over time the lanthanide core UC emission while promoting the bio- and hemocompatibility of the nanosystem. Consistently, these UCNPs represent a promising alternative to be tested as *in vivo* biolabels, as the concentration range could be increased until 5 mg/mL to get a detectable signal without losing bio- or hemocompatibility. These results encourage further research into potential applications of the herein synthesized silica gel-coated UCNPs as biomarkers for biological detections, in cellular and animal imaging systems by their incorporation into biomedical devices for further evaluation of these UCNPs as *in vivo* bioimaging probes.

5.5. References

1. Lahoti, H.S.; Jogdand, S.D. Bioimaging: Evolution, Significance, and Deficit. Cureus 2022, 14, e28923. https://doi.org/10.7759/cureus.28923.
2. Wang, C.; Li, X.; Zhang, F. Bioapplications and Biotechnologies of Upconversion Nanoparticle-Based Nanosensors. Analyst 2016, 141, 3601–3620. https://doi.org/10.1039/C6AN00150E.
3. Hu, Y.; Wu, B.; Jin, Q.; Wang, X.; Li, Y.; Sun, Y.; Huo, J.; Zhao, X. Facile Synthesis of 5 Nm $NaYF_4$:Yb/Er Nanoparticles for Targeted Upconversion Imaging of Cancer Cells. Talanta 2016, 152, 504–512. https://doi.org/10.1016/j.talanta.2016.02.039.
4. Gerelkhuu, Z.; Lee, Y.-I.; Yoon, T.H. Upconversion Nanomaterials in Bioimaging and Biosensor Applications and Their Biological Response. Nanomaterials 2022, 12, 3470. https://doi.org/10.3390/nano12193470.
5. Malhotra, K.; Hrovat, D.; Kumar, B.; Qu, G.; Houten, J.V.; Ahmed, R.; Piunno, P.A.E.; Gunning, P.T.; Krull, U.J. Lantha-nide-Doped Upconversion Nanoparticles: Exploring A Treasure Trove of NIR-Mediated Emerging Applications. ACS Appl. Mater. Interfaces 2023, 15, 2499–2528. https://doi.org/10.1021/acsami.2c12370.
6. Mahata, M.K.; De, R.; Lee, K.T. Near-Infrared-Triggered Upconverting Nanoparticles for Biomedicine Applications. Biomedicines 2021, 9, 756. https://doi.org/10.3390/biomedicines9070756.
7. Vorotnikov, Y.A.; Vorotnikova, N.A.; Shestopalov, M.A. Silica-Based Materials Containing Inorganic Red/NIR Emitters and Their Application in Biomedicine. Materials 2023, 16, 5869. https://doi.org/10.3390/ma16175869.
8. Le, X.T.; Youn, Y.S. Emerging NIR Light-Responsive Delivery Systems Based on Lanthanide-Doped Upconverting Nanoparticles. Arch. Pharm. Res. 2020, 43, 134–152. https://doi.org/10.1007/s12272-020-01208-3.
9. Tsai, S.-R.; Hamblin, M.R. Biological Effects and Medical Applications of Infrared Radiation. J. Photochem. Photobiol. B Biol. 2017, 170, 197–207. https://doi.org/10.1016/j.jphotobiol.2017.04.014.
10. Gnach, A.; Lipinski, T.; Bednarkiewicz, A.; Rybka, J.; Capobianco, J.A. Upconverting Nanoparticles: Assessing the Toxicity. Chem. Soc. Rev. 2015, 44, 1561–1584. https://doi.org/10.1039/C4CS00177J.
11. Tanaka, Y.; Tsunemi, Y.; Kawashima, M.; Nishida, H. The Impact of Near-Infrared in Plastic Surgery. Plast. Surg. Int. J. 2013, 2013, 1–13. https://doi.org/10.5171/2013.973073.

USC
DE SANTIAGO
DE COMPOSTELA

12. Zhu, X.; Zhang, J.; Liu, J.; Zhang, Y. Recent Progress of Rare-Earth Doped Upconversion Nanoparticles: Synthesis, Optimization, and Applications. Adv. Sci. 2019, 6, 1901358. https://doi.org/10.1002/advs.201901358.
13. Yi, Z.; Luo, Z.; Qin, X.; Chen, Q.; Liu, X. Lanthanide-Activated Nanoparticles: A Toolbox for Bioimaging, Therapeutics, and Neuromodulation. Acc. Chem. Res. 2020, 53, 2692–2704. https://doi.org/10.1021/acs.accounts.0c00513.
14. Liu, Q.; Chen, M.; Sun, Y.; Chen, G.; Yang, T.; Gao, Y.; Zhang, X.; Li, F. Multifunctional Rare-Earth Self-Assembled Nanosystem for Tri-Modal Upconversion Luminescence /Fluorescence /Positron Emission Tomography Imaging. Biomaterials 2011, 32, 8243–8253. https://doi.org/10.1016/j.biomaterials.2011.07.053.
15. Cheng, L.; Yang, K.; Shao, M.; Lu, X.; Liu, Z. *In Vivo* Pharmacokinetics, Long-Term Biodistribution and Toxicology Study of Functionalized Upconversion Nanoparticles in Mice. Nanomedicine 2011, 6, 1327–1340. https://doi.org/10.2217/nnm.11.56.
16. Generalova, A.N.; Chichkov, B.N.; Khaydukov, E.V. Multicomponent Nanocrystals with Anti-Stokes Luminescence as Contrast Agents for Modern Imaging Techniques. Adv. Colloid Interface Sci. 2017, 245, 1–19. https://doi.org/10.1016/j.cis.2017.05.006.
17. Min, Y.; Li, J.; Liu, F.; Padmanabhan, P.; Yeow, E.; Xing, B. Recent Advance of Biological Molecular Imaging Based on Lanthanide-Doped Upconversion-Luminescent Nanomaterials. Nanomaterials 2014, 4, 129–154. https://doi.org/10.3390/nano4010129.
18. Zhao, J.; Lu, Z.; Yin, Y.; McRae, C.; Piper, J.A.; Dawes, J.M.; Jin, D.; Goldys, E.M. Upconversion Luminescence with Tunable Lifetime in $NaYF_4$: Yb,Er Nanocrystals: Role of Nanocrystal Size. Nanoscale 2013, 5, 944–952. https://doi.org/10.1039/C2NR32482B.
19. Lingeshwar Reddy, K.; Balaji, R.; Kumar, A.; Krishnan, V. Lanthanide Doped Near Infrared Active Upconversion Nano-phosphors: Fundamental Concepts, Synthesis Strategies, and Technological Applications. Small 2018, 14, 1801304. https://doi.org/10.1002/smll.201801304.
20. Homann, C.; Krukewitt, L.; Frenzel, F.; Grauel, B.; Würth, C.; Resch-Genger, U.; Haase, M. $NaYF_4$: Yb,Er/$NaYF_4$ Core/Shell Nanocrystals with High Upconversion Luminescence Quantum Yield. Angew. Chem. Int. Ed. 2018, 57, 8765–8769. https://doi.org/10.1002/anie.201803083.
21. Wang, M.; Abbineni, G.; Clevenger, A.; Mao, C.; Xu, S. Upconversion Nanoparticles: Synthesis, Surface Modification and Bio-logical Applications. Nanomed. Nanotechnol. Biol. Med. 2011, 7, 710–729. https://doi.org/10.1016/j.nano.2011.02.013.
22. Yang, L.; Shao, B.; Zhang, X.; Cheng, Q.; Lin, T.; Liu, E. Multifunctional Upconversion Nanoparticles for Targeted Dual-Modal Imaging in Rat Glioma Xenograft. J. Biomater. Appl. 2016, 31, 400–410. https://doi.org/10.1177/0885328216658779.
23. Alkahtani, M.; Alsofyani, N.; Alfahd, A.; Almuqhim, A.A.; Almughem, F.A.; Alshehri, A.A.; Qasem, H.; Hemmer, P.R. Engi-neering Red-Enhanced and Biocompatible Upconversion Nanoparticles. Nanomaterials 2021, 11, 284. https://doi.org/10.3390/nano11020284.
24. Rafique, R.; Baek, S.H.; Park, C.Y.; Chang, S.-J.; Gul, A.R.; Ha, S.; Nguyen, T.P.; Oh, H.; Ham, S.; Arshad, M.; et al. Morphological Evolution of Upconversion Nanoparticles and Their Biomedical Signal Generation. Sci. Rep. 2018, 8, 17101. https://doi.org/10.1038/s41598-018-35513-1.
25. Zhou, R.; Ma, T.; Qiu, B.; Li, X. Controlled Synthesis of β-$NaYF_4$:Yb, Er Microphosphors and Upconversion Luminescence Property. Mater. Chem. Phys. 2017, 194, 23–28. https://doi.org/10.1016/j.matchemphys.2017.03.033.
26. Xu, D.; Li, C.; Li, W.; Lin, B.; Lv, R. Recent Advances in Lanthanide-Doped Up-Conversion Probes for Theranostics. Front. Chem. 2023, 11, 1036715. https://doi.org/10.3389/fchem.2023.1036715.
27. Yan, C.; Zhao, H.; Perepichka, D.F.; Rosei, F. Lanthanide Ion Doped Upconverting Nanoparticles: Synthesis, Structure and Properties. Small 2016, 12, 3888–3907. https://doi.org/10.1002/smll.201601565.
28. Sun, Y.; Peng, J.; Feng, W.; Li, F. Upconversion Nanophosphors $NaLu_4$: Yb,Tm for Lymphatic Imaging *In Vivo* by Real-Time Upconversion Luminescence Imaging under Ambient Light and High-Resolution X-Ray CT. Theranostics 2013, 3, 346–353. https://doi.org/10.7150/thno.5137.
29. Stöber, W.; Fink, A.; Bohn, E. Controlled Growth of Monodisperse Silica Spheres in the Micron Size Range. J. Colloid Interface Sci. 1968, 26, 62–69. https://doi.org/10.1016/0021-9797(68)90272-5.
30. Gonçalves, M.C. Sol-Gel Silica Nanoparticles in Medicine: A Natural Choice. Design, Synthesis and Products. Molecules 2018, 23, 2021. https://doi.org/10.3390/molecules23082021.
31. Muhr, V.; Wilhelm, S.; Hirsch, T.; Wolfbeis, O.S. Upconversion Nanoparticles: From Hydrophobic to Hydrophilic Surfaces. Acc. Chem. Res. 2014, 47, 3481–3493. https://doi.org/10.1021/ar500253g.

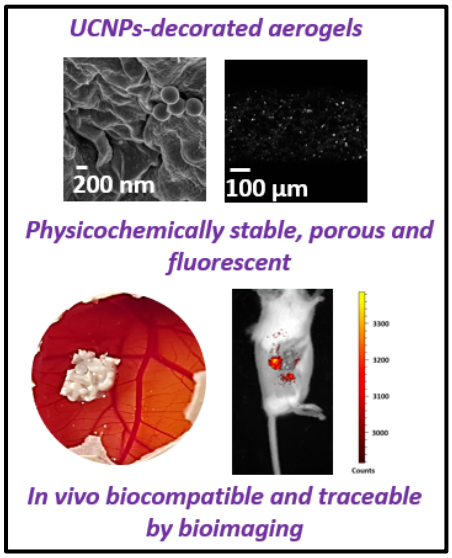
USC UNIVERSIDADE DE SANTIAGO

32. Liu, F.; Zhao, Q.; You, H.; Wang, Z. Synthesis of Stable Carboxy-Terminated $NaYF_4$: Yb^{3+}, Er^{3+} @SiO_2 Nanoparticles with Ultrathin Shell for Biolabeling Applications. Nanoscale 2013, 5, 1047–1053. https://doi.org/10.1039/C2NR33046F.
33. Guryev, E.L.; Smyshlyaeva, A.S.; Shilyagina, N.Y.; Sokolova, E.A.; Shanwar, S.; Kostyuk, A.B.; Lyubeshkin, A.V.; Schulga, A.A.; Konovalova, E.V.; Lin, Q.; et al. UCNP-Based Photoluminescent Nanomedicines for Targeted Imaging and Theranostics of Cancer. Molecules 2020, 25, 4302. https://doi.org/10.3390/molecules25184302.
34. Jin, J.; Gu, Y.-J.; Man, C.W.-Y.; Cheng, J.; Xu, Z.; Zhang, Y.; Wang, H.; Lee, V.H.-Y.; Cheng, S.H.; Wong, W.-T. Polymer-Coated $NaYF_4$: Yb^{3+}, Er^{3+} Upconversion Nanoparticles for Charge-Dependent Cellular Imaging. ACS Nano 2011, 5, 7838–7847. https://doi.org/10.1021/nn201896m.
35. Chen, J.; Zhang, D.; Zou, Y.; Wang, Z.; Hao, M.; Zheng, M.; Xue, X.; Pan, X.; Lu, Y.; Wang, J.; et al. Developing a pH-Sensitive $Al(OH)_3$ Layer-Mediated UCNP@$Al(OH)_3$/Au Nanohybrid for Photothermal Therapy and Fluorescence Imaging *in vivo*. J. Mater. Chem. B 2018, 6, 7862–7870. https://doi.org/10.1039/C8TB02213E.
36. Verma, A.; Stellacci, F. Effect of Surface Properties on Nanoparticle—Cell Interactions. Small 2010, 6, 12–21. https://doi.org/10.1002/smll.200901158.
37. Li, D.; Shao, Q.; Dong, Y.; Jiang, J. Phase-, Shape- and Size-Controlled Synthesis of $NaYF_4$:Yb^{3+},Er^{3+} Nanoparticles Using Rare Earth Acetate Precursors. J. Rare Earths 2014, 32, 1032–1036. https://doi.org/10.1016/S1002-0721(14)60179-4.
38. Nahorniak, M.; Patsula, V.; Mareková, D.; Matouš, P.; Shapoval, O.; Oleksa, V.; Vosmanská, M.; Machová Urdzíková, L.; Jendelová, P.; Herynek, V.; et al. Chemical and Colloidal Stability of Polymer-Coated $NaYF_4$:Yb, Er Nanoparticles in Aqueous Media and Viability of Cells: The Effect of a Protective Coating. Int. J. Mol. Sci. 2023, 24, 2724. https://doi.org/10.3390/ijms24032724.
39. Patsula, V.; Mareková, D.; Jendelová, P.; Nahorniak, M.; Shapoval, O.; Matouš, P.; Oleksa, V.; Konefał, R.; Vosmanská, M.; Machová-Urdziková, L.; et al. Polymer-Coated Hexagonal Upconverting Nanoparticles: Chemical Stability and Cytotoxicity. Front. Chem. 2023, 11, 1207984. https://doi.org/10.3389/fchem.2023.1207984.
40. He, S.; Xia, H.; Zhang, J.; Zhu, Y.; Chen, B. Highly Efficient Up-Conversion Luminescence in Er^{3+}/Yb^{3+} Co-Doped $Na_5Lu_9F_{32}$ Single Crystals by Vertical Bridgman Method. Sci. Rep. 2017, 7, 8751. https://doi.org/10.1038/s41598-017-09222-0.
41. Lashkovskaya, E.I.; Gaponenko, N.V.; Stepikhova, M.V.; Yablonskiy, A.N.; Andreev, B.A.; Zhivulko, V.D.; Mudryi, A.V.; Martynov, I.L.; Chistyakov, A.A.; Kargin, N.I.; et al. Optical Properties and Upconversion Luminescence of $BaTiO_3$ Xerogel Structures Doped with Erbium and Ytterbium. Gels 2022, 8, 347. https://doi.org/10.3390/gels8060347.
42. Avram, D.; Colbea, C.; Patrascu, A.A.; Istrate, M.C.; Teodorescu, V.; Tiseanu, C. Up-Conversion Emission in Transition Metal and Lanthanide Co-Doped Systems: Dimer Sensitization Revisited. Sci. Rep. 2023, 13, 2165. https://doi.org/10.1038/s41598-023-28583-3.
43. Rafique, R.; Baek, S.H.; Phan, L.M.T.; Chang, S.-J.; Gul, A.R.; Park, T.J. A Facile Hydrothermal Synthesis of Highly Lumines-cent $NaYF_4$:Yb^{3+}/Er^{3+} Upconversion Nanoparticles and Their Biomonitoring Capability. Mater. Sci. Eng. C 2019, 99, 1067–1074. https://doi.org/10.1016/j.msec.2019.02.046.
44. Gaponenko, N.V.; Sudnik, L.V.; Vityaz, P.A.; Luchanok, A.R.; Stepikhova, M.V.; Yablonskiy, A.N.; Lashkovskaya, E.I.; Shustsikava, K.V.; Radyush, Y.V.; Zhivulko, V.D.; et al. Upconversion Luminescence of Er^{3+} Ions from Barium Titanate Xero-gel Powder and Target Fabricated by Explosive Compaction Method. J. Appl. Spectrosc. 2022, 89, 238–243. https://doi.org/10.1007/s10812-022-01349-x.
45. Liu, F.; He, X.; Lei, Z.; Liu, L.; Zhang, J.; You, H.; Zhang, H.; Wang, Z. Facile Preparation of Doxorubicin-Loaded Upconver-sion@Polydopamine Nanoplatforms for Simultaneous *In Vivo* Multimodality Imaging and Chemophotothermal Synergistic Therapy. Adv. Healthc. Mater. 2015, 4, 559–568. https://doi.org/10.1002/adhm.201400676.
46. Zhou, B.; Shi, B.; Jin, D.; Liu, X. Controlling Upconversion Nanocrystals for Emerging Applications. Nat. Nanotech 2015, 10, 924–936. https://doi.org/10.1038/nnano.2015.251.
47. Campos-Gonçalves, I.; Costa, B.F.O.; Santos, R.F.; Durães, L. Superparamagnetic Core-Shell Nanocomplexes Doped with Yb^{3+}: Er^{3+}/Ho^{3+} Rare-Earths for Upconversion Fluorescence. Mater. Des. 2017, 130, 263–274. https://doi.org/10.1016/j.matdes.2017.05.064.
48. Vaz-Ramos, J.; Cordeiro, R.; Castro, M.M.C.A.; Geraldes, C.F.G.C.; Costa, B.F.O.; Faneca, H.; Durães, L. Supercritically Dried Superparamagnetic Mesoporous Silica Nanoparticles for Cancer Theranostics. Mater. Sci. Eng. C 2020, 115, 111124. https://doi.org/10.1016/j.msec.2020.111124.

49. Abdul Jalil, R.; Zhang, Y. Biocompatibility of Silica Coated $NaYF_4$ Upconversion Fluorescent Nanocrystals. Biomaterials 2008, 29, 4122–4128. https://doi.org/10.1016/j.biomaterials.2008.07.012.
50. Wong, H.-T.; Tsang, M.-K.; Chan, C.-F.; Wong, K.-L.; Fei, B.; Hao, J. *In Vitro* Cell Imaging Using Multifunctional Small Sized $KGdF_4$: Yb^{3+}, Er^{3+} Upconverting Nanoparticles Synthesized by a One-Pot Solvothermal Process. Nanoscale 2013, 5, 3465. https://doi.org/10.1039/c3nr00081h.
51. Rostami, I. Empowering the Emission of Upconversion Nanoparticles for Precise Subcellular Imaging. Nanomaterials 2021, 11, 1541. https://doi.org/10.3390/nano11061541.
52. Yi, G.; Lu, H.; Zhao, S.; Ge, Y.; Yang, W.; Chen, D.; Guo, L.-H. Synthesis, Characterization, and Biological Application of Size-Controlled Nanocrystalline $NaYF_4$: Yb,Er Infrared-to-Visible Up-Conversion Phosphors. Nano Lett. 2004, 4, 2191–2196. https://doi.org/10.1021/nl048680h.
53. Milićević, B.; Periša, J.; Ristić, Z.; Milenković, K.; Antić, Ž.; Smits, K.; Kemere, M.; Vitols, K.; Sarakovskis, A.; Dramićanin, M. Hydrothermal Synthesis and Properties of Yb^{3+}/Tm^{3+} Doped Sr_2LaF_7 Upconversion Nanoparticles. Nanomaterials 2022, 13, 30. https://doi.org/10.3390/nano13010030.
54. Zhou, X.; Wang, Z.; Li, S.; Shan, S.; Wang, X. Formation and Luminescence of Sodium Rare Earth Fluoride Nanocrystals in the Presence of Chelators. J. Nanosci. Nanotechnol. 2010, 10, 2193–2202. https://doi.org/10.1166/jnn.2010.2134.
55. Grzyb, T.; Przybylska, D. Formation Mechanism, Structural, and Upconversion Properties of Alkaline Rare-Earth Fluoride Nanocrystals Doped with Yb^{3+}/Er^{3+} Ions. Inorg. Chem. 2018, 57, 6410–6420. https://doi.org/10.1021/acs.inorgchem.8b00484.

USC UNIVERSIDADE DE SANTIAGO DE COMPOSTELA

CHAPTER 6. 3D-PRINTED AEROGELS AS THERANOSTIC IMPLANTS MONITORED BY FLUORESCENCE BIOIMAGING



The content in this chapter was submitted in part in **A. Iglesias-Mejuto**, R. Pinto, P. Faísca, J. Catarino, J. Rocha, L. Durães, M.M. Gaspar, C. Pinto Reis, C.A. García-González; 3D-printed aerogels as theranostic implants monitored by fluorescence bioimaging, in: Bioactive Materials.

The work described in this chapter was carried out in collaboration with the University of Coimbra and the University of Lisbon.

USC UNIVERSIDADE DE SANTIAGO DE COMPOSTELA

6.1. Introduction

Bioimaging allows the cellular and molecular study of disorders by the *in vivo* detection, visualization, quantification and tracing of biological and pathological changes targeted by a fluorescent probe [1,2]. Different non-invasive techniques such as positron emission tomography, magnetic resonance, computed tomography, fluorescence, Raman, optical or ultrasound imaging as well as photodynamic, photothermal, and photoacoustic methods are employed as tools for molecular imaging [3,4]. Namely, in fluorescence-based bioimaging, fluorophores are activated at specific excitation wavelengths in a safe and non-invasive way [5,6]. Visible light has a tissue penetration of only few millimeters, so NIR fluorescent probes are under evaluation to increase the penetration capability. NIR light is non-toxic and induces low optical damage and self-fluorescence while allowing a rapid data collection and a precise control over the irradiated region. Accordingly, NIR-responsive probes are able to reach the region of interest to monitor the progress of pathologies and have been incorporated into nanodevices to significantly enhance regeneration of certain tissues like bone [5,7,8].

Contrast agents such as small molecular dyes, quantum dots, carbon nanotubes or nanodots are used for NIR bioimaging of tumor cells, vasculature, or vital organs thus enabling their anatomy and function evaluation by an image-guided therapy [6,9]. An ideal fluorescent probe may be biocompatible and stable while presenting a high signal-to-noise ratio and a low disruption effect on cell function [3]. Nanoparticles (NPs) from silica, metals or polymers conjugated with contrast agents have been studied as bioimaging tools [4]. NPs can effectively transport imaging probes to target tissues for monitoring and treating their state thereby presenting diagnostic and therapeutic capabilities simultaneously [3]. For these reasons, nanodevices usually replace traditional molecular probes in bioimaging applications reaching preclinical and clinical trials [4]. Namely, the advanced photophysical properties of UCNPs make them excellent candidates for non-invasive intravital imaging and diagnosis thereby translating their *in vitro* NIR-responsive

USC DE COMPOSTELA

fluorescence into an *in vivo* imaging approach [10]. Lanthanides are commonly used to synthesize UCNPs due to their luminescent properties, such as high stability, long lifetimes and narrow emission bands [11]. UCNPs composition typically also includes LaF_3, $BaYF_5$ or $NaYF_4$ as host matrices, Yb^{3+} or Nd^{3+} as dopants, and Er^{3+} or Ho^{3+} as NIR-absorption enhancers [12]. Highly fluorescent and photostable UCNPs could be integrated into scaffolds to finally obtain 3D-nanostructures with diagnostic and therapeutic properties. The combination of UCNPs and tissue engineering scaffolds could thereby result in a bifunctional implant that allows simultaneously the dynamic monitoring and the effective promotion of tissue regeneration.

Biomaterials sought for tissue engineering applications must be able to mimic the ECM while promoting cell attachment, proliferation and migration [13–15]. High porosity, surface area and loading capacity are thus desired properties for biomaterials designed as advanced carriers for imaging probes [4]. Aerogels are nanostructured materials that can be manufactured adapted-to-patient with a dual porosity and high entrapment yield of drugs, nanofibers and NPs by a dual processing strategy combining 3D-printing and $scCO_2$ technologies [16,17]. These highly porous structures are promising tissue engineering platforms as they present personalized external shape, internal pattern and composition, while being biocompatible, bioactive, and promoters of long-term cell adhesion and migration [18,19]. The tracing of the degradation profile of biomaterials once implanted have been studied by non-invasive imaging, but is challenging when the growth of new tissue is simultaneously taking place [8]. For this purpose, fluorescent probes can enhance the accuracy of the monitoring process while being easy to synthesize, non-toxic and labeled to biodegradable materials [5,20]. Fluorescent aerogels have been proposed as novel optical sensing probes [21,22] but, to the best of our knowledge, advanced NIR-responsive systems like UCNPs doped aerogels have not been designed and tested yet. Highly fluorescent aerogel materials suitable for bioimaging applications have been thus theoretically proposed [21,22], but not practically explored as advanced theranostic biomaterials.

USC UNIVERSIDADE DE SANTIAGO DE COMPOSTELA

In this work, NIR-responsive 3D-biomaterials were manufactured from dual porous aerogels and highly fluorescent UCNPs for the first time. The effective incorporation of UCNPs into 3D-printed alginate aerogels resulted in advanced highly porous scaffolds with potential to regenerate the damaged tissue while monitoring the state and position of the implanted device. Physicochemical characterization of UCNPs-doped aerogels was studied by N_2 adsorption-desorption analysis, and microscopy evaluations (SEM, TEM and confocal microscopies). Biological performance of UCNP-labeled aerogels was assessed by biocompatibility, migration, and adhesion cell studies. Hemocompatibility of the implants was evaluated by hemolytic activity measurements and HET-CAM. *In vivo* safety assessment of the theranostic aerogel-based materials was performed by evaluating the expression of tumor necrosis alpha factor (TNF-α) and interleukins 6 (IL-6) and 10 (IL-10) as well as the histology of the main organs 1 week after subcutaneous implantation in two murine models. Finally, a 3-week bioimaging *in vivo* assay was carried out in mice to unveil the monitoring capability of the UCNPs loaded into these aerogel-based biomaterials.

6.2. Materials and Methods

6.2.1. Materials

Alginic acid sodium salt from brown algae with medium viscosity (guluronic acid/mannuronic acid ratio: 70/30, Mw 403 kDa, 3170 cps), $CaCl_2$ (Mw 110.98 g/mol, 99.99% purity), ytterbium(III) nitrate pentahydrate ($Yb(NO_3)_3{\cdot}5H_2O$, 99.9% purity), yttrium(III) nitrate hexahydrate ($Y(NO_3)_3{\cdot}6H_2O$, 99.8% purity), EDTA and sodium fluoride (99%) were obtained from Sigma Aldrich (Madrid, Spain). Erbium(III) nitrate pentahydrate ($Er(NO_3)_3{\cdot}5H_2O$, 99.9% purity), and TEOS ($Si(OC_2H_5)_4$, 98% purity), were supplied by Acros Organics (Thermo-Fisher Scientific, Geel, Belgium). HÁ (Mw 502.31 g/mol, micropowder) was obtained from Fluidinova (Moreira da Maia, Portugal). Ammonium hydroxide (25% NH_3 in H_2O) and H_2O_2 (30% aqueous solution) were

USC UNIVERSIDADE DE SANTIAGO DE COMPOSTELA

supplied by Honeywell Fluka (Madrid, Spain). CO_2 (purity > 99.9%) was provided by Nippon Gases (Madrid, Spain) and absolute EtOH by VWR (Radnor, PA, USA). Water was purified by reverse osmosis (resistivity > 18 MΩ·cm; Milli-Q, Millipore®, Madrid, Spain) before further use.

6.2.2. Synthesis of UCNPs by co-precipitation and sol-gel methods

Core-shell UCNPs with a silica shell were synthesized following a procedure described on a previous work from our team [10]. Briefly, 16 mL of 0.2 M $Y(NO_3)_3$, 3.4 mL of 0.2 M $Yb(NO_3)_3$, 0.6 mL of 0.2 M $Er(NO_3)_3$ and 20 mL of 0.2 M EDTA were mixed and injected into 60 mL of 0.8 M NaF aqueous solution. The obtained solution was stirred 1 h at RT and the resulting dispersions were centrifuged and washed three times with water and once with EtOH. Afterwards, UCNPs were dried in an oven at 60 °C. Annealing was then performed for 5 h, under a N_2 atmosphere, at 400 °C (heating rate: 20 °C/min). UCNPs were cooled down until RT under the same atmosphere. To obtain the silica shell, 30 mL of UCNPs dispersed in EtOH (3 mg/mL) were stirred at 0 °C with 0.2 mL of TEOS and, after 5 min, 3 mL of ammonium hydroxide was added. Reaction took place for 2 h and the thus the obtained UCNPs were washed three times with EtOH.

6.2.3. 3D-printing of UCNPs-labeled hydrogels

6 wt.% alginate solution was prepared at RT and 600 rpm, using a homogenizer (VWR vos 60, Radnor, PA, USA) and 0.4 wt.% or, alternatively, 0.8 wt.% of UCNPs were added to the alginate-based ink to compare their fluorescence and physicochemical behavior. For the comparison of textural properties, formulations with increasing content of HA were obtained by adding 8, 16 or 24 wt.% of HA to the 6 wt.% alginate solution with or without 0.4 wt.% of UCNPs. The formulation with 24 wt.% of HA was simply denoted as AlgHA, without specifying the wt.% of HA. The same ink formulations without UCNPs or HA was used as blank [19]. All inks were degassed for 10 min to eliminate air bubbles in a sonication bath (Branson 3510 Emerson, Ferguson, MO, USA). The filament drop test was performed and the general pore shape geometry was evaluated to assess the printability of the different inks thought a 22G nozzle [23].

USC UNIVERSIDADE DE SANTIAGO DE COMPOSTELA

Hydrogels were manufactured by 3D-printing of inks at RT with a Cellink BIOX Bioprinter (Boston, MA, USA), employing an extrusion printhead with a 3-mL syringe and a 410-µm nozzle. A printing pressure of 60 kPa, printing velocity of 12 mm/s and a grid pattern of 2 × 2 × 0.1 cm^3 with three layers, were the set parameters to print all formulations tested. After 3D-printing, hydrogels were put in contact with $CaCl_2$ 1M aqueous bath for 1 h and then with EtOH for solvent exchange.

6.2.4. Rheological evaluation of inks

Flow behavior of the inks was studied at RT from 0.05 to 200 rad/s in a Rheolyst AR-1000N rheometer (TA Instruments, Newcastle, UK) with a Peltier plate and a cone geometry (40 mm diameter, 2°). At least four replicates per formulation were evaluated. The power law Equation 6.1 was fitted to the linear region of the viscosity (η) vs shear rate (γ) curves to assess the shear thinning behavior of the inks [24].

$$\eta = b \cdot \gamma^{c} \qquad \textit{Equation 6.1}$$

where b and c are the consistency and flow coefficients, respectively.

6.2.5. scCO₂ drying of UCNPs-labeled 3D-printed alcogels

Alcogels were wrapped in filter paper, placed into a 100-mL stainless steel autoclave (Thar Process, Pittsburg, PA, USA) and immersed in 20 mL of EtOH. CO_2 was supplied with a dual-piston pump from the top of a vessel at 40 °C. A CO_2 flow rate (5-7 g/min) at 120 bar passed through the autoclave for 4 h. After a CO_2 depressurization at 2 bar/min, aerogels were collected from the autoclave for further use. Aerogels were named as "Alg (HA) UCNPs *x*" being *x* the content of UCNPs in the ink (0.4 or 0.8 wt.%). Aerogels prepared only with Alg (i.e. without UCNPs or HA) were obtained as controls and simply denoted as "Alg". The formulations studied are described in Table 6.1.

USC UNIVERSIDADE DE SANTIAGO DE COMPOSTELA

Table 6.1: Aerogel formulations with or without UCNPs studied.

Formulation	Ink composition		
	Alg (wt. %)	HA (wt. %)	UCNPs (wt. %)
Alg	6	-	-
AlgHA8	6	8	-
AlgHA16	6	16	-
AlgHA	6	24	-
Alg UCNPs 0.4	6	-	0.4
Alg UCNPs 0.8	6	-	0.8
AlgHA8 UCNPs 0.4	6	8	0.4
AlgHA16 UCNPs 0.4	6	16	0.4
AlgHA UCNPs 0.4	6	24	0.4

6.2.6. Physicochemical characterization of UCNPs-labeled aerogels

External dimensions of the gels before and after the $scCO_2$ drying step were measured with a digital caliper (Fowler™, Newton, MA, USA) to assess the volume shrinkage by Equation 6.2 and the SFF by Equation 6.3:

$$Volume\ shrinkage\ (\%) = \left(\frac{Alcogel\ volume - Aerogel\ volume}{Alcogel\ volume}\right) \cdot 100 \qquad Equation\ 6.2$$

$$SFF = \frac{Ai}{A} \qquad Equation\ 6.3$$

where A_i is the alcogel or aerogel printed area, and A is the CAD area (printing file).

Low-temperature N_2 adsorption-desorption analysis was used to evaluate the physicochemical performance of aerogels (ASAP 2000 Micromeritics Inc.; Norcross, GA, USA). Briefly, aerogels were degassed under vacuum at 40 °C for 24 h and the A_{BET} was obtained by the BET method, while V_p, and d_p were obtained by the BJH method. Aerogels were iridium-sputtered and then imaged by SEM and the chemical elements in the implants were mapped by SEM-EDX (EVO LS15, Zeiss, Oberkochen, Germany). UCNPs were imaged by TEM (TEM, JEOL JEM-2010, JEOL, Tokyo, Japan -operating at 200 kV-) and these images as well as the SEM images of the UCNPs loaded in aerogels were employed for particle size distribution analysis considering the diameter of at least 60 UCNPs. ATR/FT-IR was also performed in the mid-IR spectrum range (400-4000 cm^{-1}) to assess the chemical structure of the aerogels. Fluorescence of UCNPs-labeled aerogels was studied by confocal microscope in the 405-561 nm range (Leica TCS-SP2, Mannheim, Germany).

USC UNIVERSIDADE DE SANTIAGO DE COMPOSTELA

Fluorescence and physicochemical long-term stability of UCNPs-doped aerogels was evaluated by N_2 adsorption-desorption, SEM and confocal microscopy analysis after 3 years of store of the scaffolds in closed plastic jars at RT and protected from light. TEM was also used to explore structural differences in UCNPs after the same storage conditions.

6.2.7. Cellular studies

6.2.7.1. Cell viability tests

Aerogels of 1 × 1 × 0.1 cm^3 dimensions with and without UCNPs were UV-sterilized for 30 min before all cellular tests. Cytocompatibility of the UCNPs-labeled aerogels was evaluated by the WST-1 test, based on the degradation of WST-1 into formazan, which is correlated with the number of metabolically active cells. Mouse embryo fibroblasts (BALB/c 3T3, 6500 cells/cm^2) were seeded in 24-well plates with 1500 µL of DMEM supplemented with 15% fetal bovine serum, penicillin 100 U/mL and streptomycin 100 µg/mL. Cells were incubated at 37 °C in a humidified atmosphere enriched with 5% CO_2 and scaffolds were placed in culture inserts in contact with cells in triplicate. Positive controls (cells with 1000 µL of DMEM) were maintained at the same conditions. Scaffolds were removed after 24 and 48 h of culture. Afterwards, 250 µL of the medium was left in the wells and 25 µL of WST-1 was added. The plate was incubated at the same conditions for 2 h. After shaking the plate for 1 min, 110 µL were poured into a 96-well and absorbance was measured at λ = 450 nm in a microplate reader (Infinite® M200, Tecan Group Ltd., Männedorf, Switzerland).

6.2.7.2. Cell attachment tests

The spreading of human bone marrow MSCs on the aerogels with and without UCNPs was assessed in triplicate by DAPI staining to detect the nuclei. After 13 days of culture, aerogels were fixed with paraformaldehyde 4% w/v and washed with PBS. After Triton/PBS (0.2% v/v) incubation for 5 min, scaffolds were washed with PBS and placed on glass slides. One drop of the DAPI-containing ProLong gold antifade mountant (Molecular Probes Inc., Eugene, OR, USA) was

USC DE SANTIAGO DE COMPOSTELA

poured on each scaffold before their storage at -20 °C. Cell attachment was evaluated with a confocal microscope (Leica TCS-SP2, Mannheim, Germany) and ImageJ was used to analyze the images.

6.2.7.3. Cell migration tests

Cell migration on the aerogels with and without UCNPs was assessed by a wound healing test. After confluence, BALB/c 3T3 cells monolayer was scratched by a straight line with a pipette tip to mimic a wound *in vitro*. Cells were then washed with PBS. Aerogels with and without UCNPs were placed in culture inserts in contact with cells in triplicate. Images of the wound were taken with an inverted microscope (Olympus, Japan) immediately and after 24 h to evaluate the cell migration. The migration area (%) was calculated with Equation 6.4:

$$Migration\ area\ (\%) = \left(\frac{A_0 - A_{24}}{A_0}\right) \cdot 100 \qquad Equation\ 6.4$$

where A_0 is the initial wound area and A_{24} is the wound area after 24 h.

6.2.8. Hemocompatibility studies

6.2.8.1. Hemolytic activity test

Hemolytic activity of the UCNPs-labeled aerogels was tested with human blood (Galician Transfusion Center, Spain) obtained in accordance with the Declaration of Helsinki. Total blood was diluted to 3% v/v in 0.9% w/v NaCl solution and 1 mL was transferred to Eppendorf tubes containing either 1 × 1 × 0.1 cm^3 aerogels, 100 µL of 4% v/v Triton X-100 (positive control) or 100 µL of PBS pH 7.4 (negative control). Tests were carried out in triplicate. Samples were incubated for 60 min at 37 °C and 100 rpm and then centrifuged for 10 min at 10.000 g (Sigma 2-16P, Osterode am Harz, Germany). 150 µL of the supernatant were transferred to a 96-well plate, and the absorbance of the hemoglobin was measured at λ = 540 nm (FLUOStar Optima, BMG Labtech, Ortenberg, Germany). Hemolysis was calculated with Equation 6.5:

USC UNIVERSIDADE DE SANTIAGO DE COMPOSTELA

$$Hemolysis\ (\%) = \left(\frac{Abss - Absn}{Absp - Absn}\right) \cdot 100 \qquad Equation\ 6.5$$

where Abs_s is the absorbance of the samples in contact with aerogels, Abs_n is the absorbance of the negative control, and Abs_p is the absorbance of the positive control.

6.2.8.2. HET-CAM assay

HET-CAM test was performed according to a standard protocol [25] previously used to evaluate the hemocompatibility of implants [17] and following the Interagency Coordinating Committee on the Validation of Alternative Methods (ICCVAM) guidelines. The assay was performed with fresh, clean, and fertilized Hen´s eggs (50-60 g, Coren, Ourense, Spain). Horizontal incubation took place in a climatic chamber (Ineltec CC SR 0150, Barcelona, Spain) at 37 °C, 60 % humidity and with a scheduled rotation after 8 h. On day 9, a small window of 1 cm diameter was opened in the eggshell to access the CAM. 300 µL of 0.1 N NaOH and of 0.9% w/v NaCl were pipetted on the CAM as positive and negative controls, respectively. Aerogels with and without UCNPs were put in contact with the CAM and each sample was tested in triplicate. Vessels of the CAM were visually inspected for 5 min to assess the appearance of hemorrhage, vascular lysis, coagulation, hyperemia, or other changes in CAM vessels.

6.2.9. Animals care and subcutaneous implantation of scaffolds

6.2.9.1. Safety studies

Biocompatibility, degradation and functionality of biomaterials are usually firstly evaluated by surgical ectopic subcutaneous implantation in small animal models [26]. Mice model was chosen to evaluate the toxicity and the functionality of UCNPs-labeled aerogels as theranostic implants. Rat model is more relevant than mouse due to their articular cartilage structure that mimics better the one observed in humans, so it was selected to test formulations aimed at bone tissue engineering [26]. Wistar rats (male, 200-300 g) from Charles River (Barcelona) and mice BALB/c (male, 20-30 g) from IGC (Lisbon) were housed and maintained in compliance with the guidelines outlined in the Guide for the Care and Use of Laboratory Animals, in accordance with the national (DL 113/2013, 2880/2015, 260/2016 and 1/2019) and international (Directive

USC DE SANTIAGO DE COMPOSTELA

2010/63/EU) accepted principles for laboratory animals' use (3R's principles). Safety studies were reviewed and approved by the DGAV (national authority) and by Animal Experiment Ethics Committee (ORBEA) of the Faculty of Pharmacy of University of Lisboa following the Declaration of Helsinki. All animals had free access to acidified water and were fed with a commercial rodent chow while being maintained at 22 ± 1 °C with a controlled 12 h light/dark cycle.

The study design consisted of 3 experimental groups: (1) 2 healthy mice (n=2) with an implanted scaffold without UCNPs (Alg), (2) 2 healthy mice (n=2) with an implanted scaffold with UCNPs (Alg UCNPs 0.8), and (3) 2 healthy mice (n=2) employed as controls (surgery without scaffold implantation). Next, other 2 experimental groups were designed: (1) 2 healthy rats (n=2) with a scaffold with HA and UCNPs (AlgHA UCNPs 0.4), and (2) 2 healthy rats (n=2) employed as controls (surgery without scaffold implantation). Before implantation, the hair of the dorsal area where the implant was going to be placed was removed by using an electric shaver in all cases. Skin was prepared with 10% povidone iodine and 70% isopropanol. An incision of 1 cm was done, and a 1 x 1 x 0.1 cm^3 scaffold was implanted on a subcutaneous pocket per animal. Incision was closed in a simple interrupted suture using silk (3-0) and (2-0) for rats and mice, respectively. The implantation of biomaterials in the dorsal skinfold chamber is commonly employed to assess the interaction between the biomaterials and their host tissue in rats and mice [27].

1-week post-surgery, animals were euthanized with isoflurane and implanted scaffolds were carefully removed and photographed to visually evaluate the connective-tissue capsule around and penetrating the aerogel scaffolds. Implants employed for all *in vivo* studies were sterilized by using a $scCO_2$ fluid method previously developed in our lab without causing a detrimental effect on the physicochemical performance of the 3D-printed aerogels [19] and fulfilling the requirements for the sterilization of implantable medical devices [28].

USC UNIVERSIDADE DE SANTIAGO DE COMPOSTELA

6.2.9.1.1. Circulating Cytokine Quantification

Peripheral blood was obtained by cardiac puncture 1 week after implantation under isoflurane anesthesia. Blood was centrifuged and plasma was separated from the cellular fraction. The TNF-α, IL-6, and IL-10 expression levels were determined spectrophotometrically at 450 nm by employing an ELISA kit (Quantikine® Hycult Biotechnology, Wayne, PA, USA) and following manufacturer's instructions.

6.2.9.1.2. Histological evaluation of major organs

The tissues of major organs (liver, spleen, and right kidney) were excised, and the tissue index was calculated by weighing the organs and using Equation 6.6.

$$Tissue\ Index\ (\%) = \left(\sqrt{\frac{Organ\ weight}{Body\ weight}}\right) \cdot 100 \qquad Equation\ 6.6$$

The same tissues were subjected to histological evaluation to study the biocompatibility of implants [8]. The excised organs were fixed in 10% v/v formalin, embedded in paraffin, and sectioned at 3 µm of thickness for hematoxylin-eosin (H&E) staining following a standard protocol to assess the morphological features of each tissue. Sections were examined under a microscope (Olympus BX51, Olympus Corporation, Tokyo, Japan) and images were acquired with a NanoZoomer-SQ Digital slide scanner (Hamamatsu Photonics). The histological evaluation was carried out by a veterinary pathologist in a blinded manner.

6.2.9.2. Bioimaging studies

Swiss mice (male, 20-30 g) were supplied by the animal facilities at the University of Santiago de Compostela (CEBEGA, Santiago de Compostela, Spain). All animals had free access to tap water and to a commercial rodent chow and were housed under controlled conditions of temperature (22 ± 1 °C), humidity (60 ± 5 %), and day-night cycles (12 h/12 h). Bioimaging studies were approved by the University of Santiago de Compostela Ethics Committee for Animal Experiments and followed the Spanish and European Union (EU) rules (86/609/CEE, 2003/65/CE, 2010/63/EU,

USC UNIVERSIDADE DE SANTIAGO DE COMPOSTELA

RD 1201/2005, and RD53/2013) as well as the Declaration of Helsinki. The study design consisted of 3 healthy mice (n=3) with 2 implanted scaffolds (one without -Alg- and other with UCNPs -Alg UCNPs 0.8-) and 2 healthy mice (n=2) employed as control of fluorescence emission for all bioimaging experiments (surgery performed without scaffold implantation). Dorsal hair was clipped, and skin was prepared with iodine solution and 70% isopropanol. Two longitudinal skin incisions of 1 cm were made per animal, located approximately 3 cm from the mid dorsal line and separated between them by 6 cm. One scaffold of 1 x 1 x 0.1 cm^3 was placed on a lateral subcutaneous pocket at each incision. A single stainless-steel staple was used per incision to close each wound. Fluorescence images of animals were taken under deep-inhalation anesthesia with isoflurane at different timepoints (just after implantation, and after 4 h, 1 day and 1, 2 and 3 weeks) by using an *In Vivo* Imaging System (IVIS®, Caliper Life Sciences, Alameda, CA, USA). All images were acquired with an excitation wavelength of 745 nm and emission wavelength of 840 nm. The exposure time was 60 s per image and the same settings were used for all measurements. 3 weeks after subcutaneous implantation of scaffolds, animals were sacrificed by breaking their cervical vertebra. The surrounding tissue where scaffold was placed was opened with scissors and this skin area and the major organs were evaluated *ex vivo* regarding their fluorescence emission.

6.2.10. Statistical analysis

Results obtained from at least 3 experiments were denoted as mean value ± standard deviation. Post hoc Tukey HSD multiple comparison tests were performed to assess the statistical significance of the differences between groups and controls. Values of $p < 0.05$ were considered as statistically significant.

USC UNIVERSIDADE DE SANTIAGO DE COMPOSTELA

6.3. Results and Discussion

6.3.1. Rheological assessment of inks

Ink printability requires a correct fiber formation and shear thinning properties [29]. The printability must be adapted to the 3D-printing process to manufacture gels with high shape fidelity. The filament drop test and the evaluation of the pore shape geometry have been reported as useful methods to predict ink printability and shape fidelity [23,29]. The different inks studied by the filament drop test formed continuous and straight fibers with good integrity of the 3D-printed filament just after extrusion (Fig. 6.1a). Squared and closed pores formed a coherent grid pattern without relevant ink spreading or filament fusion after deposition. All these findings have been previously linked to good printability [23,29,30]. Also, a uniform layer by layer structure was observed for the 3D-printed aerogels after all manufacturing process, regardless the HA or UCNPs content.

All formulations presented similar shear thinning profiles, with a typical decrease in viscosity over a shear rate ramp (Fig. 6.1b,c), predicting a good printability [24]. A plot of shear stress with respect to shear rate showed a non-linear flow curve (Fig. 6.1d) characteristic of non-Newtonian fluids [31] while the viscosity over a shear stress ramp (Fig. 6.1e) exhibited the “at-rest” behavior of the inks [24]. Regarding the shear thinning coefficients, similar values were obtained for the different inks (Table 6.6.2), thereby suggesting a close printability for all of them. It should be noted that lower values of b coefficient were found when HA was not incorporated into inks, thus suggesting a higher extrudability of these formulations probably due to their lower viscosity. Similar b and c coefficient values were previously reported in an study of the flow behavior of different alginate inks containing HA also for scaffold fabrication [32].

USC UNIVERSIDADE DE SANTIAGO DE COMPOSTELA

Table 6.2: Shear thinning coefficients values obtained through power law model.

Aerogel formulations	Shear thinning coefficients	
	b (Pa·s)	c
Alg	654.5	4.4×10^{-8}
Alg UCNPs 0.8	552.8	3.9×10^{-8}
AlgHA	831.0	3.8×10^{-8}
AlgHA UCNPs 0.4	851.6	5.3×10^{-7}

6.3.2. Physicochemical evaluation of UCNPs-decorated aerogels

All aerogel formulations (Table 6.1) were obtained with a visually homogeneous dispersion of their different components (Alg, HA or UCNPs). No relevant differences in terms of the printability window for the formulations with or without UCNPs were observed, probably due to the low concentrations employed (0.4 and 0.8 wt.%). 3D-printing process was performed without relevant clogging at concentrations of HA as high as 24 wt.% in combination with alginate and UCNPs. The addition of HA has induced long-term bioactivity on the 3D-printed scaffolds while maintaining their geometry and integrity, which is of interest in scaffolds intended for bone tissue engineering [18,19]. High fidelity of the 3D-printed aerogels was observed with respect to the original CAD design, so good SFF values were obtained for all the formulations without statistically significant differences between the different groups studied (Fig. 6.1f). This result suggests that neither the HA nor the UCNPs incorporation into the implants affects the printing fidelity of the resulting aerogels. Alcogels exhibited better values of SFF than aerogels with the same composition, linked to the volume shrinkage during the drying step undergone for all the formulations (Fig. 6.1g). All UCNPs-labeled aerogels showed values of volume shrinkage close to the same formulations without UCNPs, so volumetric shrinkage is not related to the UCNPs content. Nevertheless, a decreasing tendency in the volume shrinkage was observed when HA was incorporated into UCNPs-loaded aerogels, thereby suggesting that the HA promotes a lower shrinkage of the aerogels. Same tendency was previously described for aerogels with the same composition but without UCNPs [18,19], thus endorsing the neglectable effect of the UCNPs in the morphological performance of aerogels.

USC UNIVERSIDADE DE SANTIAGO DE COMPOSTELA

The ATR/FT-IR spectra of the Alg aerogels showed the characteristics peaks of alginate in the 1400-4000 cm^{-1} region for all aerogel formulations studied (Fig. 6.1h). Namely, the band at 1646 cm^{-1} results from the interaction of the carboxylic groups of the alginate with the Ca^{2+} ions of the crosslinker used. The band at 1587 cm^{-1} denotes the asymmetric stretching vibration (-C=O) due to the carboxylic acid salts related to the ionic crosslinking [33,34]. The broad band around 3252 cm^{-1} (O-H stretching vibration) and the one at 1407 cm^{-1} (symmetric COO stretching vibration), are also related to alginate [35]. In the UCNPs spectrum, bands related to the silica coating appeared in the 800-1080 cm^{-1} region [10]. The broad peaks at 1080 and at 1175 cm^{-1} (red and green circles, respectively, in Fig. 6.1h) were related to Si-O-Si vibrations. The peaks at 970 and 800 cm^{-1} (blue and purple circles, respectively, in Fig. 6.1h) were described as a result of the Si-O vibration. These bands related to silica functionalization appeared also in the UCNPs-labeled aerogels thereby suggesting the correct incorporation of UCNPs into the 3D-printed aerogels.

USC
UNIVERSIDADE DE SANTIAGO DE COMPOSTELA

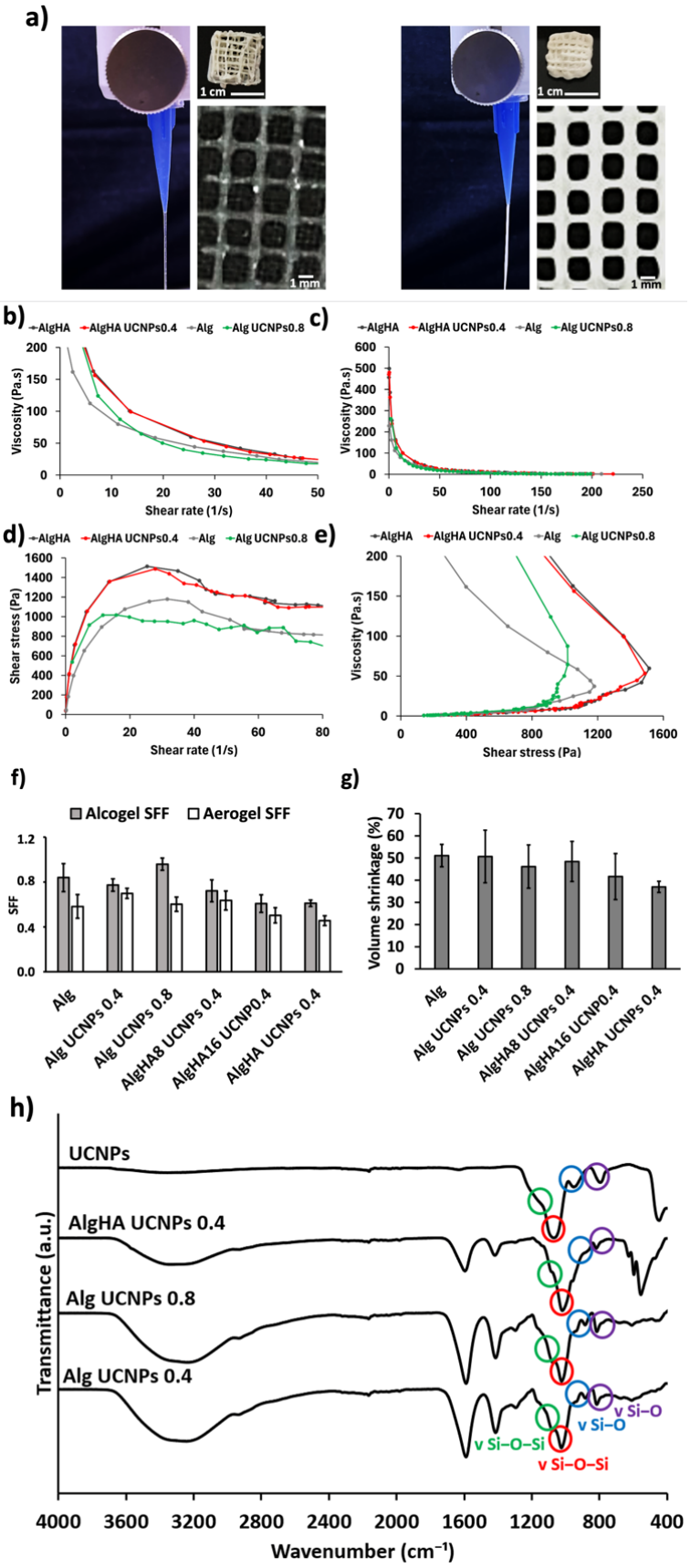


Figure 6.1. Physicochemical evaluation of UCNPs-decorated aerogels. **a)** Filament drop test, general pore shape geometry and visual appearance of aerogels obtained from different ink formulations: Alg

UCNPs 0.8 (left) and AlgHA UCNPs 0.4 (right). **b-e)** Rheological evaluation of inks. **b, c)** overall viscosity with respect to the shear rate; **d)** shear stress with respect to the shear rate; **e)** overall viscosity with respect to the shear stress. **f)** SFF of UCNPs-loaded aerogels. **g)** Volume shrinkage (in percentage) of UCNPs-decorated aerogels. No statistically significant differences among groups were obtained after post hoc Tukey HSD multiple comparison test ($p < 0.05$). **h)** ATR/FT-IR spectra of UCNPs and aerogel formulations.

A homogeneous 3D-printed structure with strands aligned to form the designed grid pattern was observed by SEM imaging for all aerogel formulations (Fig. 6.2a,c,e). A highly porous structure with an interconnected fibrous network was observed for the different formulations studied (Fig. 6.2b,d,f). A similar smooth and open porous network was previously described for other 3D-printed alginate aerogels [18,36] and for hybrid alginate scaffolds aimed at tissue engineering applications [33,37]. A homogeneous distribution of UCNPs throughout the porous structure of aerogels was clearly observed. A relevant higher amount of UCNPs was visually detected for Alg UCNPs 0.8 with respect to the other formulations (Alg UCNPs 0.4 and AlgHA UCNPs 0.4) thus being consistent with the higher initial amount of UCNPs incorporated into the inks. Furthermore, the presence of UCNPs was confirmed by the EDX spectrum taken in a region with UCNPs (Fig. 6.2g). The peaks of the lanthanide ions initially used to synthesize the UCNPs (Y, Yb and Er) were clearly detected in the EDX spectrum, thus endorsing the correct doping of the aerogels with the UCNPs. Particle size distribution of the UCNPs just after synthesis displayed a normal distribution with a mean particle size of 419 ± 38 nm. A normal particle size distribution was also found after the analysis of the UCNPs incorporated into aerogels and located by SEM imaging, with a mean size of 407 ± 37 nm. The physicochemical integrity of the UCNPs was preserved after all the manufacturing process needed for the fabrication of the UCNPs-decorated aerogels.

Regarding textural parameters, the best values of A_{BET} were obtained when HA was not incorporated into aerogels regardless the UCNPs content (Table 6.3). A decreasing tendency in A_{BET} and V_p were observed with increasing HA content, as previously described for AlgHA aerogels [18,19]. The doping of UCNPs in Alg aerogels lightly increased the A_{BET} at the lowest

UCNPs concentration studied and this tendency was also preserved when HA was incorporated into aerogels. However, the A_{BET} values were maintained when working with the highest concentration of UCNPs.

Stability studies of natural polymers are still scarce so the long-term stability (3 years) of 3D-printed aerogels was studied for the first time. After 3 years of storage, a decrease in A_{BET} and V_p was observed for Alg aerogels but when HA was incorporated into the structures this effect was less marked. A decrease in textural properties of Alg aerogels was previously described after a storage of 3 months [38]. Stability studies of starch aerogels were performed with a marked decrease in A_{BET} and V_p observed after a shorter time (3 months) than the herein evaluated [39]. SEM images of aerogels 3 years after synthesis showed an external structure with the fibers still arranged to form the designed grid pattern (Fig. 6.2m,o,q). Also, the porous structure of the aerogels was mainly preserved, with the UCNPs homogeneously distributed through it (Fig. 6.2n,p,r). Stability of 3D-printed aerogels in terms of mid-term (3 and 7 months) maintenance of their textural performance were previously performed with good results for 3D-printed methylcellulose aerogels [16,17]. TEM images of UCNPs obtained just after synthesis exhibited a spherical shape and a homogeneous particle size distribution, comparable to that found after 3 years of storage at RT and protected from light (Fig. 6.2i,j). Confocal images of UCNPs-decorated aerogels exhibited fluorescence with a similar intensity to the same formulations evaluated just after their synthesis, thus indicating the long-term maintenance of their fluorescence properties (Fig. 6.2l). The obtained results suggest the physicochemical and functional stability after 3 years of the theranostic implants at the conditions of the study (storage at RT in closed plastic jars). Storage studies of the aerogels under harsher conditions than the herein reported could be performed to unveil the textural properties dependance of the different storage conditions.

USC UNIVERSIDADE DE SANTIAGO DE COMPOSTELA

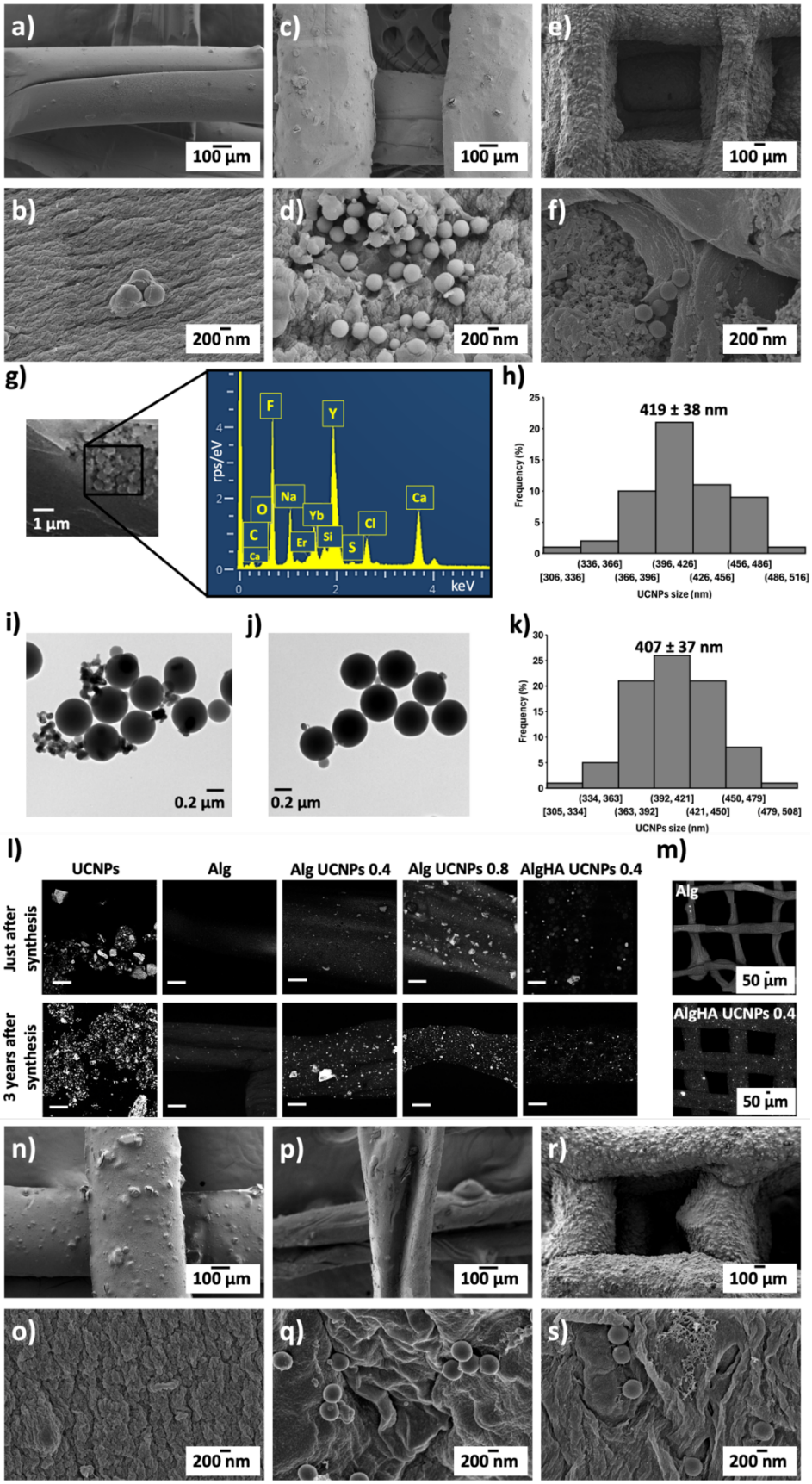


Figure 6.2. Microscopy analysis of UCNPs-decorated aerogels. **a-f)** SEM images of different aerogel formulations observed at two different magnifications: **a, b)** Alg UCNPs 0.4; **c, d)** Alg UCNPs 0.8; **e, f)**

AlgHA UCNPs 0.4. **g)** EDX spectrum of Alg UCNPs 0.8 aerogels. **h)** Particle size distribution of the UCNPs loaded in Alg UCNPs 0.8 aerogels. **i, j)** TEM images of UCNPs. **i)** UCNPs obtained just after synthesis; **j)** UCNPs obtained 3 years after synthesis. **k)** Particle size distribution of UCNPs. **l, m)** Confocal images of different formulations of UCNPs-decorated aerogels (scale bar: 100 μm). **n-s)** SEM images of different aerogel formulations 3 years after synthesis observed at two different magnifications: **n,o)** Alg; **p,q)** Alg UCNPs 0.8; **r,s)** AlgHA UCNPs 0.4.

Table 6.3. Textural properties of aerogels with or without UCNPs just after synthesis and after 3 years of storage. **Notation:** A_{BET}: BET-specific surface area, d_p: BJH-mean pore diameter, V_p: BJH-specific pore volume. S: aerogels evaluated after 3 years of storage. * Data obtained from reference [18].

Formulation	A_{BET} (m^2/g)	d_p (nm)	V_p (cm^3/g)
Alg*	183 ± 9	19 ± 1	1.16 ± 0.06
AlgHA8*	118 ± 6	24 ± 1	0.99 ± 0.05
AlgHA16*	67 ± 3	26 ± 1	0.60 ± 0.03
AlgHA*	29 ± 2	31 ± 2	0.21 ± 0.01
Alg UCNPs 0.4	218 ± 11	19 ± 1	1.54 ± 0.08
Alg UCNPs 0.8	190 ± 10	18 ± 1	1.24 ± 0.06
AlgHA8 UCNPs 0.4	138 ± 7	24 ± 1	1.21 ± 0.06
AlgHA16 UCNPs 0.4	66 ± 3	28 ± 1	0.59 ± 0.03
AlgHA UCNPs 0.4	49 ± 2	31 ± 2	0.50 ± 0.03
Alg S	80 ± 4	15 ± 1	0.40 ± 0.02
AlgHA8 S	67 ± 3	22 ± 1	0.46 ± 0.02
AlgHA16 S	53 ± 3	25 ± 1	0.41 ± 0.02
AlgHA S	39 ± 2	21 ± 1	0.23 ± 0.01
Alg UCNPs 0.4 S	123 ± 6	15 ± 1	0.65 ± 0.03
Alg UCNPs 0.8 S	82 ± 4	16 ± 1	0.45 ± 0.02
AlgHA8 UCNPs 0.4 S	76 ± 4	19 ± 1	0.49 ± 0.02
AlgHA16 UCNPs 0.4 S	39 ± 2	29 ± 1	0.34 ± 0.02
AlgHA UCNPs S	29 ± 1	25 ± 1	0.18 ± 0.01

6.3.3. Cell studies

UCNPs-labeled aerogels are bifunctional structures able to maintain the biocompatibility of the implant. High values of cell viability were observed after 24 and 48 h of contact with different aerogel formulations (Fig. 6.3a). No statistically significant differences were found between the cell viability values of positive controls and fibroblasts after contact with UCNPs-loaded aerogels, indicating that implants did not induce any cytotoxic effects on BALB/c 3T3 cells thereby being biocompatible [40]. These are good results since neither the implant itself nor the UCNPs, that could be released into the culture medium after 24 or 48 h, affect the BALB/c 3T3 cells' viability. In contrast, certain metals are incorporated into implants without being part of a nanocomplex were reported to neglect the biocompatibility of the end structure [7]. Other core-shell UCNPs protected also with silica coating, are cytotoxic after 24 h above certain concentration (100

USC UNIVERSIDADE DE SANTIAGO DE COMPOSTELA

μg/mL) [41]. The herein synthesized UCNPs were *in vitro* tested beyond this threshold (until 5 mg/mL) with good results in terms of biocompatibility, thereby suggesting their safety use [10].

Cell migration capability into the wound site during the inflammatory phase of defect repair is essential for tissue repair [15]. Similar values of migration area were measured for fibroblasts after contact with aerogels labeled or not with UCNPs, without statistically significant differences between both groups (Fig. 6.3b). Moreover, no relevant differences were observed between the MSCs adhesion to a control scaffold (Alg) and to an UCNPs-labeled one (Alg UCNPs 0.8) (Fig. 6.3c). It has been reported that UCNPs can significantly affect long-term cell functionality [42], but the herein obtained results suggest the lack of impact of the synthesized UCNPs on cell migration or adhesion processes. Confocal images of UCNPs-decorated aerogels exhibited fluorescence at the characteristic wavelengths of the upconversion process undergone by UCNPs (405, 488 and 561 nm), showing that nanocomplexes are still present and functional in the theranostic system after the test (13 days). These are good results since it was previously reported that UCNPs in aqueous environments could not be detected in the long-term due to the intensity loss of the upconversion process after only several hours were elapsed [43].

USC
UNIVERSIDADE DE SANTIAGO DE COMPOSTELA

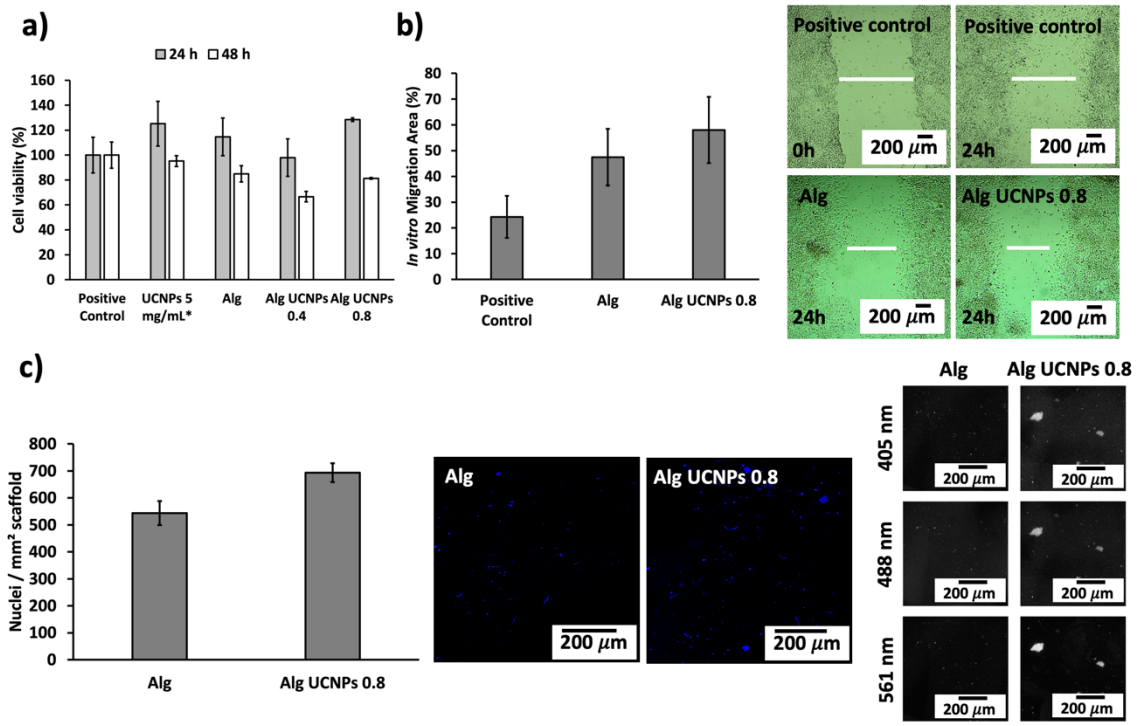


Figure 6.3. Cellular studies of different aerogel formulations. **a)** Cell viability test on BALB/c 3T3 cells. Viability (expressed in %) of BALB/c 3T3 cells after 24 and 48 h in contact with aerogels measured by WST-1 test. Positive controls: BALB/c 3T3 cells without contact with UCNPs or aerogels. * Data obtained from Ref. [10]. **b)** Scratch test on BALB/c 3T3 cells. Quantitative analysis (expressed in %) of the BALB/c 3T3 cells migration area after 24 h in cell culture and microscopy images after 0 and 24 h. Positive controls: BALB/c 3T3 cells without contact with UCNPs or aerogels. **c)** Cell attachment test on MSCs. Quantitative analysis (expressed in nuclei number per mm^2 of scaffold) after 13 days in cell culture (left) and confocal images of DAPI-stained MSCs seeded on aerogels (middle) and of aerogels after cell attachment tests (right). No statistically significant differences among groups were obtained after post hoc Tukey HSD multiple comparison test ($p < 0.05$).

6.3.4. Hemocompatibility studies

Interactions between blood and the implant after the initial trauma could lead to a localized edema at the implantation site [44,45]. No hemolytic activity was detected upon contact of the different aerogel formulations with human blood (Fig. 6.4a). Results endorse the properties of these aerogels as scaffolds sought to minimize the foreign body reaction [46]. Moreover, *in ovo* HET-CAM assays are a suitable method to predict tissue toxicity [47]. No hemorrhage, clotting, vascular lysis, or vessel bleeding were observed when UCNPs-labeled aerogels contacted the CAM (Fig. 6.4b) for the standard test time (5 min), with similar results to those observed for the positive control. Similar results were observed for polycaprolactone and for methylcellulose-

USC UNIVERSIDADE DE SANTIAGO DE COMPOSTELA

based scaffolds [16,17,47]. Both tests suggest the hemocompatibility of the formulations with biological tissues.

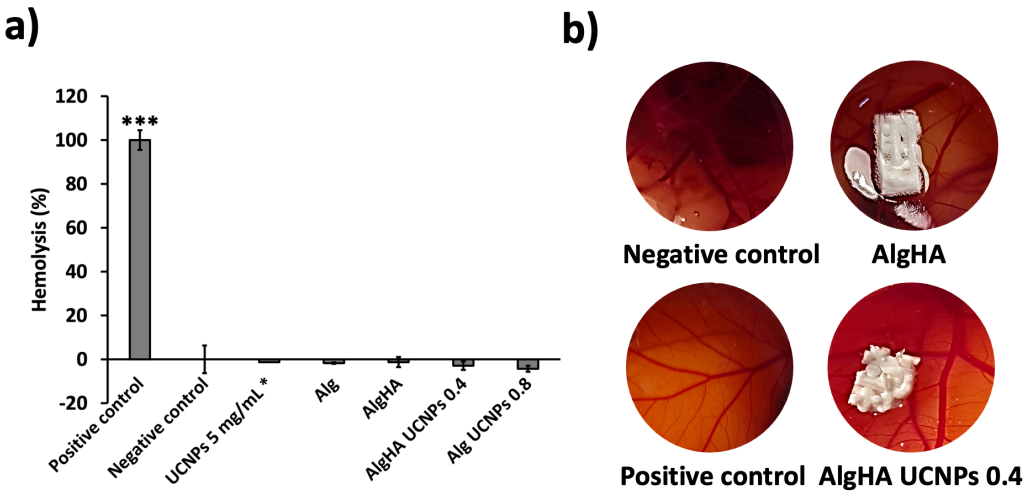


Figure 6.4. Hemocompatibility evaluation of different aerogel formulations. **a)** Hemolysis percentage of UCNPs and UCNPs-labeled aerogels. Positive control: 4% v/v Triton X-100 and negative control PBS pH 7.4. * Data obtained from Ref. [10]. Statistically significant differences among groups were denoted as *** (post hoc Tukey HSD multiple comparison test, $p < 0.001$). **b)** HET-CAM test of aerogels. Negative control: 0.9% w/v NaCl, positive control: 0.1 N NaOH.

6.3.5. Safety studies

6.3.5.1. Determination of plasmatic cytokines

Polymeric devices commonly induce inflammation after implantation and an immunologic response through a foreign body reaction [48]. Immune cells express pro-inflammatory cytokines such as TNF-α, IL-1 and IL-6 or anti-inflammatory cytokines like IL-10 and transforming growth factor β [49]. These biomarkers could differentiate the physiological healing from the pathological fibrosis [50,51]. *In vitro* downregulation of IL-6 and TNF-α was described as an anti-inflammatory response [52]. In fact, inflammation is mimicked *in vitro* by incorporating these cytokines in a very low concentration (ng/mL levels) to cell culture medium [15]. For these reasons, the expression of IL-6 and TNF-α is commonly studied after scaffold implantation [53]. An anti-inflammatory microenvironment characterized by low expression of pro-inflammatory cytokines was observed after 1-week subcutaneous scaffold implantation in mice and rats. In this

work, all groups presented similar levels of TNF-α and IL-10 (Fig. 6.5a,b) and no detectable IL-6 levels were obtained. A low level of pro-inflammatory and anti-inflammatory cytokines reported on the tissue surrounding a bone implant was related to the inflammation regression and the long-term tissue growth [49,53].

Potential toxicity of aerogels was also evaluated by the tissue index values without observing statistically significant differences among the different groups studied (Fig. 6.5a,b), thus suggesting the lack of organ toxicity [8]. All these results are aligned with the detected low production of cytokines. IL-6 and TNF-α are up-regulated after implantation while IL-10 is up-regulated in the later stage of the foreign body reaction [44].

All implant sites exhibited a complete wound healing 1 week after the *in vivo* safety test and 3 weeks after *in vivo* bioimaging assay. No adverse effects appeared in terms of infection or inflammation signs around the surgical area, with sutures still present in all animals. Ciprofloxacin is commonly used to prevent infection after implantation of scaffolds [54], but antibiotics were not needed in this study. For bioimaging assay, where staples were used instead of sutures, wound were completely closed without a relevant scar. Similar results in terms of visual inspection were found after a similar surgical intervention [53]. The final part of the foreign body reaction is the fibrous capsule formation around the implant that ends with the isolation of the biomaterial from the local environment [44]. A connective tissue capsule was observed immediately around the implant in all cases (with or without UCNPs) (Fig. 6.5c) suggesting that the presence of UCNPs did not interfere with the normal wound healing process. Finally, all implants were visually inspected by removal after sacrifice. Structure biodegradation was more significant after the bioimaging assay than after safety test due to the longer duration of the experiment (1 week vs 3 weeks).

USC UNIVERSIDADE DE SANTIAGO DE COMPOSTELA

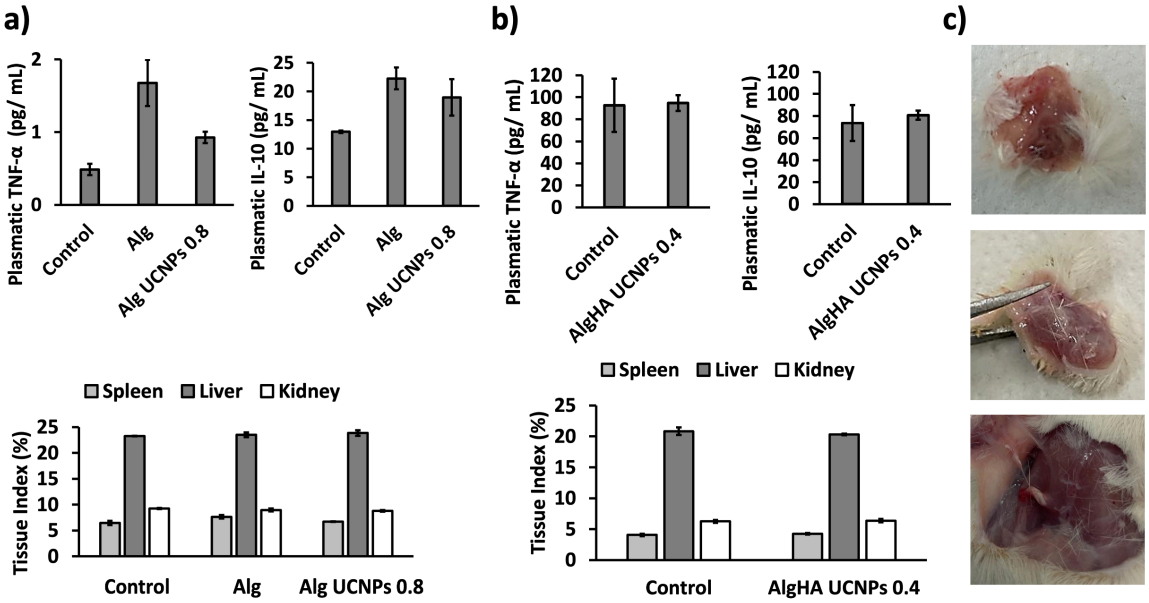


Figure 6.5. a) Plasmatic cytokines (TNF-α and IL-10) concentration (expressed in pg/mL) and tissue index (of spleen, liver, and kidney) values (expressed in %) of mice 1 week after subcutaneous implantation of different aerogel formulations (Alg, and Alg UCNPs 0.8). **b)** Plasmatic cytokines (TNF-α and IL-10) concentration (expressed in pg/mL) and tissue index (of spleen, liver, and kidney) values (expressed in %) of rats 1 week after subcutaneous implantation of different aerogel formulations (Alg, and AlgHA UCNPs 0.4). Control: animals with a surgical incision without scaffold implantation. Plasmatic concentration of IL-6 was not detected. No statistically significant differences among groups were obtained after post hoc Tukey HSD multiple comparison test ($p < 0.01$). **c)** Images of the connective tissue capsule developed 1 week after subcutaneous implantation of UCNPs-labeled aerogels (AlgHA UCNPs 0.4).

6.3.5.2. Histological evaluation of major organs

All animals presented a subcutaneous granulomatous inflammatory reaction surrounding the implant, composed of inflammatory infiltrates rich in macrophages, lymphocytes and plasma cells (Fig. 6.6a,b). Control animals (without scaffold implantation) exhibited a minimal scar reaction, with epidermal hyperplasia and a minimal inflammatory reaction secondary to the incisional surgical procedure. As control animals also showed tissue damage, the observed foreign body reaction could be a response to the silk suture rather than to the presence of the implant [55]. The inflammatory response is an expected secondary reaction to the presence of a foreign body and could be part of the healing process and play an important role in other physiological processes like osteogenesis [56]. It should be noted that the HA-loaded implants herein tested have previously demonstrated to be long-term bioactive and promoters of cell adhesion and migration, so they were proposed as bone tissue engineering scaffolds [18,19].

USC UNIVERSIDADE DE SANTIAGO

Implants coatings or strategies to trigger macrophage polarization have been developed to promote an adequate foreign body reaction but a similar response was observed in the skin surrounding polycaprolactone scaffolds with cellular exosomes incorporated to minimize the foreign body reaction [46,56].

Regarding the other organs studied, no morphological abnormalities were identified, and they were histologically similar to the controls. Similar results in terms of main organ histology were reported after subcutaneous implantation of 3D-printed polycaprolactone-based scaffolds while necrosis clearly appeared in the H&E histological sections of the same tissues when photothermal therapy was applied [57]. Isolated UCNPs or UCNPs aggregates were not histologically detected on liver, kidney, and spleen thus suggesting that they were not accumulated on these organs. Same organs were histologically examined after subcutaneous implantation of polycaprolactone scaffolds loaded with gold nanoclusters in mice for 4 week without relevant differences with respect to the controls [8]. Aggregates were also searched in the same major organs without detecting them so it was hypothesized that nanocomplexes did not form aggregates *in vivo* and could be metabolized by urine. These results indicate good biocompatibility of UCNPs-labeled aerogels 1 week after subcutaneous implantation in mice and rat and suggest that the granulomatous reaction is a local response.

USC UNIVERSIDADE DE SANTIAGO DE COMPOSTELA

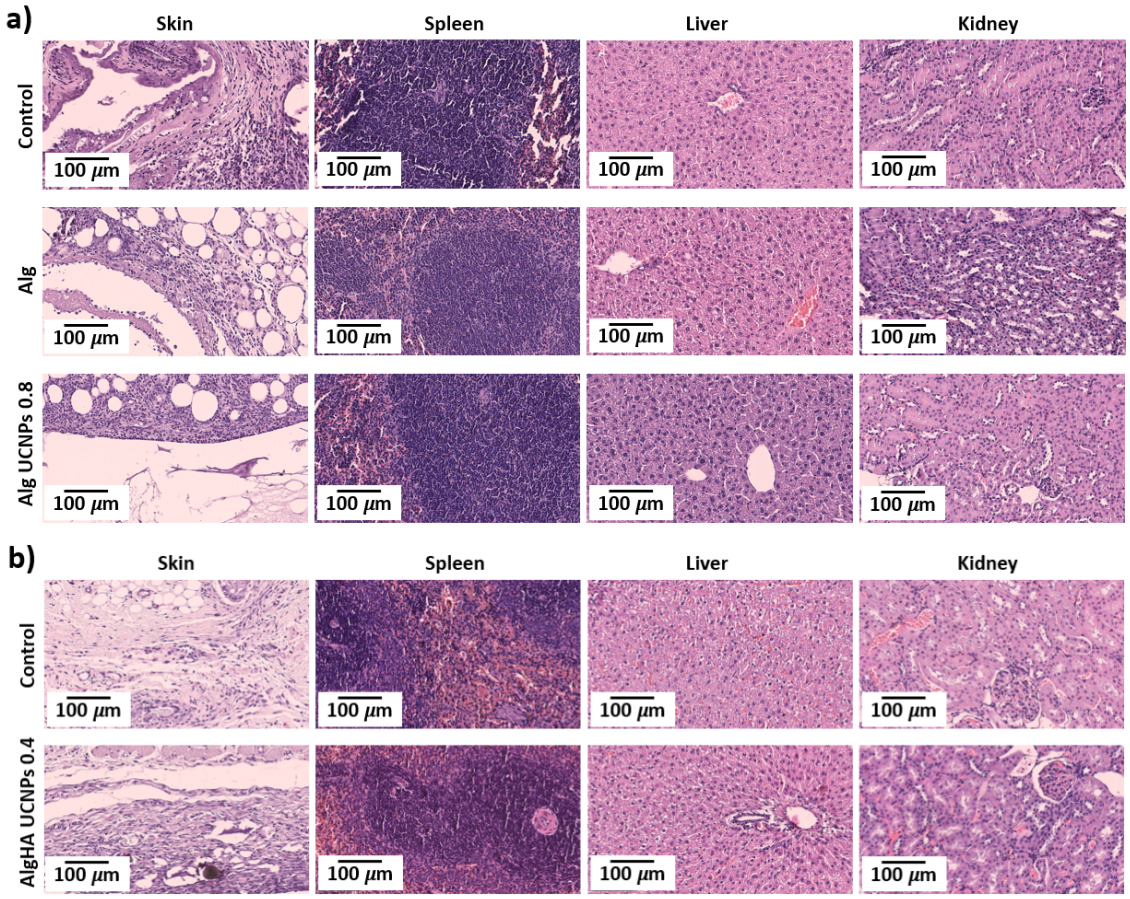


Figure 6.6. a) Histological images obtained by H&E staining of different tissues (skin, spleen, liver, and kidney) of mice 1 week after subcutaneous implantation of different aerogel formulations (Alg, and Alg UCNPs 0.8). **b)** Histological images obtained by H&E staining of different tissues (skin, spleen, liver, and kidney) of rats 1 week after subcutaneous implantation of different aerogel formulations (Alg, and AlgHA UCNPs 0.4). Control: animals with a surgical incision without scaffold implantation.

6.3.6. Bioimaging studies

Fluorescence intensity was homogeneously distributed throughout the UCNPs-labeled aerogels (Fig. 6.7a). In contrast, no fluorescence was detected due the non-loaded aerogels before (Fig. 6.7a) or after (Fig. 6.7b) *in vivo* subcutaneous implantation by the set up used for the bioimaging assay. Fluorescence was specifically accumulated only in the area were the theranostic nanodevice was implanted for all the assay duration (Fig. 6.7c-h). The ability to *in situ* monitor aerogels once implanted was possible from the moment of implantation until 21 days after the surgery in a real-time and non-invasive manner. Lower fluorescence accumulation in the implant site was detected only in the last timepoint (21 days), probably due to the partial biodegradation

USC DE COMPOSTELA

of the implant that could leach UCNPs from the aerogel thereby decreasing the fluorescence intensity and monitoring capability from this moment on. The tissue engineering process undergone by the UCNPs-labeled scaffold starts just after implantation and proceed until the complete resorption of the structure. It should be noted that after the duration of the bioimaging assay (21 days) aerogels had undergone a partial resorption but were still detectable by fluorescence-based bioimaging. If the lesion sought to be regenerated by the scaffold needs more time to be completely recovered, further adjustments at biomaterial and 3D-printing levels that warrants longer biodegradation times must be performed before the theranostic device can be tested in a clinical setting.

Regarding the excised organs, fluorescence was detected just in the spleen after 21 days. This could be due to the low concentration of UCNPs incorporated into the theranostic device and to the clearance of part of these UCNPs. The fluorescence intensity detected at spleen level could indicate the involvement of this tissue in the metabolism of UCNPs or the accumulation of the nanocomplexes at that level. Further experiments at different timepoints must be performed to unveil the biodistribution profile of the UCNPs once the theranostic device is implanted.

Previous works aimed to trace the *in vivo* degradation of poly-lactic-co-glycolic acid (PLGA) scaffolds have detected a relevant decrease in the recorded fluorescence intensity 4 weeks after implantation [8]. More time recording fluorescence in that case than in the herein reported could be due to the longer times required for the *in vivo* biodegradation of PLGA with respect to the alginate herein employed. Moreover, the long-term high fluorescence of the UCNPs could enhance their monitoring capability thereby increasing the sensitivity of the bioimaging approach. Consistently, due to the high sensitivity of the upconversion process undergone by UCNPs, these nanocomplexes have been employed for *in vivo* cell tracking by fluorescence bioimaging [58]. Alkaline phosphatase (ALP) was targeted by a molecular probe loaded in polycaprolactone-based scaffolds to thus induce fluorescence and turn the implant monitorable

USC UNIVERSIDADE DE SANTIAGO

for 4 week [59]. However, ALP is not an exclusive biomarker of the bone tissue and was previously related to different pathological pathways. Moreover, cytotoxicity of the molecular probe must be confirmed for their safety use [60].

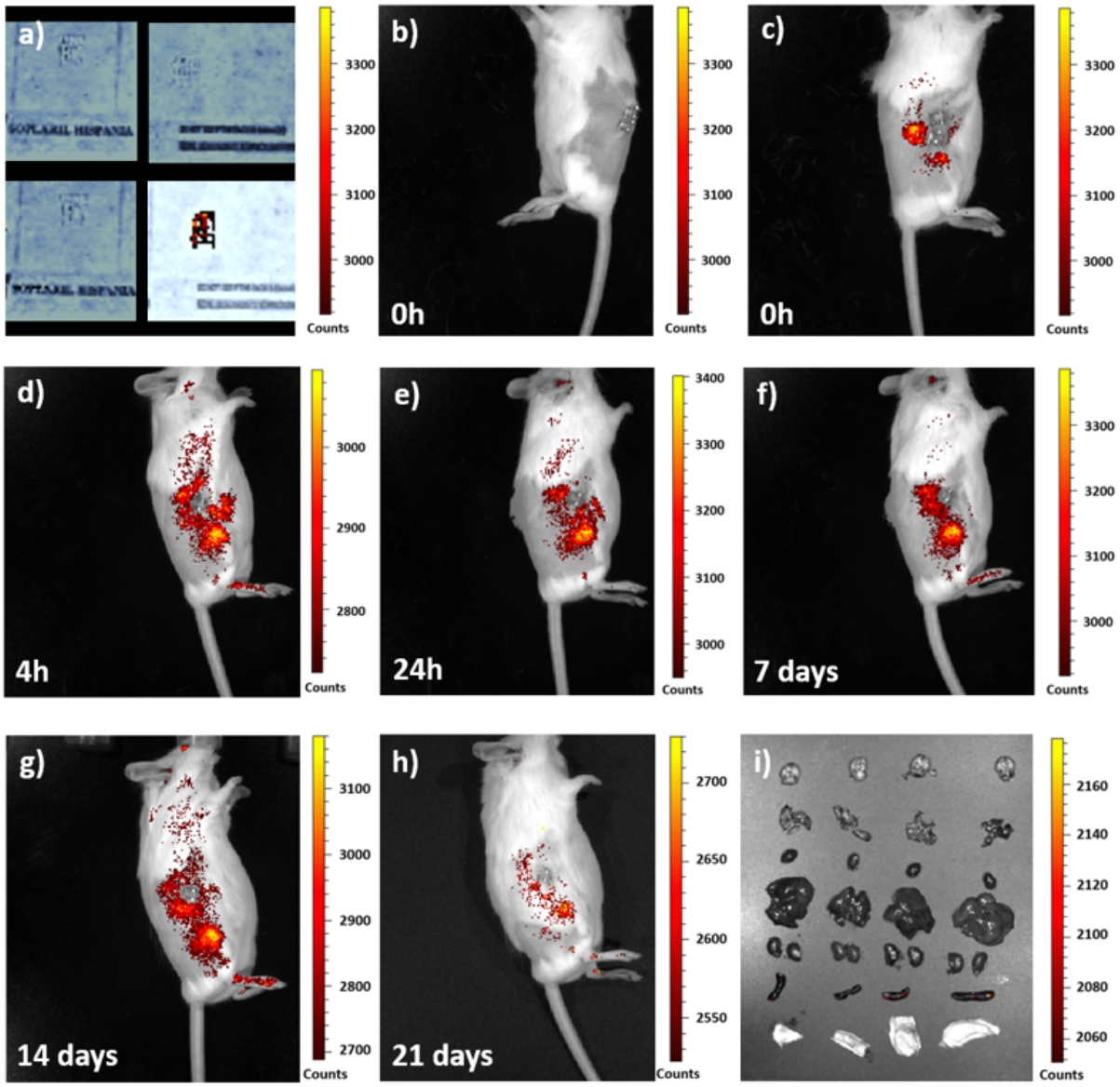


Figure 6.7. Fluorescence intensity maps (expressed in normalized counts) obtained at the excitation wavelength of 745 nm and emission wavelength of 840 nm. **a)** Alg (left) and Alg UCNPs 0.8 implants (right) without (top) and with (bottom) fluorescence excitation. **b)** *in vivo* fluorescence image of Alg implant (control of fluorescence emission). **c-h)** *in vivo* fluorescence images recorded at different timepoints post-implantation of mice bearing Alg UCNPs 0.8 implants. **i)** Fluorescence image of excised brain, liver, heart, lungs, kidneys, spleen, and skin surrounding the implant (rows from top to bottom) of a control animal (without scaffold implantation) and of the 3 animals with Alg UCNPs 0.8 theranostic implant (columns from left to right).

USC UNIVERSIDADE DE SANTIAGO DE COMPOSTELA

6.4. Conclusions

Bifunctional implants were successfully manufactured and *in vivo* traceable by fluorescence measurements until 3 weeks after subcutaneous implantation thus enabling the *in vivo* monitoring of aerogels fate in a safe and non-invasive way. UCNPs present advanced long-term photophysical and fluorescence properties for bioimaging that are preserved after their incorporation into aerogels. A homogeneous distribution of UCNPs was observed throughout the pores of the 3D-printed aerogels. UCNPs-decorated aerogels are biocompatible structures able to promote cell adhesion and cell migration. Results indicate a minimal systemic toxicity without relevant inflammatory response or foreign body reaction in terms of cytokine expression and histology of main organs 1 week after subcutaneous implantation of the theranostic device, thus potentially promoting good tissue development. Specific metabolic pathways involving these UCNPs-labeled aerogels could be studied in future by *in vivo* bioimaging experiments in a time- and dose-dependent manner to determine their internalization and excretion process. This work opens up the possibility of studying *in vivo* the resorption rates and toxicity of aerogels and their degradation products in a long-term study. Tissue regeneration process could be thereby in situ monitored as well as the scaffold position and state providing useful information for disease treatment in real-time by *in vivo* fluorescence imaging.

6.5. References

1. Yamaoka, T. Bioimaging Materials. In Encyclopedia of Polymeric Nanomaterials; Kobayashi, S., Müllen, K., Eds.; Springer Berlin Heidelberg: Berlin, Heidelberg, 2014; pp. 1–6 ISBN 978-3-642-36199-9.
2. Wang, J.; Jiang, Z.; Huang, C.; Zhao, S.; Zhu, S.; Liu, R.; Zhu, H. Self-Assembled BODIPY Nanoparticles for Near-Infrared Fluorescence Bioimaging. Molecules 2023, 28, 2997, doi:10.3390/molecules28072997.
3. Ganguly, S.; Margel, S. Bioimaging Probes Based on Magneto-Fluorescent Nanoparticles. Pharmaceutics 2023, 15, 686, doi:10.3390/pharmaceutics15020686.
4. Sobhanan, J.; Anas, A.; Biju, V. Nanomaterials for Fluorescence and Multimodal Bioimaging. The Chemical Record 2023, 23, e202200253, doi:10.1002/tcr.202200253.
5. Feng, Q.; Zhou, X.; He, C. NIR Light-facilitated Bone Tissue Engineering. WIREs Nanomed Nanobiotechnol 2024, 16, e1925, doi:10.1002/wnan.1925.
6. García-González, C.A.; Iglesias-Mejuto, A.; López-Iglesias, C.; Santos-Rosales, V.; Ardao, I.; Alvarez-Lorenzo, C. Natural Polymer Hydrogels and Aerogels for Biomedical Applications. In Engineering of Natural Polymeric Gels and Aerogels for Multifunctional Applications; Elsevier, 2024; pp. 125–157 ISBN 978-0-12-823135-7.
7. Wang, H.; Zeng, X.; Pang, L.; Wang, H.; Lin, B.; Deng, Z.; Qi, E.L.X.; Miao, N.; Wang, D.; Huang, P.; et al. Integrative Treatment of Anti-Tumor/Bone Repair by Combination of MoS_2 Nanosheets with 3D Printed Bioactive Borosilicate Glass Scaffolds. Chem. Eng. J. 2020, 396, 125081, doi:10.1016/j.cej.2020.125081.

8. Wang, X.; Ai, A.; Yu, Z.; Deng, M.; Liu, W.; Zhou, G.; Li, W.; Zhang, W.; Cao, Y.; Wang, X. Dual-Modal Non-Invasive Imaging *in Vitro* and *in Vivo* Monitoring Degradation of PLGA Scaffold Based Gold Nanoclusters. Mat. Sci. Eng. C 2020, 107, 110307, doi:10.1016/j.msec.2019.110307.
9. Guryev, E.L.; Smyshlyaeva, A.S.; Shilyagina, N.Y.; Sokolova, E.A.; Shanwar, S.; Kostyuk, A.B.; Lyubeshkin, A.V.; Schulga, A.A.; Konovalova, E.V.; Lin, Q.; et al. UCNP-Based Photoluminescent Nanomedicines for Targeted Imaging and Theranostics of Cancer. Molecules 2020, 25, 4302, doi:10.3390/molecules25184302.
10. Iglesias-Mejuto, A.; Lamy-Mendes, A.; Pina, J.; Costa, B.F.O.; García-González, C.A.; Durães, L. Synthesis of Highly Luminescent Silica-Coated Upconversion Nanoparticles from Lanthanide Oxides or Nitrates Using Co-Precipitation and Sol–Gel Methods. Gels 2023, 10, 13, doi:10.3390/gels10010013.
11. Yang, Y.; Xie, Y.; Zhang, F. Second Near-Infrared Window Fluorescence Nanoprobes for Deep-Tissue *in Vivo* Multiplexed Bioimaging. Advanced Drug Delivery Reviews 2023, 193, 114697, doi:10.1016/j.addr.2023.114697.
12. Vorotnikov, Y.A.; Vorotnikova, N.A.; Shestopalov, M.A. Silica-Based Materials Containing Inorganic Red/NIR Emitters and Their Application in Biomedicine. Materials 2023, 16, 5869, doi:10.3390/ma16175869.
13. Rashad, A.; Suliman, S.; Mustafa, M.; Pedersen, T.; Campodoni, E.; Sandri, M.; Syverud, K.; Mustafa, K. Inflammatory Responses and Tissue Reactions to Wood-Based Nanocellulose Scaffolds. Mat. Sci. Eng. C 2019, 97, 208–221, doi:10.1016/j.msec.2018.11.068.
14. Cicuéndez, M.; Portolés, P.; Montes-Casado, M.; Izquierdo-Barba, I.; Vallet-Regí, M.; Portolés, M.T. Effects of 3D Nanocomposite Bioceramic Scaffolds on the Immune Response. J. Mater. Chem. B 2014, 2, 3469, doi:10.1039/c4tb00106k.
15. He, S.; Hou, T.; Zhou, J.; Ai, Q.; Dou, C.; Luo, F.; Xu, J.; Xing, J. Endothelial Cells Promote Migration of Mesenchymal Stem Cells via PDGF-BB/PDGFRβ-Src-Akt in the Context of Inflammatory Microenvironment upon Bone Defect. Stem Cells International 2022, 2022, 1–15, doi:10.1155/2022/2401693.
16. Iglesias-Mejuto, A.; Malandain, N.; Ferreira-Gonçalves, T.; Ardao, I.; Reis, C.P.; Laromaine, A.; Roig, A.; García-González, C.A. Cellulose-in-Cellulose 3D-Printed Bioaerogels for Bone Tissue Engineering. Cellulose 2024, 31, 515–534, doi:10.1007/s10570-023-05601-1.
17. Iglesias-Mejuto, A.; Magariños, B.; Ferreira-Gonçalves, T.; Starbird-Pérez, R.; Álvarez-Lorenzo, C.; Reis, C.P.; Ardao, I.; García-González, C.A. Vancomycin-Loaded Methylcellulose Aerogel Scaffolds for Advanced Bone Tissue Engineering. Carbohydr. Polym. 2024, 324, 121536, doi:10.1016/j.carbpol.2023.121536.
18. Iglesias-Mejuto, A.; García-González, C.A. 3D-Printed Alginate-Hydroxyapatite Aerogel Scaffolds for Bone Tissue Engineering. Mat. Sci. Eng. C 2021, 131, 112525, doi:10.1016/j.msec.2021.112525.
19. Iglesias-Mejuto, A.; García-González, C.A. 3D-Printed, Dual Crosslinked and Sterile Aerogel Scaffolds for Bone Tissue Engineering. Polymers 2022, 14, 1211, doi:10.3390/polym14061211.
20. Dong, Y.; Lin, M.; Jin, G.; Il Park, Y.; Qiu, M.; Zhao, Y.; Yang, H.; Li, A.; Jian Lu, T. Fabrication of Fluorescent Composite Hydrogel Using *in Situ* Synthesis of Upconversion Nanoparticles. Nanotechnology 2017, 28, 175702, doi:10.1088/1361-6528/aa6564.
21. Zhang, Z.; Liu, G.; Li, X.; Zhang, S.; Lü, X.; Wang, Y. Design and Synthesis of Fluorescent Nanocelluloses for Sensing and Bioimaging Applications. ChemPlusChem 2020, 85, 487–502, doi:10.1002/cplu.201900746.
22. Király, G.; Egu, J.C.; Hargitai, Z.; Kovács, I.; Fábián, I.; Kalmár, J.; Szemán-Nagy, G. Mesoporous Aerogel Microparticles Injected into the Abdominal Cavity of Mice Accumulate in Parathymic Lymph Nodes. IJMS 2021, 22, 9756, doi:10.3390/ijms22189756.
23. Gillispie, G.; Prim, P.; Copus, J.; Fisher, J.; Mikos, A.G.; Yoo, J.J.; Atala, A.; Lee, S.J. Assessment Methodologies for Extrusion-Based Bioink Printability. Biofabrication 2020, 12, 022003, doi:10.1088/1758-5090/ab6f0d.
24. Paxton, N.; Smolan, W.; Böck, T.; Melchels, F.; Groll, J.; Jungst, T. Proposal to Assess Printability of Bioinks for Extrusion-Based Bioprinting and Evaluation of Rheological Properties Governing Bioprintability. Biofabrication 2017, 9, 044107, doi:10.1088/1758-5090/aa8dd8.
25. Recommended Test Method Protocol: Hen's Egg Test – Chorioallantoic Membrane (HET-CAM) Test Method 2010.
26. Da Silva Morais, A.; Oliveira, J.M.; Reis, R.L. Small Animal Models. In Osteochondral Tissue Engineering; Oliveira, J.M., Pina, S., Reis, R.L., San Roman, J., Eds.; Advances in Experimental Medicine and Biology; Springer International Publishing: Cham, 2018; Vol. 1059, pp. 423–439 ISBN 978-3-319-76734-5.

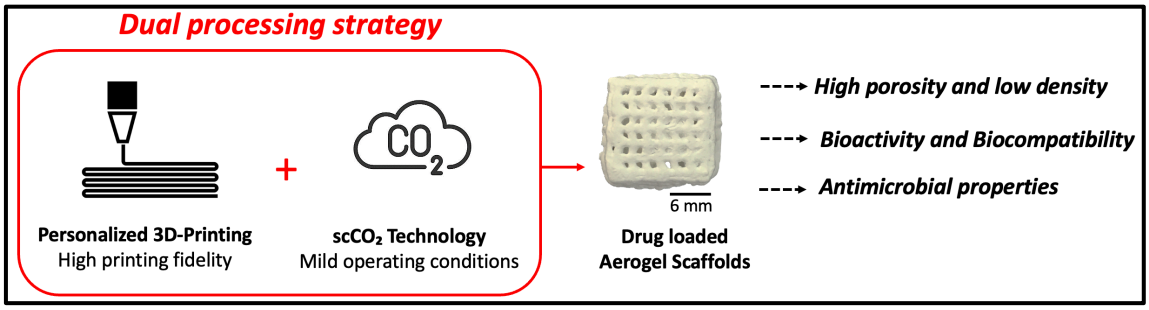
USC DE SANTIAGO DE COMPOSTELA

27. Laschke, M.; Vollmar; Menger, M. The Dorsal Skinfold Chamber: Window into the Dynamic Interaction of Biomaterials with Their Surrounding Host Tissue. eCM 2011, 22, 147–167, doi:10.22203/eCM.v022a12.
28. ISO 14937:2009 Sterilization of Health Care Products — General Requirements for Characterization of a Sterilizing Agent and the Development, Validation and Routine Control of a Sterilization Process for Medical Devices 2009.
29. Ribeiro, A.; Blokzijl, M.M.; Levato, R.; Visser, C.W.; Castilho, M.; Hennink, W.E.; Vermonden, T.; Malda, J. Assessing Bioink Shape Fidelity to Aid Material Development in 3D Bioprinting. Biofabrication 2017, 10, 014102, doi:10.1088/1758-5090/aa90e2.
30. Rodríguez-Rego, J.M.; Mendoza-Cerezo, L.; Macías-García, A.; Carrasco-Amador, J.P.; Marcos-Romero, A.C. Methodology for Characterizing the Printability of Hydrogels. IJB 2023, 9, 667, doi:10.18063/ijb.v9i2.667.
31. Herrada-Manchón, H.; Fernández, M.A.; Aguilar, E. Essential Guide to Hydrogel Rheology in Extrusion 3D Printing: How to Measure It and Why It Matters? Gels 2023, 9, 517, doi:10.3390/gels9070517.
32. Tian, X.Y.; Li, M.G.; Cao, N.; Li, J.W.; Chen, X.B. Characterization of the Flow Behavior of Alginate/Hydroxyapatite Mixtures for Tissue Scaffold Fabrication. Biofabrication 2009, 1, 045005, doi:10.1088/1758-5082/1/4/045005.
33. Greco, I.; Varon, C.; Iorio, C.S. Synthesis and Characterization of a New Alginate-Gelatine Aerogel for Tissue Engineering. In Proceedings of the 2022 44th Annual International Conference of the IEEE Engineering in Medicine & Biology Society (EMBC); IEEE: Glasgow, Scotland, United Kingdom, July 11 2022; pp. 3915–3918.
34. Guo, N.; Xia, Y.; Zeng, W.; Chen, J.; Wu, Q.; Shi, Y.; Li, G.; Huang, Z.; Wang, G.; Liu, Y. Alginate-Based Aerogels as Wound Dressings for Efficient Bacterial Capture and Enhanced Antibacterial Photodynamic Therapy. Drug Delivery 2022, 29, 1086–1099, doi:10.1080/10717544.2022.2058650.
35. Athamneh, T.; Amin, A.; Benke, E.; Ambrus, R.; Leopold, C.S.; Gurikov, P.; Smirnova, I. Alginate and Hybrid Alginate-Hyaluronic Acid Aerogel Microspheres as Potential Carrier for Pulmonary Drug Delivery. J. Supercrit. Fluids 2019, 150, 49–55, doi:10.1016/j.supflu.2019.04.013.
36. Remuiñán-Pose, P.; López-Iglesias, C.; Iglesias-Mejuto, A.; Mano, J.F.; García-González, C.A.; Rial-Hermida, M.I. Preparation of Vancomycin-Loaded Aerogels Implementing Inkjet Printing and Superhydrophobic Surfaces. Gels 2022, 8, 417, doi:10.3390/gels8070417.
37. Wright, C.J.; Molino, B.Z.; Chung, J.H.Y.; Pannell, J.T.; Kuester, M.; Molino, P.J.; Hanks, T.W. Synthesis and 3D Printing of Conducting Alginate–Polypyrrole Ionomers. Gels 2020, 6, 13, doi:10.3390/gels6020013.
38. Rodríguez-Dorado, R.; López-Iglesias, C.; García-González, C.; Auriemma, G.; Aquino, R.; Del Gaudio, P. Design of Aerogels, Cryogels and Xerogels of Alginate: Effect of Molecular Weight, Gelation Conditions and Drying Method on Particles' Micromeritics. Molecules 2019, 24, 1049, doi:10.3390/molecules24061049.
39. Santos-Rosales, V.; Alvarez-Rivera, G.; Hillgärtner, M.; Cifuentes, A.; Itskov, M.; García-González, C.A.; Rege, A. Stability Studies of Starch Aerogel Formulations for Biomedical Applications. Biomacromolecules 2020, 21, 5336–5344, doi:10.1021/acs.biomac.0c01414.
40. ISO 10993-5:2009 Biological Evaluation of Medical Devices — Part 5: Tests for *in Vitro* Cytotoxicity 2009.
41. Zhang, Y.; Wiesholler, L.M.; Rabie, H.; Jiang, P.; Lai, J.; Hirsch, T.; Lee, K.-B. Remote Control of Neural Stem Cell Fate Using NIR-Responsive Photoswitching Upconversion Nanoparticle Constructs. ACS Appl. Mater. Interfaces 2020, 12, 40031–40041, doi:10.1021/acsami.0c10145.
42. Stochaj, U.; Rodríguez Burbano, D.C.; Cooper, D.R.; Kodiha, M.; Capobianco, J.A. The Effects of Lanthanide-Doped Upconverting Nanoparticles on Cancer Cell Biomarkers. Nanoscale 2018, 10, 14464–14471, doi:10.1039/C8NR01451E.
43. Dukhno, O.; Przybilla, F.; Muhr, V.; Buchner, M.; Hirsch, T.; Mély, Y. Time-Dependent Luminescence Loss for Individual Upconversion Nanoparticles upon Dilution in Aqueous Solution. Nanoscale 2018, 10, 15904–15910, doi:10.1039/C8NR03892A.
44. Kastellorizios, M.; Tipnis, N.; Burgess, D.J. Foreign Body Reaction to Subcutaneous Implants. In Immune Responses to Biosurfaces; Lambris, J.D., Ekdahl, K.N., Ricklin, D., Nilsson, B., Eds.; Advances in Experimental Medicine and Biology; Springer International Publishing: Cham, 2015; Vol. 865, pp. 93–108 ISBN 978-3-319-18602-3.
45. Díaz-Rodríguez, P.; González, P.; Serra, J.; Landin, M. Key Parameters in Blood-Surface Interactions of 3D Bioinspired Ceramic Materials. Mat. Sci. Eng. C 2014, 41, 232–239, doi:10.1016/j.msec.2014.04.058.

46. Xiang, Z.; Guan, X.; Ma, Z.; Shi, Q.; Panteleev, M.; Ataullakhanov, F.I. Bioactive Engineered Scaffolds Based on PCL-PEG-PCL and Tumor Cell-Derived Exosomes to Minimize the Foreign Body Reaction. Biomaterials and Biosystems 2022, 7, 100055, doi:10.1016/j.bbiosy.2022.100055.
47. Salerno, A.; Diéguez, S.; Diaz-Gomez, L.; Gómez-Amoza, J.L.; Magariños, B.; Concheiro, A.; Domingo, C.; Alvarez-Lorenzo, C.; García-González, C.A. Synthetic Scaffolds with Full Pore Interconnectivity for Bone Regeneration Prepared by Supercritical Foaming Using Advanced Biofunctional Plasticizers. Biofabrication 2017, 9, 035002, doi:10.1088/1758-5090/aa78c5.
48. Yoon, S.J.; Kim, S.H.; Ha, H.J.; Ko, Y.K.; So, J.W.; Kim, M.S.; Yang, Y.I.; Khang, G.; Rhee, J.M.; Lee, H.B. Reduction of Inflammatory Reaction of Poly(D,L-Lactic-C o -Glycolic Acid) Using Demineralized Bone Particles. Tissue Eng. Part A 2008, 14, 539–547, doi:10.1089/tea.2007.0129.
49. Zheng, H.; Cheng, X.; Jin, L.; Shan, S.; Yang, J.; Zhou, J. Recent Advances in Strategies to Target the Behavior of Macrophages in Wound Healing. Biomed. Pharmacother. 2023, 165, 115199, doi:10.1016/j.biopha.2023.115199.
50. Weiskirchen, R.; Weiskirchen, S.; Tacke, F. Organ and Tissue Fibrosis: Molecular Signals, Cellular Mechanisms and Translational Implications. Mol. Aspects Med. 2019, 65, 2–15, doi:10.1016/j.mam.2018.06.003.
51. Dong, C.; Tan, G.; Zhang, G.; Lin, W.; Wang, G. The Function of Immunomodulation and Biomaterials for Scaffold in the Process of Bone Defect Repair: A Review. Front. Bioeng. Biotechnol. 2023, 11, 1133995, doi:10.3389/fbioe.2023.1133995.
52. Vahedian, V.; Asadi, A.; Esmaeili, P.; Zamani, S.; Zamani, R.; Hajazimian, S.; Isazadeh, A.; Shanehbandi, D.; Maroufi, N.F. Anti-Inflammatory Activity of Emu Oil-Based Nanofibrous Scaffold through Downregulation of IL-1, IL-6, and TNF-α pro-Inflammatory Cytokines. HMBCI 2020, 41, 20190052, doi:10.1515/hmbci-2019-0052.
53. Villa, O.; P. Lyngstadaas, S.; Monjo, M.; Satué, M.; J. Rønold, H.; Petzold, C.; C. Wohlfahrt, J. Suture Materials Affect Peri-Implant Bone Healing and Implant Osseointegration. J. Oral Sci. 2015, 57, 219–227, doi:10.2334/josnusd.57.219.
54. Kang, K.; Kim, Y.; Jeon, H.; Lee, S.B.; Kim, J.S.; Park, S.A.; Kim, W.D.; Yang, H.M.; Kim, S.J.; Jeong, J.; et al. Three-Dimensional Bioprinting of Hepatic Structures with Directly Converted Hepatocyte-Like Cells. Tissue Eng. Part A 2018, 24, 576–583, doi:10.1089/ten.tea.2017.0161.
55. Javed, F.; Al-Askar, M.; Almas, K.; Romanos, G.E.; Al-Hezaimi, K. Tissue Reactions to Various Suture Materials Used in Oral Surgical Interventions. ISRN Dentistry 2012, 2012, 1–6, doi:10.5402/2012/762095.
56. Fuest, S.; Smeets, R.; Gosau, M.; Aavani, F.; Knipfer, C.; Grust, A.L.C.; Kopp, A.; Becerikli, M.; Behr, B.; Matthies, L. Layer-by-Layer Deposition of Regenerated Silk Fibroin–An Approach to the Surface Coating of Biomedical Implant Materials. ACS Biomater. Sci. Eng. 2023, 9, 6644–6657, doi:10.1021/acsbiomaterials.3c00852.
57. Yang, C.; Ma, H.; Wang, Z.; Younis, M.R.; Liu, C.; Wu, C.; Luo, Y.; Huang, P. 3D Printed Wesselsite Nanosheets Functionalized Scaffold Facilitates NIR-II Photothermal Therapy and Vascularized Bone Regeneration. Advanced Science 2021, 8, 2100894, doi:10.1002/advs.202100894.
58. Xiang, J.; Xu, L.; Gong, H.; Zhu, W.; Wang, C.; Xu, J.; Feng, L.; Cheng, L.; Peng, R.; Liu, Z. Antigen-Loaded Upconversion Nanoparticles for Dendritic Cell Stimulation, Tracking, and Vaccination in Dendritic Cell-Based Immunotherapy. ACS Nano 2015, 9, 6401–6411, doi:10.1021/acsnano.5b02014.
59. Yang, C.; Gao, X.; Younis, M.R.; Blum, N.T.; Lei, S.; Zhang, D.; Luo, Y.; Huang, P.; Lin, J. Non-Invasive Monitoring of *in Vivo* Bone Regeneration Based on Alkaline Phosphatase-Responsive Scaffolds. Chem.Eng. J. 2021, 408, 127959, doi:10.1016/j.cej.2020.127959.
60. Gao, X.; Ma, G.; Jiang, C.; Zeng, L.; Jiang, S.; Huang, P.; Lin, J. *In Vivo* Near-Infrared Fluorescence and Photoacoustic Dual-Modal Imaging of Endogenous Alkaline Phosphatase. Anal. Chem. 2019, 91, 7112–7117, doi:10.1021/acs.analchem.9b00109.

USC UNIVERSIDADE DE SANTIAGO DE COMPOSTELA

CHAPTER 7. VANCOMYCIN-LOADED METHYLCELLULOSE AEROGEL SCAFFOLDS FOR ADVANCED BONE TISSUE ENGINEERING



The content in this chapter was published in part in **A. Iglesias-Mejuto,** B. Magariños, T. Ferreira-Gonçalves, R. Starbird-Pérez, C. Álvarez-Lorenzo, C.P. Reis, I. Ardao, C.A. García-González; Vancomycin-Loaded Methylcellulose Aerogel Scaffolds for Advanced Bone Tissue Engineering, in: *Carbohydrate Polymers* 324 (2024) 121536. doi:10.1016/j.carbpol.2023.121536.

The work described in this chapter was carried out in collaboration with the University of Lisbon and with the Tecnológico de Costa Rica.

USC UNIVERSIDADE

7.1. Introduction

The incidence of bone lesions due to falls and traffic accidents is increasing with the progressive ageing of the population as major cause. Patients usually present open wounds and bone defects, commonly accompanied with the activation of infection and inflammation molecular pathways, that significantly hamper the natural healing process [1]. Furthermore, implant-associated post-operative and post-traumatic bone infections commonly come up with antibiotics side effects, hospitalization, and the subsequent health economics costs [2]. *S. aureus* is the most prevalent microorganism leading to graft-associated bone infections [3]. Debridement and intravenous administration of antibiotics is the conventional treatment for open bone injuries with important drawbacks, like the low antibiotic concentration at the wound site that can promote the development of methicillin-resistant *S. aureus* (MRSA) resulting in repeated bacterial infections [4,5]. VAN is the only antibiotic sensitive to MRSA and effective in inhibiting inflammatory reactions in bone infections [6]. Advanced on-site delivery systems of VAN are required for an effective treatment of orthopaedical surgery-related bone infections, avoiding or reducing VAN side effects.

3D-printing is a simple and versatile manufacturing technology that enables the production of intricate and multicomponent grafts employed as provisional supports for new tissue formation [7]. Different 3D-printing strategies have been used in different biomedical fields [8]. Specifically, extrusion-based 3D-printing is the most widely employed for tissue scaffolding [9], allowing the generation of well-organized, and hierarchical tissue equivalents composed by polymers, bioactive molecules and cells [10]. Methylcellulose is a biocompatible and biodegradable cellulose derivative commonly used as 3D graft matrix (Ahlfeld et al., 2020; Shin et al., 2020). Methylcellulose is a thermo-gelling polysaccharide with a fully reversible gelation in aqueous media.

USC
UNIVERSIDADE DE SANTIAGO DE COMPOSTELA

Aerogels are low density and highly mesoporous materials intensively employed for medical (e.g., tissue scaffolds or drug delivery systems) and non-medical (e.g., water purification or

thermal insulation) applications [11,12]. They are obtained from wet gels by processing techniques (typically, $scCO_2$ drying) able to replace the liquid inside these gel networks with a gas under mild operating conditions [13]. Particularly, the outstanding structural performance of aerogels and the excellent biological behavior of polysaccharides (biocompatibility, biodegradability) unveiled polysaccharide aerogels as promising candidates for the development of advanced tissue engineering scaffolds for regenerative medicine [14–16]. Moreover, the recently proposed dual processing strategy combining 3D-printing and $scCO_2$ drying leads to personalized aerogels with dual porosity adequate for bone tissue engineering [14,17].

New formulations for an efficient delivery of VAN triggered by implantation to reach and maintain antibiotic therapeutic levels in the injury site, while promoting long-term osseointegration and ensuring biocompatibility are needed for the treatment of infections associated to bone defects. In this work, 3D-printed and VAN-loaded polysaccharide aerogels were manufactured for the first time with a personalized shape and drug content and specifically evaluated for simultaneous bone tissue engineering and infection management. Aerogels were loaded with nHA, a common bone repair component with good osteoconduction and osteoinduction [18]. $scCO_2$ drying was performed to obtain the drug-loaded aerogels. The textural characteristics of the aerogels were analyzed by BET and SEM analyses, the printing fidelity was evaluated with respect to the original design and their mechanical performance was assessed by dynamic mechanical analysis (DMA). Bioactivity of aerogels was tested by immersion in SBF, biocompatibility by cellular assays, hemocompatibility by HET-CAM tests and their safety by *A. salina* assays. Microbiological tests against *S. aureus*, loading efficiency, entrapment yield and VAN release tests were also carried out. A spatial personalization in the drug dose (with two different VAN contents in one structure) and in the morphology of the aerogels were achieved for the first time by the dual processing strategy herein used. 3D-printed aerogels exhibited a sustained VAN release profile essential for bone infection management as well as the long-term bioactivity required for bone tissue engineering applications.

USC UNIVERSIDADE DE SANTIAGO DE COMPOSTELA

7.2. Materials and Methods

7.2.1. Materials

Methylcellulose (viscosity: 15cP), nHA (M_w: 502.31 g/mol, purity ≥ 97%), alizarin red and cetylpyridinium chloride were provided by Sigma-Aldrich (Steinheim, Germany). Hydroxyapatite (HA, M_w 502.31 g/mol, reagent grade purity, micropowder) was supplied by Fluidinova (Moreira da Maia, Portugal). VAN hydrochloride (M_w: 486.0 g/mol, purity: 94.3%) was provided by Guinama (La Pobla de Vallbona, Spain). CO_2 (purity >99.9%) was supplied by Nippon Gases (Madrid, Spain) and absolute EtOH by VWR (Radnor, PA, USA). Water was purified by reverse osmosis (resistivity >18 MΩ·cm; Milli-Q, Millipore®, Madrid, Spain).

7.2.2. 3D-printing of hydrogels

Milli-Q water was used as solvent to prepare aqueous inks. Different concentrations of methylcellulose (12, 15 and 18 wt. %), nHA/HA (0, 6, 12 and 24 wt. %) and/or VAN (0, 5, 10 and 15 wt. %) with respect to water were employed. Methylcellulose solutions were firstly prepared, and nHA/HA and/or VAN were then added. Inks were prepared under vigorous agitation (600 rpm) employing a homogenizer (VWR vos 60, Radnor, PA, USA) for at least 1 h at RT. They were degassed in a sonication bath (Branson 3510 Emerson, Ferguson, MO, USA) for 10 min to eliminate air bubbles prior to their use as inks for their rheological evaluation and subsequent 3D-printing.

3D-printed hydrogels were obtained with a Cellink BIOX Bioprinter (Boston, MA, USA) using an extrusion printhead at 40°C, a 3-mL syringe and a 410-µm nozzle at a printing pressure of 40 kPa and a printing velocity of 3 mm/s. Hydrogel dimensions were 2 x 2 x 0.3 cm^3 with a grid pattern and 8 layers. After the printing process, all scaffolds were put in contact with EtOH and alcogels were thus obtained.

USC UNIVERSIDADE DE SANTIAGO DE COMPOSTELA

7.2.3. Rheological evaluation of inks

Flow behavior of inks was recorded at 20 and 40°C between 0.05 and 200 rad/s in a Rheolyst AR-1000N rheometer (TA Instruments, Newcastle, UK) equipped with a Peltier plate and a cone geometry (40 mm diameter, 2°) with a solvent trap. For each formulation, at least four replicates were evaluated. The Equation 7.1 (power law) was fitted to the linear region of the viscosity (η) vs shear rate (γ) curves.

$$\eta = b \cdot \gamma^{c} \qquad \textit{Equation 7.1}$$

where *b* and *c* are the consistency and flow indices, respectively.

7.2.4. scCO$_2$ drying of 3D-printed alcogels

Alcogels were placed into a 100-mL stainless steel autoclave (Thar Process, Pittsburg, PA, USA) and immersed in 25 mL of EtOH. A continuous CO_2 flow rate (5-7 g/min) at 120 bar was supplied for 4 h into the autoclave, maintained at 40 °C. After CO_2 depressurization to atmospheric pressure at a constant rate of 2 bar/min, aerogels were collected from the autoclave and stored at RT for further analysis. Aerogels obtained were described in Table 7.1 and denoted as MC *x* nHA (or HA) *y* VAN *z* (being *x*=12, 15, 18, 20 wt.%; *y*= 6, 12, 24 wt.%; *z*=5, 10, 15, 5/15 wt.%- 5 and 15 wt.% in alternative layers-). When the formulation contained MC and nHA/HA/VAN, the MC percentage was set always to 12 wt.% and simply denoted as “MC” (i.e. without *x*).

USC UNIVERSIDADE DE SANTIAGO DE COMPOSTELA

Table 7.1. MC aerogel formulations studied.

Aerogels	Ink composition			
	MC (wt. %)	HA (wt. %)	nHA (wt. %)	VAN (wt. %)
MC	12	-	-	-
MC 15	15	-	-	-
MC 18	18	-	-	-
MC HA 6	12	6	-	-
MC HA 12	12	12	-	-
MC HA 24	12	24	-	-
MC nHA 6	12	-	6	-
MC nHA 12	12	-	12	-
MC nHA 24	12	-	24	-
MC VAN 5	12	-	-	5
MC VAN 10	12	-	-	10
MC VAN 15	12	-	-	15
MC nHA 24 VAN 10	12	-	24	10
MC VAN 5/15	12	-	-	5 (4 layers) 15 (4 layers)

7.2.5. Physicochemical characterization of 3D-printed aerogels

ρ_{skel} of aerogels was measured at RT with a helium pycnometer (Quantachrome, Boynton Beach, FL, USA) at the pressure of 1.01 bar. Values were obtained from five replicates. ρ_{app} of scaffolds was calculated from Equation 7.2, and ε was determined according to Equation 7.3:

$$\rho_{app} = \frac{Aerogel\ mass}{Aerogel\ volume} \qquad \textit{Equation 7.2}$$

$$\varepsilon\ (\%) = \left[1 - \left(\frac{\rho app}{\rho skel}\right)\right] \cdot 100 \qquad \textit{Equation 7.3}$$

External dimensions of scaffolds were measured to determine step and overall volume shrinkages following Equations 7.4 and 7.5, respectively:

$$\textit{Step volume shrinkage}\ (\%) = \left(\frac{Alcogel\ volume - Aerogel\ volume}{Alcogel\ volume}\right) \cdot 100 \qquad \textit{Equation 7.4}$$

$$\textit{Overall volume shrinkage}\ (\%) = \left(\frac{Hydrogel\ volume - Aerogel\ volume}{Hydrogel\ volume}\right) \cdot 100 \qquad \textit{Equation 7.5}$$

Low-temperature N_2 adsorption-desorption analysis (ASAP 2000 Micromeritics Inc.; Norcross, GA, USA) was employed to evaluate aerogels' textural parameters. Samples were degassed under vacuum at RT for 24 h before being analyzed. A_{BET} of aerogels was obtained applying the BET method. V_p, and d_p were calculated by using the BJH method. Morphology of aerogels was assessed by SEM (SEM, EVO LS15, Zeiss, Oberkochen, Germany). Samples were iridium-sputtered

USC UNIVERSIDADE DE SANTIAGO DE COMPOSTELA

before being imaged to improve image quality by decreasing charging. 7-month textural stability tests of the most promising formulation (MC nHA 24 VAN 10) and MC aerogels as controls were also performed by N_2 adsorption–desorption and SEM studies after storage of the aerogels at RT, protected from light and stored in closed plastic jars.

ATR/FT-IR was performed with a Gladi-ATR accessory using a diamond crystal (Pike, Madison, WI, USA) to evaluate the chemical structure and confirm the presence of all components on the end structures. Raw materials and aerogels were characterized in the mid-IR spectrum range (400-4000 cm^{-1}) using 32 scans and at a resolution of 2 cm^{-1}. XRD (XRD, PW-1710, Philips, Eindhoven, The Netherlands) was used to test possible physical modifications in aerogels when VAN was incorporated. Diffractograms were collected in the 2–50◦ (2θ-range) using a 0.02◦ step and CuKα_1 radiation.

7.2.6. Printing fidelity tests

SFF index was employed to assess the fidelity of alcogels and aerogels with respect to the original printing file. SFF was calculated from Equation 7.6:

$$SFF = \frac{Ai}{A} \qquad \textit{Equation 7.6}$$

where A_i is the hydrogel, alcogel or aerogel printed area, and A is the CAD area (printing file).

7.2.7. Mechanical evaluation by DMA

Storage modulus (E´), loss modulus (E´´), and damping ratio tan δ (E"/E') of 3D-printed biocomposites were measured at RT. Compression tests were performed using a DMA RSA-G2 equipment (TA Instruments, Waters, New Castle, DE, USA) with a 5 mm compression geometry. A 0.01 N pre-load was applied to ensure contact between the samples and the adapted parallel plates at a strain value of 0.5 % and from 0.1 to 50 Hz as frequency range. At least three measurements were performed for each formulation.

USC UNIVERSIDADE DE SANTIAGO DE COMPOSTELA

7.2.8. Bioactivity tests

SBF medium was prepared with ion concentrations nearly equal to those of human plasma and adjusted to pH 7.4 [19]. Aerogels were cut into 1 × 1 × 0.3 cm^3 samples, placed into plastic conical tubes and immersed in 35 mL of SBF at 37 °C to evaluate aerogels bioactivity. After 13 and 26 days, wet gels were immediately rinsed three times with deionized water and dried by lyophilization. Bioactivity was assessed by SEM and EDX focusing on surface mineral depositions [20].

7.2.9. VAN loading and entrapment yield on aerogels

VAN entrapment yield was assessed by immersing VAN-loaded aerogels of known dimensions (1 × 1 × 0.3 cm^3) and weight (*ca.* 50 mg) in 25 mL of phosphate buffer saline (PBS) pH 7.4. Samples were kept under magnetic stirring (1000 rpm) until being completely dissolved. Obtained solutions were measured by UV/Vis spectroscopy (8453, Agilent, Santa Clara, CA, USA) at a wavelength of 281 nm. Tests were carried out in triplicate and aerogels without VAN were also tested to eliminate the interference of MC or nHA in UV/Vis measurements. VAN loading and entrapment yield were obtained from Equations 7.7 and 7.8, respectively.

$$Drug\ Loading\ (\%) = \left(\frac{Wp}{Waer}\right) \cdot 100 \qquad \text{Equation 7.7}$$

$$Drug\ entrapment\ yield\ (\%) = \left(\frac{Wp}{Wt}\right) \cdot 100 \qquad \text{Equation 7.8}$$

where W_p is the VAN amount in aerogels measured by UV/Vis analysis, W_{aer} is the total weight of aerogels, and W_t is the initial VAN amount added for aerogels preparation. VAN calibration curve in PBS pH 7.4 medium was obtained and validated in the 0.05-0.22 mg/mL range (R^2 > 0.99).

7.2.10. VAN release tests from aerogels

VAN-loaded aerogels of known weight (*ca.* 20 mg) were placed into plastic conical tubes with 25 mL of PBS pH 7.4. Samples were put into an oscillating bath (P Selecta Unitronic 320 OR, Barcelona, Spain) at 37 °C and 100 rpm for 72 h. 1-mL aliquots of medium were sampled at

USC UNIVERSIDADE DE SANTIAGO

selected times (0, 0.25, 0.5, 1, 2, 4, 8, 24, 48 and 72 h), measured by UV/Vis spectroscopy at the wavelength of 281 nm (8453, Agilent, Santa Clara, CA, USA), and replaced with 1 mL of fresh PBS. VAN release profiles were fitted to the first-order release pharmacokinetic model according to Equation 7.9.

$$VAN\ release\ (\%) = 100 \cdot (1 - e^{-kt}) \qquad Equation\ 7.9$$

where k is the kinetic coefficient and t is the elapsed release time.

7.2.11. Cell viability and mineralization tests

Cytocompatibility of 3D-printed aerogels was determined by assessing the viability of mouse embryo fibroblasts (NIH/3T3) after 24 and 72 h of culture in the presence of aerogels employing a resazurin assay, based on mitochondrial activity of living cells. Fibroblasts (2000 cells/cm^2) were seeded in 24-well plates containing 600 µL of Dulbecco's Modified Eagle's Medium growth media supplemented with 10% bovine calf serum, penicillin 100 U/mL and streptomycin 100 g/mL and were incubated at 37 °C in a humidified atmosphere enriched with 5% CO_2. Aerogels (0.5 × 0.5 × 0.3 cm^3) were UV-sterilized for 30 min and then placed in the wells with cells using culture inserts. Positive controls of cells without aerogels exposure were maintained at the same conditions and all tests were performed in triplicate. After 24 and 72 h of culture, aerogels were removed, growth medium was aspirated and 100 µL of 44 µM resazurin in growth medium was added into each well. Resazurin solution alone was tested as blank. After 3 h incubation under same conditions, fluorescence was measured at an excitation wavelength of 544 nm and emission wavelength of 590 nm in a microplate reader (Infinite® M200, Tecan Group Ltd., Männedorf, Switzerland).

MC3T3-E1 pre-osteoblastic cells were also employed to perform alizarin red staining test. Cells were incubated at 37 °C in a humidified atmosphere enriched with 5% CO_2 and cultured with alpha minimum essential medium supplemented with 10% fetal bovine calf serum, penicillin 100 U/mL and streptomycin 100 g/mL, at a cell density of 1 x 10^5 cells/well in 12-well plates. After 24

USC UNIVERSIDADE DE SANTIAGO DE COMPOSTELA

h of culture, 3D-printed aerogels (0.5 × 0.5 × 0.3 cm^3) were UV-sterilized for 30 min and then placed in the wells with cells using culture inserts. Experiments were carried out in triplicate for each formulation tested. Osteogenic medium was prepared by the addition of 50 µg/mL ascorbic acid, 10 mM glycerophosphate, and 100 nM dexamethasone to the previous medium, added to pre-osteoblastic cells and subsequently replaced every 2-3 days. After 14 and 21 days, cells were washed 3 times with PBS to remove cells debris and fixed with EtOH at 4 °C for 1 h. Cells were then washed twice with water and stained with 40 mM alizarin red (pH 4.2) by incubating for 10 min at RT. After shaking plates moderately, cells were washed once with water and three times with PBS. Residual stain was removed with 10% cetylpyridinium chloride for 15 min and the absorbance was measured at 562 nm using a microplate reader (Infinite® M200, Tecan Group Ltd., Männedorf, Switzerland).

7.2.12. Safety tests using *A. salina* model

All *in vivo* studies were conducted in accordance with the European regulation (Directive 2010/63/EU) on care and use of animals in experimental procedures and the ARRIVE guidelines. Experiments were reviewed and approved by the Animal Experiment Ethics Committee (ORBEA) of the Faculty of Pharmacy of the University of Lisbon. Safety of VAN-loaded aerogels was evaluated by measuring the mortality of *A. salina* after 24 h of contact with aerogels as a preliminary *in vivo* model [21,22]. Commercial sea water salt was dissolved in tap water according to the instructions of the supplier. *A. salina* eggs were left to hatch in that solution at 25-30 °C for 48 h, under aeration and illumination. 1 mL of sea water with 10-15 nauplii was transferred to individual wells of a 24-well plate and aerogels (0.5 × 0.5 × 0.3 cm^3) were also added to wells using six replicates per formulation. 100 µL of artificial sea water and 100 µL of DMSO 100% were used as negative and positive controls, respectively. Nauplii in contact with aerogels were incubated for 24 h under the same conditions and dead *A. salina* per well were

USC UNIVERSIDADE DE SANTIAGO DE COMPOSTELA

counted. 100 µL of DMSO 100% was added to kill the remaining alive nauplii after 24 h, total *A. salina* per well were counted and the mortality was then calculated according to Equation 7.10.

$$Mortality\ (\%) = \left(\frac{Dead\ 24\ h}{Dead\ total}\right) \cdot 100 \qquad Equation.\ 7.10$$

where Dead 24h is the number of dead nauplii after 24 h of contact with aerogels and Dead total is the total number of nauplii per well.

7.2.13. HET-CAM test

VAN-loaded aerogels were evaluated by HET-CAM according to ICCVAM guidelines [23,24]. Test was carried out using fresh and fertilized hens' eggs (50-60 g, Coren, Ourense, Spain) after horizontal incubation in a climatic chamber (Ineltec CC SR 0150, Barcelona, Spain) at 37 °C and 60% humidified atmosphere with an 8-hour scheduled rotation. On day 9, a small window was open in the eggshell with a scalpel to access the CAM. 300 µL of 0.1 N NaOH and 0.9% NaCl were put in contact with CAM as positive and negative controls, respectively. Aerogels were also put in contact with CAM and each test was carried out in triplicate. Vessels of CAM were observed for 5 min to evaluate the appearance of hemorrhage (vessels bleeding), vascular lysis (vessels disintegration), clotting (denaturalization of intra and extravascular proteins), hyperemia (increase of blood flow) or changes in small vessel diameter of CAM by visual inspection and compared to controls.

7.2.14. Antimicrobial tests of 3D-printed aerogels

Sterile VAN-loaded aerogels were put in contact with a susceptible strain of *S. aureus* (ATCC 25923) previously seeded in a TSA plate for inhibition zone (halo) evaluation after 24 h of incubation at 37 °C. Same procedure was performed using TSB tubes (*S. aureus* concentration: 6 x 10^8). Sterile aerogels without VAN were used as controls.

USC UNIVERSIDADE DE SANTIAGO DE COMPOSTELA

7.2.15. scCO$_2$ sterilization of 3D-printed aerogels

Aerogels were introduced into thermally sealed sterilization pouches and placed in a high-pressure 600-mL autoclave (NovaGenesis, NovaSterilis Inc., Ithaca, NY, USA) at 40 °C. 1200 ppm of H_2O_2 were introduced into the autoclave before being pressurized with CO_2 until 100 bar. After 30 min of contact time, the system was depressurized at a constant flow rate of 5 bar/min until atmospheric pressure. Sterilization efficacy was confirmed by seeding the thus sterilized aerogels in a TSA plate for CFU quantification and in TSB tubes, at 37 °C for 24 h. Textural properties of the sterilized aerogels were compared with the corresponding untreated formulations.

7.2.16. Statistical analysis

Results were reported as mean value ± standard deviation and post hoc Tukey HSD multiple comparison tests were carried out to determine the statistical significance of the differences among groups and the concerning controls. Values of $p < 0.05$ were considered as statistically significant.

7.3. Results and Discussion

7.3.1. Rheological evaluation of inks

Methylcellulose inks were homogeneously manufactured with different concentrations of nHA and/or VAN and the 3D-printing was performed without relevant clogging for all the studied formulations (Table 7.1). Extrusion-based 3D-printing process was simulated by analyzing the viscosity of the inks with respect to the shear rate [25]. Flow tests of the inks demonstrated the shear-thinning behavior at low shear-stress conditions (Fig. 7.1a), which should facilitate the extrusion during the 3D-printing at moderate pressures. Shear thinning properties are essential to promote 3D-printing fidelity and a homogeneous distribution of the drug in the end structures. All formulations reached higher viscosities at 40°C than at 20°C, which is coherent

USC DE COMPOSTELA

with the thermal-responsiveness behavior of methylcellulose [7,26]. Moreover, a non-linear relation was observed between shear stress and shear rate thus suggesting a pseudoplastic behavior, displayed for all formulations (Fig. 7.1b).

All rheological measurements were fitted to the power law equation (Equation 7.1). *b* values suggest higher extrudability at 20°C (Table 7.2), probably due to the lower viscosities reached by methylcellulose at lower temperatures (Fig. 7.1a). *c* values obtained were closer to 0 if the rheology tests were performed at 40°C (Table 7.2), indicating a more pronounced shear thinning behavior and a better suitability for extrusion-based 3D-printing.

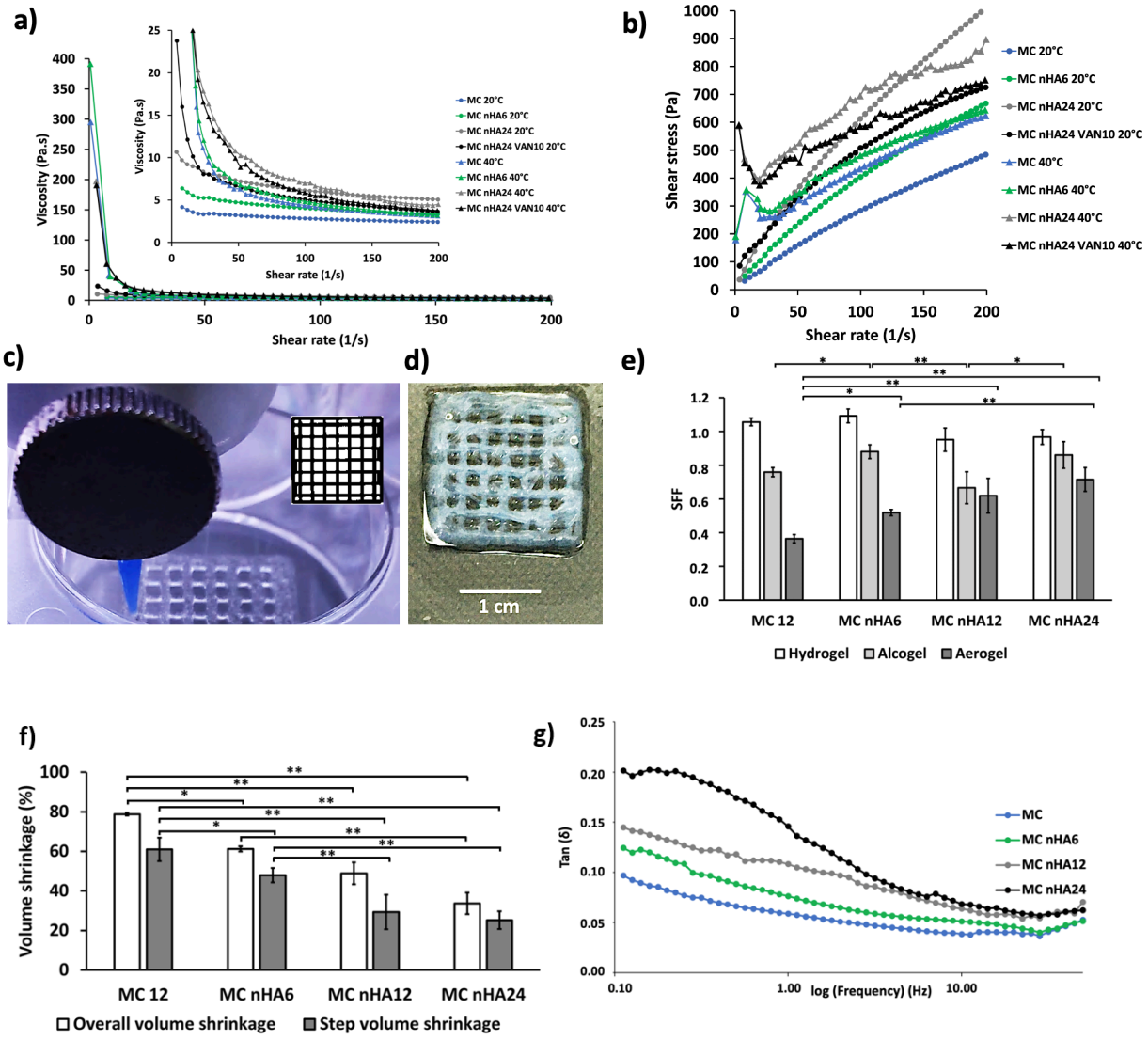


Figure 7.1. Rheological evaluation of different ink formulations. **a)** Overall viscosity variation with respect to the shear rate. **b)** Shear stress with respect to shear rate. **c)** MC hydrogel scaffolds during the 3D-printing process and CAD printing file (intake). **d)** MC hydrogel scaffolds after solvent exchange to EtOH. **e)** SFF index of different hydrogel formulations, alcogels and aerogels. **f)** Overall and step volume

shrinkage of different aerogel formulations. **g)** DMA frequency sweep of tan δ for aerogels with increasing nHA content. Significant differences among groups were represent as * or ** (post hoc Tukey HSD multiple comparison test, $p < 0.05$ or $p < 0.01$, respectively).

Table 7.2. Shear thinning coefficient values of inks calculated through power law model.

Aerogel formulations	20 ° C		40 ° C	
	b	c	b	c
MC	6.95	0.80	61.74	0.43
MC nHA 6	12.19	0.76	85.85	0.38
MC nHA 24	19.86	0.74	203.80	0.27
MC nHA 24 VAN 10	33.96	0.58	223.50	0.22

7.3.2. Physicochemical characterization of 3D-printed aerogels

Highly mesoporous 3D-printed aerogel scaffolds were manufactured with different methylcellulose concentrations (12 to 20 wt.%; Fig. 7.2a and Fig. 7.3). The high textural properties obtained in all cases confirmed that the filaments of the 3D-printed structure were highly mesoporous (Table 7.4 and Table 3). Similar textural parameters, pore morphology and distribution to those obtained for these filaments of the MC aerogels were also described for nanofibrous cellulose aerogels [27]. Methylcellulose concentration was set at 12 wt.% for ulterior tests in combination with nHA/HA and/or VAN as the 3D-printing process was difficult (frequent clogging of the printhead upon printing) when higher methylcellulose concentrations were employed.

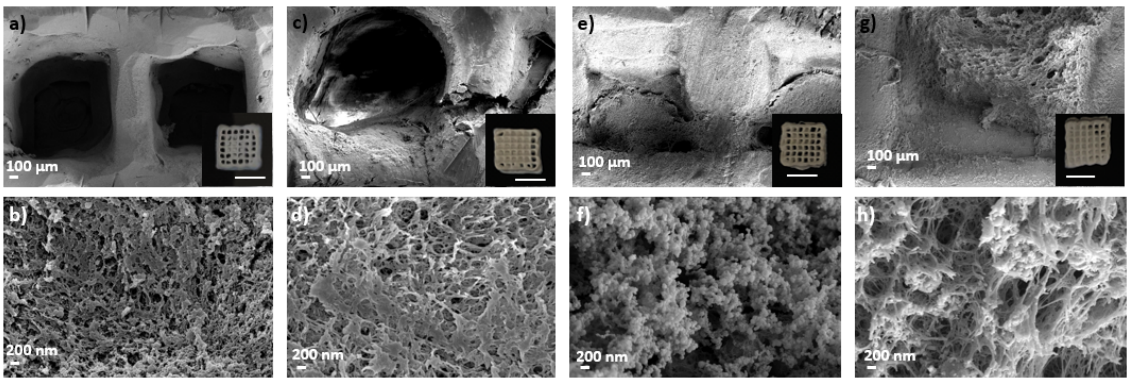


Figure 7.2. SEM images of MC nHA aerogels. **a,b)** MC 12; **c,d)** MC nHA 6; **e,f)** MC nHA 12; **g,h)** MC nHA 24. Intake in **a,c,e,g)** Visual appearance of the 3D-pattern of aerogels (scale bar: 1 cm).

USC UNIVERSIDADE DE SANTIAGO DE COMPOSTELA

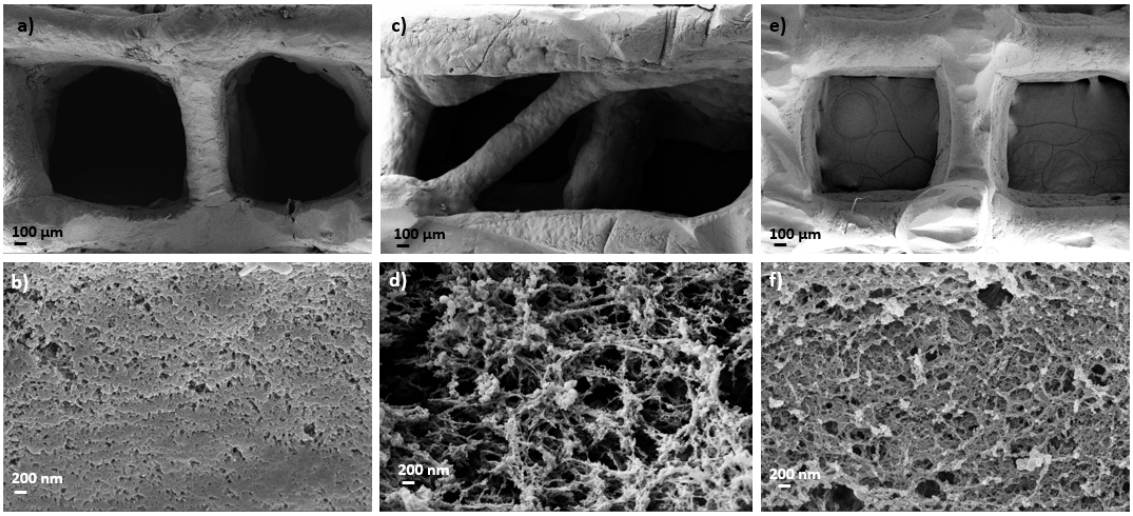


Figure 7.3. SEM images of MC-aerogels (from left to right with increasing MC content). **a,b)** MC 15; **c,d)** MC 18; **e,f)** MC 20.

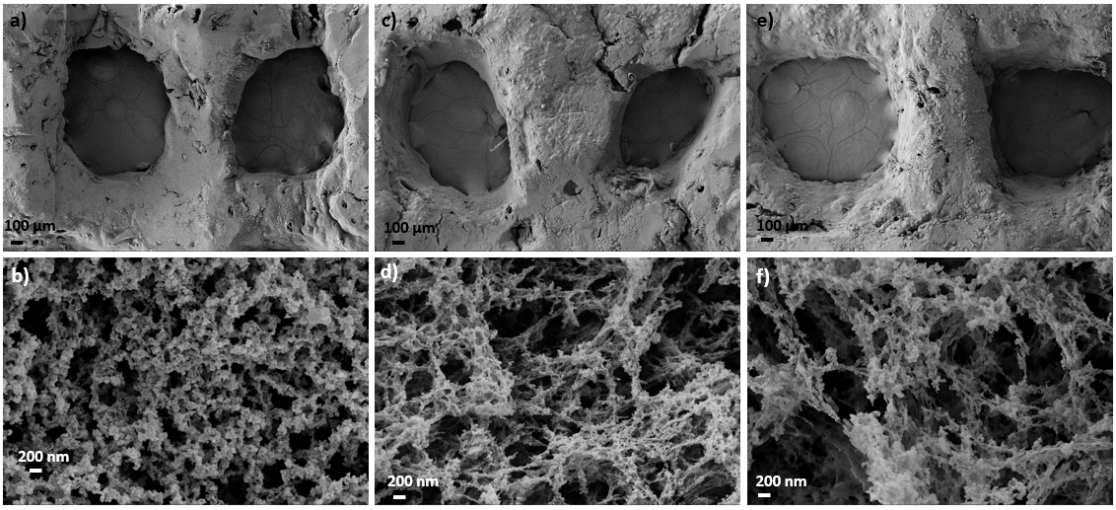


Figure 7.4. SEM images of MC HA (6, 12, 24) aerogels (from left to right with increasing HA content). **a,b)** MC HA 6; **c,d)** MC HA 12; **e,f)** MC HA 24.

MC aerogels containing nHA showed good textural properties regardless of the nHA content (Table 7.4). nHA has been previously linked to higher specific surface areas, bioactivity and closer elasticity to the cortical bone with respect to HA, being able to address HA poor toughness and better repair bone defects (Chen et al., 2021). HA was incorporated into MC aerogels, i.e. alternatively to nHA, for the sake of textural properties comparison (Table 3 and Fig. 7.4). The addition of HA caused a dramatic decrease in A_{BET} proportional to HA content (Table 3), as

USC DE COMPOSTELA

previously reported for alginate-HA scaffolds [14]. Nevertheless, the incorporation of nHA in MC aerogels did not cause such a sharp decline in textural properties (Table 7.4) resulting in MC nHA scaffolds with improved textural properties with respect to their MC HA counterparts. Moreover, macroscopical SEM images show an accuracy loss in the 3D-pattern when HA was employed (Fig. 7.4a,c,e) maybe due to the increase of the ink viscosity with the HA content. For all these reasons, nHA-loaded aerogels were selected for further physicochemical and biological characterizations.

Aerogels porosity (83-87 %, Table 7.4) is higher than those reported for other cellulose aerogels (60-90 %) [29], maybe due to the presence of large macropores originated from the 3D-pattern design on the herein manufactured structures.

Table 7.3. Textural properties of MC and MC-HA aerogels.

Aerogel scaffold	A_{BET} (m^2/g)	d_p (nm)	V_p (cm^3/g)
MC	267 ± 13	18.5 ± 0.9	1.71 ± 0.09
MC 15	249 ± 12	18.0 ± 0.9	1.57 ± 0.08
MC 18	356 ± 18	16.8 ± 0.8	2.18 ± 0.11
MC 20	302 ± 15	12.5 ± 0.6	1.49 ± 0.07
MC HA 6	281 ± 14	19.6 ± 1.0	1.80 ± 0.09
MC HA 12	187 ± 9	21.3 ± 1.1	1.33 ± 0.07
MC HA 24	74 ± 4	22.6 ± 1.1	0.56 ± 0.03

Notation: A_{BET}: BET-specific surface area, d_p: BJH-mean pore diameter, V_p: BJH-specific pore volume, ρ_{app}: apparent density, ρ_{skel}: skeletal density, ε: scaffold porosity.

Table 7.4. Textural properties of MC nHA (6, 12, 24) loaded aerogels.

Aerogel scaffold	A_{BET} (m^2/g)	d_p (nm)	V_p (cm^3/g)	ρ_{app} (g/mL)	ρ_{skel} (g/ cm^3)	ε (%)
MC	268 ± 13	19 ± 1	1.71 ± 0.09	0.18 ± 0.04	1.35 ± 0.03	87 ± 3
MC nHA 6	259 ± 13	24 ± 1	1.83 ± 0.09	0.22 ± 0.02	1.54 ± 0.04	86 ± 1
MC nHA 12	235 ± 12	23 ± 1	1.76 ± 0.09	0.31 ± 0.01	1.76 ± 0.02	83 ± 1
MC nHA 24	165 ± 8	24 ± 1	1.36 ± 0.07	0.32 ± 0.03	1.92 ± 0.02	83 ± 2

Notation: A_{BET}: BET-specific surface area, d_p: BJH-mean pore diameter, V_p: BJH-specific pore volume, ρ_{app}: apparent density, ρ_{skel}: skeletal density, ε: scaffold porosity.

A highly porous and interconnected microstructure was observed by SEM images for all nHA-loaded aerogels with a rougher pore structure when higher nHA contents were incorporated with respect to lower nHA contents (Fig. 7.2b,d vs Fig. 7.2f,h). Similar findings were reported for

USC DE COMPOSTELA

cellulose aerogels (Chen et al., 2021) and for alginate-cellulose scaffolds loaded with different HA concentrations [30].

Direct solvent exchange to EtOH results in aerogels with low step and overall volume shrinkages (Fig. 7.1f). Aerogels with the highest nHA content present the lowest step and overall volume shrinkages, with statistically significant differences with respect to the other formulations studied ($p < 0.01$). Higher volume shrinkages were reported for aerogels with lower nHA content, similar to those herein obtained for MC aerogels and also found for nanocellulose-based aerogels (50 %) (Zhang et al., 2021).

Good textural properties were found for VAN-loaded aerogels, with a slight increase in A_{BET} (Table 7.5). Highly interconnected and irregular pores with a dual size (mesopores and macropores) were found in nHA-VAN aerogels (Fig. 7.6b,d,f), suggesting that VAN incorporation did not induce relevant modifications in the porous structure of aerogels. Absence of relevant morphological changes due to VAN addition was also reported in chitosan-HA aerogels (Zhang et al., 2012). Finally, 3D-printed MC aerogels consisting of alternative layers containing two different VAN concentrations (5 and 15 wt.%) were successfully manufactured (MC VAN5/15) with a good textural performance. The low impact in the microstructure due to the customization of the drug concentration distribution within the scaffolds opens the possibility of developing specific gradient concentration profiles adapted to patient therapies necessities. Moreover, textural parameters after 7 months of storage had no relevant differences with respect to the same formulations evaluated just after their preparation (Table 7.5). SEM images still showed the dual porous structure essential for bone tissue engineering after storage in mild conditions (Fig. 7.5) and endorses the mid-term storage stability of MC and MC nHA 24 VAN 10 aerogels.

USC UNIVERSIDADE DE SANTIAGO DE COMPOSTELA

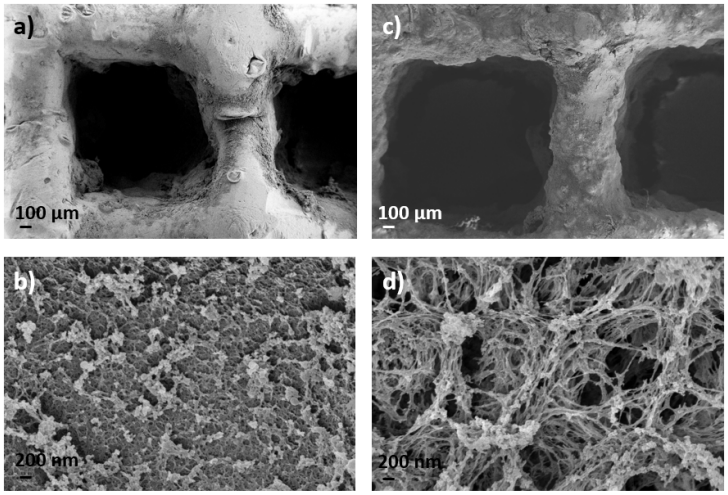


Figure 7.5. SEM images of aerogels after 7 months of storage. **a, b)** MC; **c, d)** MC nHA 24 VAN 10.

Table 7.5. Textural properties of VAN-loaded polysaccharide aerogels.

Aerogel scaffold	A_{BET} (m^2/g)	d_p (nm)	V_p (cm^3/g)
MC VAN 5	376 ± 19	17.1 ± 0.8	2.20 ± 0.11
MC VAN 10	374 ± 19	23.3 ± 1.2	2.75 ± 0.14
MC VAN 15	326 ± 16	24.6 ± 1.2	2.68 ± 0.13
MC VAN 5/15	174 ± 9	19.3 ± 1.0	1.12 ± 0.06
MC nHA 6 VAN 10	254 ± 13	17.0 ± 0.8	1.46 ± 0.07
MC nHA 12 VAN 10	163 ± 8	21.7 ± 1.1	1.20 ± 0.06
MC nHA 24 VAN 10	106 ± 5	23.1 ± 1.2	0.82 ± 0.04
MC 12 st	170 ± 9	17.4 ± 0.9	1.04 ± 0.05
MC 12 nHA 6 st	139 ± 7	18.8 ± 0.9	0.89 ± 0.04
MC 12 nHA 12 st	192 ± 10	20.9 ± 1.0	1.33 ± 0.07
MC 12 nHA 24 st	227 ± 11	23.5 ± 1.2	1.78 ± 0.09
MC 12 S	213 ± 11	22.4 ± 1.1	1.59 ± 0.08
MC nHA 24 VAN 10 S	93 ± 5	20.8 ± 1.0	0.66 ± 0.03

Notation: st: $scCO_2$ sterilized aerogels, S: aerogels after 7 months of storage, A_{BET}: BET-specific surface area, d_p: BJH-mean pore diameter, V_p: BJH-specific pore volume.

USC UNIVERSIDADE DE SANTIAGO DE COMPOSTELA

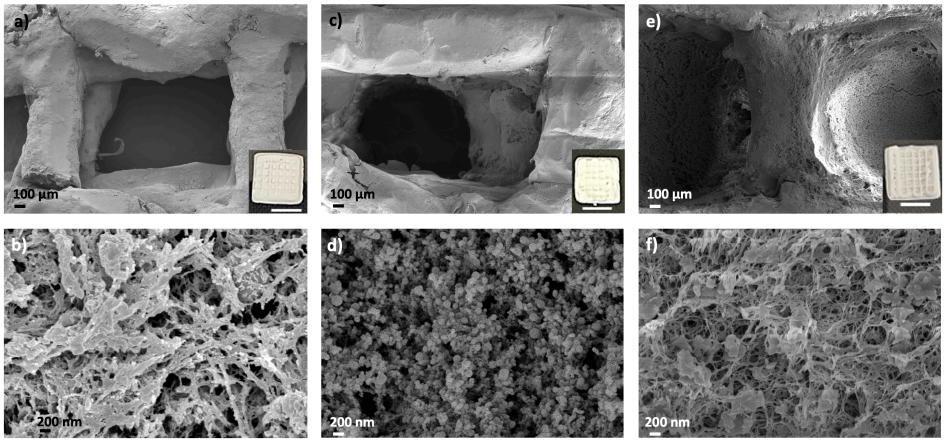


Figure 7.6. SEM images of MC nHA VAN aerogels. **a,b)** MC nHA 6 VAN 10; **c,d)** MC nHA 12 VAN 10; **e,f)** MC nHA 24 VAN 10. Intake in **a,c,e)** Visual appearance of the 3D-pattern of aerogels (scale bar: 1 cm).

The XRD diffractograms of aerogels (Fig. 7.7a) exhibit its amorphous nature with two amorphous halos (7-15 ° and 15-25 °) that could be attributed to the methylcellulose polymer network [33]. Similar XRD patterns were obtained for MC and MC VAN 10 aerogels, suggesting that the amorphous structure of aerogels did not change due to VAN incorporation. ATR/FT-IR spectroscopy was also performed to evaluate the effect of VAN incorporation on the chemical structure of aerogels. Interactions between aerogel components were observed in formulations loaded with VAN and/or nHA (Fig. 7.7b). Absorption bands detected at 3430 cm^{-1} and at 1631 cm^{-1} were assigned to hydroxyl groups and to H_2O, respectively, both present on nHA surface and previously described as essential for VAN bonding (Zhang et al., 2012). Absorption bands of the VAN are present on ATR/FT-IR spectra at 3450, 1654, 1540 and 1230 cm^{-1} due to hydroxyl stretching, C=O stretching, C=C and phenol groups. These bands were in the spectra of VAN raw powder as well as on VAN-loaded 3D-printed aerogels, thus confirming the effective incorporation of VAN on aerogels. Finally, three specific nHA bands were clearly detected in the region close to 600 cm^{-1} of nHA raw powder and nHA-loaded aerogels, thus confirming the correct incorporation of nHA after all processing steps into the 3D-printed aerogels.

USC UNIVERSIDADE DE SANTIAGO DE COMPOSTELA

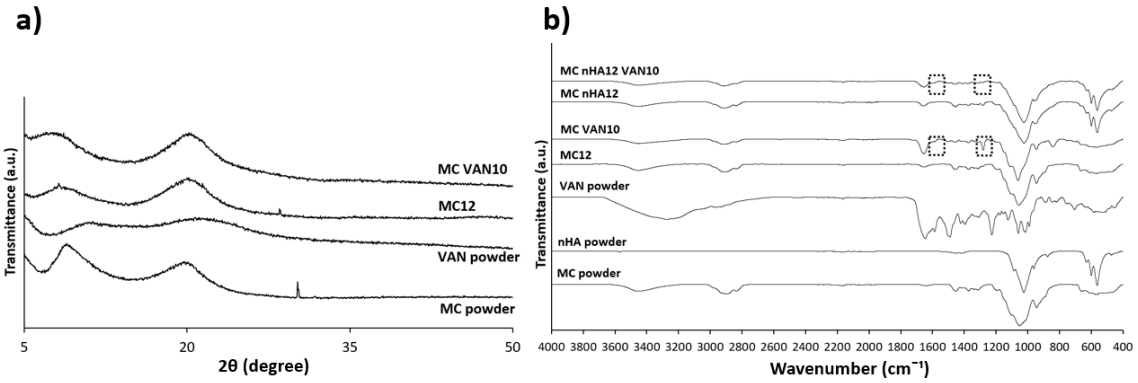


Figure 7.7. Physicochemical characterization of MC-aerogels. **a)** XRD patterns. **b)** ATR/FT-IR spectra of different aerogel formulations. Results from the raw materials (pure MC, nHA and VAN powders) are also included for the sake of comparison.

7.3.3. Printing fidelity evaluation

High printing fidelity was observed during the 3D-printing process (Fig. 7.1c) and after solvent exchange to EtOH (Fig. 7.1d). SFF is an index employed to assess the fidelity of 3D-printed structures with respect to the original CAD [34]. Highest SFF values for aerogels were found at highest nHA content ($p < 0.01$, Fig. 7.1e). Lower SFF was observed in aerogels with respect to the corresponding alcogels precursors, as also described for alginate-HA scaffolds [14]. Similar fidelity values were described for alginate-gelatin hydrogels, pointing out the high accuracy with respect to the CAD as well as the absence of a fidelity loss due to the solvent exchange [35]. Finally, SFF of MC nHA 24 alcogels is close to the described for cellulose hydrogels with similar cellulose content (12.5 %) but without nHA, thus indicating the lack of a negative impact on the printing fidelity due to nHA incorporation [34]. These results further endorse the choice for nHA.

USC UNIVERSIDADE DE SANTIAGO DE COMPOSTELA

7.3.4. Mechanical analysis

The compressive modulus of the 3D-printed biocomposites was greatly influenced by its composition, displaying best values with the highest nHA content in aerogels (Table 7.6). The internal friction between nHA and methylcellulose chains have previously resulted in the increment of E´ [36]. A similar trend was observed after quantifying energy dissipation by damping measurements (Fig. 7.1g), phenomena occurring also in natural bone [37]. Those data indicate a more elastic than viscous response with an increase in the inorganic content, tendency previously observed in the literature (Chen et al., 2019; Kumar et al., 2014). It is important to note that natural bone is also a viscoelastic material with moduli depending on frequency, behavior also displayed by aerogels formulations herein studied. Changes in bone damping factor are more relevant than changes in bone density as a consequence of strength because bone damping could attenuate locomotion impacts and it have been considered as indicative of integrity [37].

Table 7.6. E´, E´´, and tan δ at 1 Hz for aerogels with increasing nHA content.

Aerogel scaffold	tan δ	E´ (MPa)	E´´ (MPa)
MC 12	0.061 ± 0.002	7.8 ± 1.6	0.47 ± 0.09
MC nHA 6	0.089 ± 0.012	8.5 ± 2.7	0.75 ± 0.20
MC nHA 12	0.100 ± 0.009	13.2 ± 4.7	1.33 ± 0.52
MC nHA 24	0.131 ± 0.015	15.4 ± 3,2	2.06 ± 1.70

Notation: E´: storage modulus, E´´: loss modulus, damping ratio tan δ (E”/E’).

7.3.5. Bioactivity assessment

After 13 days in SBF, a smooth porous surface was observed in MC aerogels (Fig. 7.8a), whereas small apatite depositions in the granular form were found dispersed only in the surface of nHA-loaded aerogels (Fig. 7.8b,c,d,e,f). EDX spectrum of the granules present marked peaks for Ca, P and O (Fig. 7.8g, Spectrum 1) confirming the presence of apatite depositions, while different peaks were detected in other regions of the same formulation (Na, Cl and Ca; Fig. 7.8g, Spectrum 2). EDX spectrum for a wider region of nHA-loaded aerogels revealed peaks for Ca, P, O, Cl, K and Na (Fig. 7.8g, Spectrum 3), also described for alginate-cellulose scaffolds loaded with HA after

USC UNIVERSIDADE DE SANTIAGO DE COMPOSTELA

SBF immersion [30]. EDX mapping of nHA-loaded aerogels (Fig. 7.8h) and the high Ca/P molar ratio suggest a good integrity and bonding between the organic and inorganic aerogel components, as well as the stimulation of bone tissue formation and functionality.

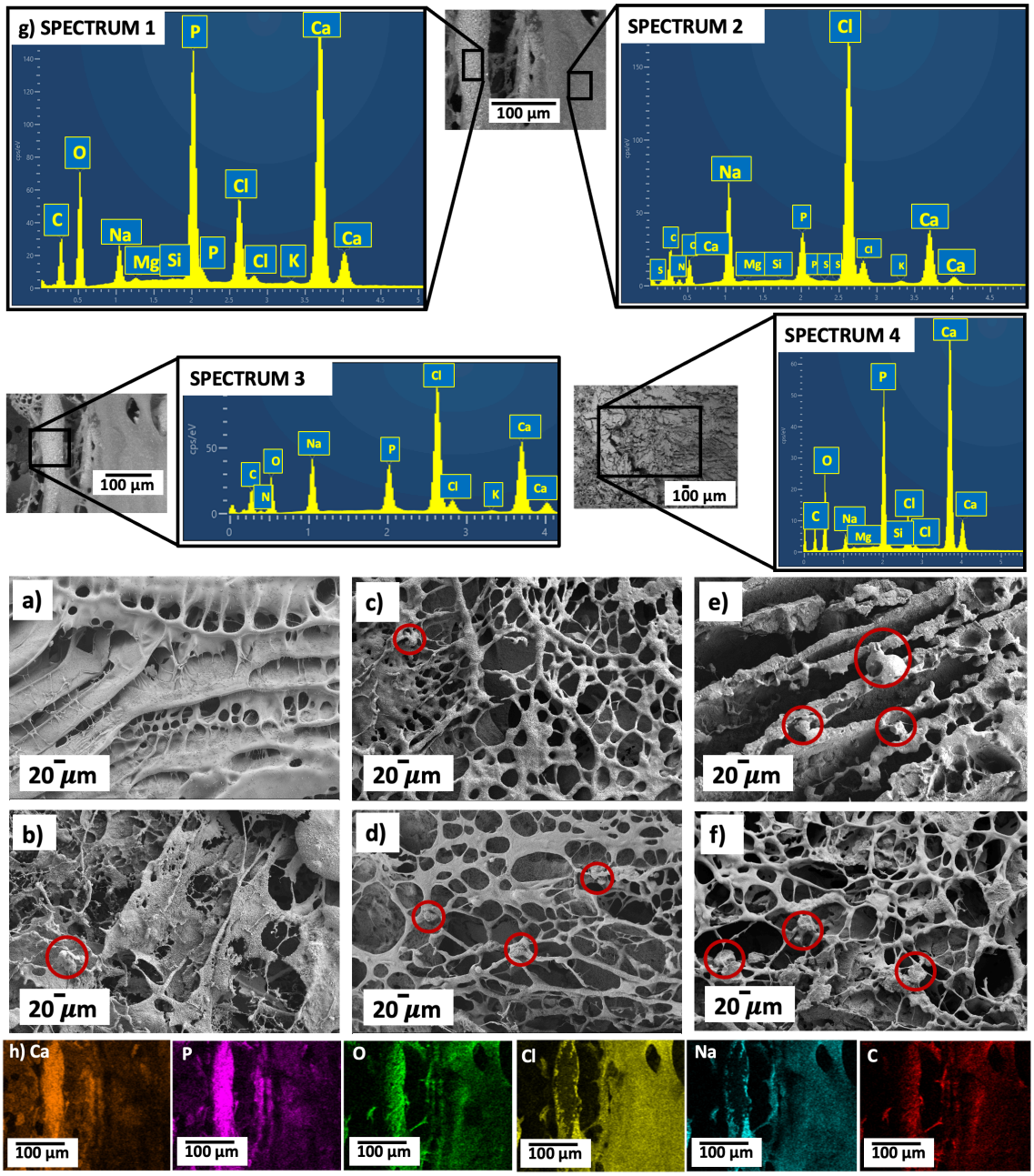


Figure 7.8. SEM pictures of different formulations of aerogels after bioactivity tests. **a)** MC; **b)** MC nHA 6; **c)** MC nHA 12; **d)** MC nHA 24 after 13 days of bioactivity tests. **e)** MC nHA 24; **f)** MC nHA 24 VAN 10 after 26 days of bioactivity tests. **g)** EDX spectra of MC nHA 12 aerogels after 13 days in SBF in an apatite deposition zone (Spectrum 1), in a background zone (Spectrum 2), in general (Spectrum 3) and of MC nHA 24 VAN10 aerogels after 26 days in SBF (Spectrum 4). **h)** EDX mapping of MC nHA 12 aerogels after 13 days in SBF. Red circles represent zones where the apatite depositions were detected by visual inspection.

USC UNIVERSIDADE DE SANTIAGO DE COMPOSTELA

Apatite depositions found in nHA-loaded aerogels increased in size and number after 26 days (Fig. 7.8e,f; red circles). This apatite layer covering aerogel surface in a flower-like morphology in formulations loaded with nHA was previously described in MC nHA composites and was related to the presence of bone-like apatite [40,41]. Change in intensity of Ca, P and O peaks (Fig. 7.8g, Spectrum 1) was very noticeable with respect to zones where apatite depositions were not found (i.e. without nHA) (Fig. 7.8g, Spectrum 2) endorsing that nHA presence clearly enhanced apatite formation. Aerogels exhibiting higher bioactivity (MC nHA24) were loaded with VAN for implement a strategy of advanced bone tissue engineering, combining bone infection treatment and tissue engineering simultaneously. MC nHA24 scaffolds show similar apatite depositions in number and size with (Fig. 7.8f) and without VAN (Fig. 7.8e) after immersion in SBF for 26 days. This finding indicates the absence of VAN interaction with the bioactivity process and suggests the suitability of this formulation for advanced bone tissue engineering.

7.3.6. VAN loading, entrapment yield, and release from aerogels

PBS was used as release medium to mimic the continuously renewed biological fluid [42]. VAN release tests (Fig. 7.9) exhibited a two-stage profile with a 3-day sustained release (Fig. 7.9a,c) occurring after an initial burst release (Fig. 7.9b,d) for all formulations. VAN minimum inhibitory concentration (MIC) against *S. aureus* is 2.0 μg/mL [42], so an effective VAN concentration was maintained for all formulations from the beginning of the drug release. Thereby, aerogels provided concentrations above MIC upon implantation, potentially preventing bacterial growth over time. Similar release profiles were found for VAN-loaded nanocellulose scaffolds [43] and chitosan-HA scaffolds [32]. Initial burst release was attributed to VAN release weakly adsorbed in the mesopores, while the subsequent slow VAN release was assigned to the strong interaction between the gel matrix and the VAN that retards the diffusion of the drug to the medium (Zhang et al., 2012).

USC UNIVERSIDADE DE SANTIAGO DE COMPOSTELA

VAN release profiles were similar regardless of the VAN content (Fig. 7.9). Interestingly, aerogels formed by alternative layers of different VAN content (MC VAN 5/15) showed a slower release than other aerogels of similar VAN content but with a homogeneous distribution of the drug (MC VAN 15). On the other hand, the comparison of the release profiles of MC nHA24 VAN10 and MC VAN10 aerogels (Fig. 7.9) unveiled that the presence of nHA seems to retard the VAN release from the scaffolds into the liquid medium.

High VAN entrapment yields were achieved (Table 7.7), indicating the suitability of the dual processing strategy to effectively load VAN in MC aerogels maybe due to the no necessity of a gelation bath in which VAN could be solubilized. All VAN release profiles fitted to the first-order pharmacokinetic model (Table 7.7), where the amount of drug released decreased with time and it is proportional to the amount of drug remaining in the matrix [44]. VAN dissolution in PBS medium is faster than the drug release from VAN-loaded aerogels, so aerogels promoted VAN sustained release. Similar release patterns were reported for VAN-loaded chitosan aerogels [45].

Table 7.7. VAN loading, entrapment yield and kinetic fitting parameters (k and R^2) of VAN release profiles of different aerogel formulations.

Aerogel formulation	Loading (%)	Entrapment yield (%)	k (h^{-1})	R^2
MC VAN 5	21.99 ± 0.04	74.78 ± 0.12	5.53 ± 1.25	0.90
MC VAN 10	30.71 ± 2.09	67.57 ± 4.61	4.32 ± 1.52	0.79
MC VAN 15	36.02 ± 1.55	64.84 ± 2.80	1.90 ± 0.60	0.83
MC VAN 5/15	34.77 ± 0.19	81.83 ± 0.44	2.94 ± 0.64	0.86
MC nHA 24 VAN 10	13.77 ± 4.25	63.36 ± 19.57	8.11 ± 1.25	0.92

USC UNIVERSIDADE DE SANTIAGO DE COMPOSTELA

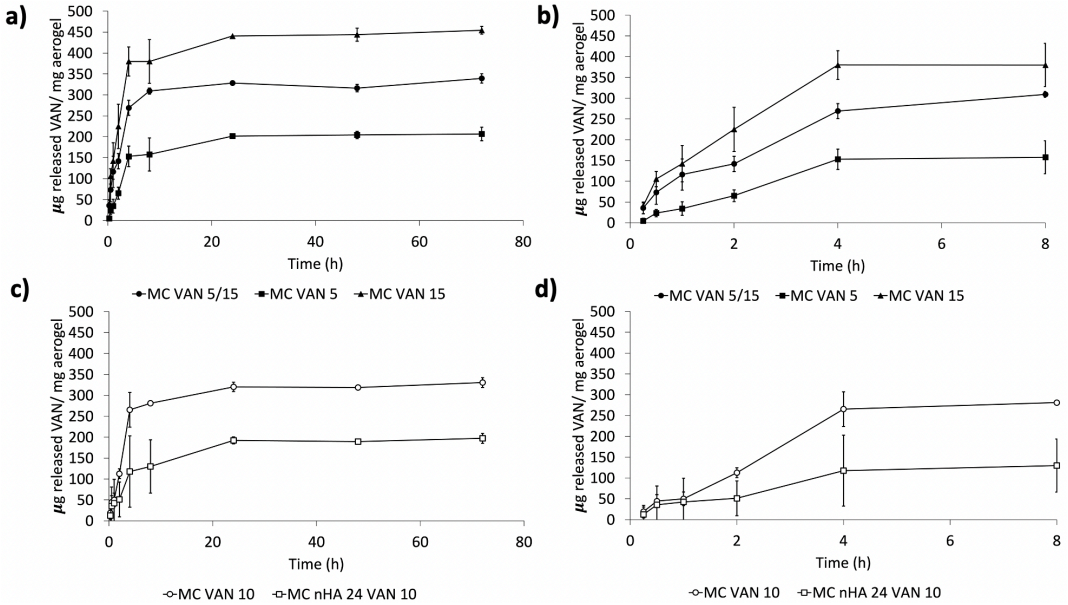


Figure 7.9. VAN release profile of different aerogel formulations in PBS pH 7.4, at 37 °C and 100 rpm. **a,b)** MC VAN 5/15, MC VAN 5, MC VAN 15. **c,d)** MC VAN 10, MC nHA 24 VAN 10.

7.3.7. Cytocompatibility tests

Good cytocompatibility was obtained for all formulations at different timepoints after contact with fibroblasts without statistically significant differences between aerogels and positive controls (Fig. 7.10a). Cell viability results are close to previously reported ones for 3D-printed MC structures after contact with NIH/3T3 cells for 24 and 48 h [26]. Similar cytocompatibility was also reported for composite scaffolds loaded with same VAN concentrations after 24 h in contact with mesenchymal stem cells [46], thus suggesting that the drug released from the matrix do not present an impact on cell survival. The high cell viability obtained suggest that neither aerogel composition (MC, nHA and/or VAN, at the component contents studied) nor material processing strategies (3D-printing and $scCO_2$ drying) compromised the cytocompatibility of 3D-printed aerogels [47].

USC UNIVERSIDADE DE SANTIAGO DE COMPOSTELA

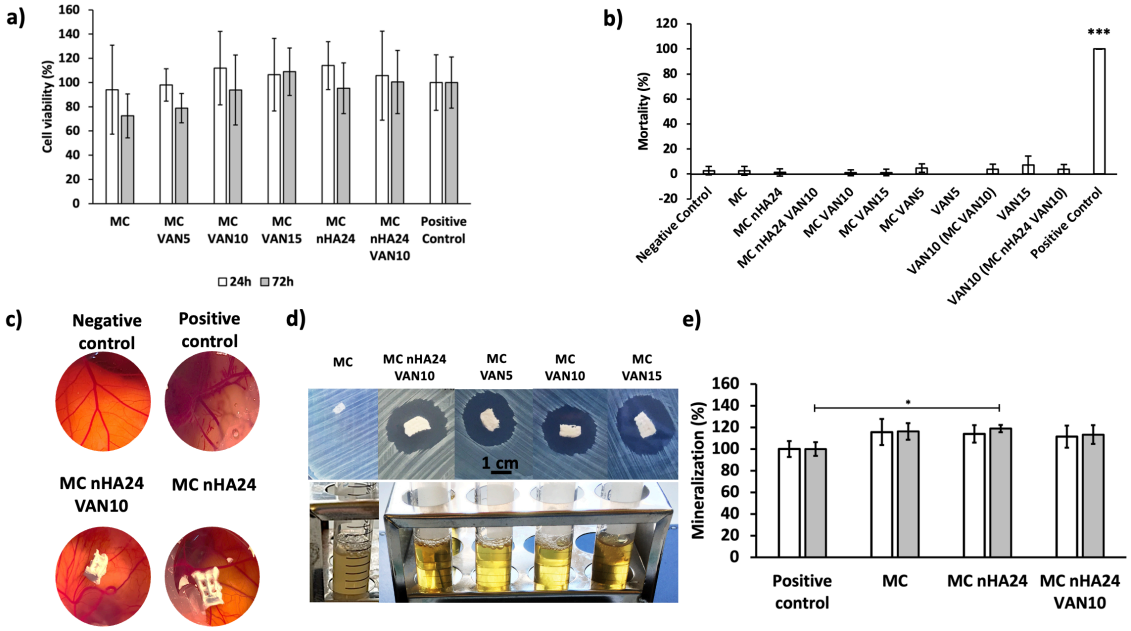


Figure 7.10. Biological evaluation of 3D-printed aerogel scaffolds. **a)** Cell viability tests of aerogels. Viability (%) of NIH/3T3 cells after 24 and 72 h of contact with scaffolds determined by the Resazurin cytotoxicity assay. There were no statistically significant differences among groups. **b)** HET-CAM test of aerogels. Negative control: 0.9 % (w/v) NaCl; positive control: 0.1 N NaOH. **c)** Mortality of *A. salina* after 24 h in contact with aerogels. Negative control: DMSO; positive control: artificial sea water. **d)** Aerogels after 24 h of culture on TSA plates (top) and on the corresponding TSB tubes (down) seeded with *S. aureus*. **e)** Mineralization values obtained after 14 and 21 days for different aerogel formulations by Alizarin red staining test. Post hoc Tukey HSD multiple comparison tests were performed and significant differences among groups were reported as * or *** for $p < 0.05$ or $p < 0.001$, respectively.

7.3.8. Safety tests using *A. salina* model

A. salina model is employed as a method to check the safety of aerogels [21]. Statistically significant differences were found between the mortality of *A. salina* due to 24 h of contact with aerogel formulations and the positive control (DMSO) (Fig. 7.10b). These results confirm the safety of VAN and/or nHA-loaded aerogels and are coherent with the ones previously reported for *A. salina* in contact with vancomycin, being VAN extremely toxic at 10 g/L (100 % mortality of *A. salina*) and moderately toxic or non-toxic at decreasing concentrations like the herein employed (1.8 – 3.9 g/ L) [48].

USC UNIVERSIDADE DE SANTIAGO DE COMPOSTELA

7.3.9. HET-CAM test

3D-printed aerogels were evaluated regarding their irritative potential for being used as medical devices by HET-CAM test [49]. No visual signs of hemorrhage or vascular lysis were observed after 5 min of aerogels contact with CAM, in contrast to the positive control where CAM vessels bleeding and clotting were clearly present (Fig. 7.10c). Close CAM structure was observed in negative controls and in CAM contacted with aerogels, suggesting the absence of impact in CAM morphology due to aerogels contact.

7.3.10. Antimicrobial assessment of 3D-printed aerogels

VAN-loaded aerogels were able to induce an inhibition zone in TSA plates seeded with *S. aureus* (Fig. 7.10d). The remarkable halos herein observed are more pronounced than the ones previously reported for other VAN-loaded scaffolds (Chen et al., 2019; Krishnan et al., 2020; Vismara et al., 2019), maybe due to the increased contact area of aerogel formulations with TSA plates. VAN-loaded aerogels also show absence of bacterial growth in TSB tubes (Fig. 7.10d) confirming the high potential of these formulations as effective antimicrobial composites against *S. aureus*. Scaffolds aimed at bone pathology effective treatment must have dual antibacterial properties: contact bactericidal ability and drug release from the material (an initial rapid bactericidal ability followed by a sustained antibacterial release to avoid infection recurrence) [51]. All VAN-loaded aerogels present contact bactericidal ability (Fig. 7.10d) and the initial and sustained antibiotic release (Fig. 7.9) critical for successful bone repair.

7.3.11. Mineralization assay

Alizarin red staining experiment was performed with relevant differences after 21 days of mineralization between the positive control (osteoblast-like cells, MC3T3 cells) and the cells in contact with MC nHA 24 aerogels (Fig. 7.10e). Significantly higher levels of calcium deposition ($p < 0.05$) were found for MC nHA 24 formulations thus suggesting the triggering of the mineralization process. Scaffolds with the same nHA content but also loaded with VAN (MC

nHA24 VAN10) had no relevant differences in the mineralization process with respect to the controls. This was related to a decrease in the early proliferation rate of bone marrow mesenchymal stem cells in the presence of VAN as previously reported in the 0−2000 μg/mL range [52–54]. Finally, scaffolds without nHA (MC in Fig. 7.10e) had no statistically significant influence on mineralization in comparison to the control, thus highlighting the key effect of nHA in the mineralization promotion. Results are coherent with previous studies where different biopolymers (regenerated cellulose, chitosan) induced mineralization after 14 and 21 days in culture with MC3T3 cells when nHA was incorporated in the formulation [55,56].

7.3.12. Sterility procedure evaluation

Sterility assurance levels (SAL 6) against bacterial endospores are required for biomaterials prior to be implanted [57]. Different processes have been employed for medical devices sterilization but most of them are not suitable for polymeric materials as they induce changes in important features like rheological properties or stability [10]. $scCO_2$ is effective for inhibiting bacterial growth arising as a green, rapid, and economic method adequate for biomaterials sterilization [58–60]. Cytoplasm and extracellular medium acidification due to CO_2 dissolution have been described as most important inactivation mechanisms of microorganisms due to the presence of $scCO_2$ [60].

No relevant changes in aerogels morphology, pore size and pore distribution were observed before (Fig. 7.2) and after $scCO_2$ sterilization (Fig. 7.11b,c,d,e). Adequate textural parameters for bone tissue engineering were obtained for sterilized aerogels (Table 7.5), with similar values with respect to the untreated ones (Table 7.4). Finally, aerogels were immersed in TSB tubes and put in contact with TSA plates to evaluate the bacterial growth on $scCO_2$ sterilized aerogel structures (Fig. 7.11a). After 24 h of culture, TSB medium was cultured in a TSA plate for 24 h and absence of bacterial growth was observed. Sterility of biomaterials was thus confirmed by both tests.

USC UNIVERSIDADE DE SANTIAGO DE COMPOSTELA

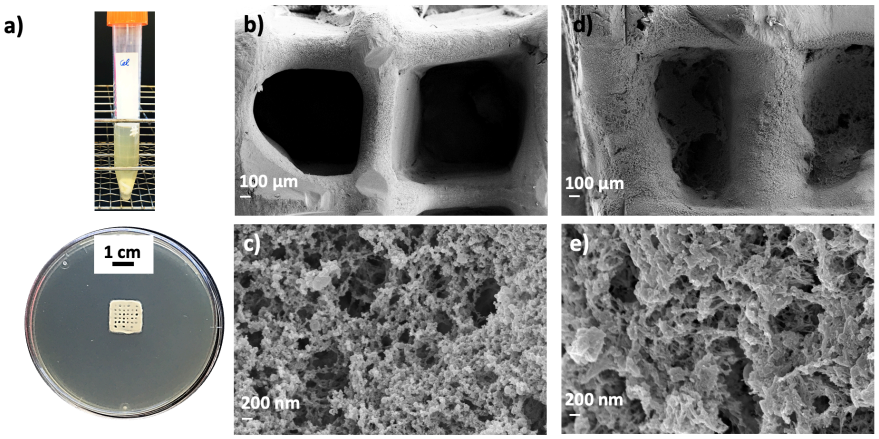


Figure 7.11. a) Microbiological tests of sterilized MC nHA24 aerogels seeded on TSB tubes (top) and on TSA plates (down) after 24 h of culture. No microbial growth was observed in none of the tested cases. **b-e)** SEM images of sterilized aerogels. **b,c)** MC; **d,e)** MC nHA 24.

7.4. Conclusions

VAN-loaded polymer-based bone scaffolds obtained by the combination of 3D-printing and aerogel technologies promise to promote bone defects repair while controlling bone infection progress in a personalized way. 3D-printed aerogels present excellent physicochemical performance (macro- and mesoporosity), high printing fidelity with respect to the original design and high drug entrapment yields, which endorse the suitability of this technological combination for the manufacturing of drug-loaded nanostructured scaffolds. Biological performances of aerogels containing nHA and/or VAN are very attractive for bone repair (high apatite mineralization appeared after bioactivity and alizarin red staining tests) and bone infection mitigation (two-stage VAN release profile providing drug therapeutic levels, and antimicrobial efficacy against *S. aureus*). *In vitro* assays in murine fibroblasts, *in vivo* tests in *A. salina* model and *in ovo* HET-CAM tests preliminarily revealed the safety of VAN-loaded aerogels. *In vivo* efficacy of the VAN-loaded aerogel scaffolds in bone infection treatments need to be evaluated. Sterilization of 3D-printed aerogels using $scCO_2$ as sterilant agent turn out to be very adequate, as it resulted in minor physicochemical changes of scaffolds. Furthermore, no relevant textural changes were observed in the scaffolds after 7 months of storage under mild conditions. Finally,

the absence of a negative impact in the microstructure due to the customization of the drug concentration distribution within the aerogels offer new personalized applications, e.g., scaffolds with patient specific external dimensions fitting the defect and with tailored gradient drug concentration profiles to optimize the long-term performance of aerogels.

7.5. References

1. Spellberg, B.; Lipsky, B.A. Systemic Antibiotic Therapy for Chronic Osteomyelitis in Adults. Clin. Infect. Dis. 2012, 54, 393–407, doi:10.1093/cid/cir842.
2. Trampuz, A.; Zimmerli, W. Diagnosis and Treatment of Implant-Associated Septic Arthritis and Osteomyelitis. Curr. Infect. Dis. Rep. 2008, 10, 394–403, doi:10.1007/s11908-008-0064-1.
3. Gallarate, M.; Chirio, D.; Chindamo, G.; Peira, E.; Sapino, S. Osteomyelitis: Focus on Conventional Treatments and Innovative Drug Delivery Systems. CDD 2021, 18, 532–545, doi:10.2174/1567201817666200915093224.
4. Poeppl, W.; Lingscheid, T.; Bernitzky, D.; Schwarze, U.Y.; Donath, O.; Perkmann, T.; Kozakowski, N.; Plasenzotti, R.; Reznicek, G.; Burgmann, H. Efficacy of Fosfomycin Compared to Vancomycin in Treatment of Implant-Associated Chronic Methicillin-Resistant Staphylococcus Aureus Osteomyelitis in Rats. Antimicrob. Agents Chemother. 2014, 58, 5111–5116, doi:10.1128/AAC.02720-13.
5. Barakat, A.; Schilling, W.HK.; Sharma, S.; Guryel, E.; Freeman, R. Chronic Osteomyelitis: A Review on Current Concepts and Trends in Treatment. Orthopaedics and Trauma 2019, 33, 181–187, doi:10.1016/j.mporth.2019.03.005.
6. Lv, X.-F.; Zhou, D.-M.; Sun, X.-H.; Zhao, Z. Nano Sized Hydroxyapatite-Polylactic Acid-Vancomycin in Alleviation of Chronic Osteomyelitis. DDDT 2022, Volume 16, 1983–1993, doi:10.2147/DDDT.S356257.
7. Shin, J.Y.; Yeo, Y.H.; Jeong, J.E.; Park, S.A.; Park, W.H. Dual-Crosslinked Methylcellulose Hydrogels for 3D Bioprinting Applications. Carbohydr. Polym. 2020, 238, 116192, doi:10.1016/j.carbpol.2020.116192.
8. Jiang, W.; Mei, H.; Zhao, S. Applications of 3D Bio-Printing in Tissue Engineering and Biomedicine. J. Biomed. Nanotechnol. 2021, 17, 989–1006, doi:10.1166/jbn.2021.3078.
9. Derakhshanfar, S.; Mbeleck, R.; Xu, K.; Zhang, X.; Zhong, W.; Xing, M. 3D Bioprinting for Biomedical Devices and Tissue Engineering: A Review of Recent Trends and Advances. Bioactive Materials 2018, 3, 144–156, doi:10.1016/j.bioactmat.2017.11.008.
10. Ahlfeld, T.; Guduric, V.; Duin, S.; Akkineni, A.R.; Schütz, K.; Kilian, D.; Emmermacher, J.; Cubo-Mateo, N.; Dani, S.; Witzleben, M. v.; et al. Methylcellulose – a Versatile Printing Material That Enables Biofabrication of Tissue Equivalents with High Shape Fidelity. Biomater. Sci. 2020, 8, 2102–2110, doi:10.1039/D0BM00027B.
11. Yahya, E.B.; Amirul, A.A.; H.P.S., A.K.; Olaiya, N.G.; Iqbal, M.O.; Jummaat, F.; A.K., A.S.; Adnan, A.S. Insights into the Role of Biopolymer Aerogel Scaffolds in Tissue Engineering and Regenerative Medicine. Polymers 2021, 13, 1612, doi:10.3390/polym13101612.
12. Tetik, H.; Wang, Y.; Sun, X.; Cao, D.; Shah, N.; Zhu, H.; Qian, F.; Lin, D. Additive Manufacturing of 3D Aerogels and Porous Scaffolds: A Review. Adv. Funct. Mater. 2021, 31, 2103410, doi:10.1002/adfm.202103410.
13. García-González, C.A.; Sosnik, A.; Kalmár, J.; De Marco, I.; Erkey, C.; Concheiro, A.; Alvarez-Lorenzo, C. Aerogels in Drug Delivery: From Design to Application. Journal of Controlled Release 2021, 332, 40–63, doi:10.1016/j.jconrel.2021.02.012.
14. Iglesias-Mejuto, A.; García-González, C.A. 3D-Printed Alginate-Hydroxyapatite Aerogel Scaffolds for Bone Tissue Engineering. Mater. Sci. Eng. C 2021, 131, 112525, doi:10.1016/j.msec.2021.112525.
15. Bernardes, B.G.; Del Gaudio, P.; Alves, P.; Costa, R.; García-Gonzaléz, C.A.; Oliveira, A.L. Bioaerogels: Promising Nanostructured Materials in Fluid Management, Healing and Regeneration of Wounds. Molecules 2021, 26, 3834, doi:10.3390/molecules26133834.
16. Ng, P.; Pinho, A.R.; Gomes, M.C.; Demidov, Y.; Krakor, E.; Grume, D.; Herb, M.; Lê, K.; Mano, J.; Mathur, S.; et al. Fabrication of Antibacterial, Osteo-Inductor 3D Printed Aerogel-Based Scaffolds by Incorporation

of Drug Laden Hollow Mesoporous Silica Microparticles into the Self-Assembled Silk Fibroin Biopolymer. Macromol. Biosci. 2022, 22, 2100442, doi:10.1002/mabi.202100442.
17. Iglesias-Mejuto, A.; García-González, C.A. 3D-Printed, Dual Crosslinked and Sterile Aerogel Scaffolds for Bone Tissue Engineering. Polymers 2022, 14, 1211, doi:10.3390/polym14061211.
18. Kohyama, K.; Morishima, Y.; Arisawa, K.; Arisawa, Y.; Kato, H. Immediate and Long-Term Results of Unsintered Hydroxyapatite and Poly L-Lactide Composite Sheets for Orbital Wall Fracture Reconstruction. JPRAS 2018, 71, 1069–1075, doi:10.1016/j.bjps.2018.03.006.
19. Kokubo, T.; Takadama, H. How Useful Is SBF in Predicting *in Vivo* Bone Bioactivity? Biomaterials 2006, 27, 2907–2915, doi:10.1016/j.biomaterials.2006.01.017.
20. Duarte, A.R.C.; Caridade, S.G.; Mano, J.F.; Reis, R.L. Processing of Novel Bioactive Polymeric Matrixes for Tissue Engineering Using Supercritical Fluid Technology. Mater. Sci. Eng. C 2009, 29, 2110–2115, doi:10.1016/j.msec.2009.04.012.
21. Ferreira-Gonçalves, T.; Iglesias-Mejuto, A.; Linhares, T.; Coelho, J.M.P.; Vieira, P.; Faísca, P.; Catarino, J.; Pinto, P.; Ferreira, D.; Ferreira, H.A.; et al. Biological Thermal Performance of Organic and Inorganic Aerogels as Patches for Photothermal Therapy. Gels 2022, 8, 485, doi:10.3390/gels8080485.
22. R. Hamidi, M.; Jovanova, B.; Kadifkova Panovska, T. Toxicological Evaluation of the Plant Products Using Brine Shrimp (Artemia Salina L.) Model. Maced. Pharm. Bull. 2014, 60, 9–18, doi:10.33320/maced.pharm.bull.2014.60.01.002.
23. Recommended Test Method Protocol: Hen's Egg Test – Chorioallantoic Membrane (HET-CAM) Test Method 2010.
24. Salerno, A.; Diéguez, S.; Diaz-Gomez, L.; Gómez-Amoza, J.L.; Magariños, B.; Concheiro, A.; Domingo, C.; Alvarez-Lorenzo, C.; García-González, C.A. Synthetic Scaffolds with Full Pore Interconnectivity for Bone Regeneration Prepared by Supercritical Foaming Using Advanced Biofunctional Plasticizers. Biofabrication 2017, 9, 035002, doi:10.1088/1758-5090/aa78c5.
25. Corker, A.; Ng, H.C.-H.; Poole, R.J.; García-Tuñón, E. 3D Printing with 2D Colloids: Designing Rheology Protocols to Predict 'Printability' of Soft-Materials. Soft Matter 2019, 15, 1444–1456, doi:10.1039/C8SM01936C.
26. Cochis, A.; Bonetti, L.; Sorrentino, R.; Contessi Negrini, N.; Grassi, F.; Leigheb, M.; Rimondini, L.; Farè, S. 3D Printing of Thermo-Responsive Methylcellulose Hydrogels for Cell-Sheet Engineering. Materials 2018, 11, 579, doi:10.3390/ma11040579.
27. Wang, Z.; Zhu, W.; Huang, R.; Zhang, Y.; Jia, C.; Zhao, H.; Chen, W.; Xue, Y. Fabrication and Characterization of Cellulose Nanofiber Aerogels Prepared via Two Different Drying Techniques. Polymers 2020, 12, 2583, doi:10.3390/polym12112583.
28. Chen, Z.-J.; Shi, H.-H.; Zheng, L.; Zhang, H.; Cha, Y.-Y.; Ruan, H.-X.; Zhang, Y.; Zhang, X.-C. A New Cancellous Bone Material of Silk Fibroin/Cellulose Dual Network Composite Aerogel Reinforced by Nano-Hydroxyapatite Filler. Int. J. Biol. Macromol. 2021, 182, 286–297, doi:10.1016/j.ijbiomac.2021.03.204.
29. Lin, R.; Li, A.; Lu, L.; Cao, Y. Preparation of Bulk Sodium Carboxymethyl Cellulose Aerogels with Tunable Morphology. Carbohydr. Polym. 2015, 118, 126–132, doi:10.1016/j.carbpol.2014.10.075.
30. Tohamy, K.M.; Soliman, I.E.; Mabrouk, M.; ElShebiney, S.; Beherei, H.H.; Aboelnasr, M.A.; Das, D.B. Novel Polysaccharide Hybrid Scaffold Loaded with Hydroxyapatite: Fabrication, Bioactivity, and *in Vivo* Study. Mater. Sci. Eng. C 2018, 93, 1–11, doi:10.1016/j.msec.2018.07.054.
31. Zhang, M.; Jiang, S.; Han, F.; Li, M.; Wang, N.; Liu, L. Anisotropic Cellulose Nanofiber/Chitosan Aerogel with Thermal Management and Oil Absorption Properties. Carbohydr. Polym. 2021, 264, 118033, doi:10.1016/j.carbpol.2021.118033.
32. Zhang, J.; Wang, C.; Wang, J.; Qu, Y.; Liu, G. *In Vivo* Drug Release and Antibacterial Properties of Vancomycin Loaded Hydroxyapatite/Chitosan Composite. Drug Delivery 2012, 19, 264–269, doi:10.3109/10717544.2012.704093.
33. Tohamy, K.M.; Mabrouk, M.; Soliman, I.E.; Beherei, H.H.; Aboelnasr, M.A. Novel Alginate/Hydroxyethyl Cellulose/Hydroxyapatite Composite Scaffold for Bone Regeneration: *In Vitro* Cell Viability and Proliferation of Human Mesenchymal Stem Cells. Int. J. Biol. Macromol. 2018, 112, 448–460, doi:10.1016/j.ijbiomac.2018.01.181.
34. Panraksa, P.; Udomsom, S.; Rachtanapun, P.; Chittasupho, C.; Ruksiriwanich, W.; Jantrawut, P. Hydroxypropyl Methylcellulose E15: A Hydrophilic Polymer for Fabrication of Orodispersible Film Using Syringe Extrusion 3D Printer. Polymers 2020, 12, 2666, doi:10.3390/polym12112666.
35. Giuseppe, M.D.; Law, N.; Webb, B.; A. Macrae, R.; Liew, L.J.; Sercombe, T.B.; Dilley, R.J.; Doyle, B.J. Mechanical Behaviour of Alginate-Gelatin Hydrogels for 3D Bioprinting. J. Mech. Behav. Biomed. Mater. 2018, 79, 150–157, doi:10.1016/j.jmbbm.2017.12.018.

36. Trakulsujaritchok, T.; Hourston, D.J. Damping Characteristics and Mechanical Properties of Silica Filled PUR/PEMA Simultaneous Interpenetrating Polymer Networks. Eur. Polym. J. 2006, 42, 2968–2976, doi:10.1016/j.eurpolymj.2006.07.028.
37. Buechner, P.M.; Lakes, R.S. Size Effects in the Elasticity and Viscoelasticity of Bone. Biomech. Model. Mechan. 2003, 1, 295–301, doi:10.1007/s10237-002-0026-8.
38. Kumar, A.; Negi, Y.S.; Choudhary, V.; Bhardwaj, N.K. Microstructural and Mechanical Properties of Porous Biocomposite Scaffolds Based on Polyvinyl Alcohol, Nano-Hydroxyapatite and Cellulose Nanocrystals. Cellulose 2014, 21, 3409–3426, doi:10.1007/s10570-014-0339-7.
39. Chen, S.; Shi, Y.; Zhang, X.; Ma, J. 3D Printed Hydroxyapatite Composite Scaffolds with Enhanced Mechanical Properties. Ceram. Int. 2019, 45, 10991–10996, doi:10.1016/j.ceramint.2019.02.182.
40. Valarmathi, N.; Sumathi, S. Zinc Substituted Hydroxyapatite/Silk Fiber/Methylcellulose Nanocomposite for Bone Tissue Engineering Applications. Int. J. Biol. Macromol. 2022, 214, 324–337, doi:10.1016/j.ijbiomac.2022.06.033.
41. Drouet, C. Apatite Formation: Why It May Not Work as Planned, and How to Conclusively Identify Apatite Compounds. BioMed Res. Int. 2013, 2013, 1–12, doi:10.1155/2013/490946.
42. Oungeun, P.; Rojanathanes, R.; Pinsornsak, P.; Wanichwecharungruang, S. Sustaining Antibiotic Release from a Poly(Methyl Methacrylate) Bone-Spacer. ACS Omega 2019, 4, 14860–14867, doi:10.1021/acsomega.9b01472.
43. Vismara, E.; Bernardi, A.; Bongio, C.; Farè, S.; Pappalardo, S.; Serafini, A.; Pollegioni, L.; Rosini, E.; Torri, G. Bacterial Nanocellulose and Its Surface Modification by Glycidyl Methacrylate and Ethylene Glycol Dimethacrylate. Incorporation of Vancomycin and Ciprofloxacin. Nanomaterials (Basel) 2019, 9, E1668, doi:10.3390/nano9121668.
44. López-Iglesias, C.; Quílez, C.; Barros, J.; Velasco, D.; Alvarez-Lorenzo, C.; Jorcano, J.L.; Monteiro, F.J.; García-González, C.A. Lidocaine-Loaded Solid Lipid Microparticles (SLMPs) Produced from Gas-Saturated Solutions for Wound Applications. Pharmaceutics 2020, 12, 870, doi:10.3390/pharmaceutics12090870.
45. López-Iglesias, C.; Barros, J.; Ardao, I.; Monteiro, F.J.; Alvarez-Lorenzo, C.; Gómez-Amoza, J.L.; García-González, C.A. Vancomycin-Loaded Chitosan Aerogel Particles for Chronic Wound Applications. Carbohydr. Polym. 2019, 204, 223–231, doi:10.1016/j.carbpol.2018.10.012.
46. Krishnan, A.G.; Biswas, R.; Menon, D.; Nair, M.B. Biodegradable Nanocomposite Fibrous Scaffold Mediated Local Delivery of Vancomycin for the Treatment of MRSA Infected Experimental Osteomyelitis. Biomater. Sci. 2020, 8, 2653–2665, doi:10.1039/D0BM00140F.
47. ISO 10993-5:2009 Biological Evaluation of Medical Devices — Part 5: Tests for *in Vitro* Cytotoxicity 2009.
48. Hernández Martínez, E.M.; Carrazana García, D. I.; González González, R.; García López, A.; Marrero Chang, O.; Águila Jiménez, E.; Morales Monteagudo, A.; López Hernández, Y. Ecotoxicidad Aguda En Physa Cubensis P. y Artemia Salina L. de 8 Antibacterianos Con Riesgo Ambiental. Rev. Toxicol. 2018, 34, 118–123.
49. Coelho, C.C.; Grenho, L.; Gomes, P.S.; Quadros, P.A.; Fernandes, M.H. Nano-Hydroxyapatite in Oral Care Cosmetics: Characterization and Cytotoxicity Assessment. Sci Rep 2019, 9, 11050, doi:10.1038/s41598-019-47491-z.
50. Chen, X.; Gao, C.; Jiang, J.; Wu, Y.; Zhu, P.; Chen, G. 3D Printed Porous PLA/nHA Composite Scaffolds with Enhanced Osteogenesis and Osteoconductivity *in Vivo* for Bone Regeneration. Biomed. Mater. 2019, 14, 065003, doi:10.1088/1748-605X/ab388d.
51. Fang, B.; Qiu, P.; Xia, C.; Cai, D.; Zhao, C.; Chen, Y.; Wang, H.; Liu, S.; Cheng, H.; Tang, Z.; et al. Extracellular Matrix Scaffold Crosslinked with Vancomycin for Multifunctional Antibacterial Bone Infection Therapy. Biomaterials 2021, 268, 120603, doi:10.1016/j.biomaterials.2020.120603.
52. Antoci, V.; Adams, C.S.; Hickok, N.J.; Shapiro, I.M.; Parvizi, J. Antibiotics for Local Delivery Systems Cause Skeletal Cell Toxicity *In Vitro*. Clin. Orthop. Relat. R. 2007, 462, 200–206, doi:10.1097/BLO.0b013e31811ff866.
53. García-González, C.A.; Barros, J.; Rey-Rico, A.; Redondo, P.; Gómez-Amoza, J.L.; Concheiro, A.; Alvarez-Lorenzo, C.; Monteiro, F.J. Antimicrobial Properties and Osteogenicity of Vancomycin-Loaded Synthetic Scaffolds Obtained by Supercritical Foaming. ACS Appl. Mater. Interfaces 2018, 10, 3349–3360, doi:10.1021/acsami.7b17375.
54. Mantripragada, V.P.; Jayasuriya, A.C. Effect of Dual Delivery of Antibiotics (Vancomycin and Cefazolin) and BMP-7 from Chitosan Microparticles on Staphylococcus Epidermidis and Pre-Osteoblasts *in Vitro*. Mater. Sci. Eng. C 2016, 67, 409–417, doi:10.1016/j.msec.2016.05.033.

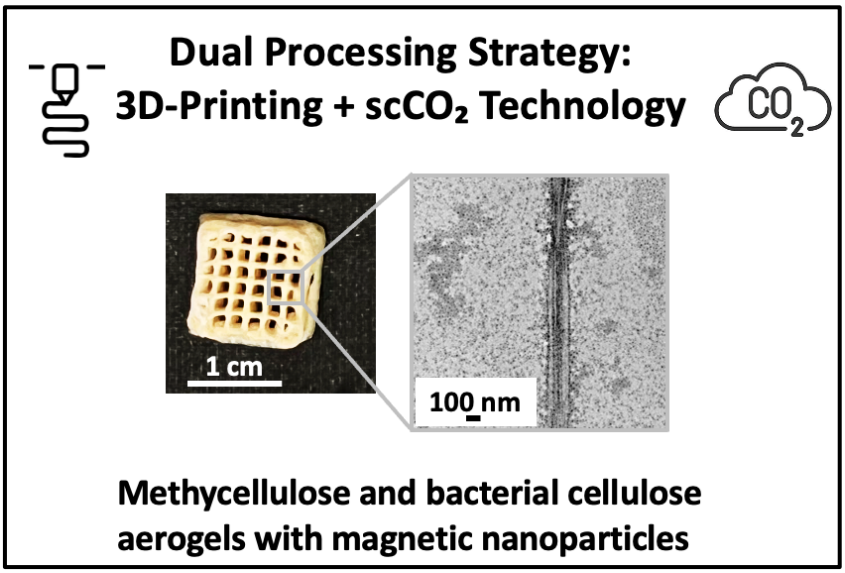
USC DE SANTIAGO

55. Maharjan, B.; Park, J.; Kaliannagounder, V.K.; Awasthi, G.P.; Joshi, M.K.; Park, C.H.; Kim, C.S. Regenerated Cellulose Nanofiber Reinforced Chitosan Hydrogel Scaffolds for Bone Tissue Engineering. Carbohydr. Polym. 2021, 251, 117023, doi:10.1016/j.carbpol.2020.117023.
56. Ryu, J.-H.; Kang, T.-Y.; Shin, H.; Kim, K.-M.; Hong, M.-H.; Kwon, J.-S. Osteogenic Properties of Novel Methylsulfonylmethane-Coated Hydroxyapatite Scaffold. IJMS 2020, 21, 8501, doi:10.3390/ijms21228501.
57. ISO 14937:2009 Sterilization of Health Care Products — General Requirements for Characterization of a Sterilizing Agent and the Development, Validation and Routine Control of a Sterilization Process for Medical Devices 2009.
58. Sun, Y.; Lovric, V.; Wang, T.; Oliver, R.A.; Walsh, W.R. Effects of $scCO_2$, Gamma Irradiation, and Sodium Dodecyl Sulfate Treatments on the Initial Properties of Tendon Allografts. IJMS 2020, 21, 1565, doi:10.3390/ijms21051565.
59. Ribeiro, N.; Soares, G.C.; Santos-Rosales, V.; Concheiro, A.; Alvarez-Lorenzo, C.; García-González, C.A.; Oliveira, A.L. A New Era for Sterilization Based on Supercritical CO_2 Technology. J. Biomed. Mater. Res. 2020, 108, 399–428, doi:10.1002/jbm.b.34398.
60. Spilimbergo, S.; Dehghani, F.; Bertucco, A.; Foster, N.R. Inactivation of Bacteria and Spores by Pulse Electric Field and High Pressure CO_2 at Low Temperature. Biotechnol. Bioeng. 2003, 82, 118–125, doi:10.1002/bit.10554.

USC UNIVERSIDADE DE SANTIAGO DE COMPOSTELA

USC
UNIVERSIDADE
DE SANTIAGO
DE COMPOSTELA

CHAPTER 8. CELLULOSE-IN-CELLULOSE 3D-PRINTED BIOAEROGELS FOR BONE TISSUE ENGINEERING



The content in this chapter was published in part in **A. Iglesias-Mejuto,** N. Malandain, T. Ferreira-Gonçalves, I. Ardao, C.P. Reis, A. Laromaine, A. Roig, C.A. García-González; Cellulose-in-cellulose 3D-printed bioaerogels for bone tissue engineering, in: Cellulose 31 (2024) 515–534. https://doi.org/10.1007/s10570-023-05601-1.

The work described in this chapter was carried out in collaboration with the Institut de Ciència de Materials de Barcelona (ICMABCSIC) and the University of Lisbon.

USC UNIVERSIDADE DE SANTIAGO DE COMPOSTELA

8.1. Introduction

Clinically treating large bone lesions resulting from tumor ablation, trauma, or bone fractures require autologous tissues, allografts, or bone graft substitutes for long-term regeneration [1]. Due to the limited availability of biological grafts and the increment in the morbidity associated with tissue transplants, emerging technologies are proliferating to fabricate bone tissue substitutes [2]. Biocompatible, highly porous, and hierarchical architectures capable of host blood-biomaterial interaction and harboring neo-tissue regeneration are critical factors when designing bone tissue substitutes [2,3].

Natural biopolymers and their derivatives (e.g., methylcellulose, hydroxypropyl cellulose, or hyaluronic acid) have often been used in bone tissue engineering because of their hydrophilicity, biocompatibility, and bioadhesiveness [4,5]. The incorporation of these biopolymers into scaffolds can improve the osseointegration, inflammation, and bone healing if adequately designed from the composition and morphological points of view [3,5]. Bioaerogels, i.e., aerogels obtained from natural polymers, are mesoporous and nanostructured materials with outstanding physicochemical performances and relevant properties for biomedical applications like biocompatibility or biodegradability [6–9]. The medical field quests to translate those requirements to 3D scaffolds with precise features and replication of functional human native systems [10]. Specifically, 3D printing technologies are being explored for bone lesion management to manufacture reproducible and scalable scaffolds with tunable physicochemical properties and patient-specific performances [11]. Macroporosity was thus conferred to bioaerogels in 3D-printed alginate-hydroxyapatite aerogel scaffolds resulting in excellent cyto- and hemocompatibility, bioactivity, and stable integrity [12]. The dual processing strategy used in that case combined the advantages of supercritical fluid technology, such as the nanostructuration of aerogels, with the customization related to the 3D-printed constructs [13]. The technological combination provides a materials processing solution aligned with circular economy principles since it minimizes waste production and valorizes a residue ($scCO_2$). This

USC UNIVERSIDADE DE SANTIAGO

environmentally friendly approach can be further endorsed if raw materials from sustainable sources are used [14]. Different bioaerogel composites such as silk fibroin/cellulose or gelatin/collagen have been studied for bone tissue engineering but so far, only silk fibroin and alginate-based aerogels have been successfully manufactured by 3D-printing for bone regeneration purposes [12,13,15–17].

Cellulose aerogels, also known as the third generation of aerogels, have demonstrated outstanding potential for bone tissue regeneration [18,19]. Namely, methylcellulose is a biocompatible polymer with high affinity to water molecules, resulting in highly viscous solutions with shear-thinning behavior, a key factor for 3D-printing [20]. The outstanding printability of methylcellulose-based inks results in end structures with a well-defined shape, following the initial CAD design and suitable for personalized medicine.

Bacterial cellulose (BC) is another important cellulosic material with attractive properties for biomedical applications [21,22]. Among those, BC has high crystallinity, high purity, excellent ability to retain water, and favorable mechanical performance. BC constitutes low-density hydrogels composed of nanocellulose fibrils (NF) secreted by bacteria like *Komagataeibacter xylinus* [23] from low molecular weight carbon sources, free of lignin and hemicellulose [18]. Nevertheless, the tight arrangement of BC nanofibers (NF) results in low printability when employed as the main component of 3D-printing inks [24]. Consequently, BC-NF have been successfully used with other polymers and nanomaterials as artificial scaffolds with enhanced mechanical performance [21,25]. Methylcellulose polymer was successfully employed to prevent the delamination and aggregation of nanocellulose [18]. Furthermore, BC-metal oxide hybrid nanomaterials have been synthesized to improve the physicochemical characteristics of BC [23,26]. Specifically, biocompatible SPIONs are one of the most prominent nanostructures, often incorporated into biomaterials to endow them with magnetic capability while enhancing their stability in physiological fluids for different tissue engineering applications [27–32]. SPIONs have also demonstrated to improve scaffold functionality and mechanical performance [31], to

USC UNIVERSIDADE DE SANTIAGO

confer anti-biofilm [33] and bacteriostatic properties [11], to improve *in vivo* imaging [34] and to elicit bone repair in tissue engineering [32].

The hypothesis of our work is that a new combination of methylcellulose and BC-NF in one single structure is feasible via a dual processing strategy comprising 3D-printing and supercritical fluid technologies and that the resulting cellulose-in-cellulose aerogels would have an enhanced structural resolution with high printing fidelities. Moreover, the use of BC-NF doped with SPIONs and blended with methylcellulose as aqueous inks to 3D-print gels should not modify the safety of the structures in terms of cell toxicity and hemolytic activity. After the 3D-printing of the wet gels, $scCO_2$ drying was then employed afterward to obtain the aerogels. The printability by rheological assays and the morphological properties by N_2 adsorption-desorption tests, SEM and TEM microscopies were used to assess the morphological and textural characteristics of the cellulose-in-cellulose 3D-printed aerogels. The magnetic performance of SPIONs-doped cellulose-in-cellulose aerogels was explored in view of potential tissue engineering applications. Bio- and hemocompatibility by *in vitro* and *in ovo* HET-CAM and a preliminary *in vivo* safety assessment based on *A. salina* were also carried out to unveil the biological performance of the scaffolds.

8.2. Materials and Methods

8.2.1. Materials

Methylcellulose (viscosity 15 cps, Mw 14 kDa, DS 1.5–1.9), citric acid monohydrate ($C_6H_8O_7 \cdot H_2O$), NaOH, iron (III) acetylacetonate ($Fe(acac)_3$, 97%), titanium (IV) butoxide (TBOT, 97%), oleyamine (OA, 70%), polyvinylpyrrolidone (PVP, Mw 10 kDa) were supplied by Sigma-Aldrich (Steinheim, Germany). CO_2 (purity >99.9%) was provided by Nippon Gases (Madrid, Spain) and absolute EtOH by VWR (Radnor, PA, USA). Water was purified by reverse osmosis (resistivity >18 MΩ·cm; Milli-Q, Millipore®, Madrid, Spain).

USC UNIVERSIDADE DE SANTIAGO DE COMPOSTELA

K. xylinus bacterial strain (NCIMB 5346) was supplied by the Spanish Type Culture Collection (CECT, Spain) and Hestrin-Schramm (HS) culture medium was prepared with dextrose, peptone, yeast extract by Condalab (Madrid, Spain), and sodium phosphate dodecahydrate, and citric acid monohydrate. Sodium hydroxide (NaOH) at 0.1 M was used for cleaning BC pellicles. *A. salina* eggs and artificial sea water salt for its growth were purchased from JBL GmbH and Co., KG (Neuhofen, Germany).

8.2.2. Preparation of BC-NF and SPIONs doped BC-NF

K. xylinus was grown in 5 mL of HS culture medium and incubated statically for 7 days at 30 °C [35]. 4 mL of bacterial broth was mixed with 56 mL of fresh HS medium and incubated at 30 °C for 5 days. BC pellicles were obtained, and posteriorly cleaned by immersion in 50% EtOH for 10 min, followed by two boiling steps in Milli-Q water for 20 min and twice in 0.1 M NaOH at 90 °C for 20 min. BC films were washed until pH was neutralized, and autoclaved in Milli-Q water at 121 °C for 30 min. Finally, BC pellicles were blended in 1 L of Milli-Q water for 10 min at the maximum speed of a commercial household blender (Jata electro Mod. BT1200, Tudela, Spain), obtaining BC-NF, which were then filtered with a Stericup Quick Release Filter Millipore with a PES membrane of 0.22 µm, autoclaved (121 °C, 30 min) and dispersed at 12 mg/mL in Milli-Q water.

BC-NF doped with SPIONs were synthesized by mixing 15 g of never-dried BC-NF with 40 mL of benzyl alcohol and 1100 mg of $Fe(acac)_3$ in a microwave vessel. After overnight incubation to allow the homogenization of reagents, the mixture was heated for 5 min at 60 °C (300 W) and 10 min at 210 °C (750 W) in a microwave oven (advanced flexible microwave synthesis platform from Milestone, Sorisole, Italy) operating at a frequency of 2.45 GHz and a maximum power of 750 W and 5 % agitation. Finally, BC-NF decorated with SPIONs were cooled down, filtered, cleaned twice with acetone and once with Milli-Q water, and autoclaved (121 °C for 20 min). The obtained solution was composed of BC-NF decorated with SPIONs and some unbonded SPIONs.

USC UNIVERSIDADE DE SANTIAGO

8.2.3. 3D-printing of cellulose-in-cellulose hydrogels

Aqueous 12 wt. % methylcellulose inks were firstly prepared, and then BC-NF suspensions (0.5, 1, 10, and 20 vol. %) doped or not with SPIONs were added to the methylcellulose inks under vigorous agitation (600 rpm) with a homogenizer (VWR vos 60, Radnor, PA, USA) for 1 h at RT. Inks were degassed for 10 min in a sonication bath (Branson 3510 Emerson, Ferguson, MO, USA) to eliminate air bubbles. 3D-printed hydrogels were obtained with a Cellink BIOX Bioprinter (Boston, MA, USA) employing an extrusion printhead at 40°C, 40 kPa and 3 mm/s, a 3-mL syringe, and a 410-µm nozzle. The resulting hydrogels had dimensions of 20 x 20 x 3 mm, a grid pattern, and 8 layers. Scaffolds were immersed in EtOH after the printing process to obtain alcogels.

8.2.4. Rheological evaluation of aqueous cellulose-in-cellulose inks

Flow behavior of the inks was recorded between 0.05 and 200 rad/s, at 20°C and at 40°C. Rheolyst AR-1000N rheometer (TA Instruments, Newcastle, UK) equipped with a Peltier plate and a cone geometry (40 mm diameter, 2°) with a solvent trap was employed. At least four replicates were evaluated for each ink formulation. The Equation 8.1 (power law mathematical regression model) was fitted to the linear region of the viscosity vs shear rate- curves.

$$\eta = b \cdot \gamma^{c} \qquad \textit{Equation 8.1}$$

where η is the viscosity, b and c are the shear-thinning coefficients (consistency and flow indices, respectively) and γ is the shear rate.

8.2.5. scCO$_2$ drying of cellulose-in-cellulose alcogels

Alcogels were immersed in EtOH and placed into a 100-mL stainless steel autoclave (Thar Process, Pittsburg, PA, USA). A CO_2 flow (6 g/min) was supplied to the autoclave at 120 bar and 40°C for 4 h. After CO_2 depressurization at a constant rate of 2 bar/min, aerogels were collected and stored at RT for further analysis. Aerogels were denoted as MC NF*x*-*y*; being *x* the content of BC-NF in the ink (0.5, 1, 10 or 20 vol.%), and *y* the concentration of the BC-NF suspension added (6 or 12 mg/mL) (Table 1). Aerogel formulations manufactured with BC-NF doped with

USC UNIVERSIDADE DE SANTIAGO DE COMPOSTELA

SPIONs were indicated by the suffix *S*. Aerogels prepared only with methylcellulose (i.e. without BC-NF) were obtained as controls and simply denoted as MC. Alternatively, hydrogel precursors were submitted to freeze drying (-80 °C, vacuum) to obtain cryogels or to traditional evaporative drying methods (ambient drying at RT or oven drying at 37°C) to obtain xerogels to compare the different gel drying methods. Finally, a thaw test was performed as reported elsewhere [25]. Hydrogels were frozen in liquid N_2 and thawed at RT to study the preservation of the macroscopical robustness.

Table 8.1. Cellulose-in-cellulose aerogel formulations studied. At least 6 replicates were used per aerogel formulation.

Aerogels	Ink composition			
	MC (wt. %)	NF (vol. %)	NF (mg/ mL)	SPIONs
MC	12	-	-	-
MC NF0.5-6	12	0.5	6	-
MC NF1-6	12	1	6	-
MC NF10-6	12	10	6	-
MC NF20-6	12	20	6	-
MC NF0.5-6 S	12	0.5	6	yes
MC NF1-6 S	12	1	6	yes
MC NF10-6 S	12	10	6	yes
MC NF0.5-12 S	12	0.5	12	yes
MC NF1-12 S	12	1	12	yes
MC NF10-12 S	12	10	12	yes

8.2.6. Physicochemical characterization of cellulose-in-cellulose aerogels

ρ_{skel} was obtained at RT and 1.01 bar using a helium pycnometer (Quantachrome, Boynton Beach, FL, USA) and measuring five replicates. ρ_{app} was calculated from Equation 8.2, while ε of scaffolds was determined employing Equation 8.3. Volume shrinkage (%) was also determined from the external dimensions of the structures before and after $scCO_2$ drying following Equation 8.4:

$$\rho_{app} = \frac{Aerogel\ mass}{Aerogel\ volume} \qquad \textit{Equation 8.2}$$

$$\varepsilon\ (\%) = \left[1 - \left(\frac{\rho app}{\rho skel}\right)\right] \cdot 100 \qquad \textit{Equation 8.3}$$

$$\textit{Volume shrinkage}\ (\%) = \left(\frac{Alcogel\ volume - Aerogel\ volume}{Alcogel\ volume}\right) \cdot 100 \qquad \textit{Equation 8.4}$$

USC UNIVERSIDADE DE SANTIAGO DE COMPOSTELA

Low-temperature N_2 adsorption–desorption analysis (ASAP 2000 Micromeritics Inc.; Norcross, GA, USA) was used to determine the textural parameters of the scaffolds. Aerogel samples were degassed under vacuum at RT for 24 h. A_{BET} of samples was obtained by the BET method. V_p, and d_p were calculated by BJH method from the desorption branch of the isotherm. Morphology of aerogels was analyzed by scanning and transmission electron microscopy (SEM, EVO LS15, Zeiss, Oberkochen, Germany; TEM, JEOL JEM-2010, JEOL, Tokyo, Japan -operating at 200 kV-). Aerogels were iridium-sputtered before being imaged by SEM, whereas phosphotungstic acid (aqueous 1%) was used as the staining solution of aerogels before TEM analysis. SEM-EDX and mapping of the chemical elements present in the aerogel scaffolds were also performed. Magnetic response of SPIONs trapped in aerogels was studied by Superconducting Quantum Interface Device analysis. Aerogels (0.5 x 0.5 x 0.3 cm^3) were placed in a plastic tube. Magnetization vs applied magnetic field was obtained in the -6/6 T range at 5 K (Quantum Design MPMS-3, VSM mode). Water contact angle was determined to evaluate the effect of SPIONs incorporation on the surface hydrophilicity. 9 µL of Milli-Q water were deposited on the surface of the aerogel scaffolds and the drop shape was recorded. The water contact angle was obtained using ImageJ software (2 measurements per replicate, 4 replicates per formulation). 4-month stability analysis of aerogels was performed by N_2 adsorption–desorption and SEM analysis after conservation of the structures at RT, protected from light and stored in closed plastic jars.

8.2.7. Printing fidelity tests

SFF for alcogels and aerogels was calculated from Equation 8.5. For SPIONs doped samples, further fidelity indexes (α, L, D, A) were calculated from Equations 8.6 to 8.9 [36].

$$SFF = \frac{Ai}{A} \qquad \textit{Equation 8.5}$$

where A_i is the alcogel or aerogel printed area, and A is the CAD area (printing file).

$$\alpha = \frac{angle\ between\ printed\ strands}{designed\ angle\ between\ printed\ strands} \qquad \textit{Equation 8.6}$$

$$L = \frac{length\ of\ printed\ strand}{length\ of\ designed\ strand} \qquad \textit{Equation 8.7}$$

USC UNIVERSIDADE DE SANTIAGO DE COMPOSTELA

$$D = \frac{diameter\ of\ printed\ strand}{diameter\ of\ designed\ strand} \qquad \textit{Equation 8.8}$$

$$A = \frac{area\ between\ printed\ strands}{designed\ area\ between\ printed\ strands} \qquad \textit{Equation 8.9}$$

8.2.8. Cytocompatibility tests

The resazurin (Sigma- Aldrich) conversion into resorufin by metabolically active cells was used to assess the cytocompatibility of aerogels. Viability after 24 and 72 h of mouse embryo fibroblasts (NIH/3T3) in contact with aerogels was evaluated. Cells at concentration of 12000 cells/cm^2 were seeded in 24-well plates with 600 µL of Dulbecco's Modified Eagle's Medium growth media supplemented with 10% bovine calf serum, penicillin 100 U/mL and streptomycin 100 g/mL and were incubated at 37 °C in a humidified atmosphere enriched with 5% CO_2. Aerogels (0.5 × 0.5 × 0.3 cm^3) were UV-sterilized for 30 min and placed in culture inserts. After 24 and 72 h of culture, scaffolds were removed, the growth medium was aspirated and 100 µL of 44 µM resazurin in fresh growth medium was added into each well. Resazurin solution alone was used as a blank. After 3 h of incubation under the same conditions, fluorescence was measured at an excitation wavelength of 544 nm and emission wavelength of 590 nm in a microplate reader (Infinite® M200, Tecan Group Ltd., Männedorf, Switzerland). Cells in the absence of aerogels were maintained at the same conditions to be used as positive controls and cells in contact with cisplatin 10 µM were used as negative controls. All tests were run in triplicate.

8.2.9. Hemolytic activity test

The hemolytic activity of aerogels was assessed using human blood (Galician Transfusion Center, Spain) obtained in accordance with the Declaration of Helsinki. Fresh human blood was diluted to 3% (v/v) in 0.9% (w/v) NaCl. 1 mL of diluted blood was transferred to Eppendorf tubes containing the aerogels (0.5 × 0.5 × 0.3 cm^3), 100 µL of 4% (v/v) Triton X-100 (positive control) or 100 µL of PBS pH 7.4 (negative control). Tests were carried out in triplicate. Samples were incubated for 60 min at 37 °C and 100 rpm and centrifuged at 10.000 g for 10 min (Sigma 2-16P, Sigma Laboratory Centrifuges, Osterode am Harz, Germany). 150 µL of supernatant were

USC UNIVERSIDADE DE SANTIAGO DE COMPOSTELA

transferred to a 96-well plate, and the absorbance of the haemoglobin was measured at λ = 540 nm (FLUOStar Optima, BMG Labtech, Ortenberg, Germany). Hemolysis was determined by Equation 8.10:

$$Hemolysis\ (\%) = \left(\frac{Abss - Absn}{Absp - Absn}\right) \cdot 100 \qquad Equation\ 8.10$$

where Abss is the absorbance of the samples containing the aerogels, Absn is the absorbance of the negative control, and Absp is the absorbance of the positive control.

8.2.10. HET-CAM test

Aerogels were evaluated by a HET-CAM test according to ICCVAM guidelines [37,38]. Fertilized hens' eggs (50–60 g, Coren, Ourense, Spain) were used after incubation at 37 °C in a 60% humidified atmosphere with an 8 h scheduled rotation (incubator Ineltec CC SR 0150, Barcelona, Spain). On day 9, a small window was opened to access the CAM and aerogels (0.5 × 0.5 × 0.3 cm^3) were placed there. 300 µL of 0.1 N NaOH or PBS pH 7.4 were put in contact with CAM as positive and negative controls, respectively. Each test was carried out in duplicate, and vessels of CAM were observed for 5 min after aerogels contact to evaluate the appearance of haemorrhage, vascular lysis, clotting, hyperemia, or changes in small vessel diameter of CAM by visual inspection.

8.2.11. Preliminary safety test

The safety of aerogels was evaluated by measuring the mortality of *A. salina* as a preliminary *in vivo* model [39,40]. Commercial seawater salt was dissolved in tap water according to supplier instructions, and *A. salina* eggs were left to hatch at 25-30 °C for 48 h, under aeration and illumination. 1 mL of seawater with 10-15 nauplii was transferred to a 24-well plate using six replicates per formulation. 100 µL of seawater salt was used as negative control and 100 µL of DMSO 100% was used as positive control. Nauplii in contact with aerogels (0.5 × 0.5 × 0.3 cm^3) were incubated for 24 h under the same conditions. Mortality was then calculated according to Equation 8.11. 100 µL of DMSO 100% was added to kill the remaining alive nauplii.

USC UNIVERSIDADE DE SANTIAGO DE COMPOSTELA

$$Mortality\ (\%) = \left(\frac{Dead\ 24\ h}{Dead\ total}\right) \cdot 100 \qquad Equation\ 8.11$$

Dead 24 h is the number of dead nauplii after 24 h of contact with aerogels and Dead total is the total number of nauplii per well, as counted in a magnifying glass.

8.2.12. scCO$_2$ sterilization of aerogels

Aerogels were placed into thermally sealed sterilization pouches in a high-pressure 600-mL autoclave (NovaGenesis, NovaSterilis Inc., Ithaca, NY, USA). 1200 ppm of H_2O_2 were introduced into the autoclave before pressurization with CO_2 until 100 bar at 40 °C. After 30 min contact time, the autoclave was depressurized at 5 bar/min. The texture and morphology of the sterilized aerogels were compared with the unsterilized formulations. Sterilized aerogel formulations were denoted with the *-st* suffix.

8.2.13. Statistical analysis

Results were reported as mean value ± standard deviation and post hoc Tukey HSD multiple comparison tests were performed to determine the statistical significance of differences between formulations concerning controls. Values of $p<0.05$ were considered statistically significant.

8.3. Results and discussion

8.3.1. Aerogel processing and printing fidelity assessment

Different nanocellulose-based biomaterials have previously displayed good printability and shear-thinning behavior under the applied pressures required for 3D-printing [41]. Cellulose-in-cellulose inks were herein homogeneously obtained with different proportions of BC-NF (Table 1). 3D-printing was performed without relevant clogging of the nozzle for the different formulations studied, thus allowing the incorporation of BC-NF concentrations as high as 20 vol.%. The rheological properties of the inks were analyzed by studying their viscosity *versus* shear rate sweep, simulating the extrusion-based 3D-printing process by rotational rheology [42]. Shear-thinning behavior was observed for all the formulations regardless the presence of SPIONs or the experimental temperature (Fig. 8.1a). Nevertheless, higher viscosities were

USC UNIVERSIDADE DE SANTIAGO

reached at higher printing temperatures (40°C) for all the formulations studied. This observation is coherent with the methylcellulose gelation at temperatures above RT, due to the methylcellulose thermal-responsiveness behavior [43,44]. The herein obtained shear-thinning effect was less accused in the case of pure methylcellulose inks and reached the highest viscosities for those inks containing the highest BC-NF concentration (MC NF10-12 S). A tighter arrangement of the BC-NF could explain this observation, which could increase the ink's viscosity when the BC-NF concentration rises. Furthermore, pseudoplastic behavior was displayed for all formulations tested (Fig. 8.1b), as non-linear behavior was observed between shear stress and shear rate especially at 40°C.

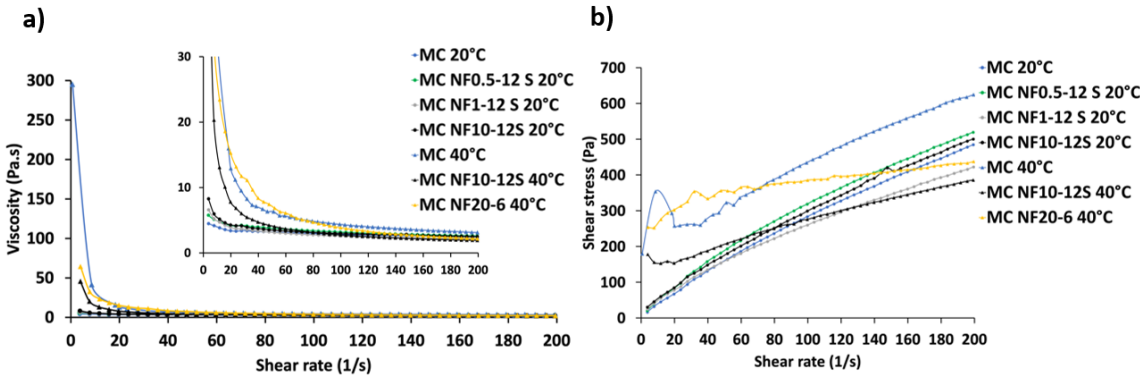


Figure 8.1. Rheological characteristics of different ink formulations. **a)** Overall viscosity variation with respect to the shear rate. **b)** Shear stress with respect to shear rate.

Rheological measurements were fitted to the power law equation (Equation 8.1). c values closer to zero (Table 2) were obtained when rheology experiments were performed at 40°C than at 20°C, thus suggesting a more pronounced shear-thinning behavior and consequently, a better performance for extrusion-based 3D-printing. Regarding b values, results show higher extrudability at lower temperature for both formulations, maybe due to the lower viscosities achieved by methylcellulose at lower temperatures (Fig. 8.1a).

USC UNIVERSIDADE DE SANTIAGO DE COMPOSTELA

Table 8.2. Shear-thinning coefficient values of inks calculated through power law model.

Aerogel formulations	20°C		40°C	
	b	c	b	c
MC	6.947	0.8033	61.74	0.4311
MC NF10-12 S	9.204	0.7562	49.98	0.3780

Notation: b and c are the shear-thinning coefficients (consistency and flow indices, respectively).

The 3D-printed gel scaffolds were firstly immersed in EtOH to obtain an alcogel, aerogel scaffolds were then produced after the supercritical drying of the alcogels. The overall process was evaluated regarding its reproducibility (Fig. 8.2a-d). Aerogels showed typical volume shrinkage values (50-60 %) for bioaerogels with no relevant differences between the aerogel formulations loaded and unloaded with BC-NF (Fig. 8.2a). SFF values of alcogels and aerogels were determined to study the printing fidelity. Alcogels loaded with different concentrations of BC-NF displayed similar SFF values while aerogels displayed higher SFF values at the highest BC-NF concentrations (Fig. 8.2b). Volume shrinkage of gels loaded with BC-NF and SPIONs was lower at the highest concentration of BC-NF, showing a significant decreasing tendency with increasing concentration of BC-NF doped with SPIONs (Fig. 8.2c). The presence of the nanofibers may split the total volume of the gel into interfibrillar subregions limiting the processing stresses and thus hindering the shrinkage of the gel [45]. In general, the presence of BC-NF in the aerogel scaffolds resulted in a better-defined 3D-printed pattern with respect to their non-BC-NF loaded counterparts. An enhancement in the printing fidelity was also observed due to the incorporation of increasing concentration of BC-NF doped with SPIONs into the aerogel structure (Fig. 8.2d). BC-NF also promoted shape fidelity and enhanced the reinforcement and 3D-printing resolution in silk fibroin scaffolds [46]. Similar SFF values were herein obtained with and without SPIONs, thus suggesting that the incorporation of SPIONs is not causing any negative impact on the printing fidelity of aerogels (Fig. 8.2b vs Fig. 8.2d).

The scaffolds containing BC-NF doped with SPIONs were selected for a complete printability study and further fidelity indexes were calculated (Fig. 8.2e). Angles and diameter of strands of scaffolds were printed with a high fidelity as compared to their computer-designed counterparts for all formulations with values close to one for α and D indexes. Area (A) and length (L) indexes

USC UNIVERSIDADE DE SANTIAGO DE COMPOSTELA

of the aerogels were lower than 0.4 and 0.7 respectively, due to the volume shrinkage of the 3D-printed gel after supercritical drying, showing the best values at intermediate concentrations of BC-NF doped with SPIONs.

Contact angle measurements have a strong correlation with the wettability of the surfaces [47]. Lower contact angles were obtained in aerogel surfaces when SPIONs were incorporated (Fig. 8.2f), possibly due to an increment in the surface roughness and in the hydrophobic behavior. Similar behavior were described for gelatin-based materials when iron oxide nanoparticles were incorporated [48] and silk-fibroin NF doped with SPIONs incorporated into scaffolds [49].

USC
UNIVERSIDADE DE SANTIAGO DE COMPOSTELA

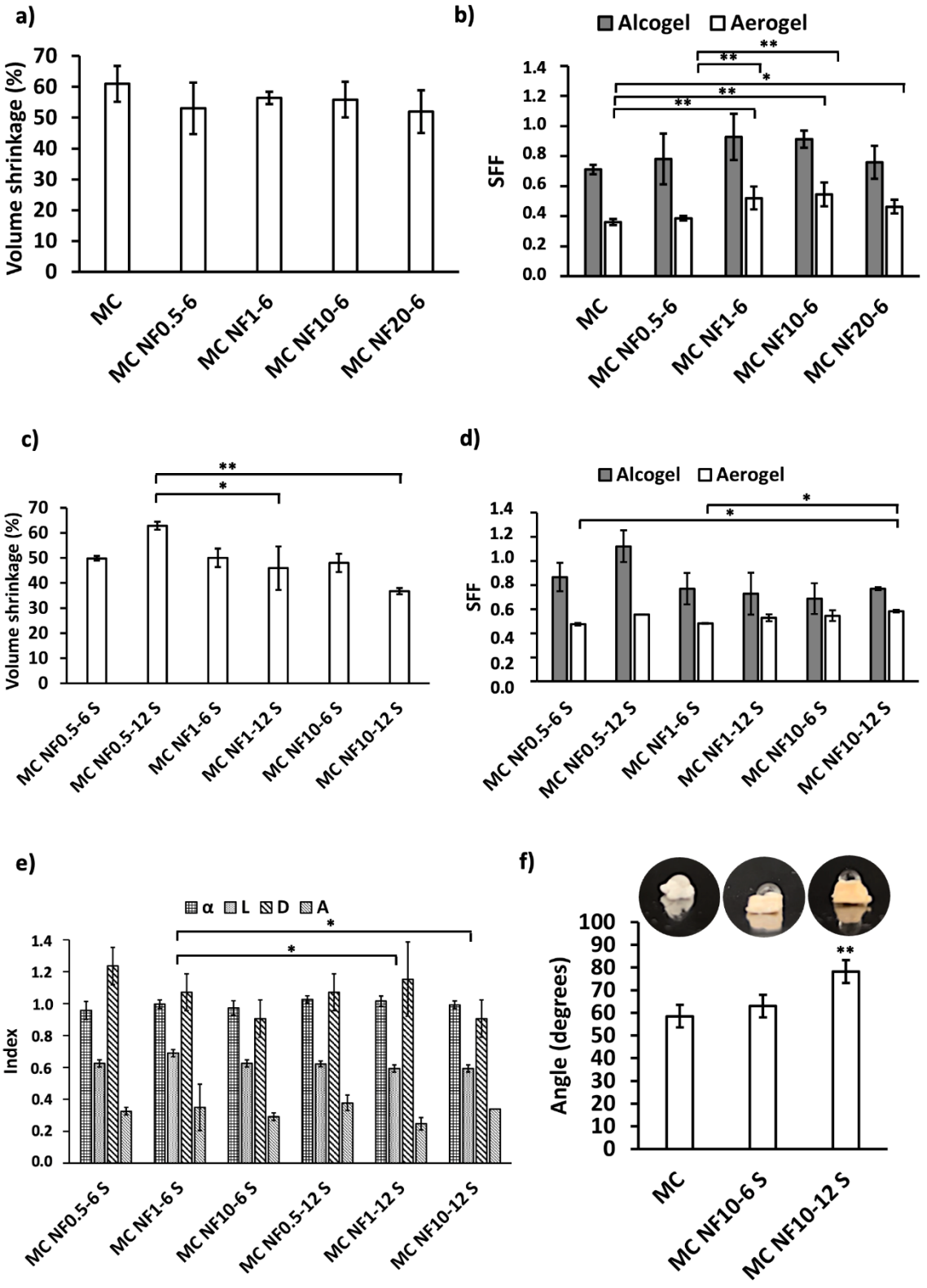


Figure 8.2. a) Volume shrinkage of aerogels prepared with increasing concentrations of BC-NF (0 – 20 vol.%). **b)** SFF of aerogels prepared with increasing concentrations of BC-NF (0 – 20 vol.%). **c)** Volume shrinkage of aerogels decorated with SPIONs. **d)** SFF of aerogels decorated with SPIONs. **e)** Printing fidelity indexes (α, L, D, A) of MC aerogels decorated with SPIONs. **f)** Contact angle measurements of aerogels decorated with SPIONs. Significant differences among groups were represented as * or ** (post hoc Tukey HSD multiple comparison test, $p < 0.05$ or $p < 0.01$, respectively).

USC UNIVERSIDADE DE SANTIAGO DE COMPOSTELA

8.3.2. Physicochemical characterization of cellulose-in-cellulose aerogels

Hierarchical porous methylcellulose aerogels with an open and interconnected porosity of different scale sizes were fabricated with and without BC-NF (Fig. 8.3). Visual observation of the aerogel formulations unveiled 3D-grid patterns with open macroporosities (Fig. 8.3, inserts). The highest structural resolution in visual appearance was observed for aerogels containing the highest amount of BC-NF (Fig. 8.3e vs Fig. 8.3a,c). The porosity of methylcellulose aerogels (ε in Table 8.3) was close to the previously reported nanocellulose synthesized by a similar procedure [50]. All aerogel formulations presented meso- and macropores within the filaments, but larger macropores were observed when BC-NF were incorporated (Fig. 8.3d,f vs Fig. 8.3b). Macropores are essential for tissue engineering applications, specifically, the presence of pores between 10 and 20 μm were related to cell infiltration [46], as the herein observed inside the printed filaments when BC-NF were incorporated into aerogels. Macropores between 100 and 600 μm found between printed strands are linked to good nutrient supply. The open porous and hierarchical structure with meso- and macropores of aerogels with BC-NF (Fig. 8.3d,f), was previously associated with BC-NF based biomaterials [50].

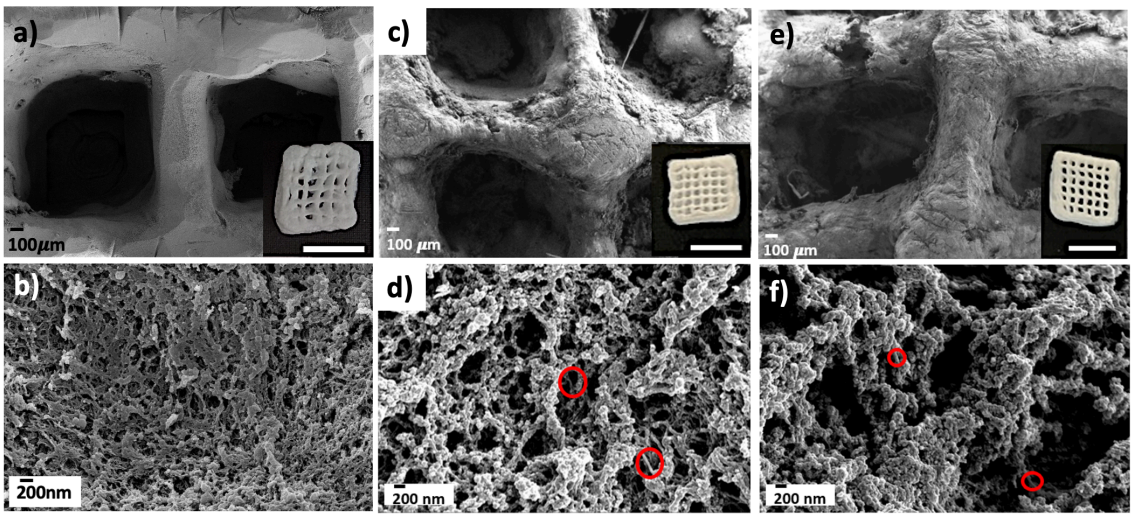


Figure 8.3. SEM pictures of cellulose-in-cellulose aerogels. **a,b)** MC; **c,d)** MC NF0.5-6; **e,f)** MC NF20-6. Aerogels imaged at two different magnifications. Inserts in **a,c,e)** Visual appearance of the aerogel scaffolds (scale bar: 1 cm). Red circles represent zones where the presence of BC-NF was detected by visual inspection.

USC UNIVERSIDADE DE SANTIAGO DE COMPOSTELA

Similar porosity (ε, 80-85%) was obtained for the different aerogel formulations studied (Table 8.3). Similar values (80%) were also reported for BC-NF scaffolds [51]. The tight arrangement described for BC-NF may help maintain the aerogel structure without modifying their porosity. The apparent density of the aerogels significantly changed when BC-NF were incorporated into the scaffolds once a threshold BC-NF concentration value (above 0.5 vol.%) was used. These results are coherent with the observed decreasing tendency in volume shrinkage of gels when BC-NF were incorporated at higher concentration (12 mg/mL) in higher volumes (0.5 vs 1-10 vol. %) (Fig. 8.2c). The increase in mass with the addition of the nanofibers was compensated by the lower shrinkage in volume of the gels resulting in lower apparent densities of aerogels, as similarly reported for certain fiber-reinforced aerogels in the literature [45].

The specific surface area and pore volume were similar for all the formulations studied, suggesting that incorporating BC-NF into the structures did not have any detrimental effect on the textural properties of the aerogels. Indeed, an important increase in the specific pore volume of ca. 35% was observed for the scaffolds with the highest concentration of BC-NF. Similar BET surface area (241 m^2/g) and interconnected nanostructure were described for BC-NF loaded glass scaffolds, but with lower pore volumes (0.33 cm^3/g) [52].

Table 8.3. Textural properties of cellulose-in-cellulose aerogels.

Aerogel scaffold	A_{BET} (m^2/g)	d_p (nm)	V_p (cm^3/g)	ρ_{app} (g/cm^3)	ρ_{skel} (g/cm^3)	ε (%)
MC	268 ± 13	19 ± 1	1.71 ± 0.09	0.18 ± 0.04[a]	1.35 ± 0.03	87 ± 3
MC NF0.5-6	241 ± 12	22 ± 1	1.77 ± 0.09	0.19 ± 0.03[a]	1.27 ± 0.03	85 ± 2
MC NF1-6	237 ± 12	22 ± 1	1.75 ± 0.09	0.12 ± 0.02[b]	1.12 ± 0.03	83 ± 2
MC NF10-6	256 ± 13	21 ± 1	1.83 ± 0.09	0.13 ± 0.02[b]	1.23 ± 0.03	84 ± 2
MC NF20-6	283 ± 14	25 ± 1	2.37 ± 0.12	0.13 ± 0.01[b]	1.22 ± 0.02	84 ± 2
MC st	171 ± 9	17 ± 1	1.04 ± 0.05	0.19 ± 0.01	1.45 ± 0.02	85 ± 1
MC NF0.5-6 st	154 ± 8	19 ± 1	1.00 ± 0.05	0.22 ± 0.01	1.30 ± 0.09	83± 1
MC NF1-6 st	188 ± 9	20 ± 1	1.25 ± 0.06	0.23 ± 0.03	1.16 ± 0.02	80 ± 2
MC NF10-6 st	197 ± 10	17± 1	1.13 ± 0.06	0.20 ± 0.03	1.27 ± 0.02	84 ± 2
MC NF20-6 st	238 ± 12	23 ± 1	1.76 ± 0.09	0.18 ± 0.02	0.80 ± 0.08	77 ± 3

Equal letter (a or b) denotes statistically homogeneous group (ANOVA Tukey's test, $p < 0.05$). **Notation:** st: $scCO_2$ sterilized samples, A_{BET}: BET-specific surface area, d_p: BJH-mean pore diameter, V_p: BJH-specific pore volume, ρ_{app}: apparent density, ρ_{skel}: skeletal density, ε: scaffold porosity.

USC UNIVERSIDADE DE SANTIAGO DE COMPOSTELA

BC-NF decorated with SPIONs were homogeneously incorporated in the aerogel structures resulting in a change of color of the printed aerogels from white to orange when SPIONs were

present. BC-NF doped with SPIONs were randomly distributed throughout the porous structure of the matrix (Fig. 8.4b,c) with similar nanofibrillar organization in the material to aerogels containing BC-NF without SPIONs (Fig. 8.4a) and to other scaffolds with BC-NF [53]. EDX spectra of the aerogels confirmed the presence of SPIONs in the scaffolds (Fig. 8.4). Accordingly, no Fe peaks were observed when SPIONs were not added (Fig. 8.4a), while these peaks appeared when SPIONs were incorporated at a low (Fig. 8.4b) or a high (Fig. 8.4c) concentration. Furthermore, the mapping of the chemical elements in the aerogels confirmed the presence of Fe homogeneously distributed throughout the aerogel structure due to SPIONs doping (Fig. 8.4d). SEM image of the zone where the mapping was performed shows also white granules that could be due to SPIONs aggregates in the scaffold, similarly to those previously described for pectin aerogels monoliths [54].

USC
UNIVERSIDADE DE SANTIAGO DE COMPOSTELA

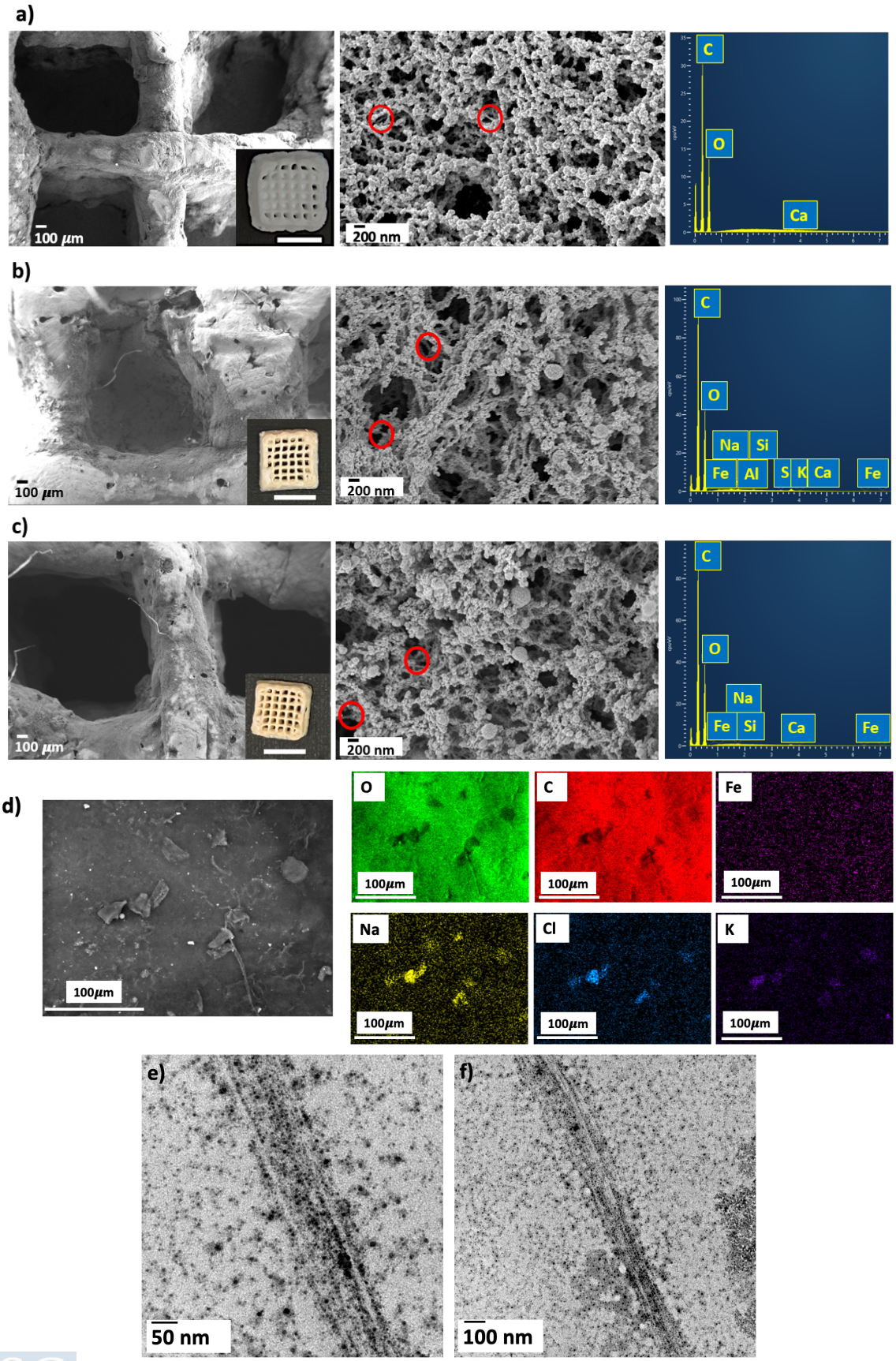


Figure 8.4. SEM images (left and middle) and EDX spectra (right) of different cellulose-in-cellulose aerogels. **a)** MC NF10-6; **b)** MC NF10-6 S; **c)** MC NF10-12 S. **d)** SEM image and mapping of the chemical elements present in MC NF10-12 S aerogels. Inserts: visual appearance of the aerogel scaffolds (scale bar: 1 cm). Red circles represent zones where the presence of BC-NF was detected by visual inspection.

e,f) TEM images of cellulose-in-cellulose aerogels (MC NF10-12 mg/ mL S) observed at two different magnifications. Black dots in TEM images are probably due to the formation of SPIONs clusters and their accumulation in the aerogels.

The presence of BC-NF in the aerogels and the preservation of their integrity after all the processing steps were also confirmed by TEM imaging (Fig. 8.4e,f), where the BC-NF had diameters very close to those measured by SEM imaging (42 $\pm$ 7 nm vs 46 $\pm$ 8 nm). SPIONs in aerogels (Fig. 8.4e,f) have a size and morphology coherent with previous measurements of SPIONs not incorporated into aerogels (12 ± 2 nm) thus indicating the stability of the nanoparticles after the dual processing strategy.

The dual porous structure of the 3D-printed structures was preserved for BC-NF doped SPIONs aerogels (Fig. 8.4b,c). No relevant differences were observed regarding the textural properties of different SPIONs-decorated aerogels (Table 8.4), thus suggesting the lack of effect of incorporating SPIONs in the aerogel structure. An important improvement in the BET surface area was herein reported with respect to previous magnetite aerogels obtained by supercritical drying (120 m^2/g) [55]. The morphology of these aerogels can only be obtained when the supercritical drying method was used, regardless the selected printed pattern or external shape (Fig. 8.5a,b,c). Using other drying methods, the shape was not maintained (Fig. 8.5d,e,f), and the textural parameters dramatically decreased after ambient, oven or freeze drying of hydrogel scaffolds (A_{BET} for cryogels and xerogels were below de detection limit, i.e. < 5 m^2/g). In the case of freeze-dried gels (i.e. cryogels), the interfibrillar macroporosity was lost and several cracks appeared along the structure (Fig. 8.5d). After ambient and oven dried gels, a dramatic volume shrinkage (*ca.* 90%) and, in the case of presence of SPIONs, a darker color were obtained (Fig. 8.5e,f). These results are coherent with those obtained for other polysaccharide cryogels and xerogels [56,57] and confirm that ambient, oven or freeze drying are inadequate methods to obtain the advanced textural performance essential for bone tissue engineering. Also, hydrogels were frozen in liquid N_2 and thawed at RT. After freezing, only the external shape was preserved but not the 3D-printed pattern (Fig. 8.5g). Consequently, after thawing at RT the 3D-printed

USC UNIVERSIDADE DE SANTIAGO

hydrogel did not return into their initial morphology (Fig. 8.5h), thus suggesting that this procedure was not adequate to preserve the robustness and the advanced 3D-printed structure. Hydrogels without an internal 3D-printed pattern have previously maintained their external shape after freezing in liquid N_2 [25].

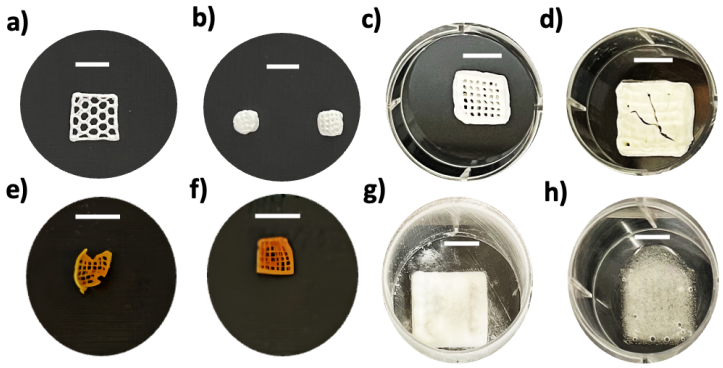


Figure 8.5. Effect of drying method for cellulose-in-cellulose formulations on the resulting cellulose-in-cellulose-dried gels. **a,b,c)** MC NF20-6 aerogel obtained after $scCO_2$ drying. **d)** MC NF20-6 cryogel obtained after freeze drying. **e)** MC NF10-6 S xerogel obtained after ambient drying at RT. **f)** MC NF10-6 S xerogel obtained after oven drying at 37°C. **g)** MC NF20-6 hydrogel just after freezing in liquid N_2. **h)** MC NF20-6 hydrogel after thawing at RT. Scale bar: 1 cm.

Table 8.4. Textural properties of cellulose-in-cellulose aerogels.

Aerogel scaffold	A_{BET} (m^2/g)	d_p (nm)	V_p (cm^3/g)
MC NF0.5-6 S	229 ± 11	19± 1	1.49 ± 0.07
MC NF1-6 S	235 ± 12	21 ± 1	1.63 ± 0.08
MC NF10-6 S	250 ± 13	20 ± 1	1.65 ± 0.08
MC NF0.5-12 S	221 ± 11	19 ± 1	1.46 ± 0.07
MC NF1-12 S	245 ± 12	21 ± 1	1.71 ± 0.09
MC NF10-12 S	209 ± 11	19 ± 1	1.30 ± 0.07

Notation: A_{BET}: BET-specific surface area, d_p: BJH-mean pore diameter, V_p: BJH-specific pore volume.

No relevant changes in terms of textural properties were observed after storage of different aerogel formulations in closed plastic jars for 4 months (Table 8.5). Moreover, the high structural resolution was preserved after this time period (Fig. 8.6a,c) as well as the dual porous structure with the BC-NF randomly distributed on it (Fig. 8.6b,d). All these results suggest the preliminary stability at RT of the 3D-printed cellulose-in-cellulose aerogels with and without SPIONs.

USC UNIVERSIDADE DE SANTIAGO DE COMPOSTELA

Table 8.5. Textural properties of cellulose-in-cellulose aerogels after 4 months of storage.

Aerogel scaffold	A_{BET} (m^2/g)	d_p (nm)	V_p (cm^3/g)
MC	273 ± 14	18 ± 1	1.66 ± 0.08
MC NF0.5-6 S	164 ± 8	18 ± 1	1.01 ± 0.05
MC NF1-6 S	295 ± 15	19 ± 1	1.79 ± 0.09
MC NF10-6 S	229 ± 11	18 ± 1	1.35 ± 0.07
MC NF0.5-12 S	259 ± 13	14 ± 1	1.13 ± 0.06
MC NF1-12 S	230 ± 12	21 ± 1	1.57 ± 0.08
MC NF10-12 S	206 ± 10	21 ± 1	1.41 ± 0.07

Notation: A_{BET}: BET-specific surface area, d_p: BJH-mean pore diameter, V_p: BJH-specific pore volume.

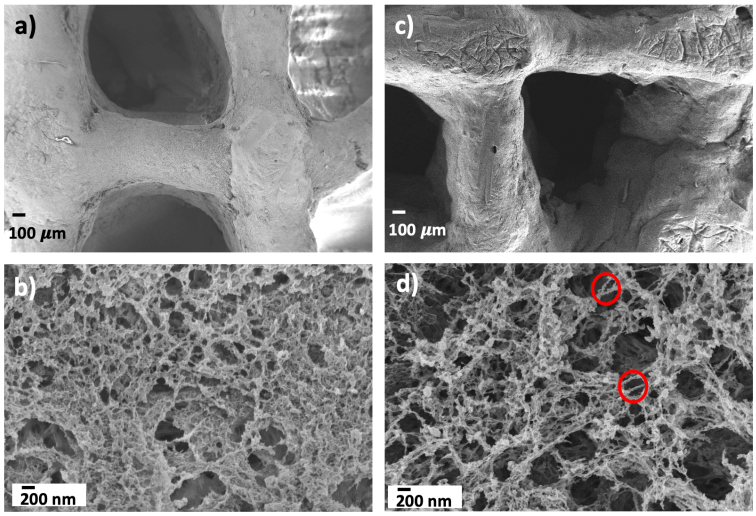


Figure 8.6. SEM pictures of cellulose-in-cellulose aerogels after 4-month storage. **a,b)** MC; **c,d)** MC NF10-6 S. Aerogels imaged at two different magnifications. Red circles represent zones where the presence of BC-NF was detected by visual inspection.

8.3.3. Magnetic properties of SPIONs decorated aerogels

SPIONs were not functionally affected by the 3D-printing or the $scCO_2$ processing as the normalized magnetization vs temperature plot of aerogel composites and of BC-NF doped with SPIONs had similar magnetization behavior (Fig. 8.7a). Zero-field cooled magnetization increases with temperature until it reached the blocking temperature (T_B = 140K). Above this temperature, aerogels were superparamagnetic; below the blocking temperature, samples were ferrimagnetic (Fig. 8.7b). Remanent magnetization value (M_R) at 5K was used to know the content of BC-NF doped with SPIONs in the aerogels. M_R of SPIONs was 30 emu/g at 5K (previous work). Accordingly, MC NF10-12 aerogels had 1.1 ± 0.1 wt.% of BC-NF labelled with SPIONs and 0.15 ± 0.02 wt.% of SPIONs. MC NF10-6 formulations had 0.42 ± 0.06 wt.% of BC-NF doped with

SPIONs and 0.06 ± 0.01 wt.% of SPIONs. Similar results in terms of magnetic behavior were reported for pectin aerogels loaded with iron oxide magnetic nanoparticles [54]. Further SPIONs contents should be incorporated into aerogel structure to confer magnetic properties at levels of relevance for biomedical applications.

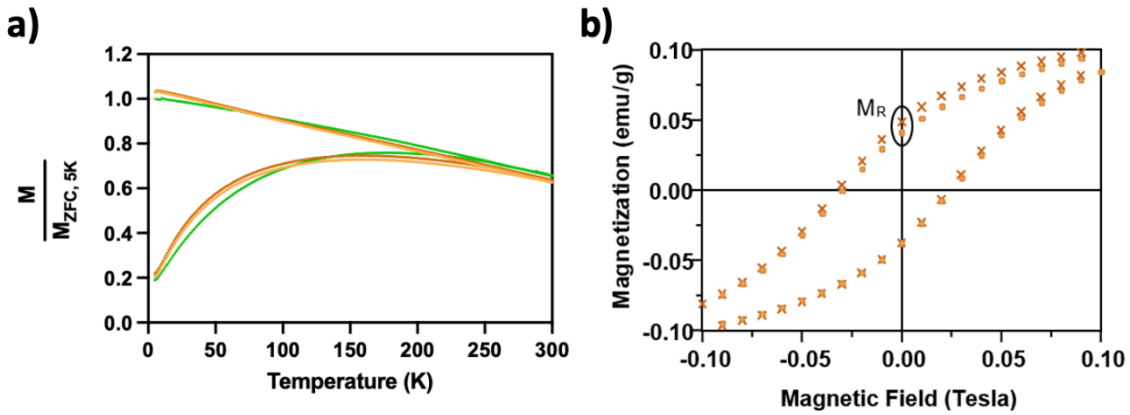


Figure 8.7. Magnetic performance of aerogels. **a)** Zero-field cooled – field cooled temperature dependent magnetization curves. **b)** magnetization *versus* field at 5 K of aerogels. BC-NF decorated with SPIONs (green) and incorporated into aerogels (orange and brown: two replicates of MC NF10-12 S aerogels).

8.3.4. Biocompatibility and preliminary safety tests

High viability of fibroblast cells assessed by resazurin test was obtained after 24 and 72 h in contact with cellulose-in-cellulose aerogels (Fig. 8.8a). An increase in cell viabilities after 72 h were observed for the different formulations studied with respect to 24 h in culture. Moreover, all formulations showed very relevant differences with respect to the negative controls, after 24 and 72 h. However, no significant differences were observed in cell viabilities for the aerogels loaded with different BC-NF contents, thus indicating no negative impact of the BC-NF on cell survival. Nanocellulose has previously shown excellent biocompatibility and the ability to support cell growth in 3D-printed biomaterials [41]. BC-NF composites have also been demonstrated to be biocompatible and able to promote cellular adhesion and proliferation of human mesenchymal stem cells [58].

Preliminary safety assays showed high viability of *A. salina* after 24 h of contact with aerogels loaded with different BC-NF concentrations (Fig. 8.8b) and these results endorse the previous ones. Aerogels doped with SPIONs also induced a neglectable mortality of *A. salina*, suggesting

USC UNIVERSIDADE DE SANTIAGO DE COMPOSTELA

the preliminary safety of the BC-NF aerogels decorated with SPIONs. Similar results were reported for pectin aerogels [39].

Biomaterials contact with blood is the first event in a bone wound after implantation, broadly affecting the subsequent bone healing [59]. Moreover, bone defects are commonly associated with a damage to blood vessels in the surrounding tissue. The contact of implants with blood induces the formation of a blood clot and the recruitment of inflammatory cells, the first steps in bone regeneration [60]. Consequently, studying interactions between host blood and biomaterials is crucial to ensure the hemostasis process [61]. No hemolytic activity was detected for the aerogels containing the highest concentration of NF studied doped with SPIONs, with significant differences to the positive control (Fig. 8.8c) and similar results to magnetite-loaded aerogels [55]. These results suggest the absence of hemolysis due to BC-NF-loaded aerogels, either with or without SPIONs. HET-CAM images obtained after the contact of SPIONs doped samples were in accordance with these results, with no hemorrhage detected by visual inspection (Fig. 8.8d). All these data indicate that the studied aerogel scaffolds triggered no lysis or coagulation phenomena of blood cells. These are good results since coatings like polyethylene glycol were needed to coat iron oxide nanoparticles before obtaining functionalized and biocompatible BC-NF [62]. At the SPIONs concentrations herein employed, no coating of SPIONs was required to enhance their biocompatibility, maybe due to their inclusion inside the aerogel structure.

USC
UNIVERSIDADE DE SANTIAGO DE COMPOSTELA

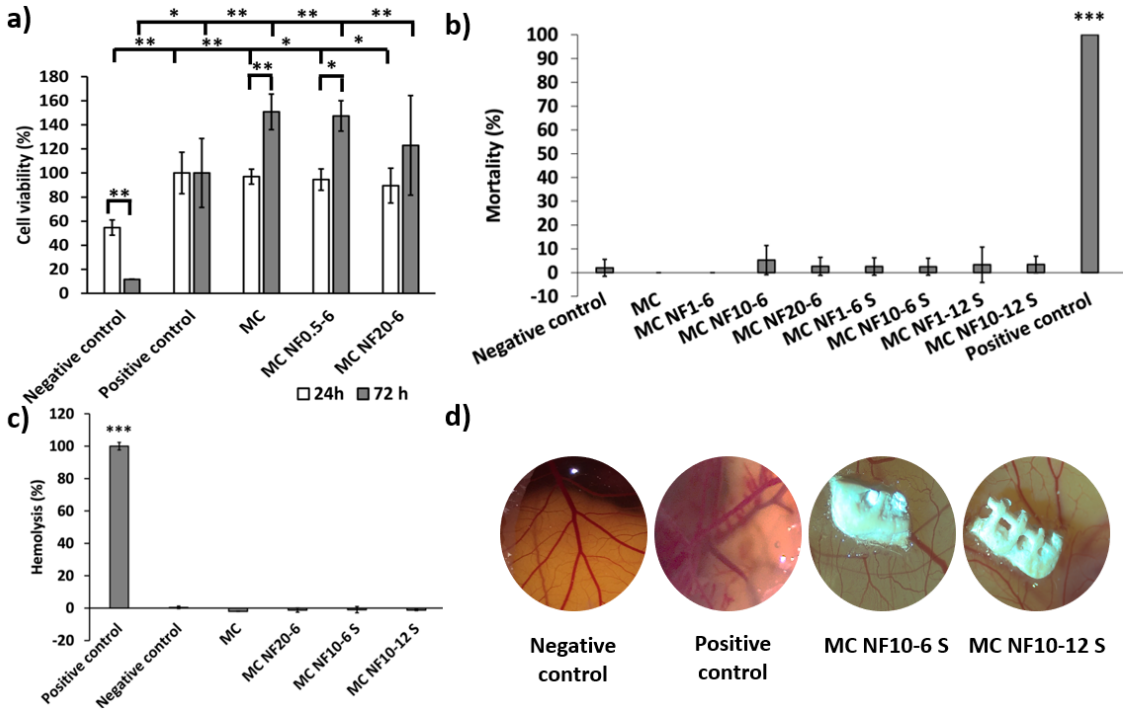


Figure 8.8. Biological evaluation of cellulose-in-cellulose aerogels. **a)** Viability of NIH/3T3 cells after 24 and 72 h of contact with aerogels, determined by resazurin cytotoxicity assay. Negative control: 10 µM; positive control: NIH/3T3 cells. **b)** Mortality of *A. salina* after 24 h in contact with aerogels. Negative control: DMSO; positive control: artificial sea water. **c)** Hemolytic activity tests of aerogels. Positive control: Triton; negative control: PBS pH 7.4. (d) HET-CAM test of aerogels. Negative control: PBS pH 7.4, positive control: 0.1N NaOH. Significant differences among groups were represented as * or ** (post hoc Tukey HSD multiple comparison test, $p < 0.05$ or $p < 0.01$, respectively).

8.3.5. Sterility procedure evaluation

Different methods like gamma radiation or ethylene oxide are being used to sterilize biomaterials; most of these options were unsuitable for polymeric structures due to their negative impact on their physicochemical characteristics [20,63]. For this reason, $scCO_2$ is increasingly studied as a sterilizing agent able to preserve the physicochemical features of implants and achieve the sterility levels required for implantable medical devices [64,65]. After the sterilization procedure, no relevant morphological and textural changes on aerogels due to $scCO_2$ postprocessing were observed (Table 8.3). A similar porous structure (pore size distribution and morphology) was also observed for all the formulations studied, including the ones without BC-NF, by comparison of the SEM images obtained before (Fig. 8.1) and after the sterilization (Fig. 8.9). There was no statistical difference in the values of porosity of the aerogel scaffolds before and after the supercritical sterilization treatment (Table 8.3). The distribution

USC DE COMPOSTELA

and structure of BC-NF were preserved and intercalated in the porous aerogel structure after the $scCO_2$-assisted sterilization (Fig. 8.9, red circles).

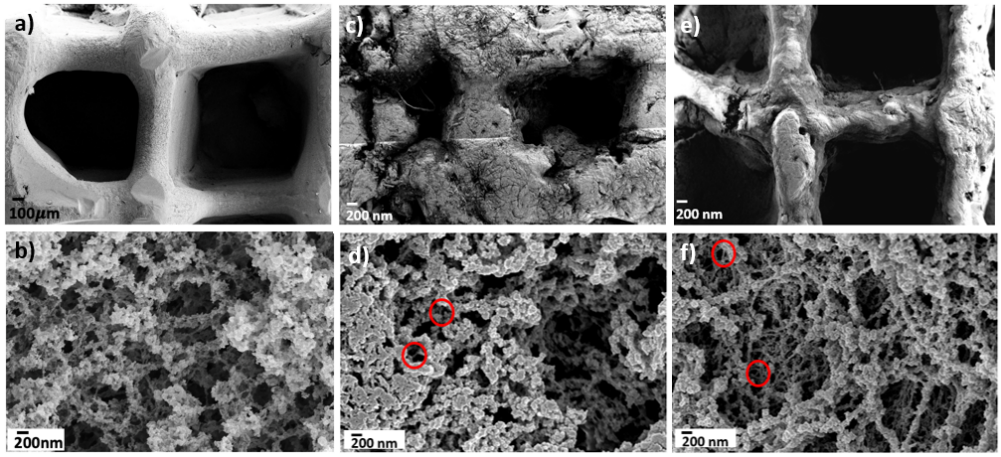


Figure 8.9. SEM pictures of cellulose-in-cellulose aerogels after $scCO_2$ sterilization. **a,b)** MC st; **c,d)** MC NF0.5-6 st; **e,f)** MC NF20-6 st. Aerogels imaged at two different magnifications. Red circles represent zones where the presence of BC-NF was detected by visual inspection.

8.4. Conclusions

Dual porous cellulose-in-cellulose aerogels were obtained for the first time by combining 3D-printing and $scCO_2$ drying technologies. An enhancement in the printing fidelity (higher SFF) and an improvement in the structural resolution (lower volume shrinkage) were observed due to incorporating BC-NF into the aerogel structure. No detrimental effect on the viability of murine fibroblasts, hemolytic activity of human blood cells nor mortality of *A. salina* occurred after contact with cellulose-in-cellulose aerogels. Magnetic performance of SPIONs decorated aerogels was demonstrated and can be enhanced by doping with higher contents of these nanoparticles. Finally, either the $scCO_2$-based sterilization or storage for months of 3D-printed cellulose-in-cellulose aerogels did not have any detrimental effect on their physicochemical performance and validated this method for manufacturing sterilized cellulose-in-cellulose aerogel scaffolds. Magnetic properties achieved in this work opens up the avenue for unique structures, providing new understanding on the SPIONs' performance and its potential transitional application for bone tissue engineering. The reported results endorse the candidacy of these cellulose-based bioaerogels for bone tissue engineering applications.

USC UNIVERSIDADE DE SANTIAGO DE COMPOSTELA

8.5. References

1. Feng, Y.; Zhu, S.; Mei, D.; Li, J.; Zhang, J.; Yang, S.; Guan, S. Application of 3D Printing Technology in Bone Tissue Engineering: A Review. Curr. Drug Deliv. 2021, 18, 847–861, doi:10.2174/1567201817999201113100322.
2. Qu, M.; Wang, C.; Zhou, X.; Libanori, A.; Jiang, X.; Xu, W.; Zhu, S.; Chen, Q.; Sun, W.; Khademhosseini, A. Multi-Dimensional Printing for Bone Tissue Engineering. Adv. Healthcare Mater. 2021, 10, 2001986, doi:10.1002/adhm.202001986.
3. Zhao, N.; Wang, X.; Qin, L.; Zhai, M.; Yuan, J.; Chen, J.; Li, D. Effect of Hyaluronic Acid in Bone Formation and Its Applications in Dentistry: Effect of HA on Cell Proliferation and Osteogenic Differentiation. J. Biomed. Mater. Res. 2016, 104, 1560–1569, doi:10.1002/jbm.a.35681.
4. Li, H.; Chen, S. Biomedical Coatings on Polyethylene Terephthalate Artificial Ligaments: BIOMEDICAL COATINGS ON PET. J. Biomed. Mater. Res. 2015, 103, 839–845, doi:10.1002/jbm.a.35218.
5. Gerasimenko, A.Yu.; Zhurbina, N.N.; Cherepanova, N.G.; Semak, A.E.; Zar, V.V.; Fedorova, Y.O.; Eganova, E.M.; Pavlov, A.A.; Telyshev, D.V.; Selishchev, S.V.; et al. Frame Coating of Single-Walled Carbon Nanotubes in Collagen on PET Fibers for Artificial Joint Ligaments. Int. J. Mol. Sci. 2020, 21, 6163, doi:10.3390/ijms21176163.
6. Budtova, T.; Aguilera, D.A.; Beluns, S.; Berglund, L.; Chartier, C.; Espinosa, E.; Gaidukovs, S.; Klimek-Kopyra, A.; Kmita, A.; Lachowicz, D.; et al. Biorefinery Approach for Aerogels. Polymers 2020, 12, 2779, doi:10.3390/polym12122779.
7. Maleki, H.; Durães, L.; García-González, C.A.; del Gaudio, P.; Portugal, A.; Mahmoudi, M. Synthesis and Biomedical Applications of Aerogels: Possibilities and Challenges. Adv. Colloid Interface Sci. 2016, 236, 1–27, doi:10.1016/j.cis.2016.05.011.
8. Bernardes, B.G.; Del Gaudio, P.; Alves, P.; Costa, R.; García-Gonzaléz, C.A.; Oliveira, A.L. Bioaerogels: Promising Nanostructured Materials in Fluid Management, Healing and Regeneration of Wounds. Molecules 2021, 26, 3834, doi:10.3390/molecules26133834.
9. Budtova, T. Cellulose II Aerogels: A Review. Cellulose 2019, 26, 81–121, doi:10.1007/s10570-018-2189-1.
10. Wang, S.; Zhao, S.; Yu, J.; Gu, Z.; Zhang, Y. Advances in Translational 3D Printing for Cartilage, Bone, and Osteochondral Tissue Engineering. Small 2022, 18, 2201869, doi:10.1002/smll.202201869.
11. Shokouhimehr, M.; Theus, A.S.; Kamalakar, A.; Ning, L.; Cao, C.; Tomov, M.L.; Kaiser, J.M.; Goudy, S.; Willett, N.J.; Jang, H.W.; et al. 3D Bioprinted Bacteriostatic Hyperelastic Bone Scaffold for Damage-Specific Bone Regeneration. Polymers 2021, 13, 1099, doi:10.3390/polym13071099.
12. Iglesias-Mejuto, A.; García-González, C.A. 3D-Printed, Dual Crosslinked and Sterile Aerogel Scaffolds for Bone Tissue Engineering. Polymers 2022, 14, 1211, doi:10.3390/polym14061211.
13. Iglesias-Mejuto, A.; García-González, C.A. 3D-Printed Alginate-Hydroxyapatite Aerogel Scaffolds for Bone Tissue Engineering. Mater. Sci. Eng. C 2021, 131, 112525, doi:10.1016/j.msec.2021.112525.
14. Tang, H.; Kankala, R.K.; Wang, S.; Chen, A. Supercritical Fluid-Assisted Controllable Fabrication of Open and Highly Interconnected Porous Scaffolds for Bone Tissue Engineering. Sci. China Life Sci. 2019, 62, 1670–1682, doi:10.1007/s11427-018-9393-8.
15. Karamat-Ullah, N.; Demidov, Y.; Schramm, M.; Grumme, D.; Auer, J.; Bohr, C.; Brachvogel, B.; Maleki, H. 3D Printing of Antibacterial, Biocompatible, and Biomimetic Hybrid Aerogel-Based Scaffolds with Hierarchical Porosities via Integrating Antibacterial Peptide-Modified Silk Fibroin with Silica Nanostructure. ACS Biomater. Sci. Eng. 2021, 7, 4545–4556, doi:10.1021/acsbiomaterials.1c00483.
16. Ng, P.; Pinho, A.R.; Gomes, M.C.; Demidov, Y.; Krakor, E.; Grume, D.; Herb, M.; Lê, K.; Mano, J.; Mathur, S.; et al. Fabrication of Antibacterial, Osteo-Inductor 3D Printed Aerogel-Based Scaffolds by Incorporation of Drug Laden Hollow Mesoporous Silica Microparticles into the Self-Assembled Silk Fibroin Biopolymer. Macromol. Biosci. 2022, 22, 2100442, doi:10.1002/mabi.202100442.
17. Al-Jawuschi, N.; Chen, S.; Abie, N.; Fischer, T.; Fare, S.; Maleki, H.H. Self-Assembly-Driven Bi_2S_3 Nanobelts Integrated a Silk-Fibroin-Based 3D-Printed Aerogel-Based Scaffold with a Dual-Network Structure for Photothermal Bone Cancer Therapy. Langmuir 2023, 39, 4326–4337, doi:10.1021/acs.langmuir.2c03334.
18. Zhang, Y.; Jiang, S.; Xu, D.; Li, Z.; Guo, J.; Li, Z.; Cheng, G. Application of Nanocellulose-Based Aerogels in Bone Tissue Engineering: Current Trends and Outlooks. Polymers 2023, 15, 2323, doi:10.3390/polym15102323.
19. Chen, Y.; Zhang, L.; Yang, Y.; Pang, B.; Xu, W.; Duan, G.; Jiang, S.; Zhang, K. Recent Progress on Nanocellulose Aerogels: Preparation, Modification, Composite Fabrication, Applications. Adv. Mater. 2021, 33, 2005569, doi:10.1002/adma.202005569.

20. Ahlfeld, T.; Guduric, V.; Duin, S.; Akkineni, A.R.; Schütz, K.; Kilian, D.; Emmermacher, J.; Cubo-Mateo, N.; Dani, S.; Witzleben, M. v.; et al. Methylcellulose – a Versatile Printing Material That Enables Biofabrication of Tissue Equivalents with High Shape Fidelity. Biomater. Sci. 2020, 8, 2102–2110, doi:10.1039/D0BM00027B.
21. Mbituyimana, B.; Liu, L.; Ye, W.; Ode Boni, B.O.; Zhang, K.; Chen, J.; Thomas, S.; Vasilievich, R.V.; Shi, Z.; Yang, G. Bacterial Cellulose-Based Composites for Biomedical and Cosmetic Applications: Research Progress and Existing Products. Carbohydr. Polym. 2021, 273, 118565, doi:10.1016/j.carbpol.2021.118565.
22. Manan, S.; Ullah, M.W.; Ul-Islam, M.; Shi, Z.; Gauthier, M.; Yang, G. Bacterial Cellulose: Molecular Regulation of Biosynthesis, Supramolecular Assembly, and Tailored Structural and Functional Properties. Prog. Mater. Sci. 2022, 129, 100972, doi:10.1016/j.pmatsci.2022.100972.
23. Roig-Sanchez, S.; Torrecilla, O.; Floriach-Clark, J.; Parets, S.; Levkin, P.A.; Roig, A.; Laromaine, A. One-Step Biosynthesis of Soft Magnetic Bacterial Cellulose Spheres with Localized Nanoparticle Functionalization. ACS Appl. Mater. Interfaces 2021, 13, 55569–55576, doi:10.1021/acsami.1c17752.
24. Wang, X.; Tang, S.; Chai, S.; Wang, P.; Qin, J.; Pei, W.; Bian, H.; Jiang, Q.; Huang, C. Preparing Printable Bacterial Cellulose Based Gelatin Gel to Promote *in Vivo* Bone Regeneration. Carbohydr. Polym. 2021, 270, 118342, doi:10.1016/j.carbpol.2021.118342.
25. Roig-Sanchez, S.; Kam, D.; Malandain, N.; Sachyani-Keneth, E.; Shoseyov, O.; Magdassi, S.; Laromaine, A.; Roig, A. One-Step Double Network Hydrogels of Photocurable Monomers and Bacterial Cellulose Fibers. Carbohydr. Polym. 2022, 294, 119778, doi:10.1016/j.carbpol.2022.119778.
26. Oun, A.A.; Shankar, S.; Rhim, J.-W. Multifunctional Nanocellulose/Metal and Metal Oxide Nanoparticle Hybrid Nanomaterials. Crit. Rev. Food Sci. Nutr. 2020, 60, 435–460, doi:10.1080/10408398.2018.1536966.
27. Luque-Michel, E.; Lemaire, L.; Blanco-Prieto, M.J. SPION and Doxorubicin-Loaded Polymeric Nanocarriers for Glioblastoma Theranostics. Drug Deliv. and Transl. Res. 2021, 11, 515–523, doi:10.1007/s13346-020-00880-8.
28. Singh, S.; Singh, G.; Bala, N.; Aggarwal, K. Characterization and Preparation of Fe3O4 Nanoparticles Loaded Bioglass-Chitosan Nanocomposite Coating on Mg Alloy and *in Vitro* Bioactivity Assessment. Int. J. Biol. Macromol. 2020, 151, 519–528, doi:10.1016/j.ijbiomac.2020.02.208.
29. Pankhurst, Q.A.; Connolly, J.; Jones, S.K.; Dobson, J. Applications of Magnetic Nanoparticles in Biomedicine. J. Phys. D: Appl. Phys. 2003, 36, R167–R181, doi:10.1088/0022-3727/36/13/201.
30. Chiang, W.-H.; Huang, W.-C.; Chang, C.-W.; Shen, M.-Y.; Shih, Z.-F.; Huang, Y.-F.; Lin, S.-C.; Chiu, H.-C. Functionalized Polymersomes with Outlayered Polyelectrolyte Gels for Potential Tumor-Targeted Delivery of Multimodal Therapies and MR Imaging. JCR 2013, 168, 280–288, doi:10.1016/j.jconrel.2013.03.029.
31. Charoensuk, T.; Sirisathitkul, C.; Boonyang, U.; Macha, I.J.; Santos, J.; Grossin, D.; Ben-Nissan, B. *In Vitro* Bioactivity and Stem Cells Attachment of Three-Dimensionally Ordered Macroporous Bioactive Glass Incorporating Iron Oxides. JNCS 2016, 452, 62–73, doi:10.1016/j.jnoncrysol.2016.08.019.
32. Mortimer, C.J.; Wright, C.J. The Fabrication of Iron Oxide Nanoparticle-Nanofiber Composites by Electrospinning and Their Applications in Tissue Engineering. Biotechnol. J. 2017, 12, 1600693, doi:10.1002/biot.201600693.
33. Gholami, A.; Ebrahiminezhad, A.; Abootalebi, N.; Ghasemi, Y. Synergistic Evaluation of Functionalized Magnetic Nanoparticles and Antibiotics Against Staphylococcus Aureus and Escherichia Coli. Pharm. Nanotechnol. 2019, 6, 276–286, doi:10.2174/2211738506666181031143048.
34. Hu, S.; Zhou, Y.; Zhao, Y.; Xu, Y.; Zhang, F.; Gu, N.; Ma, J.; Reynolds, M.A.; Xia, Y.; Xu, H.H.K. Enhanced Bone Regeneration and Visual Monitoring via Superparamagnetic Iron Oxide Nanoparticle Scaffold in Rats. J Tissue Eng Regen Med 2018, 12, e2085–e2098, doi:10.1002/term.2641.
35. Mira-Cuenca, C.; Meslier, T.; Roig-Sanchez, S.; Laromaine, A.; Roig, A. Patterning Bacterial Cellulose Films with Iron Oxide Nanoparticles and Magnetic Resonance Imaging Monitoring. ACS Appl. Polym. Mater. 2021, 3, 4959–4965, doi:10.1021/acsapm.1c00723.
36. Theus, A.S.; Ning, L.; Kabboul, G.; Hwang, B.; Tomov, M.L.; LaRock, C.N.; Bauser-Heaton, H.; Mahmoudi, M.; Serpooshan, V. 3D Bioprinting of Nanoparticle-Laden Hydrogel Scaffolds with Enhanced Antibacterial and Imaging Properties. iScience 2022, 25, 104947, doi:10.1016/j.isci.2022.104947.
37. Recommended Test Method Protocol: Hen's Egg Test – Chorioallantoic Membrane (HET-CAM) Test Method 2010.
38. Salerno, A.; Diéguez, S.; Diaz-Gomez, L.; Gómez-Amoza, J.L.; Magariños, B.; Concheiro, A.; Domingo, C.; Alvarez-Lorenzo, C.; García-González, C.A. Synthetic Scaffolds with Full Pore Interconnectivity for Bone Regeneration Prepared by Supercritical Foaming Using Advanced Biofunctional Plasticizers. Biofabrication 2017, 9, 035002, doi:10.1088/1758-5090/aa78c5.

39. Ferreira-Gonçalves, T.; Iglesias-Mejuto, A.; Linhares, T.; Coelho, J.M.P.; Vieira, P.; Faísca, P.; Catarino, J.; Pinto, P.; Ferreira, D.; Ferreira, H.A.; et al. Biological Thermal Performance of Organic and Inorganic Aerogels as Patches for Photothermal Therapy. Gels 2022, 8, 485, doi:10.3390/gels8080485.
40. R. Hamidi, M.; Jovanova, B.; Kadifkova Panovska, T. Toxicological Evaluation of the Plant Products Using Brine Shrimp (Artemia Salina L.) Model. Maced. Pharm. Bull. 2014, 60, 9–18, doi:10.33320/maced.pharm.bull.2014.60.01.002.
41. Athukoralalage, S.S.; Balu, R.; Dutta, N.K.; Roy Choudhury, N. 3D Bioprinted Nanocellulose-Based Hydrogels for Tissue Engineering Applications: A Brief Review. Polymers 2019, 11, 898, doi:10.3390/polym11050898.
42. Corker, A.; Ng, H.C.-H.; Poole, R.J.; García-Tuñón, E. 3D Printing with 2D Colloids: Designing Rheology Protocols to Predict 'Printability' of Soft-Materials. Soft Matter 2019, 15, 1444–1456, doi:10.1039/C8SM01936C.
43. Cochis, A.; Bonetti, L.; Sorrentino, R.; Contessi Negrini, N.; Grassi, F.; Leigheb, M.; Rimondini, L.; Farè, S. 3D Printing of Thermo-Responsive Methylcellulose Hydrogels for Cell-Sheet Engineering. Materials 2018, 11, 579, doi:10.3390/ma11040579.
44. Shin, J.Y.; Yeo, Y.H.; Jeong, J.E.; Park, S.A.; Park, W.H. Dual-Crosslinked Methylcellulose Hydrogels for 3D Bioprinting Applications. Carbohydr. Polym. 2020, 238, 116192, doi:10.1016/j.carbpol.2020.116192.
45. Linhares, T.; Pessoa De Amorim, M.T.; Durães, L. Silica Aerogel Composites with Embedded Fibres: A Review on Their Preparation, Properties and Applications. J. Mater. Chem. A 2019, 7, 22768–22802, doi:10.1039/C9TA04811A.
46. Huang, L.; Du, X.; Fan, S.; Yang, G.; Shao, H.; Li, D.; Cao, C.; Zhu, Y.; Zhu, M.; Zhang, Y. Bacterial Cellulose Nanofibers Promote Stress and Fidelity of 3D-Printed Silk Based Hydrogel Scaffold with Hierarchical Pores. Carbohydr. Polym. 2019, 221, 146–156, doi:10.1016/j.carbpol.2019.05.080.
47. García-González, C.A.; Fraile, J.; López-Periago, A.; Domingo, C. Preparation of Silane-Coated TiO2 Nanoparticles in Supercritical CO_2. J. Colloid and Interface Sci. 2009, 338, 491–499, doi:10.1016/j.jcis.2009.06.035.
48. Drobota, M.; Vlad, S.; Gradinaru, L.M.; Bargan, A.; Radu, I.; Butnaru, M.; Rîmbu, C.M.; Ciobanu, R.C.; Aflori, M. Composite Materials Based on Gelatin and Iron Oxide Nanoparticles for MRI Accuracy. Materials 2022, 15, 3479, doi:10.3390/ma15103479.
49. Nazari, H.; Heirani-Tabasi, A.; Hajiabbas, M.; Salimi Bani, M.; Nazari, M.; Pirhajati Mahabadi, V.; Rad, I.; Kehtari, M.; Ahmadi Tafti, S.H.; Soleimani, M. Incorporation of SPION-casein Core-shells into Silk-fibroin Nanofibers for Cardiac Tissue Engineering. J Cell Biochem 2020, 121, 2981–2993, doi:10.1002/jcb.29553.
50. Zeng, M.; Laromaine, A.; Roig, A. Bacterial Cellulose Films: Influence of Bacterial Strain and Drying Route on Film Properties. Cellulose 2014, 21, 4455–4469, doi:10.1007/s10570-014-0408-y.
51. Panaitescu, D.M.; Stoian, S.; Frone, A.N.; Vlăsceanu, G.M.; Baciu, D.D.; Gabor, A.R.; Nicolae, C.A.; Radiţoiu, V.; Alexandrescu, E.; Căşărică, A.; et al. Nanofibrous Scaffolds Based on Bacterial Cellulose Crosslinked with Oxidized Sucrose. Int. J. Biol. Macromol. 2022, 221, 381–397, doi:10.1016/j.ijbiomac.2022.08.189.
52. Luo, H.; Li, W.; Ao, H.; Li, G.; Tu, J.; Xiong, G.; Zhu, Y.; Wan, Y. Preparation, Structural Characterization, and *in Vitro* Cell Studies of Three-Dimensional SiO_2–CaO Binary Glass Scaffolds Built Ofultra-Small Nanofibers. Mater. Sci. and Eng. C 2017, 76, 94–101, doi:10.1016/j.msec.2017.02.134.
53. Li, Y.; Xun, X.; Xu, Y.; Zhan, A.; Gao, E.; Yu, F.; Wang, Y.; Luo, H.; Yang, C. Hierarchical Porous Bacterial Cellulose Scaffolds with Natural Biomimetic Nanofibrous Structure and a Cartilage Tissue-Specific Microenvironment for Cartilage Regeneration and Repair. Carbohydr. Polym. 2022, 276, 118790, doi:10.1016/j.carbpol.2021.118790.
54. García-González, C.A.; Carenza, E.; Zeng, M.; Smirnova, I.; Roig, A. Design of Biocompatible Magnetic Pectin Aerogel Monoliths and Microspheres. RSC Adv. 2012, 2, 9816, doi:10.1039/c2ra21500d.
55. Anastasova, E.I.; Belyaeva, A.A.; Tsymbal, S.A.; Vinnik, D.A.; Vinogradov, V.V. Hierarchical Porous Magnetite Structures: From Nanoparticle Assembly to Monolithic Aerogels. J. Colloid Interface Sci. 2022, 615, 206–214, doi:10.1016/j.jcis.2022.01.154.
56. López-Iglesias, C.; Barros, J.; Ardao, I.; Monteiro, F.J.; Alvarez-Lorenzo, C.; Gómez-Amoza, J.L.; García-González, C.A. Vancomycin-Loaded Chitosan Aerogel Particles for Chronic Wound Applications. Carbohydr. Polym. 2019, 204, 223–231, doi:10.1016/j.carbpol.2018.10.012.
57. Groult, S.; Buwalda, S.; Budtova, T. Pectin Hydrogels, Aerogels, Cryogels and Xerogels: Influence of Drying on Structural and Release Properties. Eur. Polym. J. 2021, 149, 110386, doi:10.1016/j.eurpolymj.2021.110386.

58. Jin, L.; Zeng, Z.; Kuddannaya, S.; Wu, D.; Zhang, Y.; Wang, Z. Biocompatible, Free-Standing Film Composed of Bacterial Cellulose Nanofibers–Graphene Composite. ACS Appl. Mater. Interfaces 2016, 8, 1011–1018, doi:10.1021/acsami.5b11241.
59. Lagadec, P.; Balaguer, T.; Boukhechba, F.; Michel, G.; Bouvet-Gerbettaz, S.; Bouler, J.-M.; Scimeca, J.-C.; Rochet, N. Calcium Supplementation Decreases BCP-Induced Inflammatory Processes in Blood Cells through the NLRP3 Inflammasome down-Regulation. Acta Biomater. 2017, 57, 462–471, doi:10.1016/j.actbio.2017.05.039.
60. Yang, J.; Zhou, Y.; Wei, F.; Xiao, Y. Blood Clot Formed on Rough Titanium Surface Induces Early Cell Recruitment. Clin. Oral Impl. Res. 2016, 27, 1031–1038, doi:10.1111/clr.12672.
61. Shiu, H.T.; Goss, B.; Lutton, C.; Crawford, R.; Xiao, Y. Formation of Blood Clot on Biomaterial Implants Influences Bone Healing. Tissue Eng. Part B: Rev. 2014, 20, 697–712, doi:10.1089/ten.teb.2013.0709.
62. Arias, S.L.; Shetty, A.R.; Senpan, A.; Echeverry-Rendón, M.; Reece, L.M.; Allain, J.P. Fabrication of a Functionalized Magnetic Bacterial Nanocellulose with Iron Oxide Nanoparticles. JoVE 2016, 52951, doi:10.3791/52951.
63. Ribeiro, N.; Soares, G.C.; Santos-Rosales, V.; Concheiro, A.; Alvarez-Lorenzo, C.; García-González, C.A.; Oliveira, A.L. A New Era for Sterilization Based on Supercritical CO $_2$ Technology. J. Biomed. Mater. Res. 2020, 108, 399–428, doi:10.1002/jbm.b.34398.
64. Santos-Rosales, V.; Magariños, B.; Starbird, R.; Suárez-González, J.; Fariña, J.B.; Alvarez-Lorenzo, C.; García-González, C.A. Supercritical CO_2 Technology for One-Pot Foaming and Sterilization of Polymeric Scaffolds for Bone Regeneration. Int. J. Pharm. 2021, 605, 120801, doi:10.1016/j.ijpharm.2021.120801.
65. Santos-Rosales, V.; Ardao, I.; Alvarez-Lorenzo, C.; Ribeiro, N.; Oliveira, A.; García-González, C. Sterile and Dual-Porous Aerogels Scaffolds Obtained through a Multistep Supercritical CO_2-Based Approach. Molecules 2019, 24, 871, doi:10.3390/molecules24050871.

USC UNIVERSIDADE DE SANTIAGO DE COMPOSTELA

CHAPTER 9. GENERAL DISCUSSION

The dual processing strategy combining 3D-printing and SCF technology was reported in this PhD Thesis for the first time and has demonstrated to be suitable for the manufacturing of 3D-printed aerogels of different composition. An adjustment of the 3D-printing method was successfully carried out to produce ionic crosslinked alginate gels and thermally gelled methylcellulose. Rheological studies of the different inks exhibited the shear thinning properties essential for 3D-printing, with an increase in this behavior when higher HA concentrations were incorporated, for alginate- and methylcellulose-based inks. The incorporation of HA in the 3D-printed aerogels also had other advantages such as the induction of a high long-term bioactivity, the decrease of their volume shrinkage and the increase of the printing fidelity at the expense of a decrease in their textural parameters.

The concentrations of alginate and $CaCl_2$ influenced the textural performance of the 3D-printed aerogels, with an improvement in A_{BET} and V_p values reported for the lowest alginate content studied. Moreover, the 3D-printed scaffolds with fibers more homogeneously arranged have been obtained at the highest $CaCl_2$ concentration studied, probably due to the presence of more Ca^{2+} ions involved in the crosslinking of alginate. The incorporation of HA into the alginate aerogels had a detrimental effect on their textural parameters but the dual porous structure, with mesopores and macropores in the same structure, was still preserved as well as the geometry and arrangement of the strands of the scaffolds. Furthermore, the apatite depositions observed after 28 days of SBF immersion confirmed the achievement of the bioactivity required for scaffolds aimed at bone tissue engineering applications. Consistently, HA added into 3D-printed aerogels rendered improved implants for bone repair.

The dual crosslinking strategy of $CaCl_2$ bath and GA vapor slightly decreased the textural parameters and the porosity of the 3D-printed alginate aerogels, probably due to the fusion of the alginate fibers at their junctions due to the covalent bonds generated by the GA crosslinking.

USC UNIVERSIDADE DE SANTIAGO DE COMPOSTELA

Nevertheless, the GA crosslinking resulted in 3D-printed aerogels with an improved integrity and the biocompatibility of the 3D-printed aerogels was preserved, with values of hemocompatibility and murine fibroblasts viability higher than 80% for the different formulations studied. These results were related to the crosslinking method employed, being the GA atmosphere less toxic than the GA immersion. Consistently, the dual crosslinking method yielded biocompatible and non-brittle 3D-printed aerogels with tight junctions between fibers.

A strategy to monitor bone scaffolds and their degradation products after *in vivo* implantation was developed in the frame of this PhD Thesis for the first time. A novel synthetic procedure was developed by combining the co-precipitation of a highly fluorescent lanthanide core with the sol-gel formation of a protective silica coating. Core-shell UCNPs were successfully synthesized with an effective silica coating able to yield bio- and hemocompatible UCNPs at very high concentrations (10 mg/mL). Highly spherical UCNPs with high fluorescence properties were obtained from the oxides and nitrates of the lanthanides (namely, erbium, ytterbium and yttrium), thus suggesting the shape-and phase-controlling capabilities of the developed synthetic approach. The physicochemical stability of the UCNPs after three years of storage was unveiled in terms of morphological and fluorescence analysis thereby indicating the high stability of the UCNPs.

The doping of the UCNPs into the alginate aerogels was carried out by direct incorporation into the 3D-printing inks to manufacture theranostic implants with a homogeneous distribution of UCNPs in their structure. Physicochemical properties of the 3D-printed aerogels were maintained after UCNPs doping, with similar volume shrinkage, textural parameters, printing fidelity and pore morphology distribution throughout the structure of the material. Stability studies of aerogels after 3 years of storage were carried out for the first time. Similar textural parameters, and fluorescence properties were observed with respect to the same aerogels analyzed just after synthesis, thus suggesting the high physicochemical stability of the UCNPs-

USC DE COMPOSTELA

decorated aerogels. Furthermore, UCNPs loaded into scaffolds did not alter their biological performance, as no statistically significant differences were detected between the cell compatibility, migration, and adhesion properties of the UCNPs-loaded and non-loaded aerogels. All results were consistent with the absence of cellular toxicity of the high UCNPs concentrations previously tested on murine fibroblasts and human blood. Safety tests demonstrated the *in vivo* biocompatibility of the theranostic implants, as similar results in terms of TNF-α, IL-6 and IL-10 cytokines expression, tissue index and histological sections of major organs were observed for controls and for animals after 1-week subcutaneous implantation of UCNPs-decorated aerogels. A subcutaneous foreign body reaction was detected in all animals suggesting the silk suture as its main cause and not the theranostic device itself. The low expression of plasmatic pro-inflammatory cytokines further confirmed the anti-inflammatory microenvironment. Furthermore, *in vivo* fluorescence measurements in a Swiss mouse model allowed the monitoring of the state of the aerogels until 3 weeks after implantation due to the UCNPs doping into their matrix, pointing out the long-term bioimaging capabilities of the developed theranostic implants.

The decrease in textural properties for 3D-printed alginate scaffolds after the HA incorporation and dual crosslinking was avoided in their methylcellulose counterparts by changing the biopolymer matrix, the HA size and 3D-printing design. In general, methylcellulose yielded aerogels with an improved textural performance with respect to alginate, after incorporation of high contents of HA in both cases. VAN was selected to be incorporated into scaffolds due to their application in the management of bone infections after implantation surgeries. Different concentrations of VAN were incorporated in alternative layers of the same scaffold, thus achieving the customization of the drug content distribution in the aerogels. The absence of physicochemical changes or printing fidelity losses due to the loading of the drug points out the possibility of developing adapted-to-patient implants by the dual processing strategy. Furthermore, a sustained drug release for 72 h was achieved with an effective inhibition of the

USC UNIVERSIDADE DE SANTIAGO DE COMPOSTELA

growth of *S. aureus,* the main pathogen source for bone infections after implantation. Mineralization assessments suggested a stimulation of the bone tissue formation as well as the achievement of the long-term bioactivity, an essential requirement for scaffolds aimed at bone regeneration. Bioactivity, drug release and antimicrobial effect are not characteristics of common bone implants and represent important advantages of the developed drug-loaded 3D-printed aerogels with regards to current commercial solutions.

Bio and hemocompatibility of the drug-loaded aerogels as well as its preliminary *in vivo* safety suggests its suitability as implants for bone tissue engineering. Mechanical properties of the 3D-printed aerogels increased with the content of HA, indicating a more elastic than viscous response, similar to the viscoelasticity performance of the natural bone. The inorganic part of the 3D-printed scaffolds can be increased to yield mechanical characteristics closer to the ones of human bone tissue. The decrease in porosity and textural parameters with the HA increment was less noteworthy in this case than in 3D-printed alginate aerogels, so the methylcellulose formulations represent a more suitable alternative to increase the inorganic part of the scaffolds as part of future work. Furthermore, the change of the biopolymer and drug loading into scaffolds pointed out the versatility of the dual processing strategy so tailoring the drug gradient, the HA content, or the printing design to improve the customization of the 3D-printed aerogels can be further studied towards an optimization of the formulations.

3D-printing fidelity is a key factor in personalized medicine, so this parameter was studied. The best results were obtained always with the highest HA content, both in alginate and methylcellulose aerogels. BC-NF were added into scaffolds as a strategy to improve their 3D-printing fidelity and resolution, resulting in a better-defined 3D-printed pattern with a higher fidelity with respect to the designed printing file. Reinforcement of the structures in relation to the concentration of BC-NF incorporated into inks could also be studied to unveil their influence in the mechanical properties of the 3D-printed aerogels. Further increase in the content of BC-

USC DE COMPOSTELA

NF are hypothesized to preserve the porosity and the dual pore sizes, while increasing the 3D-printing fidelity. Moreover, a higher macroporous population was observed when BC-NF were incorporated into aerogels, thereby being beneficial for their application in the bone tissue engineering field, as pores in the range of 100-300 µm are desired for the promotion of bone regeneration.

SPIONs were employed to localize the BC-NF as well as to promote the magnetic behavior of the scaffolds without observing a detrimental effect in the textural performance of the aerogels. Nevertheless, the magnetization of the aerogels should be enhanced for their application in the biomedical field. An increase in the SPIONs content is hypothesized to yield the intended magnetic behavior. Bio- and hemocompatibility as well as the preliminary *in vivo* safety of aerogels doped with SPIONs-labeled BC-NF were demonstrated. Higher SPIONs doping to enhance the magnetic behavior, as well as the biocompatibility of the modified aerogels should be investigated.

The dual porous structure and the physicochemical parameters of the 3D-printed aerogels were preserved after storage of alginate and methylcellulose scaffolds for 3 years and 7 months, respectively, thereby suggesting their stability. Further studies in different ambient conditions and for higher time periods in the case of methylcellulose aerogels could be conducted to unveil the physicochemical stability of 3D-printed aerogels and their dependency on these factors. Physicochemical performance did not exhibit relevant changes in terms of porous structure and textural parameters after sterilization of alginate and methylcellulose aerogels, thus suggesting the post-processing step by $scCO_2$ and the use of H_2O_2 as sterilization additive as a suitable method to sterilize 3D-printed biopolymer scaffolds.

USC
UNIVERSIDADE DE SANTIAGO DE COMPOSTELA

USC
UNIVERSIDADE
DE SANTIAGO
DE COMPOSTELA

CHAPTER 10. CONCLUSIONS

In this PhD Thesis, a dual processing strategy combining the 3D-printing and SCF technologies was developed for the manufacturing of sterile, dual porous and 3D-printed aerogels for bone tissue engineering applications. Namely, customized alginate scaffolds with high cell compatibility, migration and adhesion capacities were obtained and doped with UCNPs to provide them with monitoring capabilities. Moreover, methylcellulose aerogels with an improved structural integrity and a sustained release of VAN were also manufactured. The following main conclusions are drawn from this PhD Thesis:

1. A dual processing strategy was developed by the technological combination of 3D-printing of alginate gels and their subsequent drying by $scCO_2$. The 3D-printing conditions were adjusted to obtain gels with a grid pattern and a high printing fidelity with respect to the original printing file in an automatic and reproducible process. Dual porous aerogels with mesopores and macropores in the same structure were observed by SEM imaging with porosities higher than 80% for the different formulations. Cell compatibility, migration and adhesion capacity of 3D-printed aerogels were demonstrated with murine fibroblasts and MSCs. HA incorporated into alginate-based inks induced bioactivity with a high number of apatite depositions after 28 days of aerogels immersion in SBF medium. GA-vapor crosslinking applied in the 3D-printed aerogels improved the structural integrity of scaffolds while maintaining their textural and biological performances. A post-sterilization procedure based on the use of $scCO_2$ and using H_2O_2 as additive was developed to achieve the sterilization levels required for implantable medical devices and with preserved textural performances.
2. A strategy to allow the monitoring of the 3D-printed aerogels once implanted *in vivo* was developed by the novel synthesis of UCNPs incorporating lanthanides as fluorescent probes and their subsequent incorporation into the 3D-printed aerogels. Highly

USC UNIVERSIDADE DE SANTIAGO DE COMPOSTELA

fluorescent UCNPs were synthesized by an approach combining the co-precipitation of a lanthanide core with the formation of an extra-thin silica coating using a sol-gel method, thereby manufacturing core-shell UCNPs. A high fluorescence and physicochemical stability of the UCNPs was confirmed as well as the effectiveness of the silica as a protective layer after compatibility tests at high concentrations of UCNPs (10 mg/mL) with murine fibroblasts and human blood, with values of bio- and hemocompatibility higher than 90%. Neither the lanthanide nitrates-based UCNPs incorporation into 3D-printed alginate aerogels, nor the storage for 3 years, modified the physicochemical structure of aerogel scaffolds. Cell studies with UCNPs-doped aerogels showed no relevant differences with respect to the same formulations without UCNPs in terms of bio- and hemocompatibility, adhesion and migration performance. *In vivo* safety studies in a murine model unveiled no statistically significant differences with respect to control animals in terms of cytokines expression, tissue index and histological sections of major organs after 1-week subcutaneous implantation of UCNPs-decorated aerogels. *In vivo* bioimaging studies allow the traceability of the aerogels until a 3-week post-subcutaneous implantation due to the fluorescence properties of the UCNPs-labeled aerogels, thereby highlighting their monitoring capabilities.

3. The versatility of the dual processing manufacturing strategy was demonstrated by the production of sterile cellulose-in-cellulose aerogels and VAN-loaded methylcellulose aerogels. The high porosity in the 3D-printed methylcellulose scaffolds was preserved with mesopores and macropores homogeneously distributed throughout the aerogel structure. High cell viability and hemocompatibility was observed after murine fibroblasts and human blood contact with VAN- and HA-loaded aerogels as well as by HET-CAM test. Bioactivity was confirmed by immersion of HA-doped formulations in SBF medium and by mineralization tests in pre-osteoblasts. High loading and entrapment yield of VAN were detected for the different aerogel formulations, with a sustained

USC UNIVERSIDADE DE SANTIAGO DE COMPOSTELA

release of the antibiotic for 72 h and a coherent antimicrobial activity against *S. aureus*. Further personalization of the implants was achieved by 3D-printing of layers of different drug contents in the same scaffold structure, with a sustained release over time. The incorporation of BCNF increased the printing fidelity and structural integrity of the cellulose-in-cellulose aerogels. The doping of BCNF with SPIONs induced magnetization to the aerogel structures after application of an external magnetic field and this behavior was enhanced by increasing the content of SPIONs in the aerogels. Sterilization by using SCF in a post-processing step did not induce relevant physicochemical modifications in the 3D-printed cellulose-in-cellulose aerogels. Storage after different time periods (4 and 7 months) did not cause a detrimental effect on the textural performance of aerogels. The physicochemical stability of 3D-printed aerogels was confirmed after 3 years for alginate aerogels and after 7 months for their methylcellulose counterparts.

USC
UNIVERSIDADE DE SANTIAGO DE COMPOSTELA

USC
UNIVERSIDADE
DE SANTIAGO
DE COMPOSTELA

ANNEX 1: AUTHOR DECLARATION

DECLARACIÓNS, CONFLITO DE INTERESES E RELACIÓN DE PUBLICACIÓNS

QUE ACHEGAN CONTIDOS

CONFLITO DE INTERESE

O doutorando declara non ter ningún conflito de interese en relación coa Tese de Doutoramento.

USC
UNIVERSIDADE DE SANTIAGO DE COMPOSTELA

USC
UNIVERSIDADE
DE SANTIAGO
DE COMPOSTELA

ANNEX 2: PERMISSIONS

PERMISOS DE REPRODUCIÓN TOTAL OU PARCIAL DE TRABALLOS PUBLICADOS POLO DOUTORANDO

Source: Journal of Citation Reports and to Scopus (access date: 21/05/2024)

CHAPTER 1. INTRODUCTION

The content in this section was published in part in C.A. García-González[1*], **A. Iglesias-Mejuto[1]**, C. López-Iglesias[1], V. Santos-Rosales[1], I. Ardao[2], C. Alvarez-Lorenzo[1]; Chapter 6. Natural polymer hydrogels and aerogels for biomedical applications, in: Engineering of Natural Polymeric Gels and Aerogels for Multifunctional Applications, Elsevier, 2024: pp. 125–157. https://doi.org/10.1016/B978-0-12-823135-7.00001-2.

[1] AerogelsLab, I+D Farma group (GI-1645), Department of Pharmacology, Pharmacy and Pharmaceutical Technology, I+D Farma group (GI-1645), Faculty of Pharmacy, iMATUS and Health Research Institute of Santiago de Compostela (IDIS), Universidade de Santiago de Compostela, E-15782 Santiago de Compostela, Spain.

[2] BioFarma Research group, Centro Singular de Investigación en Medicina Molecular y Enfermedades Crónicas (CiMUS), Universidade de Santiago de Compostela, E-15782, Santiago de Compostela, Spain.

Author contribution: Bibliographic research and participation in the writing of the review text.

Journal: Elsevier Book Chapter

Peer reviewed

Editors: Sabu Thomas, Bastien Seantier, Blessy Joseph

ISBN: 9780128231364

USC UNIVERSIDADE DE SANTIAGO DE COMPOSTELA

Reproduction Permission: Permission of book chapter and figures was obtained for their reproduction in the framework of this PhD Thesis.

CHAPTER 3. 3D-PRINTED ALGINATE-HYDROXYAPATITE AEROGEL SCAFFOLDS FOR BONE TISSUE ENGINEERING

The content in this chapter was published in part in **A. Iglesias-Mejuto**, C.A. García-González*; 3D-printed alginate-hydroxyapatite aerogel scaffolds for bone tissue engineering, in: Materials Science and Engineering: C 131 (2021) 112525. https://doi.org/10.1016/j.msec.2021.112525.

Department of Pharmacology, Pharmacy and Pharmaceutical Technology, I+D Farma group (GI-1645), Faculty of Pharmacy and Health Research Institute of Santiago de Compostela (IDIS), Universidade de Santiago de Compostela, E-15782 Santiago de Compostela, Spain.

Author contribution: Investigation, methodology, and writing of the original draft of the article.

Journal: Materials Science & Engineering C-Materials for Biological Applications

ISSN: 0928-4931

Journal Impact Factor (JIF): 8.5

JIF Rank Category:

- Materials science, biomaterials: Q1 (9/45)

Citations: 70

Reproduction Permission: The article was published in Open Access.

USC UNIVERSIDADE DE SANTIAGO DE COMPOSTELA

CHAPTER 4. 3D-PRINTED, DUAL CROSSLINKED AND STERILE AEROGEL SCAFFOLDS FOR BONE TISSUE ENGINEERING

The content in this chapter was published in part in **A. Iglesias-Mejuto**, C.A. García-González*; 3D-Printed, Dual Crosslinked and Sterile Aerogel Scaffolds for Bone Tissue Engineering, in: Polymers 14 (2022) 1211. https://doi.org/10.3390/polym14061211.

Department of Pharmacology, Pharmacy and Pharmaceutical Technology, I+D Farma group (GI-1645), Faculty of Pharmacy and Health Research Institute of Santiago de Compostela (IDIS), Universidade de Santiago de Compostela, E-15782 Santiago de Compostela, Spain.

Author contribution: Investigation, methodology, and writing of the original draft of the article.

Journal: Polymers

EISSN: 2073-4360

Journal Impact Factor (JIF): 5

JIF Rank Category:

- Polymers science: Q1 (16/86)

Citations: 23

Reproduction Permission: The article was published in Open Access.

USC UNIVERSIDADE DE SANTIAGO DE COMPOSTELA

CHAPTER 5. SYNTHESIS OF HIGHLY LUMINESCENT SILICA-COATED UPCONVERSION NANOPARTICLES FROM LANTHANIDE OXIDES OR NITRATES USING CO-PRECIPITATION AND SOL–GEL METHODS

The content in this chapter was published in part in **A. Iglesias-Mejuto[1*],** A. Lamy-Mendes[2], J. Pina[3], B.F.O. Costa[4], C.A. García-González[1*], L. Durães[2]; Synthesis of Highly Luminescent Silica-Coated Upconversion Nanoparticles from Lanthanide Oxides or Nitrates Using Co-Precipitation and Sol–Gel Methods, in: Gels 10 (2023) 13. https://doi.org/10.3390/gels10010013.

[1] AerogelsLab, I + D Farma Group (GI-1645), Department of Pharmacology, Pharmacy and Pharmaceutical Technology, Faculty of Pharmacy, iMATUS and Health Research Institute of Santiago de Compostela (IDIS), Universidade de Santiago de Compostela, E-15782 Santiago de Compostela, Spain

[2] CIEPQPF, Department of Chemical Engineering, University of Coimbra, 3030-790 Coimbra, Portugal.

[3] CQC-IMS, Department of Chemistry, University of Coimbra, 3004-535 Coimbra, Portugal.

[4] CFisUC, Physics Department, University of Coimbra, 3004-516 Coimbra, Portugal.

Author contribution: Study conception, design, and investigation. Methodology, data curation, and formal analysis. Writing of the original draft of the manuscript.

The work described in this chapter was carried out in collaboration with the University of Coimbra.

Journal: Gels

EISSN: 2310-2861

Journal Impact Factor (JIF): 4.6

JIF Rank Category:

USC UNIVERSIDADE DE SANTIAGO DE COMPOSTELA

- Polymer science: Q1 (18/86)

Citations: 1

Reproduction Permission: The article was published in Open Access.

USC
UNIVERSIDADE DE SANTIAGO DE COMPOSTELA

CHAPTER 6. 3D-PRINTED AEROGELS AS THERANOSTIC IMPLANTS MONITORED BY FLUORESCENCE BIOIMAGING

The content in this chapter was submitted in part in **A. Iglesias-Mejuto[1]**, R. Pinto[2,3], P. Faísca[4], J. Catarino[5], J. Rocha[2], L. Durães[6], M.M. Gaspar[2,7], C. Pinto Reis[2,7], C.A. García-González[1*]; 3D-printed aerogels as theranostic implants monitored by fluorescence bioimaging, in: Bioactive Materials.

[1] AerogelsLab, I+D Farma Group (GI-1645), Department of Pharmacology, Pharmacy and Pharmaceutical Technology, Faculty of Pharmacy, iMATUS and Health Research Institute of Santiago de Compostela (IDIS), Universidade de Santiago de Compostela, E-15782 Santiago de Compostela, Spain

[2] Research Institute for Medicines (iMed. ULisboa), Faculty of Pharmacy, Universidade de Lisboa, Av. Professor Gama Pinto, 1649-003 Lisboa, Portugal

[3] Joaquim Chaves Saúde, Joaquim Chaves Laboratório de Análises Clínicas, Miraflores, 1495069 Algés, Portugal

[4] CECAV-Faculty of Veterinary Medicina- Lusófona University- Lisbon University Center, Campo Grande 376,1749024 Lisboa, Portugal

[5] Faculty of Veterinary Medicina- Lusófona University- Lisbon University Center, Campo Grande 376,1749024 Lisboa, Portugal

[6] University of Coimbra, CERES-Chemical Engineering and Renewable Resources for Sustainability, Department of Chemical Engineering, 3030-790 Coimbra, Portugal

[7] Instituto de Biofísica e Engenharia Biomédica (IBEB), Faculdade de Ciências, Universidade de Lisboa, Campo Grande, 1749-016 Lisboa, Portugal

Author contribution: Study conception, design, and investigation. Methodology, data curation, formal analysis and writing of the original draft of the manuscript.

USC UNIVERSIDADE DE SANTIAGO DE COMPOSTELA

ANNEX 2: PERMISSIONS

The work described in this chapter was carried out in collaboration with the University of Coimbra and the University of Lisbon.

Journal: Bioactive materials

EISSN: 2452-199X

Journal Impact Factor (JIF): 18.9

JIF Rank Category:

- Biomedical engineering: Q1 (2/96)
- Materials science, biomaterials: Q1 (1/45)

USC
UNIVERSIDADE DE SANTIAGO DE COMPOSTELA

CHAPTER 7. VANCOMYCIN-LOADED METHYLCELLULOSE AEROGEL SCAFFOLDS FOR ADVANCED BONE TISSUE ENGINEERING

The content in this chapter was published in part in **A. Iglesias-Mejuto[1],** B. Magariños[2], T. Ferreira-Gonçalves[3,4], R. Starbird-Pérez[5,6], C. Álvarez-Lorenzo[1], C.P. Reis[3,4], I. Ardao[7], C.A. García-González[1*]; Vancomycin-Loaded Methylcellulose Aerogel Scaffolds for Advanced Bone Tissue Engineering, in: *Carbohydrate Polymers* 324 (2024) 121536. doi:10.1016/j.carbpol.2023.121536.

[1] I+D Farma Group (GI-1645), Department of Pharmacology, Pharmacy and Pharmaceutical Technology, Faculty of Pharmacy, iMATUS and Health Research Institute of Santiago de Compostela (IDIS), Universidade de Santiago de Compostela, E-15782 Santiago de Compostela, Spain.

[2] Departamento de Microbiología y Parasitología, Facultad de Biología, CIBUS, Universidade de Santiago de Compostela, E-15782 Santiago de Compostela, Spain.

[3] Research Institute for Medicines (iMed.ULisboa), Faculty of Pharmacy, Universidade de Lisboa, Av. Professor Gama Pinto, 1649-003 Lisboa, Portugal.

[4] Instituto de Biofísica e Engenharia Biomédica, Faculdade de Ciências, Universidade de Lisboa, Campo Grande, 1749-016 Lisboa, Portugal.

[5] Centro de Investigación y de Servicios Químicos y Microbiológicos (CEQIATEC), School of Chemistry, Instituto Tecnológico de Costa Rica, 159-7050 Cartago, Costa Rica.

[6] Centro de Investigación en Ciencia e Ingeniería de Materiales (CICIMA), Universidad de Costa Rica, 11501-2060 San José, Costa Rica.

[7] BioFarma Research group, Department of Pharmacology, Pharmacy and Pharmaceutical Technology, Innopharma Drug Screening and Pharmacogenomics Platform, Centro Singular de Investigación en Medicina Molecular y Enfermedades Crónicas (CiMUS), Universidade de Santiago de Compostela, E-15782, Santiago de Compostela, Spain.

USC UNIVERSIDADE DE SANTIAGO DE COMPOSTELA

Author contribution: Study conception and design. Material preparation, data collection and analysis. Written of the first draft of the manuscript.

The work described in this chapter was carried out in collaboration with the University of Lisbon and with the University of Costa Rica.

Journal: Carbohydrate Polymers

ISSN: 0144-8617

Journal Impact Factor (JIF): 11.2

JIF Rank Category:

- Applied chemistry: Q1 (3/73)
- Organic Chemistry: Q1 (2/52)

Citations: 2

Reproduction Permission: The article was published in Open Access.

USC
UNIVERSIDADE DE SANTIAGO DE COMPOSTELA

CHAPTER 8. CELLULOSE-IN-CELLULOSE 3D-PRINTED BIOAEROGELS FOR BONE TISSUE ENGINEERING

The content in this chapter was published in part in **A. Iglesias-Mejuto[1],** N. Malandain[2,3], T. Ferreira-Gonçalves[4,5], I. Ardao[6], C.P. Reis[4,5], A. Laromaine[2], A. Roig[2], C.A. García-González[1*]; Cellulose-in-cellulose 3D-printed bioaerogels for bone tissue engineering, in: Cellulose 31 (2024) 515–534. https://doi.org/10.1007/s10570-023-05601-1.

[1] I+D Farma Research Group (GI-1645), Department of Pharmacology, Pharmacy and Pharmaceutical Technology, Faculty of Pharmacy, iMATUS and Health Research Institute of Santiago de Compostela (IDIS), Universidade de Santiago de Compostela, E-15782 Santiago de Compostela, Spain.

[2] Institut de Ciència de Materials de Barcelona, ICMAB-CSIC, Campus UAB, 08193 Bellaterra, Spain.

[3] Unitat de Biofísica i Bioenginyeria, Facultat de Medicina i Ciències de la Salut, Universitat de Barcelona, 08036 Barcelona, Spain.

[4] Research Institute for Medicines (iMed.ULisboa), Faculty of Pharmacy, Universidade de Lisboa, Av. Professor Gama Pinto, 1649-003 Lisboa, Portugal.

[5] Instituto de Biofísica e Engenharia Biomédica (IBEB), Faculdade de Ciências, Universidade de Lisboa, Campo Grande, 1749-016 Lisboa, Portugal.

[6] BioFarma Research group, Department of Pharmacology, Pharmacy and Pharmaceutical Technology, Innopharma Drug Screening and Pharmacogenomics Platform, Centro Singular de Investigación en Medicina Molecular y Enfermedades Crónicas (CiMUS), Universidade de Santiago de Compostela, E-15782, Santiago de Compostela, Spain.

Author contribution: Study conception and design. Material preparation, data collection and analysis. Writing of the first draft of the manuscript.

USC UNIVERSIDADE DE SANTIAGO DE COMPOSTELA

ANNEX 2: PERMISSIONS

The work described in this chapter was carried out in collaboration with the Institut de Ciència de Materials de Barcelona (ICMABCSIC) and the University of Lisbon.

Journal: Cellulose

ISSN: 0969-0239

Journal Impact Factor (JIF): 5.7

JIF Rank Category:

- Materials science, paper, and wood: Q1 (1/21)
- Materials science textiles: Q1 (2/26)

Reproduction Permission: The article was published in Open Access.

USC UNIVERSIDADE DE SANTIAGO DE COMPOSTELA

USC
UNIVERSIDADE
DE SANTIAGO
DE COMPOSTELA

ANNEX 3: ETHICAL APPROVALS

ORBEA ÓRGÃO RESPONSÁVEL PELO BEM-ESTAR ANIMAL

Parecer

Foi submetido ao ORBEA da Faculdade de Farmácia da Universidade de Lisboa um pedido de parecer, para a realização de um protocolo de investigação envolvendo experimental animal, acompanhado do formulário da DGAV para pedido de autorização de projeto de utilização de animais para fins científicos.

O protocolo de experimentação animal insere-se no âmbito do projeto "**Novas nanoplataformas terapêuticas com complexos metálicos no tratamento de cancro**" sendo a investigadora responsável a Profª. Doutora Ana Catarina Beco Pinto Reis.

O protocolo de experimentação animal será realizado no Biotério do Campus do Lumiar da Faculdade de Farmácia da Universidade de Lisboa, sob a responsabilidade de investigadores creditados.

No âmbito do presente protocolo experimental foram avaliados em particular os seguintes parâmetros:

- Instrução do pedido
- Cumprimento dos 3Rs
- Benefício / Risco
- Categorias de severidade do(s) procedimento(s)
- Nº de animais e duração do protocolo

De acordo com os parâmetros avaliados e em conformidade com a legislação em vigor, o ORBEA emite parecer favorável relativamente à realização do presente protocolo de investigação.

Presidente do ORBEA, da Faculdade de Farmácia da Universidade de Lisboa

Profª Doutora Maria Beatriz da Silva Lima

Av. Prof. Gama Pinto, 1649-003 Lisboa |
t. +351 217 946 400 | f. +351 217 946 470 | orbea@ff.ulisboa.pt

USC UNIVERSIDADE DE SANTIAGO DE COMPOSTELA

XUNTA DE GALICIA | CONSELLERÍA DO MEDIO RURAL

RESOLUCIÓN DE AUTORIZACIÓN DE PROXECTO DE EXPERIMENTACIÓN ANIMAL

Expediente núm.: 15012/2023/010
Data de inicio do expediente: 3.5.2023
Persoa solicitante: Anxo Vidal Figueroa
Procedemento: resolución de autorización
Forma de inicio: solicitude da persoa interesada

ANTECEDENTES

A persoa solicitante, como representante do Centro de Biomedicina Experimental CEBEGA, presentou con data 3.5.2023 unha solicitude para a realización do proxecto de experimentación animal (entrada no Rexistro Electrónico da Xunta de Galicia 2023/1336814), cuxos datos se detallan a continuación:

Denominación do proxecto: "Estudio de las propiedades luminiscentes de aerogeles in vivo, una prueba de concepto".
Nome do centro usuario: Centro de Biomedicina Experimental CEBEGA
Persoa responsable do proxecto: Anxo Vidal Figueroa
Establecemento onde se realizarán os procedementos do proxecto (ou lugar xeográfico no caso de traballos de campo): Centro de Biomedicina Experimental da USC (CEBEGA) (ES1507800292901)
Clasificación do proxecto: Tipo I [ ] Tipo II [X] Tipo III [ ]

CONSIDERACIÓNS LEGAIS E TÉCNICAS

1 O Real decreto 53/2013, de 1 de febreiro (BOE 34, do 8 de febreiro), polo que se establecen as normas básicas aplicables para a protección dos animais utilizados en experimentación e outros fins científicos, incluíndo a docencia, establece no seu artigo 33 as condicións de autorizacións dos proxectos con animais de experimentación.

2 O artigo 88 da Lei 39/2015, de 1 de outubro, do procedemento administrativo común das administracións públicas (BOE 236, do 2 de outubro de 2015) establece que a resolución que poña fin o procedemento decidirá todas as cuestións expostas polos interesados e aquelas outras derivadas deste.

CONSELLERÍA DO MEDIO RURAL
XEFATURA TERRITORIAL
SERVIZO DE GANDARÍA
Edificio Administrativo Monelos
R/ Vicente Ferrer, 2, 4º andar
15071 A Coruña
T: 981 184 565
servizo.gandaria.a.coruna@xunta.gal
mediorural.xunta.gal

USC UNIVERSIDADE DE SANTIAGO DE COMPOSTELA

3 O Servizo de Gandaría da Coruña revisou a documentación achegada na solicitude e o resultado favorable da avaliación do proxecto realizada polo órgano habilitado, o Comité de Bioética de Experimentación Animal da Universidade de Santiago de Compostela.

Esta xefatura territorial é competente para ditar unha resolución, de conformidade co Decreto 149/2018, do 5 de decembro, polo que se establece a estrutura orgánica da Consellería do Medio Rural e se modifica parcialmente o Decreto 177/2016, do 15 de decembro, polo que se fixa a estrutura orgánica da Vicepresidencia e das consellerías da Xunta de Galicia (DOG 235, do 11 de novembro).

De acordo con todo o indicado, RESOLVO:

1 Autorizar o proxecto solicitado.

2 O proxecto non precisa someterse a unha avaliación retrospectiva.

3 A autorización deste proxecto terá unha duración de 12 meses.

A citada autorización é unicamente válida nas condicións que figuran no expediente. Ante calquera cambio significativo no proxecto que poida ter efectos negativos sobre o benestar dos animais, deberá solicitar a confirmación da autorización ao Servizo Provincial de Gandaría.

Esta autorización poderá ser suspendida no caso de que o proxecto non se leve a cabo de acordo coas condicións de autorización e retirala, previo expediente tramitado ao que se lle dará audiencia.

Contra a presente resolución, que non pon fin á vía administrativa, poderá interpoñer un recurso de alzada ante o conselleiro de Medio Rural. O prazo comezará a contar dende o día seguinte ao da recepción desta resolución. Todo isto, segundo o disposto nos artigos 121 e 122 da citada Lei 39/2015.

Mediante este escrito notificaselle a Anxo Vidal Figueroa esta resolución segundo o esixido no artigo 40.1 da antedita Lei 39/2015.

A Coruña, 10 de maio de 2023
O xefe territorial
Jose Manuel Santos Maneiro

Asinado por: JUANTOS MANEIRO, JOSÉ MANUEL
Cargo: Xefe Territorial
Data e hora: 10/05/2023 10:54:28

Verificación: https://libredoc.xunta.gal/cove

Marketplace

Order Confirmation

Thank you, your order has been placed. An email confirmation has been sent to you. Your order license details and printable licenses will be available within 24 hours. Please access Manage Account for final order details.

This is not an invoice. Please go to manage account to access your order history and invoices.

CUSTOMER INFORMATION

Payment by invoice: You can cancel your order until the invoice is generated by contacting customer service.

Billing Address

Ms. Ana Iglesias-Mejuto
Praza do Seminario de Estudos Galegos 15705
Santiago De Compostela
Spain

+34 881814993
ana.iglesias.mejuto@rai.usc.es

Customer Location

Ms. Ana Iglesias-Mejuto
Praza do Seminario de Estudos Galegos 15705
Santiago De Compostela
Spain

PO Number (optional)

N/A

Payment options

Invoice

PENDING ORDER CONFIRMATION

Confirmation Number: Pending

Order Date: 18-May-2024

1. Engineering of Natural Polymeric Gels and Aerogels for Multifunctional Applications

0,00 EUR

Article: Natural polymer hydrogels and aerogels for biomedical applications

Order License ID	Pending	**Publisher**	Elsevier Science
ISBN-13	9780128231357	**Portion**	Chapter/article
Type of Use	Republish in a thesis/dissertation		

LICENSED CONTENT

Publication Title	Engineering of Natural Polymeric Gels and Aerogels for Multifunctional Applications	**Rightsholder**	Elsevier Science & Technology Journals
		Publication Type	Book
		Start Page	125
Article Title	Natural polymer hydrogels and aerogels for biomedical applications	**End Page**	157
Date	02/19/2024		
Language	English		
Country	United States of America		

REQUEST DETAILS

Portion Type	Chapter/article	**Rights Requested**	Main product
Page Range(s)	125-157	**Distribution**	Worldwide
Total Number of Pages	32	**Translation**	Original language of publication
Format (select all that apply)	Print, Electronic	**Copies for the Disabled?**	No
Who Will Republish the Content?	Academic institution	**Minor Editing Privileges?**	No
Duration of Use	Life of current edition	**Incidental Promotional Use?**	No
Lifetime Unit Quantity	Up to 499	**Currency**	EUR

NEW WORK DETAILS

Title	Development of aerogel-based formulations for regenerative medicine	**Institution Name**	University of Santiago de Compostela
		Expected Presentation Date	2024-07-26
Instructor Name	Carlos Alberto García González		

ADDITIONAL DETAILS

Order Reference Number	N/A	**The Requesting Person / Organization to Appear on the License**	Ana Iglesias Mejuto (USC)

REQUESTED CONTENT DETAILS

Title, Description or Numeric Reference of the Portion(s)	Chapter 5-Natural polymer hydrogels and aerogels for biomedical applications	**Title of the Article / Chapter the Portion Is From**	Natural polymer hydrogels and aerogels for biomedical applications

Editor of Portion(s)	García-González, Carlos A.; Iglesias-Mejuto, Ana; López-Iglesias, Clara; Santos-Rosales, Víctor; Ardao, Inés; Alvarez-Lorenzo, Carmen	**Author of Portion(s)**	García-González, Carlos A.; Iglesias-Mejuto, Ana; López-Iglesias, Clara; Santos-Rosales, Víctor; Ardao, Inés; Alvarez-Lorenzo, Carmen
Volume / Edition	N/A	**Issue, if Republishing an Article From a Serial**	N/A
Page or Page Range of Portion	125-157	**Publication Date of Portion**	2024-01-01

RIGHTSHOLDER TERMS AND CONDITIONS

Elsevier publishes Open Access articles in both its Open Access journals and via its Open Access articles option in subscription journals, for which an author selects a user license permitting certain types of reuse without permission. Before proceeding please check if the article is Open Access on http://www.sciencedirect.com and refer to the user license for the individual article. Any reuse not included in the user license terms will require permission. You must always fully and appropriately credit the author and source. If any part of the material to be used (for example, figures) has appeared in the Elsevier publication for which you are seeking permission, with credit or acknowledgement to another source it is the responsibility of the user to ensure their reuse complies with the terms and conditions determined by the rights holder. Please contact permissions@elsevier.com with any queries.

Total Items: 1

Total Due: 0,00 EUR

Accepted: Marketplace Permissions General Terms and Conditions and any applicable Publisher Terms and Conditions

Marketplace

Order Confirmation

Thank you, your order has been placed. An email confirmation has been sent to you. Your order license details and printable licenses will be available within 24 hours. Please access Manage Account for final order details.

This is not an invoice. Please go to manage account to access your order history and invoices.

CUSTOMER INFORMATION

Payment by invoice: You can cancel your order until the invoice is generated by contacting customer service.

Billing Address

Ms. Ana Iglesias-Mejuto
Praza do Seminario de Estudos Galegos 15705
Santiago De Compostela
Spain

+34 881814993
ana.iglesias.mejuto@rai.usc.es

Customer Location

Ms. Ana Iglesias-Mejuto
Praza do Seminario de Estudos Galegos 15705
Santiago De Compostela
Spain

PO Number (optional)

N/A

Payment options

Invoice

PENDING ORDER CONFIRMATION

Confirmation Number: Pending

Order Date: 18-May-2024

1. Nanomedicine : nanotechnology, biology and medicine

0,00 EUR

Article: Bioresponsive peptide-polysaccharide nanogels — A versatile delivery system to augment the utility of bioactive cargo

Order License ID	Pending	**Publisher**	ELSEVIER INC
ISSN	1549-9634	**Portion**	Chart/graph/table/figure
Type of Use	Republish in a thesis/dissertation		

LICENSED CONTENT

Publication Title	Nanomedicine : nanotechnology, biology and medicine	**Rightsholder**	Elsevier Science & Technology Journals
Article Title	Bioresponsive peptide-polysaccharide nanogels — A versatile delivery system to augment the utility of bioactive cargo	**Publication Type**	Journal
		Start Page	391
		End Page	400
		Volume	17
Author/Editor	American Academy of Nanomedicine.	**URL**	http://www.journals.elsevier.com/nanomedicine-nanotechnology-biology-and-medicine/
Date	03/01/2005		
Language	English		
Country	United States of America		

REQUEST DETAILS

Portion Type	Chart/graph/table/figure	**Distribution**	Worldwide
Number of Charts / Graphs / Tables / Figures Requested	3	**Translation**	Original language of publication
		Copies for the Disabled?	No
Format (select all that apply)	Print, Electronic	**Minor Editing Privileges?**	No
Who Will Republish the Content?	Academic institution	**Incidental Promotional Use?**	No
Duration of Use	Life of current edition	**Currency**	EUR
Lifetime Unit Quantity	Up to 499		
Rights Requested	Main product		

NEW WORK DETAILS

Title	Development of aerogel-based formulations for regenerative medicine	**Institution Name**	University of Santiago de Compostela (USC)
		Expected Presentation Date	2024-07-26
Instructor Name	Carlos Alberto García González		

ADDITIONAL DETAILS

Order Reference Number	N/A	**The Requesting Person / Organization to Appear on the License**	Ana Iglesias Mejuto (USC)

REQUESTED CONTENT DETAILS

Title, Description or Numeric Reference of the Portion(s)	Graphical Abstract, Figure 5, Figure 6	**Title of the Article / Chapter the Portion Is From**	Bioresponsive peptide-polysaccharide nanogels — A versatile delivery system to augment the utility of bioactive cargo

Editor of Portion(s)	Simonson, Andrew W.; Lawanprasert, Atip; Goralski, Tyler D.P.; Keiler, Kenneth C.; Medina, Scott H.	**Author of Portion(s)**	Simonson, Andrew W.; Lawanprasert, Atip; Goralski, Tyler D.P.; Keiler, Kenneth C.; Medina, Scott H.
Volume / Edition	17	**Issue, if Republishing an Article From a Serial**	N/A
Page or Page Range of Portion	391-400	**Publication Date of Portion**	2019-04-01

RIGHTSHOLDER TERMS AND CONDITIONS

Elsevier publishes Open Access articles in both its Open Access journals and via its Open Access articles option in subscription journals, for which an author selects a user license permitting certain types of reuse without permission. Before proceeding please check if the article is Open Access on http://www.sciencedirect.com and refer to the user license for the individual article. Any reuse not included in the user license terms will require permission. You must always fully and appropriately credit the author and source. If any part of the material to be used (for example, figures) has appeared in the Elsevier publication for which you are seeking permission, with credit or acknowledgement to another source it is the responsibility of the user to ensure their reuse complies with the terms and conditions determined by the rights holder. Please contact permissions@elsevier.com with any queries.

Total Items: 1

Total Due: 0,00 EUR

Accepted: Marketplace Permissions General Terms and Conditions and any applicable Publisher Terms and Conditions

Marketplace

Order Confirmation

Thank you, your order has been placed. An email confirmation has been sent to you. Your order license details and printable licenses will be available within 24 hours. Please access Manage Account for final order details.

This is not an invoice. Please go to manage account to access your order history and invoices.

CUSTOMER INFORMATION

Payment by invoice: You can cancel your order until the invoice is generated by contacting customer service.

Billing Address

Ms. Ana Iglesias-Mejuto
Praza do Seminario de Estudos Galegos 15705
Santiago De Compostela
Spain

+34 881814993
ana.iglesias.mejuto@rai.usc.es

Customer Location

Ms. Ana Iglesias-Mejuto
Praza do Seminario de Estudos Galegos 15705
Santiago De Compostela
Spain

PO Number (optional)

N/A

Payment options

Invoice

PENDING ORDER CONFIRMATION

Confirmation Number: Pending

Order Date: 18-May-2024

1. The Journal of supercritical fluids

0,00 EUR

Article: An emulsification/internal setting technique for the preparation of coated and uncoated hybrid silica/alginate aerogel beads for controlled drug delivery

Order License ID	Pending	**Publisher**	ELSEVIER BV
ISSN	0896-8446	**Portion**	Chart/graph/table/figure
Type of Use	Republish in a thesis/dissertation		

LICENSED CONTENT

Publication Title	The Journal of supercritical fluids	**Rightsholder**	Elsevier Science & Technology Journals
Article Title	An emulsification/internal setting technique for the preparation of coated and uncoated hybrid silica/alginate aerogel beads for controlled drug delivery	**Publication Type**	Journal
		Start Page	1
		End Page	9
		Volume	142
Date	01/01/1988		
Language	Dutch		
Country	Netherlands		

REQUEST DETAILS

Portion Type	Chart/graph/table/figure	**Distribution**	Worldwide
Number of Charts / Graphs / Tables / Figures Requested	2	**Translation**	Original language of publication
		Copies for the Disabled?	No
Format (select all that apply)	Print, Electronic	**Minor Editing Privileges?**	No
Who Will Republish the Content?	Academic institution	**Incidental Promotional Use?**	No
Duration of Use	Life of current edition	**Currency**	EUR
Lifetime Unit Quantity	Up to 499		
Rights Requested	Main product		

NEW WORK DETAILS

Title	Development of aerogel-based formulations for regenerative medicine	**Institution Name**	University of Santiago de Compostela (USC)
		Expected Presentation Date	2024-07-26
Instructor Name	Carlos Alberto García González		

ADDITIONAL DETAILS

Order Reference Number	N/A	**The Requesting Person / Organization to Appear on the License**	Ana Iglesias Mejuto (USC)

REQUESTED CONTENT DETAILS

Title, Description or Numeric Reference of the Portion(s)	Figure3, Figure 5	**Title of the Article / Chapter the Portion Is From**	An emulsification/internal setting technique for the preparation of coated and uncoated hybrid silica/alginate aerogel beads for controlled drug delivery
Editor of Portion(s)	Banchero, Mauro; Bugnone, Cristiano Agostino; Manna, Luigi; Ronchetti, Silvia		

Volume / Edition	142	**Author of Portion(s)**	Banchero, Mauro; Bugnone, Cristiano Agostino; Manna, Luigi; Ronchetti, Silvia
Page or Page Range of Portion	1-9	**Issue, if Republishing an Article From a Serial**	N/A
		Publication Date of Portion	2018-12-01

RIGHTSHOLDER TERMS AND CONDITIONS

Elsevier publishes Open Access articles in both its Open Access journals and via its Open Access articles option in subscription journals, for which an author selects a user license permitting certain types of reuse without permission. Before proceeding please check if the article is Open Access on http://www.sciencedirect.com and refer to the user license for the individual article. Any reuse not included in the user license terms will require permission. You must always fully and appropriately credit the author and source. If any part of the material to be used (for example, figures) has appeared in the Elsevier publication for which you are seeking permission, with credit or acknowledgement to another source it is the responsibility of the user to ensure their reuse complies with the terms and conditions determined by the rights holder. Please contact permissions@elsevier.com with any queries.

Total Items: 1

Total Due: 0,00 EUR

Accepted: Marketplace Permissions General Terms and Conditions and any applicable Publisher Terms and Conditions

Marketplace

Order Confirmation

Thank you, your order has been placed. An email confirmation has been sent to you. Your order license details and printable licenses will be available within 24 hours. Please access Manage Account for final order details.

This is not an invoice. Please go to manage account to access your order history and invoices.

CUSTOMER INFORMATION

Payment by invoice: You can cancel your order until the invoice is generated by contacting customer service.

Billing Address

Ms. Ana Iglesias-Mejuto
Praza do Seminario de Estudos Galegos 15705
Santiago De Compostela
Spain

+34 881814993
ana.iglesias.mejuto@rai.usc.es

Customer Location

Ms. Ana Iglesias-Mejuto
Praza do Seminario de Estudos Galegos 15705
Santiago De Compostela
Spain

PO Number (optional)

N/A

Payment options

Invoice

PENDING ORDER CONFIRMATION

Confirmation Number: Pending

Order Date: 18-May-2024

1. Powder technology

0,00 EUR

Article: Influence of coating and wetting on the mechanical behaviour of highly porous cylindrical aerogel particles

Order License ID	Pending	**Publisher**	ELSEVIER S.A.
ISSN	0032-5910	**Portion**	Chart/graph/table/figure
Type of Use	Republish in a thesis/dissertation		

LICENSED CONTENT

Publication Title	Powder technology	**Rightsholder**	Elsevier Science & Technology Journals
Article Title	Influence of coating and wetting on the mechanical behaviour of highly porous cylindrical aerogel particles	**Publication Type**	Journal
		Start Page	34
		End Page	43
Date	01/01/1967	**Volume**	285
Language	English, English, French, German		
Country	Switzerland		

REQUEST DETAILS

Portion Type	Chart/graph/table/figure	**Distribution**	Worldwide
Number of Charts / Graphs / Tables / Figures Requested	2	**Translation**	Original language of publication
		Copies for the Disabled?	No
Format (select all that apply)	Print, Electronic	**Minor Editing Privileges?**	No
Who Will Republish the Content?	Academic institution	**Incidental Promotional Use?**	No
Duration of Use	Life of current edition	**Currency**	EUR
Lifetime Unit Quantity	Up to 499		
Rights Requested	Main product		

NEW WORK DETAILS

Title	Development of aerogel-based formulations for regenerative medicine	**Institution Name**	University of Santiago de Compostela
		Expected Presentation Date	2024-07-26
Instructor Name	Carlos Alberto García Gonzalez		

ADDITIONAL DETAILS

Order Reference Number	N/A	**The Requesting Person / Organization to Appear on the License**	Ana Iglesias Mejuto (USC)

REQUESTED CONTENT DETAILS

Title, Description or Numeric Reference of the Portion(s)	Figure 1, Figure 6	**Title of the Article / Chapter the Portion Is From**	Influence of coating and wetting on the mechanical behaviour of highly porous cylindrical aerogel particles
Editor of Portion(s)	Antonyuk, Sergiy; Heinrich, Stefan; Gurikov, Pavel; Raman, Subrahmanyam; Smirnova, Irina	**Author of Portion(s)**	Antonyuk, Sergiy; Heinrich, Stefan; Gurikov, Pavel; Raman, Subrahmanyam; Smirnova, Irina
Volume / Edition	285		

Page or Page Range of Portion	34-43	**Issue, if Republishing an Article From a Serial**	N/A
		Publication Date of Portion	2015-11-01

RIGHTSHOLDER TERMS AND CONDITIONS

Elsevier publishes Open Access articles in both its Open Access journals and via its Open Access articles option in subscription journals, for which an author selects a user license permitting certain types of reuse without permission. Before proceeding please check if the article is Open Access on http://www.sciencedirect.com and refer to the user license for the individual article. Any reuse not included in the user license terms will require permission. You must always fully and appropriately credit the author and source. If any part of the material to be used (for example, figures) has appeared in the Elsevier publication for which you are seeking permission, with credit or acknowledgement to another source it is the responsibility of the user to ensure their reuse complies with the terms and conditions determined by the rights holder. Please contact permissions@elsevier.com with any queries.

Total Items: 1

Total Due: 0,00 EUR

Accepted: Marketplace Permissions General Terms and Conditions and any applicable Publisher Terms and Conditions

Marketplace

Order Confirmation

Thank you, your order has been placed. An email confirmation has been sent to you. Your order license details and printable licenses will be available within 24 hours. Please access Manage Account for final order details.

This is not an invoice. Please go to manage account to access your order history and invoices.

CUSTOMER INFORMATION

Payment by invoice: You can cancel your order until the invoice is generated by contacting customer service.

Billing Address

Ms. Ana Iglesias-Mejuto
Praza do Seminario de Estudos Galegos 15705
Santiago De Compostela
Spain

+34 881814993
ana.iglesias.mejuto@rai.usc.es

Customer Location

Ms. Ana Iglesias-Mejuto
Praza do Seminario de Estudos Galegos 15705
Santiago De Compostela
Spain

PO Number (optional)

N/A

Payment options

Invoice

PENDING ORDER CONFIRMATION

Confirmation Number: Pending

Order Date: 18-May-2024

1. Carbohydrate polymers

0,00 EUR

Article: Characterisation of biodegradable pectin aerogels and their potential use as drug carriers.

Order License ID	Pending	**Publisher**	PERGAMON
ISSN	0144-8617	**Portion**	Chart/graph/table/figure
Type of Use	Republish in a thesis/dissertation		

LICENSED CONTENT

Publication Title	Carbohydrate polymers	**Rightsholder**	Elsevier Science & Technology Journals
Article Title	Characterisation of biodegradable pectin aerogels and their potential use as drug carriers.	**Publication Type**	Journal
		Start Page	272
		End Page	278
Date	01/01/1981	**Volume**	113
Language	English, English		
Country	United Kingdom of Great Britain and Northern Ireland		

REQUEST DETAILS

Portion Type	Chart/graph/table/figure	**Distribution**	Worldwide
Number of Charts / Graphs / Tables / Figures Requested	1	**Translation**	Original language of publication
		Copies for the Disabled?	No
Format (select all that apply)	Print, Electronic	**Minor Editing Privileges?**	No
Who Will Republish the Content?	Academic institution	**Incidental Promotional Use?**	No
Duration of Use	Life of current edition	**Currency**	EUR
Lifetime Unit Quantity	Up to 499		
Rights Requested	Main product		

NEW WORK DETAILS

Title	Development of aerogel-based formulations for regenerative medicine	**Institution Name**	University of Santiago de Compostela (USC)
		Expected Presentation Date	2024-07-26
Instructor Name	Carlos Alberto García González		

ADDITIONAL DETAILS

Order Reference Number	N/A	**The Requesting Person / Organization to Appear on the License**	Ana Iglesias Mejuto (USC)

REQUESTED CONTENT DETAILS

Title, Description or Numeric Reference of the Portion(s)	Figure 1	**Title of the Article / Chapter the Portion Is From**	Characterisation of biodegradable pectin aerogels and their potential use as drug carriers.
Editor of Portion(s)	Veronovski, Anja; Tkalec, Gabrijela; Knez, Željko; Novak, Zoran	**Author of Portion(s)**	Veronovski, Anja; Tkalec, Gabrijela; Knez, Željko; Novak, Zoran
Volume / Edition	113		

Page or Page Range of Portion	272-278	**Issue, if Republishing an Article From a Serial**	N/A
		Publication Date of Portion	2014-11-26

RIGHTSHOLDER TERMS AND CONDITIONS

Elsevier publishes Open Access articles in both its Open Access journals and via its Open Access articles option in subscription journals, for which an author selects a user license permitting certain types of reuse without permission. Before proceeding please check if the article is Open Access on http://www.sciencedirect.com and refer to the user license for the individual article. Any reuse not included in the user license terms will require permission. You must always fully and appropriately credit the author and source. If any part of the material to be used (for example, figures) has appeared in the Elsevier publication for which you are seeking permission, with credit or acknowledgement to another source it is the responsibility of the user to ensure their reuse complies with the terms and conditions determined by the rights holder. Please contact permissions@elsevier.com with any queries.

Total Items: 1

Total Due: 0,00 EUR

Accepted: Marketplace Permissions General Terms and Conditions and any applicable Publisher Terms and Conditions

Marketplace

Order Confirmation

Thank you, your order has been placed. An email confirmation has been sent to you. Your order license details and printable licenses will be available within 24 hours. Please access Manage Account for final order details.

This is not an invoice. Please go to manage account to access your order history and invoices.

CUSTOMER INFORMATION

Payment by invoice: You can cancel your order until the invoice is generated by contacting customer service.

Billing Address

Ms. Ana Iglesias-Mejuto
Praza do Seminario de Estudos Galegos 15705
Santiago De Compostela
Spain

+34 881814993
ana.iglesias.mejuto@rai.usc.es

Customer Location

Ms. Ana Iglesias-Mejuto
Praza do Seminario de Estudos Galegos 15705
Santiago De Compostela
Spain

PO Number (optional)

N/A

Payment options

Invoice

PENDING ORDER CONFIRMATION

Confirmation Number: Pending

Order Date: 18-May-2024

1. International journal of pharmaceutics

0,00 EUR

Article: Comparison of ionic and non-ionic drug release from multi-membrane spherical aerogels.

Order License ID	Pending	**Publisher**	ELSEVIER BV
ISSN	0378-5173	**Portion**	Chart/graph/table/figure
Type of Use	Republish in a thesis/dissertation		

LICENSED CONTENT

Publication Title	International journal of pharmaceutics	**Publication Type**	Journal
Article Title	Comparison of ionic and non-ionic drug release from multi-membrane spherical aerogels.	**Start Page**	58
		End Page	66
		Issue	1
		Volume	454
Date	01/01/1978		
Language	English		
Country	Netherlands		
Rightsholder	Elsevier Science & Technology Journals		

REQUEST DETAILS

Portion Type	Chart/graph/table/figure	**Distribution**	Worldwide
Number of Charts / Graphs / Tables / Figures Requested	1	**Translation**	Original language of publication
		Copies for the Disabled?	No
Format (select all that apply)	Print, Electronic	**Minor Editing Privileges?**	No
Who Will Republish the Content?	Academic institution	**Incidental Promotional Use?**	No
Duration of Use	Life of current edition	**Currency**	EUR
Lifetime Unit Quantity	Up to 499		
Rights Requested	Main product		

NEW WORK DETAILS

Title	Development of aerogel-based formulations for regenerative medicine	**Institution Name**	University of Santiago de Compostela
		Expected Presentation Date	2024-07-26
Instructor Name	Carlos Alberto García González		

ADDITIONAL DETAILS

Order Reference Number	N/A	**The Requesting Person / Organization to Appear on the License**	Ana Iglesias Mejuto (USC)

REQUESTED CONTENT DETAILS

Title, Description or Numeric Reference of the Portion(s)	Figure 6	**Title of the Article / Chapter the Portion Is From**	Comparison of ionic and non-ionic drug release from multi-membrane spherical aerogels.
Editor of Portion(s)	Veronovski, Anja; Knez, Å½eljko; Novak, Zoran	**Author of Portion(s)**	Veronovski, Anja; Knez, Å½eljko; Novak, Zoran
Volume / Edition	454		
Page or Page Range of Portion	58-66	**Issue, if Republishing an Article From a Serial**	1

Publication Date of Portion	2013-09-15

RIGHTSHOLDER TERMS AND CONDITIONS

Elsevier publishes Open Access articles in both its Open Access journals and via its Open Access articles option in subscription journals, for which an author selects a user license permitting certain types of reuse without permission. Before proceeding please check if the article is Open Access on http://www.sciencedirect.com and refer to the user license for the individual article. Any reuse not included in the user license terms will require permission. You must always fully and appropriately credit the author and source. If any part of the material to be used (for example, figures) has appeared in the Elsevier publication for which you are seeking permission, with credit or acknowledgement to another source it is the responsibility of the user to ensure their reuse complies with the terms and conditions determined by the rights holder. Please contact permissions@elsevier.com with any queries.

Total Items: 1

Total Due: 0,00 EUR

Accepted: Marketplace Permissions General Terms and Conditions and any applicable Publisher Terms and Conditions

Marketplace

Order Confirmation

Thank you, your order has been placed. An email confirmation has been sent to you. Your order license details and printable licenses will be available within 24 hours. Please access Manage Account for final order details.

This is not an invoice. Please go to manage account to access your order history and invoices.

CUSTOMER INFORMATION

Payment by invoice: You can cancel your order until the invoice is generated by contacting customer service.

Billing Address

Ms. Ana Iglesias-Mejuto
Praza do Seminario de Estudos Galegos 15705
Santiago De Compostela
Spain

+34 881814993
ana.iglesias.mejuto@rai.usc.es

Customer Location

Ms. Ana Iglesias-Mejuto
Praza do Seminario de Estudos Galegos 15705
Santiago De Compostela
Spain

PO Number (optional)

N/A

Payment options

Invoice

PENDING ORDER CONFIRMATION

Confirmation Number: Pending

Order Date: 18-May-2024

1. Journal of cell science

0,00 EUR

Article: Deconstructing the third dimension: how 3D culture microenvironments alter cellular cues.

Order License ID	Pending	**Publisher**	Company of Biologists Ltd.
ISSN	0021-9533		
Type of Use	Republish in a thesis/dissertation	**Portion**	Chart/graph/table/figure

LICENSED CONTENT

Publication Title	Journal of cell science	**Rightsholder**	The Company of Biologists Ltd.
Article Title	Deconstructing the third dimension: how 3D culture microenvironments alter cellular cues.	**Publication Type**	Journal
		Start Page	3015
		End Page	3024
Author/Editor	COMPANY OF BIOLOGISTS.	**Issue**	Pt 13
		Volume	125
Date	01/01/1966		
Language	English		
Country	United Kingdom of Great Britain and Northern Ireland		

REQUEST DETAILS

Portion Type	Chart/graph/table/figure	**Distribution**	Worldwide
Number of Charts / Graphs / Tables / Figures Requested	1	**Translation**	Original language of publication
		Copies for the Disabled?	No
Format (select all that apply)	Print, Electronic	**Minor Editing Privileges?**	No
Who Will Republish the Content?	Academic institution	**Incidental Promotional Use?**	No
Duration of Use	Life of current edition	**Currency**	EUR
Lifetime Unit Quantity	Up to 499		
Rights Requested	Main product		

NEW WORK DETAILS

Title	Development of aerogel-based formulations for regenerative medicine	**Institution Name**	University of Santiago de Compostela (USC)
		Expected Presentation Date	2024-07-26
Instructor Name	Carlos Alberto García González		

ADDITIONAL DETAILS

Order Reference Number	N/A	**The Requesting Person / Organization to Appear on the License**	Ana Iglesias Mejuto (USC)

REQUESTED CONTENT DETAILS

Title, Description or Numeric Reference of the Portion(s)	Figure 2	**Title of the Article / Chapter the Portion Is From**	Deconstructing the third dimension: how 3D culture microenvironments alter cellular cues.
Editor of Portion(s)	Baker, Brendon M.; Chen, Christopher S.		
Volume / Edition	125	**Author of Portion(s)**	Baker, Brendon M.; Chen, Christopher S.

Page or Page Range of Portion	3015-3024	**Issue, if Republishing an Article From a Serial**	Pt 13
		Publication Date of Portion	2012-07-01

RIGHTSHOLDER TERMS AND CONDITIONS

The acknowledgement should state "Reproduced / adapted with permission" and give the source journal name. The acknowledgement should either provide full citation details or refer to the relevant citation in the article reference list. The full citation details should include authors, journal, year, volume, issue and page citation. Where appearing online or in other electronic media, a link should be provided to the original article (e.g. via DOI): Development: dev.biologists.org Disease Models & Mechanisms: dmm.biologists.org Journal of Cell Science: jcs.biologists.org The Journal of Experimental Biology: jeb.biologists.org

Total Items: 1

Total Due: 0,00 EUR

Accepted: Marketplace Permissions General Terms and Conditions and any applicable Publisher Terms and Conditions

Marketplace

Order Confirmation

Thank you, your order has been placed. An email confirmation has been sent to you. Your order license details and printable licenses will be available within 24 hours. Please access Manage Account for final order details.

This is not an invoice. Please go to manage account to access your order history and invoices.

CUSTOMER INFORMATION

Payment by invoice: You can cancel your order until the invoice is generated by contacting customer service.

Billing Address

Ms. Ana Iglesias-Mejuto
Praza do Seminario de Estudos Galegos 15705
Santiago De Compostela
Spain

+34 881814993
ana.iglesias.mejuto@rai.usc.es

Customer Location

Ms. Ana Iglesias-Mejuto
Praza do Seminario de Estudos Galegos 15705
Santiago De Compostela
Spain

PO Number (optional)

N/A

Payment options

Invoice

PENDING ORDER CONFIRMATION

Confirmation Number: Pending

Order Date: 18-May-2024

1. Ceramics international

0,00 EUR

Article: A review of bioceramic porous scaffolds for hard tissue applications: Effects of structural features

Order License ID	Pending	**Publisher**	PERGAMON
ISSN	0272-8842	**Portion**	Chart/graph/table/figure
Type of Use	Republish in a thesis/dissertation		

LICENSED CONTENT

Publication Title	Ceramics international	**Publication Type**	Journal
Article Title	A review of bioceramic porous scaffolds for hard tissue applications: Effects of structural features	**Start Page**	15725
		End Page	15739
		Issue	10
		Volume	46
Date	01/01/1974		
Language	English		
Country	United Kingdom of Great Britain and Northern Ireland		
Rightsholder	Elsevier Science & Technology Journals		

REQUEST DETAILS

Portion Type	Chart/graph/table/figure	**Distribution**	Worldwide
Number of Charts / Graphs / Tables / Figures Requested	1	**Translation**	Original language of publication
		Copies for the Disabled?	No
Format (select all that apply)	Print, Electronic	**Minor Editing Privileges?**	No
Who Will Republish the Content?	Academic institution	**Incidental Promotional Use?**	No
Duration of Use	Life of current edition	**Currency**	EUR
Lifetime Unit Quantity	Up to 499		
Rights Requested	Main product		

NEW WORK DETAILS

Title	Development of aerogel-based formulations for regenerative medicine	**Institution Name**	University of Santiago de Compostela (USC)
		Expected Presentation Date	2024-07-26
Instructor Name	Carlos Alberto García González		

ADDITIONAL DETAILS

Order Reference Number	N/A	**The Requesting Person / Organization to Appear on the License**	Ana Iglesias Mejuto (USC)

REQUESTED CONTENT DETAILS

Title, Description or Numeric Reference of the Portion(s)	Figure 1	**Title of the Article / Chapter the Portion Is From**	A review of bioceramic porous scaffolds for hard tissue applications: Effects of structural features
Editor of Portion(s)	Jodati, Hossein; Yılmaz, Bengi; Evis, Zafer		
Volume / Edition	46	**Author of Portion(s)**	Jodati, Hossein; Yılmaz, Bengi; Evis, Zafer

Page or Page Range of Portion	15725-15739	**Issue, if Republishing an Article From a Serial**	10
		Publication Date of Portion	2020-07-01

RIGHTSHOLDER TERMS AND CONDITIONS

Elsevier publishes Open Access articles in both its Open Access journals and via its Open Access articles option in subscription journals, for which an author selects a user license permitting certain types of reuse without permission. Before proceeding please check if the article is Open Access on http://www.sciencedirect.com and refer to the user license for the individual article. Any reuse not included in the user license terms will require permission. You must always fully and appropriately credit the author and source. If any part of the material to be used (for example, figures) has appeared in the Elsevier publication for which you are seeking permission, with credit or acknowledgement to another source it is the responsibility of the user to ensure their reuse complies with the terms and conditions determined by the rights holder. Please contact permissions@elsevier.com with any queries.

Total Items: 1

Total Due: 0,00 EUR

Accepted: Marketplace Permissions General Terms and Conditions and any applicable Publisher Terms and Conditions

Marketplace

Order Confirmation

Thank you, your order has been placed. An email confirmation has been sent to you. Your order license details and printable licenses will be available within 24 hours. Please access Manage Account for final order details.

This is not an invoice. Please go to manage account to access your order history and invoices.

CUSTOMER INFORMATION

Payment by invoice: You can cancel your order until the invoice is generated by contacting customer service.

Billing Address

Ms. Ana Iglesias-Mejuto
Praza do Seminario de Estudos Galegos 15705
Santiago De Compostela
Spain

+34 881814993
ana.iglesias.mejuto@rai.usc.es

Customer Location

Ms. Ana Iglesias-Mejuto
Praza do Seminario de Estudos Galegos 15705
Santiago De Compostela
Spain

PO Number (optional)

N/A

Payment options

Invoice

PENDING ORDER CONFIRMATION

Confirmation Number: Pending

Order Date: 18-May-2024

1. Advanced drug delivery reviews

0,00 EUR

Article: In situ forming injectable hydrogels for drug delivery and wound repair

Order License ID	Pending	**Publisher**	ELSEVIER BV
ISSN	0169-409X	**Portion**	Chart/graph/table/figure
Type of Use	Republish in a thesis/dissertation		

LICENSED CONTENT

Publication Title	Advanced drug delivery reviews	**Rightsholder**	Elsevier Science & Technology Journals
Article Title	In situ forming injectable hydrogels for drug delivery and wound repair	**Publication Type**	Journal
		Start Page	167
		End Page	184
Date	01/01/1987	**Volume**	127
Language	English		
Country	Netherlands		

REQUEST DETAILS

Portion Type	Chart/graph/table/figure	**Distribution**	Worldwide
Number of Charts / Graphs / Tables / Figures Requested	1	**Translation**	Original language of publication
		Copies for the Disabled?	No
Format (select all that apply)	Print, Electronic	**Minor Editing Privileges?**	No
Who Will Republish the Content?	Academic institution	**Incidental Promotional Use?**	No
Duration of Use	Life of current edition	**Currency**	EUR
Lifetime Unit Quantity	Up to 499		
Rights Requested	Main product		

NEW WORK DETAILS

Title	Development of aerogel-based formulations for regenerative medicine	**Institution Name**	University of Santiago de Compostela (USC)
		Expected Presentation Date	2024-07-26
Instructor Name	Carlos Alberto García González		

ADDITIONAL DETAILS

Order Reference Number	N/A	**The Requesting Person / Organization to Appear on the License**	Ana Iglesias Mejuto (USC)

REQUESTED CONTENT DETAILS

Title, Description or Numeric Reference of the Portion(s)	Figure 1	**Title of the Article / Chapter the Portion Is From**	In situ forming injectable hydrogels for drug delivery and wound repair
Editor of Portion(s)	Dimatteo, Robert; Darling, Nicole J.; Segura, Tatiana	**Author of Portion(s)**	Dimatteo, Robert; Darling, Nicole J.; Segura, Tatiana
Volume / Edition	127		
Page or Page Range of Portion	167-184	**Issue, if Republishing an Article From a Serial**	N/A

Publication Date of Portion	2018-03-19

RIGHTSHOLDER TERMS AND CONDITIONS

Elsevier publishes Open Access articles in both its Open Access journals and via its Open Access articles option in subscription journals, for which an author selects a user license permitting certain types of reuse without permission. Before proceeding please check if the article is Open Access on http://www.sciencedirect.com and refer to the user license for the individual article. Any reuse not included in the user license terms will require permission. You must always fully and appropriately credit the author and source. If any part of the material to be used (for example, figures) has appeared in the Elsevier publication for which you are seeking permission, with credit or acknowledgement to another source it is the responsibility of the user to ensure their reuse complies with the terms and conditions determined by the rights holder. Please contact permissions@elsevier.com with any queries.

Total Items: 1

Total Due: 0,00 EUR

Accepted: Marketplace Permissions General Terms and Conditions and any applicable Publisher Terms and Conditions

Marketplace

Order Confirmation

Thank you, your order has been placed. An email confirmation has been sent to you. Your order license details and printable licenses will be available within 24 hours. Please access Manage Account for final order details.

This is not an invoice. Please go to manage account to access your order history and invoices.

CUSTOMER INFORMATION

Payment by invoice: You can cancel your order until the invoice is generated by contacting customer service.

Billing Address

Ms. Ana Iglesias-Mejuto
Praza do Seminario de Estudos Galegos 15705
Santiago De Compostela
Spain

+34 881814993
ana.iglesias.mejuto@rai.usc.es

Customer Location

Ms. Ana Iglesias-Mejuto
Praza do Seminario de Estudos Galegos 15705
Santiago De Compostela
Spain

PO Number (optional)

N/A

Payment options

Invoice

PENDING ORDER CONFIRMATION

Confirmation Number: Pending

Order Date: 18-May-2024

1. Carbohydrate polymers

0,00 EUR

Article: Prilling and supercritical drying: A successful duo to produce core-shell polysaccharide aerogel beads for wound healing.

Order License ID	Pending	**Publisher**	PERGAMON
ISSN	0144-8617	**Portion**	Chart/graph/table/figure
Type of Use	Republish in a thesis/dissertation		

LICENSED CONTENT

Publication Title	Carbohydrate polymers	**Rightsholder**	Elsevier Science & Technology Journals
Article Title	Prilling and supercritical drying: A successful duo to produce core-shell polysaccharide aerogel beads for wound healing.	**Publication Type**	Journal
		Start Page	482
		End Page	489
		Volume	147
Date	01/01/1981		
Language	English, English		
Country	United Kingdom of Great Britain and Northern Ireland		

REQUEST DETAILS

Portion Type	Chart/graph/table/figure	**Distribution**	Worldwide
Number of Charts / Graphs / Tables / Figures Requested	1	**Translation**	Original language of publication
		Copies for the Disabled?	No
Format (select all that apply)	Print, Electronic	**Minor Editing Privileges?**	No
Who Will Republish the Content?	Academic institution	**Incidental Promotional Use?**	No
Duration of Use	Life of current edition	**Currency**	EUR
Lifetime Unit Quantity	Up to 499		
Rights Requested	Main product		

NEW WORK DETAILS

Title	Development of aerogel-based formulations for regenerative medicine	**Institution Name**	University of Santiago de Compostela (USC)
		Expected Presentation Date	2024-07-26
Instructor Name	Carlos Alberto García González		

ADDITIONAL DETAILS

Order Reference Number	N/A	**The Requesting Person / Organization to Appear on the License**	Ana Iglesias Mejuto (USC)

REQUESTED CONTENT DETAILS

Title, Description or Numeric Reference of the Portion(s)	Figure 6	**Title of the Article / Chapter the Portion Is From**	Prilling and supercritical drying: A successful duo to produce core-shell polysaccharide aerogel beads for wound healing.

Editor of Portion(s)	De Cicco, Felicetta; Russo, Paola; Reverchon, Ernesto; García-González, Carlos A.; Aquino, Rita Patrizia; Del Gaudio, Pasquale	**Author of Portion(s)**	De Cicco, Felicetta; Russo, Paola; Reverchon, Ernesto; García-González, Carlos A.; Aquino, Rita Patrizia; Del Gaudio, Pasquale
Volume / Edition	147	**Issue, if Republishing an Article From a Serial**	N/A
Page or Page Range of Portion	482-489	**Publication Date of Portion**	2016-08-20

RIGHTSHOLDER TERMS AND CONDITIONS

Elsevier publishes Open Access articles in both its Open Access journals and via its Open Access articles option in subscription journals, for which an author selects a user license permitting certain types of reuse without permission. Before proceeding please check if the article is Open Access on http://www.sciencedirect.com and refer to the user license for the individual article. Any reuse not included in the user license terms will require permission. You must always fully and appropriately credit the author and source. If any part of the material to be used (for example, figures) has appeared in the Elsevier publication for which you are seeking permission, with credit or acknowledgement to another source it is the responsibility of the user to ensure their reuse complies with the terms and conditions determined by the rights holder. Please contact permissions@elsevier.com with any queries.

Total Items: 1

Total Due: 0,00 EUR

Accepted: Marketplace Permissions General Terms and Conditions and any applicable Publisher Terms and Conditions

Marketplace

Order Confirmation

Thank you, your order has been placed. An email confirmation has been sent to you. Your order license details and printable licenses will be available within 24 hours. Please access Manage Account for final order details.

This is not an invoice. Please go to manage account to access your order history and invoices.

CUSTOMER INFORMATION

Payment by invoice: You can cancel your order until the invoice is generated by contacting customer service.

Billing Address

Ms. Ana Iglesias-Mejuto
Praza do Seminario de Estudos Galegos 15705
Santiago De Compostela
Spain

+34 881814993
ana.iglesias.mejuto@rai.usc.es

Customer Location

Ms. Ana Iglesias-Mejuto
Praza do Seminario de Estudos Galegos 15705
Santiago De Compostela
Spain

PO Number (optional)

N/A

Payment options

Invoice

PENDING ORDER CONFIRMATION

Confirmation Number: Pending

Order Date: 18-May-2024

1. The Journal of supercritical fluids

0,00 EUR

Article: Alginate aerogels carrying calcium, zinc and silver cations for wound care: Fabrication and metal detection

Order License ID	Pending	**Publisher**	ELSEVIER BV
ISSN	0896-8446	**Portion**	Chart/graph/table/figure
Type of Use	Republish in a thesis/dissertation		

LICENSED CONTENT

Publication Title	The Journal of supercritical fluids	**Rightsholder**	Elsevier Science & Technology Journals
Article Title	Alginate aerogels carrying calcium, zinc and silver cations for wound care: Fabrication and metal detection	**Publication Type**	Journal
		Start Page	104545
		Volume	153
Date	01/01/1988		
Language	Dutch		
Country	Netherlands		

REQUEST DETAILS

Portion Type	Chart/graph/table/figure	**Distribution**	Worldwide
Number of Charts / Graphs / Tables / Figures Requested	1	**Translation**	Original language of publication
		Copies for the Disabled?	No
Format (select all that apply)	Print, Electronic	**Minor Editing Privileges?**	No
Who Will Republish the Content?	Academic institution	**Incidental Promotional Use?**	No
Duration of Use	Life of current edition	**Currency**	EUR
Lifetime Unit Quantity	Up to 499		
Rights Requested	Main product		

NEW WORK DETAILS

Title	Development of aerogel-based formulations for regenerative medicine	**Institution Name**	University of Santiago de Compostela
		Expected Presentation Date	2024-07-26
Instructor Name	Carlos Alberto García González		

ADDITIONAL DETAILS

Order Reference Number	N/A	**The Requesting Person / Organization to Appear on the License**	Ana Iglesias Mejuto (USC)

REQUESTED CONTENT DETAILS

Title, Description or Numeric Reference of the Portion(s)	Figure 7	**Title of the Article / Chapter the Portion Is From**	Alginate aerogels carrying calcium, zinc and silver cations for wound care: Fabrication and metal detection

Editor of Portion(s)	Raman, S.P.; Keil, Claudia; Dieringer, Paul; Hübner, Christopher; Bueno, Alberto; Gurikov, Pavel; Nissen, Jörg; Holtkamp, Michael; Karst, Uwe; Haase, Hajo; Smirnova, Irina	**Author of Portion(s)**	Raman, S.P.; Keil, Claudia; Dieringer, Paul; Hübner, Christopher; Bueno, Alberto; Gurikov, Pavel; Nissen, Jörg; Holtkamp, Michael; Karst, Uwe; Haase, Hajo; Smirnova, Irina
Volume / Edition	153	**Issue, if Republishing an Article From a Serial**	N/A
Page or Page Range of Portion	104545	**Publication Date of Portion**	2019-11-01

RIGHTSHOLDER TERMS AND CONDITIONS

Elsevier publishes Open Access articles in both its Open Access journals and via its Open Access articles option in subscription journals, for which an author selects a user license permitting certain types of reuse without permission. Before proceeding please check if the article is Open Access on http://www.sciencedirect.com and refer to the user license for the individual article. Any reuse not included in the user license terms will require permission. You must always fully and appropriately credit the author and source. If any part of the material to be used (for example, figures) has appeared in the Elsevier publication for which you are seeking permission, with credit or acknowledgement to another source it is the responsibility of the user to ensure their reuse complies with the terms and conditions determined by the rights holder. Please contact permissions@elsevier.com with any queries.

Total Items: 1

Total Due: 0,00 EUR

Accepted: Marketplace Permissions General Terms and Conditions and any applicable Publisher Terms and Conditions

Marketplace

Order Confirmation

Thank you, your order has been placed. An email confirmation has been sent to you. Your order license details and printable licenses will be available within 24 hours. Please access Manage Account for final order details.

This is not an invoice. Please go to manage account to access your order history and invoices.

CUSTOMER INFORMATION

Payment by invoice: You can cancel your order until the invoice is generated by contacting customer service.

Billing Address

Ms. Ana Iglesias-Mejuto
Praza do Seminario de Estudos Galegos 15705
Santiago De Compostela
Spain

+34 881814993
ana.iglesias.mejuto@rai.usc.es

Customer Location

Ms. Ana Iglesias-Mejuto
Praza do Seminario de Estudos Galegos 15705
Santiago De Compostela
Spain

PO Number (optional)

N/A

Payment options

Invoice

PENDING ORDER CONFIRMATION

Confirmation Number: Pending

Order Date: 18-May-2024

1. Journal of materials chemistry. B, Materials for biology and medicine

0,00 EUR

Article: Visualization of in situ hydrogels by MRI in vivo.

Order License ID	Pending	**Publisher**	Royal Society of Chemistry
ISSN	2050-750X		
Type of Use	Republish in a thesis/dissertation	**Portion**	Chart/graph/table/figure

LICENSED CONTENT

Publication Title	Journal of materials chemistry. B, Materials for biology and medicine	**Rightsholder**	Royal Society of Chemistry
Article Title	Visualization of in situ hydrogels by MRI in vivo.	**Publication Type**	Journal
Author/Editor	Royal Society of Chemistry (Great Britain)	**Start Page**	1343
Date	01/01/2012	**End Page**	1353
Language	English	**Issue**	7
Country	United Kingdom of Great Britain and Northern Ireland	**Volume**	4

REQUEST DETAILS

Portion Type	Chart/graph/table/figure	**Distribution**	Worldwide
Number of Charts / Graphs / Tables / Figures Requested	2	**Translation**	Original language of publication
Format (select all that apply)	Print, Electronic	**Copies for the Disabled?**	No
Who Will Republish the Content?	Academic institution	**Minor Editing Privileges?**	No
Duration of Use	Life of current edition	**Incidental Promotional Use?**	No
Lifetime Unit Quantity	Up to 499	**Currency**	EUR
Rights Requested	Main product		

NEW WORK DETAILS

Title	Development of aerogel-based formulations for regenerative medicine	**Institution Name**	University of Santiago de Compostela (USC)
Instructor Name	Carlos Alberto García González	**Expected Presentation Date**	2024-07-26

ADDITIONAL DETAILS

Order Reference Number	N/A	**The Requesting Person / Organization to Appear on the License**	Ana Iglesias Mejuto (USC)

REQUESTED CONTENT DETAILS

Title, Description or Numeric Reference of the Portion(s)	Figure 3, Figure 7	**Title of the Article / Chapter the Portion Is From**	Visualization of in situ hydrogels by MRI in vivo.
Editor of Portion(s)	Liu, Jia; Wang, Ke; Luan, Jie; Wen, Zhi; Wang, Lei; Liu, Zhilan; Wu, Guangyao; Zhuo, Renxi	**Author of Portion(s)**	Liu, Jia; Wang, Ke; Luan, Jie; Wen, Zhi; Wang, Lei; Liu, Zhilan; Wu, Guangyao; Zhuo, Renxi

Volume / Edition	4	**Issue, if Republishing an Article From a Serial**	7
Page or Page Range of Portion	1343-1353	**Publication Date of Portion**	2016-02-21

Total Items: 1

Total Due: 0,00 EUR

Accepted: Marketplace Permissions General Terms and Conditions and any applicable Publisher Terms and Conditions

CCC Marketplace

All types | 10.3390/s16111789 | Advanced Search | Search Tips

Filter your results:

No filters are available

0 publications and 1 articles/chapters matched your search term(s)

Hide filters

Article/Chapter Results

Sort by Relevance

Preparation, Characterization and Activity of a Peptide-Cellulosic Aerogel Protease Sensor from Cotton.

Edwards, J Vincent; Fontenot, Krystal R; Prevost, Nicolette T; ...More *Sensors*, 01 Nov 2016, Vol. 16, Issue 11, pages 1789 - ...

ISSN: 14248220
DOI: 10.3390/s16111789
PMID: 27792201
PMCID: PMC5134448

Publisher: MDPI; MOLECULAR DIVERSITY PRESERVATION INTERNATIONAL
Language: English
Country: Switzerland

Details >

Request Reprints/ePrints | Request Single Copy | Request Permission | Open Access - Creative Commons CC BY 4.0

CCC © 2024 Copyright Clearance Center, Inc. All rights reserved.

USC UNIVERSIDADE DE SANTIAGO DE COMPOSTELA

CCC RightsLink



3D-printed alginate-hydroxyapatite aerogel scaffolds for bone tissue engineering

Author: Ana Iglesias-Mejuto,Carlos A. García-González

Publication: Materials Science and Engineering: C

Publisher: Elsevier

Date: December 2021

© 2021 The Authors. Published by Elsevier B.V.

Creative Commons

This is an open access article distributed under the terms of the Creative Commons CC-BY license, which permits unrestricted use, distribution, and reproduction in any medium, provided the original work is properly cited.

You are not required to obtain permission to reuse this article.

To request permission for a type of use not listed, please contact Elsevier Global Rights Department.

Are you the author of this Elsevier journal article?

© 2024 Copyright - All Rights Reserved | Copyright Clearance Center, Inc. | Privacy statement | Data Security and Privacy | For California Residents | Terms and ConditionsComments? We would like to hear from you. E-mail us at customercare@copyright.com

USC UNIVERSIDADE DE SANTIAGO DE COMPOSTELA

CCC Marketplace

All types | 10.3390/polym14061211 | Advanced Search | Search Tips

Filter your results:

No filters are available

0 publications and 1 articles/chapters matched your search term(s)

Hide filters

Article/Chapter Results

Sort by Relevance

3D-Printed, Dual Crosslinked and Sterile Aerogel Scaffolds for Bone Tissue Engineering

Iglesias-Mejuto, Ana; García-González, Carlos A. *Polymers*, 17 Mar 2022, Vol. 14, Issue 6, pages 1211 - ...

ISSN: 20734360
DOI: 10.3390/polym14061211
PMID: 35335542
PMCID: PMC8951756

Publisher: MDPI AG; Molecular Diversity Preservation International (MDPI)
Language: English
Country: Switzerland
URL: https://www.mdpi.com/2073-4360/14/6/1211

Details >

Request Reprints/ePrints | Request Single Copy | Request Permission | Open Access - Creative Commons CC BY 4.0

CCC © 2024 Copyright Clearance Center, Inc. All rights reserved.

USC UNIVERSIDADE DE SANTIAGO DE COMPOSTELA

CCC Marketplace

All types | 10.3390/gels10010013 | Advanced Search | Search Tips

Filter your results:

No filters are available

0 publications and 1 articles/chapters matched your search term(s)

Hide filters

Article/Chapter Results

Sort by Relevance

Synthesis of Highly Luminescent Silica-Coated Upconversion Nanoparticles from Lanthanide Oxides or Nitrates Using Co-Precipitation and Sol–Gel Methods

Iglesias-Mejuto, Ana; Lamy-Mendes, Alyne; Pina, João; Costa, Benilde F. ...More *Gels*, 01 Jan 2024, Vol. 10, Issue 1, pages 13 - ...

ISSN: 23102861
DOI: 10.3390/gels10010013
PMID: 38247736
PMCID: PMC10815212

Publisher: MDPI AG
Language: English
Country: Switzerland
URL: https://www.mdpi.com/2310-2861/10/1/13

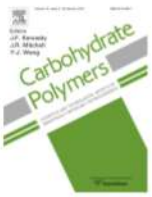
Details >

Request Reprints/ePrints | Request Single Copy | Request Permission | Open Access - Creative Commons CC BY 4.0

CCC © 2024 Copyright Clearance Center, Inc. All rights reserved.

USC UNIVERSIDADE DE SANTIAGO DE COMPOSTELA

RightsLink



Vancomycin-loaded methylcellulose aerogel scaffolds for advanced bone tissue engineering

Author:
Ana Iglesias-Mejuto,Beatriz Magariños,Tânia Ferreira-Gonçalves,Ricardo Starbird-Pérez,Carmen Álvarez-Lorenzo,Catarina Pinto Reis,Inés Ardao,Carlos A. García-González

Publication: Carbohydrate Polymers

Publisher: Elsevier

Date: 15 January 2024

© 2023 The Authors. Published by Elsevier Ltd.

Creative Commons

This is an open access article distributed under the terms of the Creative Commons CC-BY license, which permits unrestricted use, distribution, and reproduction in any medium, provided the original work is properly cited.

You are not required to obtain permission to reuse this article.

To request permission for a type of use not listed, please contact Elsevier Global Rights Department.

Are you the author of this Elsevier journal article?

© 2024 Copyright - All Rights Reserved | Copyright Clearance Center, Inc. | Privacy statement | Data Security and Privacy | For California Residents

USC UNIVERSIDADE DE SANTIAGO DE COMPOSTELA

RightsLink

SPRINGER NATURE

Cellulose-in-cellulose 3D-printed bioaerogels for bone tissue engineering

Author: Ana Iglesias-Mejuto et al

Publication: Cellulose

Publisher: Springer Nature

Date: Dec 12, 2023

Copyright © 2023, The Author(s)

Creative Commons

This is an open access article distributed under the terms of the Creative Commons CC BY license, which permits unrestricted use, distribution, and reproduction in any medium, provided the original work is properly cited.

You are not required to obtain permission to reuse this article.

To request permission for a type of use not listed, please contact Springer Nature

© 2024 Copyright - All Rights Reserved | Copyright Clearance Center, Inc. | Privacy statement | Data Security and Privacy | For California Residents | Terms and ConditionsComments? We would like to hear from you. E-mail us at customercare@copyright.com

USC UNIVERSIDADE DE SANTIAGO DE COMPOSTELA

The prevalence of infections and the absence of tissue regeneration motivate the study of new strategies for the manufacturing of bone implants. Dual porosity and drug loading into scaffolds are needed to promote the long-term new bone tissue formation while the customization of the implants is required in personalized medicine. In this PhD Thesis, a dual processing strategy was developed by combining the 3D-printing and the supercritical fluid technologies to manufacture 3D-printed and sterile aerogels for bone tissue engineering applications. Furthermore, the monitoring of aerogels and their degradation products after implantation was studied *in vivo* for the first time. This work aims to endow bioaerogels with new capabilities while preserving their safety profile and advanced physicochemical performance.